CZECH TECHNICAL UNIVERSITY IN PRAGUE
FACULTY OF CIVIL ENGINEERING
DEPARTMENT OF MECHANICS

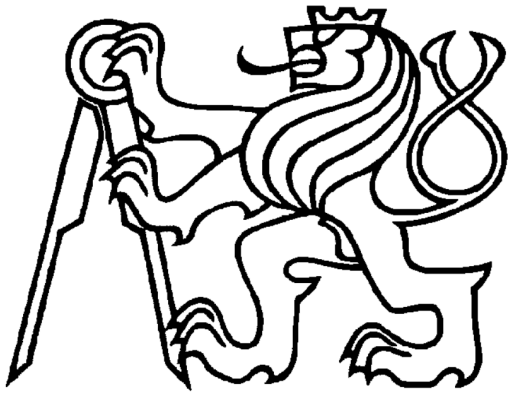

NUMERICAL ANALYSIS OF COUPLED PROBLEMS IN SELECTED ENGINEERING APPLICATIONS

By

Tomáš Krejčí

HABILITATION THESIS

Prague February 2022

Acknowledgments

First of all, I would like to express my deep gratitude and thanks to Professor Jiří Šejnoha, whose unfailing enthusiasm, tremendous support and encouragement provided continuous inspiration throughout my career. In addition, special gratitude is to my friends and colleagues Jaroslav Kruis, Tomáš Koudelka and Jiří Maděra with whom I had numerous fruitful and inspiring discussions and cooperations on topics addressed in the thesis.

I extend my deep appreciation to members of the Department, Michal Šejnoha, Daniel Rypl, Bořek Patzák, Jan Zeman, Matěj Lepš, Jan Vorel and Jan Sýkora for their encouragement, assistance and interest in many enlightening discussions.

Contents

List of Figures

List of Tables

Chapter 1

Thesis summary

1.1 Introduction

The modern design and assessment of building structures cannot be realized without assuming temperature and moisture changes caused mainly by climatic conditions. Research in concrete and other porous materials shows a correct prediction of temperature and moisture content distribution and history necessary for a realistic determination of phenomena like shrinkage, creep, aging, thermal dilatation, swelling, cracking, plastic deformation, and others. Furthermore, most of the material properties are influenced directly by temperature and moisture fields.

In the last four decades, material behavior modeling has experienced a considerable development, particularly in the connection with computer technology development. In the case of porous materials modeling, a significant progress has been made, and many material models have been developed. In many cases, they describe the behavior of only one phenomenon, and therefore it is necessary to use their combinations. In many application areas, the solution of coupled hydro-thermal or thermo-hydro-mechanical analyses is required. It includes problems such as evaluating the safety and service life of remarkable concrete structures, reconstruction of historical masonry structures, nuclear waste disposal, geomechanical issues, and many others.

Porous materials are characterized by a complicated internal structure with open and closed pores usually filled with water, water vapor, and dry air. Models describing an interaction between the constituents and their transport through a porous matrix are based on the macromechanical approach with phenomenological and mixture theory models and the micromechanical viewpoint comprising averaging theories. A comprehensive review of porous media theories can be found in [de Boer, 1996]. In this reference, the concept of volume fraction introduced in [Woltman, 1974] is discussed together with two fundamental contributions about the diffusion of mixtures [Fick, 1855] and the motion of a liquid phase [Darcy, 1856]. The fundamental works [Fillunger, 1913] and [von Terzaghi, 1923] about the deformation of saturated soils using the effective stress principle and its generalization and extension in [Biot, 1941] and [Biot, 1956] were also mentioned. As for micromechanical models, the underlying theory was formulated in [Hassanizadeh and Gray, 1979] and summarized and well-arranged together with the extended Biot's approach in [Schrefler and Lewis, 1998]. In the case of building materials, the phenomenological models are top-rated. Their advanced versions can be found, e.g., in [Pedersen, 1990] and [Künzel and Kiessl, 1997], which are based on experimental results and physical evidence.

Individual attention in mathematical modeling of porous materials was paid to concrete and concrete structures, where Bažants' models are the most popular for analyzing the long-term

behavior of concrete, including hydro-thermal effects. A typical phenomenological approach considering single moisture flux, i.e., a single fluid phase, which includes both liquid water and moist air, is introduced, e.g., in [Bažant and Najjar, 1972], [Bažant and Thonguthai, 1979], [Bažant and Chern, 1985] and [Bažant and Kaplan, 1996] considering high temperatures exposure. The model equations are usually derived employing thermodynamics of irreversible phenomena. The parameters are often determined by inverse problem solutions using known results of experimental tests to obtain the best agreement between theoretical prediction and experimental evidence. A comprehensive overview of developed models can be found in [Bažant, 1988], [Jirásek and Bažant, 2002], and in the latest book [Bažant and Jirásek, 2018], which is intended for researches, educators, and practicing engineers.

Several models have been developed to predict temperature and pore pressure distributions in concrete exposed to fire conditions. All of them utilize an analysis procedure that involves the strongly coupled heat and mass transfer within the concrete. Such models typically include consideration of the mass transfer of air and water by diffusion as mentioned above, forced convection, conversion of liquid water to vapor and release of water of hydration. They also comprise heat transfer by conduction, mass diffusion, and forced convection with the inclusion of the effects of the heat of vaporization of water, the heat of dehydration, and the thermal capacity of the concrete [Pesavento, 2000].

Many concrete modeling conclusions are extended and modified for masonry materials and structures. They are mainly models describing mechanical behavior like damage and plasticity models. Homogenization techniques usually treat the heterogeneity of masonry constituents providing effective macroscopic properties and response. A brief overview of several of them is presented in [Milani, 2015], [Lourenco et al., 2007], and [Krejčí et al., 2021]

Soils are simulated as partially saturated or fully saturated porous media in geomechanics. The description of consolidation and other slow, quasi-static phenomena coupled with moisture flow is often based on the effective stresses principle. The application area is vast, comprising, e.g., the transient analysis of footing, pile foundation, and soil-structure interaction. For this purpose, the thermo-hydro-mechanical studies are supported by linear or non-linear elastic and elastoplastic constitutive relationships suitable for quasi-static situations. Frequently used models include the Mohr-Coulomb model [Zienkiewicz and Taylor, 2000], [Nayak and Zienkiewicz, 1972] and the critical state model - Cam-clay model [Roscoe et al., 1963], [Schofield and Wroth, 1968] and its extended version [Roscoe and Burland, 1968]. In recent years, the very discussed and researched topic in geomechanical engineering is nuclear waste disposal, which demands high safety, reliability, and durability. Barriers built from bentonite as a buffer material are considered to ensure the impermeability of such safe nuclear repositories. Many constitutive models for expansive clays and bentonite were introduced, accounting for the coupling of heat, moisture (liquid water and water vapor), and air transfer in a deformable unsaturated soil with two distinct pore systems. Independent coupled models are considered for each structural level, micro and macro level. The models are linked using a coupling function to obtain a global response. A pioneering model for such a double structure approach was proposed in [Alonso et al., 1995], [Alonso et al., 1999] and [Alonso et al., 2011] combining existing plasticity models with a simple reversible model for microstructure. Recent research in modeling the hydro-mechanical or thermo-hydro-mechanical behavior of unsaturated soils shows the need to couple mechanical and hydraulic responses. The volumetric deformation of the soil skeleton influences the degree saturation and the value of suction, which affects the effective stress and mechanical properties. This dependency was introduced into the latest double structure models presented, e.g., in [Mašín, 2013],[Mašín and Khalili, 2016]

and [Mašín, 2017], where the macrostructural mechanical model is based on the existing hypoplastic model. Hydro-mechanical or thermo-hydro-mechanical coupling at each structural level is efficiently achieved by linking the effective stresses formulation with the water retention model. The benefit of the model is the small number of material parameters, which has been evaluated by simulation of comprehensive experimental data [Mašín, 2017].

The solution of complex coupled thermo-hydro-mechanical analyses usually leads to the solution of the system of non-linear partial differential equations. For the most real-world problems, it has to be solved numerically. Several numerical methods can be used for such systems, among which the Finite Element Method (FEM) is one of the most sophisticated and developed. The method transforms the solution of the continuous problem into the discrete problem, and the system of partial differential equations is transformed into the system of the algebraic equations, which can be linear or non-linear depending on the problem solved. More details about FEM discretisation can be found in [Bittnar and Šejnoha, 1996], [Schrefler and Lewis, 1998] or [Zienkiewicz and Taylor, 2000].

Using the discretisation by FEM, the mechanical problems are described by two or three unknown displacements in nodes for two-dimensional or three-dimensional issues, respectively. The temperature, relative humidity, or partial pressures are assumed in the nodes in the heat and moisture transfer, leading to two or three unknowns. So the general three-dimensional case is described by up to six unknowns in every node of the mesh. It implies that the requirements on computers are very high, and they increase rapidly with the increasing number of nodes in the mesh used.

The number of nodes in the mesh is influenced by the size and complexity of the geometry as well as by the boundary conditions and used materials, which often require adopting fine mesh due to steep gradients of the unknown function. These difficulties allow only simple three-dimensional problems to be solved on single-processor computers. Fortunately, a significant development of parallel computers and algorithms occurred during the last three decades. Parallel computers are based on two conception - systems with shared memory and distributed memory systems. In systems with shared memory, the memory is a pool shared by several processors or several processor cores, while in the case of distributed systems, several ordinary computers are connected by the high-speed network or even Ethernet. The advantage of the shared memory systems is the fast access to memory, but the high cost limits the system's evolution. The speed of distributed systems is lower due to communication overhead, but their development is almost unlimited. The advantages of parallel computing are effectively used to analyze real-world problems by the domain decomposition methods, which can deal with significantly larger problems and reasonably fine meshes [Kruis, 2006].

1.2 Scope of the thesis

This thesis was written based on experiences with modeling of real-world engineering problems, which were solved mostly as complex coupled thermo-mechanical and thermo-hydro-mechanical tasks with the author's participation at the Department of Mechanics of Faculty of Civil Engineering of Czech Technical University in Prague in the years 2003 - 2020. These problems were solved with the scope of projects supported by the Czech science foundation, and Technology Agency of the Czech Republic, research projects from Czech Ministry of Education Youth and Sports, and also in the research center CIDEAS which enabled collaboration between research teams at the

three civil engineering faculties in the Czech Republic, Czech technical university in Prague, Brno university of technology, VSB - Technical University of Ostrava in conjunction with the corporate research professionals in large building companies Skanska, a.s., Metrostav, a.s., EUROVIA CS, a.s., Zakládání staveb, a.s., where the involved companies required to solve concrete structures with advanced models taking into account creep effects, shrinkage, and damage effects. Coupled analyses were also essential parts of several European projects, e.g., past project MAECENAS (in the years 2001 - 2004) which was focused on modeling of aging in concrete nuclear power plant, and actual projects BEACON and EURAD dealing with the analysis of geological repositories for nuclear waste storage.

The present thesis aims to show possible strategies of combining the most widely used mathematical models describing heat and moisture transfer in porous media and the most widely used mathematical models describing the mechanical behavior of porous material and structures influenced by temperature and moisture changes. Such a combination of transport models and mechanical models leads to the numerical solution of coupled problems that can be thermo-mechanical, hydro-mechanical, or thermo-hydro-mechanical. Significant attention is paid to the computer implementation and practical applications to real-world engineering problems.

It should be noted that all described problems were solved by the SIFEL package which is developed at the Department of Mechanics by Jaroslav Kruis, Tomáš Koudelka, and Tomáš Krejčí as primary authors and several coworkers. SIFEL is developed under the GPL license, and its web pages can be found in [Kruis et al., 2021].

The thesis is organized into six chapters. Chapter 1 introduces a brief description of the basic governing equations for the main problem types - mechanics, heat transfer, and moisture transfer. It also contains a brief description of the discretisation of these nonlinear partial differential equations based on FEM. The main attention is paid to the two basic strategies of coupled problems solution - staggered approach and fully coupled approach.

Chapter 2 deals with the implementation of the FEM for the coupled problems in the SIFEL software package. The chapter summarizes basic ideas of the code, which is written in the C++ language. There is a short description of several base classes used in the code which store fundamental data used in the FEM analysis, such as topology, matrices, solvers, and internal state variables. The extensibility of the code is demonstrated on numerical examples of the coupled problems in the following chapters.

Chapters 3, 4, and 5 present three analyses selected as illustrative applications of numerical solution of coupled problems. The first - the analysis of the containment of nuclear powerplant in Temelín, the second - the analysis of Charles bridge and the third - the numerical model of bentonite in an engineered barrier for nuclear waste storage. All of them were solved to describe and predict long-term deformation processes in building and engineering structures. Each study is accompanied by a theoretical basis of the used mathematical models in condensed form. For numerical simulations, some approaches were modified and extended to capture the real structure behavior as best as possible. Moreover, all simulation results were compared and validated against in-situ measurements. The improvement of numerical models in conjunction with in-situ measurements is always considered as an invaluable tool.

The last Chapter 6 summarizes the main conclusions made of the performed analyses and also main capabilities that were implemented in the SIFEL package.

1.3 Main benefit of the thesis

The main benefit of the thesis is seen in gradual combinations and coupling of various mathematical models and their applications to real-world engineering problems. In Chapter 2, in the thermo-mechanical analysis of nuclear powerplant containment, a combination of the nonstationary heat transfer model with the concrete creep model influenced by thermal and moisture changes is presented. The creep model is extended and transferred into retardation spectra to speed up the computational time. In Chapter 4, the thermo-hygro-mechanical analysis of a historical masonry bridge couples a phenomenological hygro-thermal model extended by climatic conditions effect in the transport part with isotropic and orthotropic damage models in the mechanical part. In Chapter 5, a micromechanical approach-based hygro-thermal model for a porous deforming medium is connected with a complex hypoplastic model for expansive clays. The hygro-thermal model comes out from the derivation presented in [Schrefler and Lewis, 1998]. For coupling with the hypoplastic model, the hygro-thermal model is extended by the effect of the volumetric changes on the saturation degree and pore pressures distribution. Each analysis is supported by model verification and validation of material parameters against in situ measurements. Owing to the modularity of the used in-house software SIFEL, the thesis can serve as a guideline for implementing and coupling complex material models.

Chapter 2

Numerical solution of coupled problems and its computer implementation

2.1 Mechanical problem

Porous materials are materials with very complex behavior. For example, creep, shrinkage, thermal dilatancy, plasticity, damage, and crack propagation are the most important phenomena which should be taken into account for concrete modeling. Each model usually describes only one aspect of concrete behavior, and it is necessary to combine several effects. A variety of models can be found, e.g., for creep modeling in [CEB, 2008], [Jirásek and Bažant, 2002], for crack and damage modeling in [de Borst, 1987] and for modeling of plasticity in [Jirásek and Bažant, 2002], [Ottosen and Ristinmaa, 2005] or [Chen and Chen, 1975]. A standard approach for the particular effect combination comes out from the total strain decomposition. Under the assumption of sall strains, the total strain can be additively decomposed into individual components

$$\boldsymbol{\varepsilon}_{tot} = \boldsymbol{\varepsilon}_e + \boldsymbol{\varepsilon}_p + \boldsymbol{\varepsilon}_d + \boldsymbol{\varepsilon}_c + \boldsymbol{\varepsilon}_{sh} + \boldsymbol{\varepsilon}_{ag} + \boldsymbol{\varepsilon}_T, \tag{2.1}$$

where $\boldsymbol{\varepsilon}_{tot}$ denotes the total strain, $\boldsymbol{\varepsilon}_e$ denotes the elastic strain, $\boldsymbol{\varepsilon}_p$ stands for the plastic strain, $\boldsymbol{\varepsilon}_d$ stands for the damage strain, $\boldsymbol{\varepsilon}_c$ is the creep strain, $\boldsymbol{\varepsilon}_{sh}$ denotes part of strain caused by shrinkage, $\boldsymbol{\varepsilon}_{ag}$ stands for the strain caused by aging and $\boldsymbol{\varepsilon}_T$ is the free thermal strain.

In the mechanical problem, the system of equilibrium equations which describes equilibrium in the three-dimensional domain Ω can be written as follows

$$\boldsymbol{\partial}^T \boldsymbol{\sigma} + \boldsymbol{b} = \boldsymbol{o}, \tag{2.2}$$

where $\boldsymbol{\sigma}$ is the stress vector, $\boldsymbol{b}$ is the vector of body forces, $\boldsymbol{o}$ is the zero vector, and $\boldsymbol{\partial}$ is the

operator matrix defined as follows

$$\boldsymbol{\partial} = \begin{pmatrix} \dfrac{\partial}{\partial x} & 0 & 0 \\ 0 & \dfrac{\partial}{\partial y} & 0 \\ 0 & 0 & \dfrac{\partial}{\partial z} \\ 0 & \dfrac{\partial}{\partial z} & \dfrac{\partial}{\partial y} \\ \dfrac{\partial}{\partial z} & 0 & \dfrac{\partial}{\partial x} \\ \dfrac{\partial}{\partial y} & \dfrac{\partial}{\partial x} & 0 \end{pmatrix}. \tag{2.3}$$

The stresses $\boldsymbol{\sigma}$ in the Equation (2.2) are connected with the strains by the constitutive equations which can be written

$$\boldsymbol{\sigma} = \boldsymbol{f}(\boldsymbol{\varepsilon}). \tag{2.4}$$

The strain-displacement equations give the relation between strains $\boldsymbol{\varepsilon}$ and unknown displacements

$$\boldsymbol{\varepsilon} = \boldsymbol{\partial}\boldsymbol{u}, \tag{2.5}$$

where $\boldsymbol{u}$ is the displacement vector.

Appropriate boundary conditions must supplement Equations (2.2)

$$\boldsymbol{u} = \bar{\boldsymbol{u}} \quad \text{on} \quad \Gamma_u, \tag{2.6}$$

$$\boldsymbol{l}\boldsymbol{\sigma} = \bar{\boldsymbol{t}} \quad \text{on} \quad \Gamma_t, \tag{2.7}$$

where $\bar{\boldsymbol{u}}$ is the vector of prescribed displacements on the boundary Γ_u, and $\bar{\boldsymbol{t}}$ is the vector of surface tractions on the boundary Γ_t. The surfaces Γ_u and Γ_t have to satisfy the following relations

$$\Gamma = \Gamma_u \cup \Gamma_t, \tag{2.8}$$

$$\Gamma_u \cap \Gamma_t = 0, \tag{2.9}$$

where the symbol Γ represents the total boundary of the domain solved Ω. The matrix $\boldsymbol{l}$ contains components of the unit normal vector $\boldsymbol{n}$ to the boundary

$$\boldsymbol{l} = \begin{pmatrix} n_x & 0 & 0 & 0 & n_z & n_y \\ 0 & n_y & 0 & n_z & 0 & n_x \\ 0 & 0 & n_z & n_y & n_x & 0 \end{pmatrix}. \tag{2.10}$$

These basic equations can be discretized using the standard displacement version of the FEM [Zienkiewicz and Taylor, 2000], [Hughes, 1987], [Bittnar and Šejnoha, 1996], where the displacement components are approximated as linear combinations of given interpolation (shape) functions $N_k(\boldsymbol{x}), k = 1, \ldots, N_n$. Each of the functions is associated with one degree of freedom (DOF) of the modeled domain. The basic properties of every shape function are that $N_k(\boldsymbol{x}_k) = 1$ in the given k-th node and $N_k(\boldsymbol{x}_j) = 0, \quad k \neq j$ for all remaining nodes. Approximation of the displacement field can be written as follows

$$u_i(\boldsymbol{x}) \approx \sum_{k=1}^{N_n} N_k(\boldsymbol{x}) d_{ki}, \qquad i = 1, 2, 3 \tag{2.11}$$

where d_{ki} are unknown nodal displacements. Equation (2.11) can be rewritten in the matrix form as

$$\boldsymbol{u}(\boldsymbol{x}) \approx \boldsymbol{N}_u(\boldsymbol{x})\boldsymbol{d}_u, \tag{2.12}$$

$\boldsymbol{N}_u(\boldsymbol{x})$ is the matrix of shape functions, and $\boldsymbol{d}_u$ is the vector of unknown nodal displacements.

The kinematic Equation (2.5) can be approximated based on the above equation as

$$\boldsymbol{\varepsilon} \approx \boldsymbol{B}_u(\boldsymbol{x})\boldsymbol{d}_u, \tag{2.13}$$

where $\boldsymbol{B}_u(\boldsymbol{x})$ is the strain-displacement matrix containing the appropriate derivatives of the shape functions with respect to spatial coordinates.

Equation (2.13) can be substituted into the constitutive Equations (2.4), and the stress approximation reads

$$\boldsymbol{\sigma}(\boldsymbol{x}) \approx \boldsymbol{D}_u(\boldsymbol{x})\boldsymbol{B}_u(\boldsymbol{x})\boldsymbol{d}_u, \tag{2.14}$$

where $\boldsymbol{D}_u$ represents the material stiffness matrix. In general, the static Equations (2.2) cannot be satisfied for each point of the domain because the approximations depend on the finite number of unknown displacement parameters. In this case, Equation (2.2) can be replaced by virtual work principle [Hughes, 1987] which leads to the weak form of the equilibrium equations, and it is given by the equality

$$\int_\Omega \boldsymbol{\sigma}^T \delta\boldsymbol{\varepsilon}\,\mathrm{d}\Omega = \int_\Omega \boldsymbol{b}^T \delta\boldsymbol{u}\,\mathrm{d}\Omega + \int_{\Gamma_t} \bar{\boldsymbol{t}}^T \delta\boldsymbol{u}\,\mathrm{d}\Gamma_t, \tag{2.15}$$

which has to be satisfied for arbitrary virtual displacement field $\delta\boldsymbol{u}$ and virtual strain field $\delta\boldsymbol{\varepsilon}$ which satisfies the kinematic equation, $\delta\boldsymbol{\varepsilon} = \boldsymbol{\partial}\delta\boldsymbol{u}$ in Ω, and kinematic boundary conditions $\delta\boldsymbol{u} = \boldsymbol{0}$ on Γ_u. Assuming the same form of the virtual displacement field

$$\delta\boldsymbol{u} \approx \boldsymbol{N}_u \delta\boldsymbol{d}, \tag{2.16}$$

yields the virtual strain field derived from the kinematic equations

$$\delta\boldsymbol{\varepsilon} \approx \boldsymbol{B}_u \delta\boldsymbol{d}, \tag{2.17}$$

where $\delta\boldsymbol{d}$ is the vector of virtual displacement parameters. Similarly, the body forces and tractions from the Equation (2.2) and (2.7) can be approximated by suitable functions

$$\boldsymbol{b} \approx \boldsymbol{N}_b(\boldsymbol{x})\hat{\boldsymbol{b}}, \tag{2.18}$$

$$\bar{\boldsymbol{t}} \approx \boldsymbol{N}_t(\boldsymbol{x})\hat{\boldsymbol{t}}, \tag{2.19}$$

where the vectors $\hat{\boldsymbol{b}}$ and $\hat{\boldsymbol{t}}$ represent nodal values of body forces and tractions, respectively. $\boldsymbol{N}_b$ and $\boldsymbol{N}_t$ are matrices of suitable shape functions. In usual cases, the same type of shape functions is used to approximate unknown displacements, tractions and body forces, and virtual displacements.

Substituting Equation (2.16) and (2.17) into the Equation (2.15), the following condition is obtained

$$\int_\Omega \boldsymbol{d}_u^T \boldsymbol{B}_u^T(\boldsymbol{x})\boldsymbol{D}_u^T(\boldsymbol{x})\boldsymbol{B}_u(\boldsymbol{x})\delta\boldsymbol{d}\,\mathrm{d}\Omega = \int_\Omega \hat{\boldsymbol{b}}^T \boldsymbol{N}_u^T(\boldsymbol{x})\boldsymbol{N}_u(\boldsymbol{x})\delta\boldsymbol{d}\,\mathrm{d}\Omega + \int_{\Gamma_t} \hat{\boldsymbol{t}}^T \boldsymbol{N}_u^T(\boldsymbol{x})\boldsymbol{N}_u(\boldsymbol{x})\delta\boldsymbol{d}\,\mathrm{d}\Gamma_t. \tag{2.20}$$

The vectors $\delta\boldsymbol{d}$ and $\boldsymbol{d}_u$ are not functions of the spatial coordinates, and they can be taken out of integrals. Assuming the stiffness matrix as

$$\boldsymbol{K}_u = \int_\Omega \boldsymbol{B}_u^T(\boldsymbol{x})\boldsymbol{D}_u(\boldsymbol{x})\boldsymbol{B}_u(\boldsymbol{x})\,\mathrm{d}\Omega, \tag{2.21}$$

and the load vector as

$$\boldsymbol{f}_{ext} = \int_{\Omega} \boldsymbol{N}_u^T(\boldsymbol{x}) \boldsymbol{N}_u(\boldsymbol{x}) \hat{\boldsymbol{b}} \, \mathrm{d}\Omega + \int_{\Gamma_t} \boldsymbol{N}_u^T(\boldsymbol{x}) \boldsymbol{N}_u(\boldsymbol{x}) \hat{\boldsymbol{t}} \, \mathrm{d}\Gamma_t, \tag{2.22}$$

Equation (2.20) can be rewritten after some arrangements in the form

$$\boldsymbol{K}_u \boldsymbol{d}_u = \boldsymbol{f}_{ext}. \tag{2.23}$$

The equation's system (2.23) represents the discretized equations of equilibrium from which the vector of unknown nodal displacements $\boldsymbol{d}_u$ can be determined. If the material is linearly elastic and homogeneous, the stiffness matrix $\boldsymbol{D}_u$ contains constant coefficients and Equation (2.23) represents the linear algebraic equations system. In other cases, the stress-strain relation is nonlinear, and it can be written as

$$\boldsymbol{\sigma} = \bar{\boldsymbol{\sigma}}(\boldsymbol{\varepsilon}), \tag{2.24}$$

where $\bar{\boldsymbol{\sigma}}$ represents the constitutive operator. Using the same procedure for the strain approximation yields

$$\boldsymbol{\sigma}(\boldsymbol{x}) = \bar{\boldsymbol{\sigma}}(\boldsymbol{B}_u(\boldsymbol{x}) \boldsymbol{d}_u). \tag{2.25}$$

The weak form of the equilibrium equations takes the form

$$\int_{\Omega} \bar{\boldsymbol{\sigma}}^T(\boldsymbol{B}_u(\boldsymbol{x}) \boldsymbol{d}_u) \boldsymbol{B}_u(\boldsymbol{x}) \delta \boldsymbol{d} \, \mathrm{d}\Omega = \int_{\Omega} \hat{\boldsymbol{b}}^T \boldsymbol{N}_u^T(\boldsymbol{x}) \boldsymbol{N}_u(\boldsymbol{x}) \delta \boldsymbol{d} \, \mathrm{d}\Omega + \int_{\Gamma_t} \hat{\boldsymbol{t}}^T \boldsymbol{N}_u^T(\boldsymbol{x}) \boldsymbol{N}_u(\boldsymbol{x}) \delta \boldsymbol{d} \, \mathrm{d}\Gamma_t \tag{2.26}$$

which can be rewritten to the final form of discretized equations of equilibrium

$$\boldsymbol{f}_{int}(\boldsymbol{d}_u) = \boldsymbol{f}_{ext}, \tag{2.27}$$

where $\boldsymbol{f}_{int}(\boldsymbol{d}_u)$ denotes the vector of internal forces which is defined as

$$\boldsymbol{f}_{int}(\boldsymbol{d}_u) = \int_{\Omega} \boldsymbol{B}_u^T(\boldsymbol{x}) \bar{\boldsymbol{\sigma}}(\boldsymbol{B}_u(\boldsymbol{x}) \boldsymbol{d}_u) \, \mathrm{d}\Omega. \tag{2.28}$$

Relation Equation (2.27) represents the system of nonlinear algebraic equations, which is usually solved numerically by the Newton-Raphson method [Bittnar and Šejnoha, 1996].

In the case of the time-dependent analysis, it is convenient to rewrite the system (2.23) into the rate form

$$\boldsymbol{K}_u \dot{\boldsymbol{d}}_u = \dot{\boldsymbol{f}}_{ext}. \tag{2.29}$$

For the numerical solution, the above equation is transferred to the incremental form assuming the strain decompsition (2.1)

$$\boldsymbol{K}_u \Delta \boldsymbol{d}_u = \Delta \boldsymbol{f}_{ext} + \Delta \boldsymbol{f}_0, \tag{2.30}$$

where $\Delta \boldsymbol{f}_0 = \int_{\Omega} \boldsymbol{B}_u^T(\boldsymbol{x}) \boldsymbol{D}_u(\boldsymbol{x}) \Delta \boldsymbol{\varepsilon}_0(\boldsymbol{x}) \, \mathrm{d}\Omega$ is the vector including increments of non-mechanical strains $\Delta \boldsymbol{\varepsilon}_0 = \Delta \boldsymbol{\varepsilon}_p + \Delta \boldsymbol{\varepsilon}_d + \Delta \boldsymbol{\varepsilon}_c + \Delta \boldsymbol{\varepsilon}_{sh} + \Delta \boldsymbol{\varepsilon}_{ag} + \Delta \boldsymbol{\varepsilon}_T$.

2.2 Transport problem

The numerical modeling of transport processes will be shown on the heat transport problem with the unknown temperature T, which is generally spatial ($\boldsymbol{x}$) and time (t) dependent. The well known transport equation - Fourier's law expresses the relation between temperature T and the heat flux $\boldsymbol{q}$

$$\boldsymbol{q} = -\boldsymbol{\lambda}\,\boldsymbol{\nabla} T(\boldsymbol{x}, t) \tag{2.31}$$

where $\boldsymbol{\lambda}$ is the thermal conductivity tensor, and $\boldsymbol{\nabla}$ stands for the gradient operator (grad). Usually, in the matrix form, the off-diagonal components of $\boldsymbol{\lambda}$ are equal to zero for isotropic materials. The boundary flux in the direction of a normal vector $\boldsymbol{n}$ has the form

$$q_n = -\boldsymbol{n}^{\mathrm{T}}\boldsymbol{\lambda}\boldsymbol{\nabla} T. \tag{2.32}$$

The above flux can be also written via sumation rule for 3D problem

$$q_n = \sum_{i=1}^{3} q_i n_i = -\sum_{i=1}^{3}\sum_{j=1}^{3} \lambda_{ij}\frac{\partial T}{\partial x_j} n_i \ , \tag{2.33}$$

where n_i is the i-th component of the normal vector.

The energy conservation equation for the domain Ω has the following form

$$\boldsymbol{\nabla}^{\mathrm{T}}\big(\boldsymbol{\lambda}\,\boldsymbol{\nabla}\, T(\boldsymbol{x}, t)\big) - \rho c\frac{\partial T(\boldsymbol{x}, t)}{\partial t} + Q(\boldsymbol{x}, t) = 0, \qquad \boldsymbol{x} \in \Omega, \tag{2.34}$$

where $\boldsymbol{\nabla}^{\mathrm{T}}$ stands for the divergence operator (div), Q denotes the source of heat per unit volume, ρ is the density and c expresses the heat capacity. Γ is the boundary and it can be split into four parts Γ_T, Γ_{qp}, Γ_{qc}, and Γ_{qr} according to four boundary conditions type

- Dirichlet boundary condition for prescribed temperatures

$$T(\boldsymbol{x}, t) = \overline{T}(\boldsymbol{x}, t) \ , \qquad \boldsymbol{x} \in \Gamma_T \tag{2.35}$$

- Neumann boundary conditions for prescribed heat flux

$$q_n(\boldsymbol{x}, t) = \overline{q}(\boldsymbol{x}, t) \ , \qquad \boldsymbol{x} \in \Gamma_{qp} \tag{2.36}$$

- Newton or Cauchy conditions for heat transmission

$$q_n(\boldsymbol{x}, t) = \beta_T(T(\boldsymbol{x}, t) - T_{ext}(\boldsymbol{x}, t)), \qquad \boldsymbol{x} \in \Gamma_{qc} \tag{2.37}$$

- Radiation boundary condition

$$q_n(\boldsymbol{x}, t) = e_0\sigma_b(T^4(\boldsymbol{x}, t) - T_\infty^4(\boldsymbol{x}, t)) \ , \qquad \boldsymbol{x} \in \Gamma_{qr}. \tag{2.38}$$

q_n stands for the value of boundary flux in the direction of normal $\boldsymbol{n}$ vector, T_{ext} denotes the ambient temperature and β_T [$\mathrm{Wm^{-2}K^{-1}}$] is the heat transfer coefficient on the boudary, e_0 is the emisivity of the boundary ($0 < e_0 < 1$) related to the black-body radiation, and $\sigma_b = 5.68 \cdot 10^{-8}$ [$\mathrm{Wm^{-2}K^{-4}}$] is the Stefan-Boltzmann coefficient, and T_∞ is the temperature of the radiation source.

In numerical simulations, the fourth condition is ussually transferred into the flux prescribed or linearized, and it will not be used in the following text.

The heat transfer problem must be completed by initial conditions

$$T(\boldsymbol{x},0) = T_0(\boldsymbol{x}) \ . \tag{2.39}$$

The problem has non-homogeneous boundary conditions, which will be transformed into homogeneous conditions. The function T is split into two parts

$$T(\boldsymbol{x},t) = \tilde{T}(\boldsymbol{x},t) + \hat{T}(\boldsymbol{x},t), \tag{2.40}$$

which satisfy the following conditions [Kruis et al., 2021]

$$\begin{aligned} \tilde{T}(\boldsymbol{x},t) &= 0 \ , \qquad \boldsymbol{x} \in \Gamma_T, & (2.41)\\ \hat{T}(\boldsymbol{x},t) &= \overline{T}(\boldsymbol{x},t) \ , & (2.42)\\ \hat{T}(\boldsymbol{x},0) &= T_0(\boldsymbol{x}) \ . & (2.43) \end{aligned}$$

Application of the Galerkin method on (2.34) and substitution of (2.40) leads to the expression

$$\int_\Omega \delta T \ \boldsymbol{\nabla}^{\mathrm{T}} \left(\boldsymbol{\lambda} \left(\boldsymbol{\nabla} \, \tilde{T} + \boldsymbol{\nabla} \, \hat{T} \right) \right) \ \mathrm{d}\Omega + \int_\Omega \delta T Q \ \mathrm{d}\Omega = \int_\Omega \delta T \rho c \left(\frac{\partial \tilde{T}}{\partial t} + \frac{\partial \hat{T}}{\partial t} \right) \ \mathrm{d}\Omega \tag{2.44}$$

The first term of Equation (2.44) can be modified

$$\begin{aligned} &\int_\Omega \delta T \ \boldsymbol{\nabla}^{\mathrm{T}} \left(\boldsymbol{\lambda} \, \boldsymbol{\nabla} (\tilde{T} + \hat{T}) \right) \ \mathrm{d}\Omega = \\ &\int_\Gamma \delta T \left(\boldsymbol{n}^{\mathrm{T}} \boldsymbol{\lambda} (\tilde{T} + \hat{T}) \boldsymbol{n} \right) \ \mathrm{d}\Gamma - \int_\Omega (\boldsymbol{\nabla} \, \delta T)^{\mathrm{T}} \boldsymbol{\lambda} \boldsymbol{\nabla} (\tilde{T} + \hat{T}) \ \mathrm{d}\Omega = \\ &\int_{\Gamma_{qp}} -\delta T \, \overline{q} \ \mathrm{d}\Gamma + \int_{\Gamma_{qc}} -\delta T \, \beta_T (\tilde{T} + \hat{T} - T_{ext}) \ \mathrm{d}\Gamma - \int_\Omega (\boldsymbol{\nabla} \, \delta T)^{\mathrm{T}} \boldsymbol{\lambda} \boldsymbol{\nabla} (\tilde{T} + \hat{T}) \ \mathrm{d}\Omega, \end{aligned} \tag{2.45}$$

where δT represents a weight function ($\delta T = 0$ on Γ_T). The continuous functions from the previous relations are discretized by the finite element method in the following form

$$\begin{aligned} \tilde{T} &\approx \boldsymbol{N}_T \boldsymbol{d}_T, \qquad \hat{T} \approx \boldsymbol{N}^{[\overline{T}]} \overline{\boldsymbol{T}}, \qquad \delta T \approx \boldsymbol{N}^{[w]} \boldsymbol{w}, & (2.46)\\ \overline{q} &\approx \boldsymbol{N}^{[q]} \overline{\boldsymbol{q}}, \qquad Q \approx \boldsymbol{N}^{[Q]} \boldsymbol{Q}, \qquad T_{ext} \approx \boldsymbol{N}^{[T_{\mathrm{ext}}]} \boldsymbol{T}_{\mathrm{ext}}, & (2.47)\\ \boldsymbol{\nabla} \, \tilde{T} &\approx \boldsymbol{B}_T \boldsymbol{d}_T, \qquad \boldsymbol{\nabla} \, \hat{T} \approx \boldsymbol{B}^{[\overline{T}]} \overline{\boldsymbol{T}}, \qquad \boldsymbol{\nabla} \, \delta T \approx \boldsymbol{B}^{[w]} \boldsymbol{w}. & (2.48) \end{aligned}$$

In the above approximations, $\boldsymbol{d}_T$ denotes the vector of unknowns nodal temperatures, $\overline{\boldsymbol{T}}$ is the vector of prescribed nodal temperatures, $\overline{\boldsymbol{q}}$ is the vector of prescribed nodal fluxes, $\boldsymbol{T}_{\mathrm{ext}}$ is the vector of prescribed ambient nodal temperatures, $\boldsymbol{Q}$ is the vector of sources in nodes, $\boldsymbol{N}$ stands for the vector of aproximation functions, and $\boldsymbol{B}$ is the matrix of their gradients. Nodal values of the weight function δT are in the vector $\boldsymbol{w}$.

Approximation functions for continuous functions are usually identical, therefore the following relationships are valid

$$\begin{aligned} \boldsymbol{N}_T &= \boldsymbol{N}^{[\overline{T}]} = \boldsymbol{N}^{[w]} = \boldsymbol{N}^{[Q]} = \boldsymbol{N}^{[q]} = \boldsymbol{N}^{[T_{\mathrm{ext}}]} \ , & (2.49)\\ \boldsymbol{B}_T &= \boldsymbol{B}^{[w]} = \boldsymbol{B}^{[\overline{T}]} & (2.50) \end{aligned}$$

After substitution of the previous approximation to the Equations (2.44) to (2.50), the following equation is obtained

$$\begin{aligned}
&\int_\Omega \big(-\boldsymbol{w}^{\mathrm{T}}\boldsymbol{B}_T^{\mathrm{T}}\boldsymbol{\lambda}\boldsymbol{B}_T\boldsymbol{d}_T - \boldsymbol{w}^{\mathrm{T}}\boldsymbol{B}_T^{\mathrm{T}}\boldsymbol{\lambda}\boldsymbol{B}_T\overline{\boldsymbol{T}} + \boldsymbol{w}^{\mathrm{T}}\boldsymbol{N}_T^{\mathrm{T}}\boldsymbol{N}_T\boldsymbol{Q} \\
&-\boldsymbol{w}^{\mathrm{T}}\boldsymbol{N}_T^{\mathrm{T}}\rho c\boldsymbol{N}_T\dot{\boldsymbol{d}}_T - \boldsymbol{w}^{\mathrm{T}}\boldsymbol{N}_T^{\mathrm{T}}\rho c\boldsymbol{N}_T\dot{\overline{\boldsymbol{T}}}\big)\,\mathrm{d}\Omega - \int_{\Gamma_{qp}} \boldsymbol{w}^{\mathrm{T}}\boldsymbol{N}_T^{\mathrm{T}}\boldsymbol{N}_T\overline{\boldsymbol{q}}\,\mathrm{d}\Gamma \\
&+\int_{\Gamma_{qc}} \big(-\boldsymbol{w}^{\mathrm{T}}\boldsymbol{N}_T^{\mathrm{T}}\beta_T\boldsymbol{N}_T\boldsymbol{d}_T - \boldsymbol{w}^{\mathrm{T}}\boldsymbol{N}_T^{\mathrm{T}}\beta_T\boldsymbol{N}_T\overline{\boldsymbol{T}} + \boldsymbol{w}^{\mathrm{T}}\boldsymbol{N}_T^{\mathrm{T}}\beta_T\boldsymbol{N}_T\boldsymbol{T}_{ext}\big)\,\mathrm{d}\Gamma = \boldsymbol{0}\ ,
\end{aligned} \tag{2.51}$$

where the $(\dot{})$ symbol denotes the time derivative. Vector $\boldsymbol{w}$ can be factored out

$$\begin{aligned}
&\boldsymbol{w}^{\mathrm{T}}\left(\int_\Omega \big(-\boldsymbol{B}_T^{\mathrm{T}}\boldsymbol{\lambda}\boldsymbol{B}_T\boldsymbol{d}_T - \boldsymbol{B}_T^{\mathrm{T}}\boldsymbol{\lambda}\boldsymbol{B}_T\overline{\boldsymbol{T}} + \boldsymbol{N}_T^{\mathrm{T}}\boldsymbol{N}_T\boldsymbol{Q}\right. \\
&-\boldsymbol{N}_T^{\mathrm{T}}\rho c\boldsymbol{N}_T\dot{\boldsymbol{d}}_T - \boldsymbol{N}_T^{\mathrm{T}}\rho c\boldsymbol{N}_T\dot{\overline{\boldsymbol{T}}}\big)\ \mathrm{d}\Omega - \int_{\Gamma_{qp}} \boldsymbol{N}_T^{\mathrm{T}}\boldsymbol{N}_T\overline{\boldsymbol{q}}\ \mathrm{d}\Gamma \\
&\left.+\int_{\Gamma_{qc}} \big(-\boldsymbol{N}_T^{\mathrm{T}}\beta_T\boldsymbol{N}_T\boldsymbol{d}_T - \boldsymbol{N}_T^{\mathrm{T}}\beta_T\boldsymbol{N}_T\overline{\boldsymbol{T}} + \boldsymbol{N}_T^{\mathrm{T}}\beta_T\boldsymbol{N}_T\boldsymbol{T}_{ext}\big)\ \mathrm{d}\Gamma\right) = \boldsymbol{0}\ .
\end{aligned} \tag{2.52}$$

Then, the following notation can be adopted

$$\begin{aligned}
\boldsymbol{K}_T^{[T]} &= \int_\Omega \boldsymbol{B}_T^{\mathrm{T}}\boldsymbol{\lambda}\boldsymbol{B}_T\ \mathrm{d}\Omega, \qquad \boldsymbol{K}_T^{[\Gamma]} = \int_{\Gamma_{qc}} \boldsymbol{N}_T^{\mathrm{T}}\beta_T\boldsymbol{N}_T\ \mathrm{d}\Gamma, \\
\boldsymbol{C}_T &= \int_\Omega \boldsymbol{N}_T^{\mathrm{T}}\rho c\boldsymbol{N}_T\ \mathrm{d}\Omega, \\
\boldsymbol{f}_T^{[qp]} &= \int_{\Gamma_f} \boldsymbol{N}_T^{\mathrm{T}}\boldsymbol{N}_T\ \mathrm{d}\Gamma\ \overline{\boldsymbol{q}}, \quad \boldsymbol{f}_T^{[qc]} = \int_{\Gamma_t} \boldsymbol{N}_T^{\mathrm{T}}\beta_T\boldsymbol{N}_T\ \mathrm{d}\Gamma\ \boldsymbol{T}_{ext}, \quad \boldsymbol{f}_T^{[Q]} = \int_\Omega \boldsymbol{N}_T^{\mathrm{T}}\boldsymbol{N}_T\ \mathrm{d}\Omega\ \boldsymbol{Q}.
\end{aligned} \tag{2.53}$$

The balance Equation (2.52) is rewritten to the form

$$\left(\boldsymbol{K}_T^{[T]} + \boldsymbol{K}_T^{[\Gamma]}\right)\boldsymbol{d}_T + \boldsymbol{C}_T\dot{\boldsymbol{d}}_T = \boldsymbol{f}_T^{[Q]} - \left(\boldsymbol{K}_T^{[T]} + \boldsymbol{K}_T^{[\Gamma]}\right)\overline{\boldsymbol{T}} - \boldsymbol{C}_T\dot{\overline{\boldsymbol{T}}} - \boldsymbol{f}_T^{[qp]} + \boldsymbol{f}_T^{[qc]}\ , \tag{2.54}$$

which can be modified into more concise form

$$\boldsymbol{K}_T\boldsymbol{d}_T + \boldsymbol{C}_T\dot{\boldsymbol{d}}_T = \boldsymbol{f}_T\ , \tag{2.55}$$

where additional notation is used

$$\boldsymbol{K}_T = \boldsymbol{K}_T^{[T]} + \boldsymbol{K}_T^{[\Gamma]} \tag{2.56}$$

$$\boldsymbol{f}_T = \boldsymbol{f}_T^{[Q]} - \left(\boldsymbol{K}_T^{[T]} + \boldsymbol{K}_T^{[\Gamma]}\right)\overline{\boldsymbol{T}} - \boldsymbol{C}_T\dot{\overline{\boldsymbol{T}}} - \boldsymbol{f}_T^{[qp]} + \boldsymbol{f}_T^{[qc]}\ . \tag{2.57}$$

Equation (2.55) is a system of ordinary differential equations and its time integration is based on the general trapezoidal rule [Hughes, 1987]. For the clarity, vectors and matrices will be written without subscipt T.

$$\dot{\boldsymbol{d}} = \boldsymbol{v} \tag{2.58}$$

$$\boldsymbol{d}_{n+1} = \boldsymbol{d}_n + \Delta t\boldsymbol{v}_{n+\alpha} \tag{2.59}$$

$$\boldsymbol{v}_{n+\alpha} = (1-\alpha)\boldsymbol{v}_n + \alpha\boldsymbol{v}_{n+1}\ , \tag{2.60}$$

where subscripts denote the time step. The system of Equation (2.55) has the similar form at actual time step $n+1$

$$\boldsymbol{K}\boldsymbol{d}_{n+1} + \boldsymbol{C}\dot{\boldsymbol{d}}_{n+1} = \boldsymbol{f}_{n+1} \ . \tag{2.61}$$

If time approximations (2.58) to (2.60) are taken into account, the equation (2.61) leads to another form

$$(\boldsymbol{C} + \alpha\Delta t\boldsymbol{K})\,\boldsymbol{v}_{n+1} = \boldsymbol{f}_{n+1} - \boldsymbol{K}\boldsymbol{d}_n - (1-\alpha)\Delta t\boldsymbol{K}\boldsymbol{v}_n \ . \tag{2.62}$$

The predictor-corrector method can be used for the computer implementation, where the predictor reads

$$\tilde{\boldsymbol{d}}_{n+1} = \boldsymbol{d}_n + (1-\alpha)\Delta t\boldsymbol{v}_n \tag{2.63}$$

and the corrector has the form

$$\boldsymbol{d}_{n+1} = \tilde{\boldsymbol{d}}_{n+1} + \alpha\Delta t\boldsymbol{v}_{n+1} \ . \tag{2.64}$$

With the help of the predictor and corrector, Equation (2.62) is slightly modified

$$(\boldsymbol{C} + \alpha\Delta t\boldsymbol{K})\,\boldsymbol{v}_{n+1} = \boldsymbol{f}_{n+1} - \boldsymbol{K}\tilde{\boldsymbol{d}}_{n+1} \ . \tag{2.65}$$

The system (2.65) contains time derivatives of the nodal values $\boldsymbol{v}_{n+1}$. This approach is called v-form, which is not always hassle-free from the numerical point of view. Therefore additional approach, called d-form, can be used. Time derivatives of nodal values are expressed from Equation (2.64) in the form

$$\boldsymbol{v}_{n+1} = \frac{1}{\alpha\Delta t}(\boldsymbol{d}_{n+1} - \tilde{\boldsymbol{d}}_{n+1}) \tag{2.66}$$

which is reasonable for $\alpha > 0$ and $\Delta t > 0$. Substitution of expression (2.66) to the balance equation (2.65) leads to the form

$$\left(\frac{1}{\alpha\Delta t}\boldsymbol{C} + \boldsymbol{K}\right)\boldsymbol{d}_{n+1} = \boldsymbol{f}_{n+1} + \frac{1}{\alpha\Delta t}\boldsymbol{C}\tilde{\boldsymbol{d}}_{n+1} \ . \tag{2.67}$$

In case of non-linear system of Equation (2.61), where material parameters are dependent on the temperature field, the Newton-Raphson method [Bittnar and Šejnoha, 1996], [Crisfield, 1991] has to be used in every time step. For example in the v form (2.65), the trial solution $\boldsymbol{v}_{n+1,0}$ of the system of equations is used for computation of the trial nodal values $\boldsymbol{d}_{n+1,0}$ which are obtained from Equations (2.59) and (2.60). Substitution of the trial solution back to the system of Equations (2.65) with actual matrices does not generally lead to equality. An iteration loop, called the inner iteration loop, in every time step is based on residual which can be computed from the relationship

$$\begin{aligned} \boldsymbol{r}_{n+1,j} &= \boldsymbol{f}_{n+1} - \boldsymbol{K}_n\,(\boldsymbol{d}_n + \Delta t(1-\alpha)\boldsymbol{v}_n) \\ &- (\boldsymbol{C}_{n+1,j} + \Delta t\alpha\boldsymbol{K}_{n+1,j})\,\boldsymbol{v}_{n+1,j} \ , \end{aligned} \tag{2.68}$$

where $\boldsymbol{C}_{n+1,j}$ and $\boldsymbol{K}_{n+1,j}$ denote the matrices evaluated for $\boldsymbol{d}_{n+1,j}$ and j is the index of the inner loop. Corrections of nodal time derivatives are computed from the equation

$$\left(\boldsymbol{C}_{n+1,j} + \Delta t \alpha \boldsymbol{K}_{n+1,j}\right) \Delta \boldsymbol{v}_{n+1,j+1} = \boldsymbol{r}_{n+1,j} \tag{2.69}$$

and new time derivatives are obtained

$$\boldsymbol{v}_{n+1,j+1} = \boldsymbol{v}_{n+1,j} + \Delta \boldsymbol{v}_{n+1,j+1}. \tag{2.70}$$

Another approach how to solve the nonlinear algebraic Equations (2.61) comes from the equilibrium of fluxes (computed and prescribed) in nodes, which is taken over from the mechanical problems. This strategy is based on the equation

$$\boldsymbol{f}_{int} = \boldsymbol{f}_{ext} \tag{2.71}$$

where vectors $\boldsymbol{f}_{int}$ and $\boldsymbol{f}_{ext}$ contain internal values and prescribed/computed values, respectively. Both vector depend on time t, on the vector of unknown temperature $\boldsymbol{d}$ and on derivatives of unknown temperatures with respect to time $\boldsymbol{v}$. The vector $\boldsymbol{f}_{int}$ expressed at actual time step t_{n+1} has the form

$$\boldsymbol{f}_{int}(\boldsymbol{d}_{n+1}, \boldsymbol{v}_{n+1}, t_{n+1}) \approx \boldsymbol{f}_{int}(\boldsymbol{d}_n, \boldsymbol{v}_n, t_n) + \frac{\partial \boldsymbol{f}_{int}}{\partial \boldsymbol{d}} \Delta \boldsymbol{d}_n + \frac{\partial \boldsymbol{f}_{int}}{\partial \boldsymbol{v}} \Delta \boldsymbol{v}_n \ , \tag{2.72}$$

where $\Delta \boldsymbol{d}_n$ and $\Delta \boldsymbol{v}_n$ are increments over $\Delta t = t_{n+1} - t_n$. Previous relation can be rewritten with help of notation

$$\boldsymbol{K}_n = \frac{\partial \boldsymbol{f}_{int}(t_n)}{\partial \boldsymbol{d}}, \qquad \boldsymbol{C}_n = \frac{\partial \boldsymbol{f}_{int}(t_n)}{\partial \boldsymbol{v}} \ . \tag{2.73}$$

in the new expression

$$\boldsymbol{K}_n \Delta \boldsymbol{d}_n + \boldsymbol{C}_n \Delta \boldsymbol{v}_n = \boldsymbol{f}_{int}(t_{n+1}) - \boldsymbol{f}_{int}(t_n) \ . \tag{2.74}$$

There are two sets of relations

$$\boldsymbol{d}_{n+1} = \boldsymbol{d}_n + \Delta \boldsymbol{d}_n, \qquad \boldsymbol{v}_{n+1} = \boldsymbol{v}_n + \Delta \boldsymbol{v}_n \tag{2.75}$$

and recalled Equations (2.59) and (2.60)

$$\boldsymbol{d}_{n+1} = \boldsymbol{d}_n + \Delta t \boldsymbol{v}_{n+\alpha}, \qquad \boldsymbol{v}_{n+\alpha} = (1-\alpha)\boldsymbol{v}_n + \alpha \boldsymbol{v}_{n+1} \ . \tag{2.76}$$

After substitution of (2.75) and (2.76) into expression (2.74)

$$\left(\boldsymbol{C}_n + \alpha \Delta \boldsymbol{K}_n\right) \boldsymbol{v}_{n+1} = \boldsymbol{f}_{int}(t_{n+1}) - \boldsymbol{f}_{int}(t_n) + \left(\boldsymbol{C}_n - \Delta t (1-\alpha) \boldsymbol{K}_n\right) \boldsymbol{v}_n \ , \tag{2.77}$$

where

$$\boldsymbol{f}_{int}(t_n) = \boldsymbol{K}_n \boldsymbol{d}_n + \boldsymbol{C}_n \boldsymbol{v}_n \tag{2.78}$$

is applied. The new vector $\boldsymbol{v}_{n+1}$ is calculated from Equation (2.76), and the vector $\boldsymbol{d}_{n+1}$ is then obtained. Due to nonlinearity in material properties, the equality

$$\boldsymbol{f}_{int}(t_{n+1}) = \boldsymbol{f}_{ext}(t_{n+1}) \tag{2.79}$$

is generally not valid and the residuum is computed

$$\boldsymbol{R}_{n+1} = \boldsymbol{f}_{ext}(t_{n+1}) - \boldsymbol{f}_{int}(t_{n+1}) \tag{2.80}$$

The vector $\boldsymbol{v}_{n+1}$ corrections has to be evaluated from the relation

$$(\boldsymbol{C}_{n+1} + \alpha\Delta t\boldsymbol{K}_{n+1})\,\Delta\boldsymbol{v}_{n+1,j} = \boldsymbol{R}_{n+1,j}\ . \tag{2.81}$$

The final vector $\boldsymbol{v}_{n+1}^{\text{fin}}$ is the sum of contributions from inner iteraton loop

$$\boldsymbol{v}_{n+1}^{\text{fin}} = \boldsymbol{v}_{n+1} + \sum_j \Delta\boldsymbol{v}_{n+1,j}\ . \tag{2.82}$$

The final equality is reached at the and of the inner iteration process

$$\boldsymbol{f}_{int}^{\text{fin}}(\boldsymbol{d}_{n+1}^{\text{fin}}, \boldsymbol{v}_{n+1}^{\text{fin}}, t_{n+1}) = \boldsymbol{f}_{ext}^{\text{fin}}(\boldsymbol{d}_{n+1}^{\text{fin}}, \boldsymbol{v}_{n+1}^{\text{fin}}, t_n). \tag{2.83}$$

If the matrices $\boldsymbol{C}$ and $\boldsymbol{K}$ are updated in every inner step, the full Newton-Raphson method is used. If the matrices are updated only once after every time step, the modified Newton-Raphson method is used.

2.3 Coupled problem

2.3.1 Partially coupled approach

The coupled analysis is based on the equation of the mechanical problem (2.23)

$$\boldsymbol{K}_u\boldsymbol{d}_u = \boldsymbol{f}_{ext},$$

and on the equation for the transport problem (2.55)

$$\boldsymbol{K}_T\boldsymbol{d}_T + \boldsymbol{C}_T\dot{\boldsymbol{d}}_T = \boldsymbol{f}_T\ .$$

The thermal effect on the mechanical response is usually added in to the constitutive equation (Hook's law) relating the strains $\boldsymbol{\varepsilon}$ and stresses $\boldsymbol{\sigma}$

$$\boldsymbol{\sigma} = \boldsymbol{D}_u\left(\boldsymbol{\varepsilon} - \boldsymbol{\varepsilon}_T\right), \tag{2.84}$$

where $\boldsymbol{D}_u$ is the stiffness matrix of the material, $\boldsymbol{\varepsilon}$ is the vector of total strains, and the vector of thermal strains, $\boldsymbol{\varepsilon}_T$, depends on the thermal expansion coefficient, α_T, and the difference of the actual temperature T, and the initial temperature, T_0,

$$\boldsymbol{\varepsilon}_T = \boldsymbol{m}^{\mathrm{T}}\alpha_T(T - T_0), \qquad \boldsymbol{m} = (1,1,1,0,0)\,. \tag{2.85}$$

After the FEM discretisation, the right-hand side of the mechanical problem is extended by temperature effect

$$\boldsymbol{K}_u\boldsymbol{d}_u = \boldsymbol{f}_{ext}\ + \boldsymbol{f}_{Tu} \tag{2.86}$$

where

$$\boldsymbol{f}_{uT} = \int_\Omega \boldsymbol{B}_u^{\mathrm{T}}\boldsymbol{D}_u\boldsymbol{\varepsilon}_T\mathrm{d}\Omega\ . \tag{2.87}$$

The above system of Equation (2.86) represents a partially coupled problem, so-called one way coupled problem, where the mechanical problem is influenced by the heat transfer problem. For the numerical solution, it is convenient to use a staggered algorithm, in which both transport and mechanical analysis are solved simultaneously in time. The data from transport analysis are transferred only to mechanical analysis. It means the heat transfer analysis is solved first, and then in each time step, the temperatures are transferred to the mechanical part to compute thermal strains. From the numerical point of view, the rate form of Equation (2.86) is more convenient

$$\boldsymbol{K}_u\dot{\boldsymbol{d}}_u = \dot{\boldsymbol{f}}_{ext}\ + \dot{\boldsymbol{f}}_{uT} \tag{2.88}$$

2.3.2 Fully coupled approach

If the mechanical material properties are influenced by temperature changes or the mechanical response is non-linear, it is convenient to solve both transport and mechanical parts together in a fully coupled analysis. In such a problem, the vector with thermal strains is split into two parts

$$\boldsymbol{f}_{uT} = \int_\Omega \boldsymbol{B}_u^{\mathrm{T}} \boldsymbol{D}_u \boldsymbol{\varepsilon}_T \mathrm{d}\Omega \; = \int_\Omega \boldsymbol{B}_u^{\mathrm{T}} \boldsymbol{D}_u \alpha_T \boldsymbol{m}^{\mathrm{T}} \boldsymbol{N}_T \mathrm{d}\Omega \; \boldsymbol{d}_T - \int_\Omega \boldsymbol{B}_u^{\mathrm{T}} \boldsymbol{D}_u \alpha_T \boldsymbol{m}^{\mathrm{T}} \boldsymbol{N}_T \mathrm{d}\Omega \; \boldsymbol{d}_{T0} \; , \quad (2.89)$$

where the vector $\boldsymbol{d}_{T0}$ contains initial nodal temperatures. Merging of both problem (2.86) and (2.55) together and applying of previous decomposition (2.89) lead to the system of equations for the fully coupled problem

$$\begin{pmatrix} \boldsymbol{K}_{uu} & \boldsymbol{K}_{uT} \\ \boldsymbol{0} & \boldsymbol{K}_{TT} \end{pmatrix} \begin{pmatrix} \boldsymbol{d}_u \\ \boldsymbol{d}_T \end{pmatrix} + \begin{pmatrix} \boldsymbol{0} & \boldsymbol{0} \\ \boldsymbol{0} & \boldsymbol{C}_{TT} \end{pmatrix} \begin{pmatrix} \dot{\boldsymbol{d}}_u \\ \dot{\boldsymbol{d}}_T \end{pmatrix} = \begin{pmatrix} \boldsymbol{f}_{ext} + \boldsymbol{f}_{uT}^0 \\ \boldsymbol{f}_T \end{pmatrix} \; , \quad (2.90)$$

where $\boldsymbol{d}_T$ is the vector of nodal temperatures, and $\boldsymbol{f}_T$ is the vector of prescribed nodal heat fluxes and sources presented in Equation (2.56). The first equation in the system (2.90) expresses the equilibrium condition while the second equation in this system of equation represents the heat balance condition. The zero blocks in the heat balance equation determine the independence of the heat transfer on the mechanical problem. On the other hand, the mechanical problem is coupled with the heat transfer through coupling matrix $\boldsymbol{K}_{uT}$ and vector $\boldsymbol{f}_{uT}^0$ resulting from the first and the second part of the vector $\boldsymbol{f}_{uT}$ in Equation (2.89), respectively.

$$\boldsymbol{K}_{uT} = -\int_\Omega \boldsymbol{B}_u^{\mathrm{T}} \boldsymbol{D}_u \alpha_T \boldsymbol{m}^{\mathrm{T}} \boldsymbol{N}_T \mathrm{d}\Omega \quad , \quad \boldsymbol{f}_{uT}^0 = -\int_\Omega \boldsymbol{B}_u^{\mathrm{T}} \boldsymbol{D}_u \alpha_T \boldsymbol{m}^{\mathrm{T}} \boldsymbol{N}_T \mathrm{d}\Omega \; \boldsymbol{d}_{T0} \; . \quad (2.91)$$

The matrix $\boldsymbol{K}_{uu}$ is the stiffness matrix previously denoted $\boldsymbol{K}_u$, the matrix $\boldsymbol{K}_{TT}$ is the conductivity matrix $\boldsymbol{K}_T$, and the matrix $\boldsymbol{C}_{TT}$ is the capacity matrix $\boldsymbol{C}_T$, respectively.

Slightly different system of equations is obtained when using the rate form for the mechanical part (2.88)

$$\begin{pmatrix} \boldsymbol{0} & \boldsymbol{0} \\ \boldsymbol{0} & \boldsymbol{K}_{TT} \end{pmatrix} \begin{pmatrix} \boldsymbol{d}_u \\ \boldsymbol{d}_T \end{pmatrix} + \begin{pmatrix} \boldsymbol{K}_{uu} & \boldsymbol{K}_{uT} \\ \boldsymbol{0} & \boldsymbol{C}_{TT} \end{pmatrix} \begin{pmatrix} \dot{\boldsymbol{d}}_u \\ \dot{\boldsymbol{d}}_T \end{pmatrix} = \begin{pmatrix} \dot{\boldsymbol{f}}_u \\ \boldsymbol{f}_T \end{pmatrix} \; . \quad (2.92)$$

The numerical solution of the system of Equations (2.90) follows the v-form or d-form algorithms presented for the transport problem by relations (2.65) to (2.67).

In the case of a more complicated coupled thermo-hygro-mechanical problem, the system may have the form with non-zeros off-diagonal blocks

$$\begin{pmatrix} \boldsymbol{C}_{uu} & \boldsymbol{C}_{uT} & \boldsymbol{C}_{u\varphi} \\ \boldsymbol{C}_{Tu} & \boldsymbol{C}_{TT} & \boldsymbol{C}_{T\varphi} \\ \boldsymbol{C}_{\varphi u} & \boldsymbol{C}_{\varphi T} & \boldsymbol{C}_{\varphi\varphi} \end{pmatrix} \begin{pmatrix} \dot{\boldsymbol{d}}_u \\ \dot{\boldsymbol{d}}_T \\ \dot{\boldsymbol{d}}_\varphi \end{pmatrix} + \begin{pmatrix} \boldsymbol{K}_{uu} & \boldsymbol{K}_{uT} & \boldsymbol{K}_{u\varphi} \\ \boldsymbol{K}_{Tu} & \boldsymbol{K}_{TT} & \boldsymbol{K}_{T\varphi} \\ \boldsymbol{K}_{\varphi u} & \boldsymbol{K}_{\varphi T} & \boldsymbol{K}_{\varphi\varphi} \end{pmatrix} \begin{pmatrix} \boldsymbol{d}_u \\ \boldsymbol{d}_T \\ \boldsymbol{d}_\varphi \end{pmatrix} = \begin{pmatrix} \boldsymbol{f}_u \\ \boldsymbol{f}_T \\ \boldsymbol{f}_\varphi \end{pmatrix} , \quad (2.93)$$

where the subscript u denotes the displacements, the subscripts φ denotes the relative humidity and the subscript T denotes the temperature. The vectors $\boldsymbol{d}_u$, $\boldsymbol{d}_T$, and $\boldsymbol{d}_\varphi$ contain unknown nodal variables, the vectors $\boldsymbol{f}_u$, $\boldsymbol{f}_T$, and $\boldsymbol{f}_\varphi$ represent prescribed nodal forces and fluxes, the matrices $\boldsymbol{K}$ with indices stands for the stiffness, conductivity and coupling matrices and the matrices $\boldsymbol{C}$ with indices denote the capacity and coupling matrices. The vectors $\boldsymbol{f}_u$, $\boldsymbol{f}_T$, and $\boldsymbol{f}_\varphi$ are further

split into three contributions. The vector $\boldsymbol{f}_u$ is the sum of vectors $\boldsymbol{f}_{uu}$, $\boldsymbol{f}_{uT}$, $\boldsymbol{f}_{u\varphi}$ representing contributions to the nodal forces from mechanical analysis, temperature changes, and humidity changes. The meaning of other components is similar in the vectors $\boldsymbol{f}_T$ and $\boldsymbol{f}_\varphi$.

The system of differential equations (2.93) can be written more compactly in the form

$$\boldsymbol{C}(\boldsymbol{d})\dot{\boldsymbol{d}} + \boldsymbol{K}(\boldsymbol{d})\boldsymbol{d} = \boldsymbol{f} \ . \tag{2.94}$$

The dependency of the stiffness, conductivity, capacity, and coupling matrices on the attained values of variables is explicitly denoted.

It has to be noted that the permanent recalculation of matrices $\boldsymbol{K}$ and $\boldsymbol{C}$ with concerning actual nodal values is very computationally demanding. In such a case, the matrix of the system of equations $\boldsymbol{C}(\boldsymbol{d})+\Delta t\alpha_T\boldsymbol{K}(\boldsymbol{d})$ has to be always factorized, requiring additional computational time. Experiences with numerical simulation show that the modified Newton-Raphson method, which changes the system matrices only at the beginning of a new time step, is suitable for weak non-linear problems. On the other hand, the full version of the Newton-Raphson method computing matrices in each inner iteration step in each time step is the best choice for analyses with strong non-linear dependency.

2.4 SIFEL Computer Code

Experiences with the implementation of numerical methods, material models, and tools for coupled problems and parallel computing showed several contradicting requirements, namely in commercial software. It was decided to start the development of the new open-source code SIFEL [Kruis et al., 2021]. The acronym SIFEL was derived from SImple Finite ELements. The original motivation for the development of the new code was the European project MAECENAS (2001–2004). In this project, the program was successfully used for the solution of the nuclear reactor vessel, and since then, it has been developed and expanded. This section describes the SIFEL code's philosophy, the code structure, used programming techniques, and data structures. More details about this software can also be found in references [Kruis et al., 2010] and [Koudelka et al., 2010].

2.5 Philosophy of the code

SIFEL is the open-source code developed for nearly 20 years at the Department of Mechanics of Civil Engineering Faculty of the Czech Technical University in Prague. The development of the code was motivated by the European research project MAECENAS which dealt with the assessment of properties of reactor vessels of nuclear power plants at the end of their service life. The project was solved at several universities across Europe (Glasgow, Nantes, Padova, Prague, and Sheffield), and the aim was to develop an extensible software for coupled hygro-thermo-mechanical analysis. There were some computer codes for particular problems at involved universities, but their connection or merging was complicated. Therefore, the development of a new system was started. The following requirements were determined:

- Portability of the code. The universities had different hardware and software equipment. Notably, the portability between different operating systems was required (Linux, Windows, HP Unix).

- Simple programming techniques. The members of the project were experts in the branch of mechanical and transport processes with solid knowledge of programming languages but were not professional programmers. Source codes should be understandable for all team members as well as for new participants.

- Speed of program execution. The programming language should be compiled (FORTRAN, C++) rather than interpreted (Java).

Comparing to FORTRAN 77 and FORTRAN 90 languages, C++ was selected as more portable and comprehensive. Moreover, fast executable C++ compilers are other benefits. Sometimes, the extensive usage of object-oriented programming techniques decreases clarity for new participants. It was concluded that C++ language would be used without most object-oriented programming features and concepts. From the object-oriented programming point of view, data abstraction and encapsulation were found to be useful concepts and understandable for all project participants. Data are joined together with essential functions, which initialize them and perform basic operations. Compared to the usual recommendations, the data was left public initially, and it can be changed to private later depending on needs and experiences [Koudelka et al., 2011].

The easy extensibility of code is probably the most crucial requirement. Another essential need is connected with code performance. These two basic requirements for the system are contradictory because the very efficient implementation of a numerical method differs significantly from the description of the method in textbooks. Therefore the orientation in the code is complicated.

The attention was rather concentrated on the suitable formulation of the problem and the correct analysis. Detailed analysis of the system of nonlinear ordinary differential Equations (2.93) reveals the similarity of particular submatrices. The stiffness and conductivity matrices (denoted by $\boldsymbol{K}$ with appropriate subscripts) generally have the form

$$\boldsymbol{K}_{ij} = \int_{\Omega} \boldsymbol{B}_i^T \boldsymbol{D}_{ij} \boldsymbol{B}_j \mathrm{d}\Omega \ , \tag{2.95}$$

where $\boldsymbol{B}_i$ and $\boldsymbol{B}_j$ denote the gradient matrices, $\boldsymbol{D}_{ij}$ denotes the matrix of stiffness or conductivity of the material and the indexes i and j substitute any of indexes u, T, p_1 or p_2. Similarly, the capacity matrices (denoted by $\boldsymbol{C}$ with appropriate indexes) have generally the form

$$\boldsymbol{C}_{ij} = \int_{\Omega} \boldsymbol{N}_i^T \boldsymbol{H}_{ij} \boldsymbol{N}_j \mathrm{d}\Omega \ , \tag{2.96}$$

where $\boldsymbol{N}_i$ and $\boldsymbol{N}_j$ denote the matrices of base functions, and $\boldsymbol{H}_{ij}$ denotes the matrix of material parameters.

The part of SIFEL computer code dealing with coupled analyses is created for easy and clear extensibility. When modeling, e.g., geomechanics, additional variables must be introduced in the constitutive equations, and additional balance equations must be added to the system. In such a case, the thermo-mechanical problem (2.90) extended by the pore pressures and capacity terms results in the general form

$$\begin{pmatrix} \boldsymbol{C}_{uu} & \boldsymbol{C}_{uT} & \boldsymbol{C}_{up_1} & \boldsymbol{C}_{up_2} \\ \boldsymbol{C}_{Tu} & \boldsymbol{C}_{TT} & \boldsymbol{C}_{Tp_1} & \boldsymbol{C}_{Tp_2} \\ \boldsymbol{C}_{p_1u} & \boldsymbol{C}_{p_1T} & \boldsymbol{C}_{p_1p_1} & \boldsymbol{C}_{p_1p_2} \\ \boldsymbol{C}_{p_2u} & \boldsymbol{C}_{p_2T} & \boldsymbol{C}_{p_2p_1} & \boldsymbol{C}_{p_2p_2} \end{pmatrix} \begin{pmatrix} \dot{\boldsymbol{d}}_u \\ \dot{\boldsymbol{d}}_T \\ \dot{\boldsymbol{d}}_{p_1} \\ \dot{\boldsymbol{d}}_{p_2} \end{pmatrix} +$$

$$+ \begin{pmatrix} \boldsymbol{K}_{uu} & \boldsymbol{K}_{uT} & \boldsymbol{K}_{up_1} & \boldsymbol{K}_{up_2} \\ \boldsymbol{K}_{Tu} & \boldsymbol{K}_{TT} & \boldsymbol{K}_{Tp_1} & \boldsymbol{K}_{Tp_2} \\ \boldsymbol{K}_{p_1u} & \boldsymbol{K}_{p_1T} & \boldsymbol{K}_{p_1p_1} & \boldsymbol{K}_{p_1p_2} \\ \boldsymbol{K}_{p_2u} & \boldsymbol{K}_{p_2T} & \boldsymbol{K}_{p_2p_1} & \boldsymbol{K}_{p_2p_2} \end{pmatrix} \begin{pmatrix} \boldsymbol{d}_u \\ \boldsymbol{d}_T \\ \boldsymbol{d}_{p_1} \\ \boldsymbol{d}_{p_2} \end{pmatrix} =$$

$$= \begin{pmatrix} \boldsymbol{f}_u \\ \boldsymbol{f}_T \\ \boldsymbol{f}_{p_1} \\ \boldsymbol{f}_{p_2} \end{pmatrix} = \begin{pmatrix} \boldsymbol{f}_{uu} + \boldsymbol{f}_{uT} + \boldsymbol{f}_{up_1} + \boldsymbol{f}_{up_2} \\ \boldsymbol{f}_{Tu} + \boldsymbol{f}_{TT} + \boldsymbol{f}_{Tp_1} + \boldsymbol{f}_{Tp_2} \\ \boldsymbol{f}_{p_1u} + \boldsymbol{f}_{p_1T} + \boldsymbol{f}_{p_1p_1} + \boldsymbol{f}_{p_1p_2} \\ \boldsymbol{f}_{p_2u} + \boldsymbol{f}_{p_2T} + \boldsymbol{f}_{p_2p_1} + \boldsymbol{f}_{p_2p_2} \end{pmatrix}, \tag{2.97}$$

where the index u denotes the displacements, the indexes p_1 and p_2 are the pore pressures, and T represents the temperature. The vectors $\boldsymbol{d}_u$, $\boldsymbol{d}_T$, $\boldsymbol{d}_{p1}$ and $\boldsymbol{d}_{p2}$ contain unknown nodal variables. The vectors $\boldsymbol{f}_u$, $\boldsymbol{f}_T$, $\boldsymbol{f}_{p1}$, and $\boldsymbol{f}_{p2}$ represent prescribed nodal forces and fluxes. The matrices $\boldsymbol{K}$ denote the stiffness, conductivity, and the matrices $\boldsymbol{C}$ denote the capacity and coupling matrices. The vectors $\boldsymbol{f}_u$, $\boldsymbol{f}_T$, $\boldsymbol{f}_{p1}$, and $\boldsymbol{f}_{p2}$ are further split into four contributions. The right-hand side vectors f are the sum of several components, e.g., the vector $\boldsymbol{f}_u$ is the sum of vectors $\boldsymbol{f}_{uu}$, $\boldsymbol{f}_{uT}$, $\boldsymbol{f}_{up1}$, and $\boldsymbol{f}_{up2}$, which represent contributions to the nodal forces from mechanical analysis, temperature changes, and pore pressures.

The solution of the system of Equation (2.97) directly offers the instruction for efficient implementation. The implementation of the coupled hygro-thermo-mechanical problems is based on three independent modules. The first module, MEFEL, is a separate computer code for mechanical analysis that can stand alone. This module can deal with pure mechanical analyses. It assembles submatrices $\boldsymbol{K}_{uu}$,$\boldsymbol{C}_{uu}$, and subvector $\boldsymbol{f}_{uu}$. The second module, TRFEL, is an independent computer code for heat and moisture transfer, which can also be used separately. It assembles the submatrices $\boldsymbol{K}_{TT}$, $\boldsymbol{K}_{Tp_1}$, $\boldsymbol{K}_{Tp_2}$, $\boldsymbol{K}_{p_1T}$, $\boldsymbol{K}_{p_1p_1}$, $\boldsymbol{K}_{p_1p_2}$, $\boldsymbol{K}_{p_2T}$, $\boldsymbol{K}_{p_2p_1}$, $\boldsymbol{K}_{p_2p_2}$, and subvectors $\boldsymbol{f}_{TT}$, $\boldsymbol{f}_{Tp_1}$, $\boldsymbol{f}_{Tp_2}$, $\boldsymbol{f}_{p_1T}$, $\boldsymbol{f}_{p_1p_1}$, $\boldsymbol{f}_{p_1p_2}$, $\boldsymbol{f}_{p_2T}$, $\boldsymbol{f}_{p_2p_1}$, $\boldsymbol{f}_{p_2p_2}$. The coupling between the mechanical and transport part is implemented into the third module, METR, which deals with the off-diagonal terms in the coupled problem. This module assembles the submatrices $\boldsymbol{K}_{uT}$, $\boldsymbol{K}_{up_1}$, $\boldsymbol{K}_{up_2}$, $\boldsymbol{K}_{Tu}$, $\boldsymbol{K}_{p_1u}$, $\boldsymbol{K}_{p_2u}$, and subvectors $\boldsymbol{f}_{uT}$, $\boldsymbol{f}_{up_1}$, $\boldsymbol{f}_{up_2}$, $\boldsymbol{f}_{Tu}$, $\boldsymbol{f}_{p_1u}$, $\boldsymbol{f}_{p_2u}$.

At this time, many merging software concepts can be found in the literature, which consist of combinations of the existing computer codes and the data exchanges among them. Unfortunately, they result in staggered algorithms, and they cannot attain fully coupled analysis. In the SIFEL concept, the merging of the whole other parts of the code is not proceeding, but suitable subroutines from particular parts are used. Additionally, new subroutines dealing with the coupling terms had to be implemented. For an illustration of the merging complexity, the numbers of lines of the source code are summarized. The MEFEL code contains approximately 225100 lines, the TRFEL code contains 173800 lines, and the METR code contains 50900 lines. The number of lines of source code in METR is higher than the usual amount of lines in the typical merging code. On the other hand, it enables staggered and fully-coupled analysis, and the resulting code is compiled, therefore, very fast.

The additional advantage stems from the fact that any improvement of the mechanical or

transport module is automatically projected to the code for coupled problems. It is also very convenient for developers who can deal with one part of the whole system only.

The program can solve stationary and non-stationary, linear and nonlinear problems of heat and moisture transfer as well as linear and nonlinear statics, eigenvibrations, dynamics, and time-dependent problems with neglected inertial forces. Various types of finite elements can model a 2D and 3D domain. In the SIFEL program, there are bar, triangular, quadrilateral, tetrahedron, and hexahedron elements implemented. Both types of approximation functions, linear and quadratic, can be used. Other features, such as the sequential construction modeling or parallel version of the code, can be found in references [Kruis et al., 2021] and [Koudelka et al., 2011].

2.6 Code structure

The code is split into independent parts that deal with a single physics problem. The part dealing with mechanical analysis is denoted MEFEL; the part dealing with transport processes is denoted TRFEL. There is also part GEFEL, which contains comprehensive tools needed in connection with the finite element method. The link of the mechanical part and the transport part is implemented in an additional part METR.

Let the matrix $\boldsymbol{K}$ defined in Equation (2.93) be assumed. It can be split into submatrices separated by the lines

$$\boldsymbol{K} = \left(\begin{array}{c|ccc} \boldsymbol{K}_{uu} & \boldsymbol{K}_{uT} & \boldsymbol{K}_{up_1} & \boldsymbol{K}_{up_2} \\ \hline \boldsymbol{K}_{Tu} & \boldsymbol{K}_{TT} & \boldsymbol{K}_{Tp_1} & \boldsymbol{K}_{Tp_2} \\ \boldsymbol{K}_{p_1u} & \boldsymbol{K}_{p_1T} & \boldsymbol{K}_{p_1p_1} & \boldsymbol{K}_{p_1p_2} \\ \boldsymbol{K}_{p_2u} & \boldsymbol{K}_{p_2T} & \boldsymbol{K}_{p_2p_1} & \boldsymbol{K}_{p_2p_2} \end{array}\right) \tag{2.98}$$

The diagonal block $\boldsymbol{K}_{uu}$ is the stiffness matrix, and it represents mechanical analyses only. This submatrix is assembled in the MEFEL module. The second diagonal block

$$\left(\begin{array}{ccc} \boldsymbol{K}_{TT} & \boldsymbol{K}_{Tp_1} & \boldsymbol{K}_{Tp_2} \\ \boldsymbol{K}_{p_1T} & \boldsymbol{K}_{p_1p_1} & \boldsymbol{K}_{p_1p_2} \\ \boldsymbol{K}_{p_2T} & \boldsymbol{K}_{p_2p_1} & \boldsymbol{K}_{p_2p_2} \end{array}\right) \tag{2.99}$$

is the conductivity matrix, and it represents the transport process, where, e.g., heat and moisture are assumed. This submatrix is assembled in the TRFEL module. Two off-diagonal submatrices

$$\left(\begin{array}{ccc} \boldsymbol{K}_{uT} & \boldsymbol{K}_{up_1} & \boldsymbol{K}_{up_2} \end{array}\right) \tag{2.100}$$

and

$$\left(\begin{array}{c} \boldsymbol{K}_{Tu} \\ \boldsymbol{K}_{p_1u} \\ \boldsymbol{K}_{p_2u} \end{array}\right) \tag{2.101}$$

describe the coupling between mechanical behavior and transport processes, and they are assembled in the METR module.

2.6.1 Structure of MEFEL, TRFEL and METR

For each module (MEFEL, TRFEL, METR), the data describing the given problem are split into five large classes.

- `probdesc` - class containing the problem description,
- `top` - class including data relating finite element mesh,
- `mat` - class including data describing materials used,
- `crsec` - class representing data for cross-sections,
- `bclc` - class containing data representing boundary conditions and loadings.

The names of classes differ for particular problems by a postfix created from the problem name abbreviation. The data of these classes are necessary almost everywhere in the code, and this led to make them global objects. Thus, each class has one instance that is a global variable. This approach reduces the number of parameters passed to functions. In addition to that, each module contains global objects connected with the system matrices and vectors of unknowns.

The class `probdesc` contains attributes describing the solved problem. There is a group of attributes describing the type of problem, quantities computed, and solver of the systems of linear equations. Also, there is an object of class `hdbcontr`, which controls storage/re-storage of time steps to/from the disk. In the case of nonlinear problems, there are also objects of classes `timecon` and `nonlinman`. The `timecon` holds data controlling time steps while the `nonlinman` contains control parameters for the Newton-Raphson or arclength methods. The `probdesc` class has data members public because they are often used for reading, and they are seldom changed.

The class `top` contains topological data connected with the mesh of elements. It includes three essential arrays of objects of classes `node`, `element`, and `edge`. The class `node` contains data intended for the node, such as coordinates, the DOFs, and code numbers of particular DOFs. The class `element` provides nodal connectivity of the given element, type of material and cross-section, code numbers, etc. Similarly, the `edge` contains data describing boundaries. The `top` also includes arrays of adjacent nodes, elements, and distances of integration points.

The array of objects of `intpoints` is the most important data member of the class mat. The class `intpoints` contains intrinsic values computed in the particular integration points such as strains, stresses, fluxes, gradients, and other quantities. There are also arrays of initial conditions for integrations points, the array of values of unknowns from coupled problems, etc. For example, in the mechanical part, the `mechmat` class contains arrays of temperature and moisture values at integration points. The `mat` class also has arrays of objects of supported material types, i.e., implemented material models. Each material type has one object per one set of material parameters.

The class `crsec` contains arrays of objects for particular cross-section types. There are also methods for retrieving basic cross-section parameters such as thickness or area.

The `bclc` class holds data about boundary conditions that are arranged in particular load cases. Several load cases can be defined in static and also in time-dependent problems. Every load case can contain several sub-load cases due to better control of the time-dependent load. The boundary conditions can be specified for the given load case at nodes, elements, edges, and surfaces. Thus, `bclc` class contains the array of objects of the `loadcase` class, in which the boundary conditions are stored, array of initial conditions, and several auxiliary data members.

```
1   class node{
2       long ndofn;
3       long *cn;
4       double x,y,z;
5   };
```

Table 2.1: Class node

The `bclc` class has only several methods for data manipulation, and the `loadcase` class provides most of the functionality.

2.6.2 Data Storage

Two sets of data are needed in the case of problems solved by the finite element method. There is a set of data describing finite element mesh, i.e., node coordinates and node connectivity. The second set contains values of state and derived variables (displacements, strains, stresses, plastic strains, temperatures, heat fluxes, etc.).

Finite element mesh

Two arrays of objects describe finite element mesh. One array contains objects of the class `node`, and the second array contains objects of the class `element`. The class `node` represents a node of finite element mesh. The class definition is in Table 2.1. It contains node coordinates (line 4), the number of degrees of freedom (line 2), and the ordering of DOFs in the whole problem (line 3). The class `element` represents a finite element, and its definition is in Table 2.2. It does not take into account whether the element is one, two, or three dimensional and does not care about the element shape (triangular, quadrilateral, etc.). Particular standalone objects provide all functionality connected with the FEM with implemented FE routines. These individual elements are referred from the class `element` by `et` data member. The class `element` contains the number of nodes defining the element (line 2), the number of DOFs per element (line 3), the number of Lagrange multipliers (if they are needed on line 4), the list of nodes (line 5), the indicator whether the code numbers are defined on the element (line 6), the list of code numbers (line 7), the list of integration points located on the element (line 8), the number of integration points defined on the element (line 8), the number of the first integration point (line 9), and the element type identifier (line 10).

2.6.3 State variables

State variables are stored in integration points. The definition of integration point in the mechanical analysis is summarized in Table 2.3. The definition of integration point in transport processes is similar, but it contains arrays of fluxes and gradients. The integration point includes the type of material model (line 2), the number of components of strain/stress tensor (line 3). In the case of inelastic problem, some auxiliary values have to be stored. For example, in the analysis based on plasticity theory, the plastic strains and plastic multipliers have to be saved. For such purposes, the array `eqother` is defined. Unfortunately, one array is not enough because equilibrated values and trial values must be stored during global equilibrium iteration. Therefore, the array `eqother`

```
1    class element{
2        long nne;
3        long ndofe;
4        long nmult;
5        long *nodes;
6        long cne;
7        long *cn;
8        long nip;
9        long iip;
10       elemtype et;
11   };
```

Table 2.2: Class element

```
1   class intpoints{
2        mattype tm;
3        long ncompstr;
4        long ncompeqother;
5        long ncompother;
6        double *stress;
7        double *strain;
8        double *other;
9        double *eqother;
10       double *nonloc;
11  };
```

Table 2.3: Class intpoint

contains equilibrated quantities, while the array other contains their trial values. The class comprises the number of components of the array `eqother` (line 4), the number of components of the array other (line 5), the array of the stress components (line 6), the array of the strain components (line 7), the array of other values (line 8), the array of `eqother` values (line 9), and the array of nonlocal values (line 10).

2.6.4 Data access

Access to data can be described using an example dealing with stiffness matrix assembling. The function assembling global stiffness matrix contains a loop over all finite elements in a mesh. Each element calls its function for computation of the stiffness matrix. The typical form of function which computes the stiffness matrix of a single element is in Table 2.4. The number of nodes `nne` is known for each element, see 2.2. The array of node numbers `nodes` is allocated on line No. 1. The function `give_elemnodes` of the class `top` assembles appropriate node numbers to the array `nodes` (line 2). The function `give_thickness` of the class `crsec` assembles the thicknesses to the array `t`. The function `gauss_points(gp,w,nip)` assembles the coordinates of the integration points to the array `gp` and the weights to the array `w`. `ipp` denotes the number of the first integration

```
1    ivector nodes(nne);
2    Mt->give_elemnodes (eid,nodes);
3    vector t(nne);
4    Mc->give_thickness (eid,nodes,t);
5    vector w(nip);
6    vector gp(nip);
7    gauss_points (gp,w,nip);
8    ipp=Mt->elements[eid].ipp;
9    for (i=0;i<nip;i++){
10       geom_matrix (gm,x,y,gp,i,jac);
11       Mm->matstiff (d,ipp);
12       bdbjac (sm,gm,d,gm,jac);
13       ipp++;
14   }
```

Table 2.4: Function stiffness matrix

point on the current element (line 8). There is a loop over the number of integration points `nip`. The function `geom_matrix(gm,x,y,gp,i,jac)` assembles the strain-displacement matrix, function `matstiff(d,ipp)` of the class `mechmat` assembles the stiffness matrix of the material and the function `bdbjac(sm,gm,d,gm,jac)` of the current element computes matrix product $\boldsymbol{B}^T\boldsymbol{D}\boldsymbol{B}$ (line 12). The number of the integration point is incremented on line No. 13.

2.6.5 Data Transfer

The crucial part for coupled analyses is the data transfer among all modules. In the staggered algorithm, functions `trfel_mefel()` and `mefel_trfel()` transfer state variables from TRFEL to MEFEL and MEFEL to TRFEL, respectively. In the fully coupled algorithm, the code is completed by four functions `trfel_metr()`, `metr_trfel()`, `mefel_metr()`, and `metr_mefel()` transferring data between TRFEL and METR, and between MEFEL and METR. The current SIFEL version has three types of finite element meshes using the same nodes and elements numbering in all modules. Transport and mechanical parts can have polynomial approximation functions of different degrees, where linear and quadratic functions are the most used. While, the coupling - superior part adopts approximation functions from inferior MEFEL and TRFEL parts.

There are several possibilities to transfer state variables:

- by nodal values, e.g., in function `trfel_mefel_by_nodes()`, where quantities are copied to nodes from the closest integration points at the particular TRFEL elements and then passed to MEFEL elements which approximate them to the MEFEL integration points;

- by nodal values, e.g., in `trfel_mefel_by_nodes_comp()`, where nodal values are computed directly at particular TRFEL element nodes and then passed to MEFEL elements which approximate them to the MEFEL integration points;

- by integration points, e. g, in function `trfel_mefel_by_aip(Mm->tnip, MTipmap)` which computes/passes coupling data from TRFEL to MEFEL. Data are taken from the auxil-

iary integration points in TRFEL and stored in MEFEL to the `nonmechq` array for non-mechanical quantities;

- by integration points, e. g, in the function `trfel_mefel_copyip()` which transfers TRFEL quantities to MEFEL as nonmechanical quantities required in MEFEL. In this case, the meshes must be identical in both MEFEL and TRFEL modules, and individual values are copied between corresponding integration points;

The same strategy is also used among all parts - MEFEL, TRFEL, and METR.

The universal but the most challenging strategy of the data transfer for the future work, which uses benefits of the mesh adaptivity problems, is the solution of three independent finite element meshes transferring values via the global coordinate system and finite element approximation functions.

2.6.6 Extensibility

The code extensibility can be illustrated with the help of the conductivity matrix assembling for coupled problems with many variables. The matrix for heat and moisture transfer has the form in Equation (2.99), where three unknown functions are used in the model. These unknowns are temperature T, pore pressure p_1, and pore pressure p_2. Table 2.5 shows a part of the code which computes and assembles the conductivity matrix of one finite element. `ntm` denotes the number of unknown functions. In the case of matrix (2.99), `ntm`=3. The third row in Table 2.5 represents subroutine, which computes a submatrix defined by equation(2.95). The matrix is stored in `lkm`. Appropriate row and column indexes are obtained by the subroutine `codnum` (lines 4 and 5), and they are stored in `rcn` and `ccn`. The submatrix (2.95) is added to the conductivity matrix of a finite element, which is stored in `km`. Further, the element matrix is localized into the matrix of the system of algebraic equations. This subroutine shows that extensibility is ensured, and additional state variables lead to the increase of the variable `ntm`.

```
1   for (i=0;i<ntm;i++){
2       for (j=0;j<ntm;j++){
3           conductivity_matrix (i,eid,i,j,lkm);
4           codnum (rcn,i);
5           codnum (ccn,j);
6           mat_localize (km,lkm,rcn,ccn);
7       }
8   }
```

Table 2.5: Loop for assembling of the conductivity matrix

Chapter 3

Thermo-mechanical analysis of nuclear reactor containment

The numerical solutions of coupled problems are demonstrated by three real-world engineering problems. The first numerical example is the analysis of the nuclear reactor containment wall under thermal loading. It is a modern special concrete structure with the highest demands on safety, service life and reliability. The simulation of the impact of temperature changes during the service is based on staggerred approach combining heat transfer analysis with concrete creep and damage mechanical models.

3.1 Analysis of structural shrinkage and creep in concrete

The analysis of structural creep in concrete comes out from the Boltzmann principle of superposition. Considering uniaxial stress σ [Bažant, 1988], the expression (2.1) is reduced into the following form

$$\varepsilon_{tot}(t) = \varepsilon_\sigma + \varepsilon_0, \tag{3.1}$$

where ε_σ is the strain depending on the stress state, ε_0 is the strain due to effects that are not connected with the applied mechanical load.

Experimental measurements in concrete structures and specimens showed that under service load levels ($\sigma < 0.4 f_{\mathrm{ck}}$, where f_{ck} is the compressive strength), a linear relation can be adopted between stress and strain (linear creep). In cases that the Boltzmann principle of superposition can be used and the stress σ varies in time, the overall strain at time t due to variable stress is a sum of partial strains caused by the particular constant stress increments $\Delta\sigma_i$ applied at time τ_i

$$\varepsilon_{tot} = J(t, t_0)\sigma(t_0) + \int_{t_0}^{t} J(t, \tau)\mathrm{d}\sigma(\tau) + \varepsilon_0. \tag{3.2}$$

The compliance function $J(t, \tau)$ of linear viscoelastic materials represents the strain at time t due to a unit stress $\sigma = 1$ applied at time τ. Models based on extensive experiments are top-rated in the engineering community. The most useful one is Bazant's compliance function known as B3 model, which originates from the set of tests carried out in the 1970s [Baweja and Bažant, 1995].

3.1.1 Discrete model

The stress σ is assumed to be continuous in time and differentiable. The integral constitutive relation (3.2) can be transformed into a differential one. This step requires a suitable representation of the kernels $J(t, \tau)$. From the numerical point of view, the degenerate kernels (in terms of the Dirichlet-Prony series) are the most convenient choice

$$J(t, \tau) \;=\; \sum_{\mu=1}^{M} \frac{1}{D_\mu(\tau)} \left(1 - \exp\left[y_\mu(\tau) - y_\mu(t)\right]\right), \tag{3.3}$$

where $y_\mu = (t/\tau_\mu)^{q_\mu}$, τ_μ are the retardation times and M is the number of units in the Dirichlet-Prony series. The coefficient q_μ is introduced to reduce the number of terms in the expansion, and for concrete, it is usually set to $q_\mu \approx 2/3$. Explicit expressions for $D_\mu(\tau)$ are available for the most used functions J. On the other hand, they can be directly derived from the experimental data using a certain optimization technique, such as the least square method, genetic algorithms and others. Retardation times τ_μ for J must satisfy certain rules for correct calculations. Time τ_1 should be set to a small value (1×10^{-9} days), so that the first term of the Dirichlet-Prony series (3.3) is close to $\frac{1}{D_1}$, and thus D_1 expresses the instantaneous compliance realistically. Remaining values should be uniformly distributed on a logarithmic time scale, i.e., $\tau_\mu = 10^{1/q_\mu}\tau_{\mu-1}$, for $\mu = 2, 3, \ldots, M$. Finally, τ_M should meet the condition $\tau_M > 0.5 t_{\max}$, where $t_{\max}$ is the upper bound on the time interval in which the response of the structure is analyzed. If the lower bound $t_{\min}$ is contained in this interval, the condition $\tau_2 < 3t_{\min}$ has to be checked.

In the case of derivation of retardation coefficients from experimentally obtained data, the least square method leads to the system of linear algebraic equations. Retardation coefficients at time t_0 can be calculated by minimization of the function

$$F = \sum_{k=1}^{s} \Big[\sum_{\mu=1}^{M} \Big[\frac{1}{D_\mu(t_0)} \left(1 - \exp[y_\mu(\tau) - y_\mu(t)]\right) - \overline{J}(t_k, t_0) \Big]^2. \tag{3.4}$$

$\overline{J}(t_k, t_0)$ denotes a set of discrete experimental measured data or suitable approximation of the creep function at times t_k in the given interval. From derivatives of Equation (3.4) with respect to $B_\mu(t_0) = 1/D_\mu(t_0)$, $\mu = 1, 2, \ldots, M$, the system of equations is obtained in the form

$$\begin{pmatrix} a_{11} & a_{12} & \ldots & a_{1M} \\ & a_{22} & \ldots & a_{2M} \\ & & & \ldots \\ & & & a_{MM} \end{pmatrix} \begin{pmatrix} B_1 \\ B_2 \\ \ldots \\ B_M \end{pmatrix} = \begin{pmatrix} p_1 \\ p_2 \\ \ldots \\ p_M \end{pmatrix}, \tag{3.5}$$

where

$$a_{ij} = \sum_{k=1}^{s} [1 - \exp(y_i(t_0) - y_i(t_k))][1 - \exp(y_j(t_0) - y_j(t_k))], \tag{3.6}$$

$$p_i = \sum_{k=1}^{s} [1 - \exp(y_i(t_0) - y_i(t_k))] \overline{J}(t_k, t_0). \tag{3.7}$$

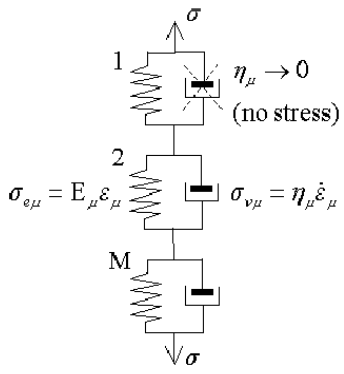

Figure 3.1: Kelvin-Voigt chain model

The total strain is calculated as a sum of individual strains, ε_μ, corresponding to the links of the Kelvin-Voigt chain model (see Figure 3.1), which is a representation of the degenerate kernels (3.3). In this case, the direct solution can be obtained based on the compliance function

giving the following set of equations

$$\varepsilon(t) = \sum_{\mu=1}^{M} \varepsilon_\mu(t) + \varepsilon_0(t), \tag{3.8}$$

$$\varepsilon_\mu(t) = \int_0^t \frac{\mathrm{d}\sigma(\tau)}{D_\mu(\tau)} - \gamma_\mu(t), \tag{3.9}$$

$$\gamma_\mu(t) = \exp\big[-y_\mu(t)\big] \int_0^t \frac{\exp[y_\mu(\tau)]}{D_\mu(\tau)} \mathrm{d}\sigma(\tau), \tag{3.10}$$

$$\mathrm{d}\sigma(\tau) = \frac{\mathrm{d}\sigma(y_\mu)}{\mathrm{d}y_\mu(t)} \frac{\mathrm{d}y_\mu(t)}{\mathrm{d}\tau} \mathrm{d}\tau. \tag{3.11}$$

These formulas assume that σ is a continuous function being equal zero at the beginning of loading ($t = 0$). The hidden variables γ_μ include the time history of loading, and it can be eliminated from Equations (3.9)) and (3.10). Differentiation of Equations (3.9) and (3.10) with respect to $y_\mu(t)$, yields

$$\frac{\mathrm{d}\gamma_\mu(t)}{\mathrm{d}y_\mu(t)} + \gamma_\mu(t) = \frac{1}{D_\mu(t)} \frac{\mathrm{d}\sigma_\mu(t)}{\mathrm{d}y_\mu(t)}, \tag{3.12}$$

$$\frac{\mathrm{d}\varepsilon_\mu(t)}{\mathrm{d}y_\mu(t)} = \gamma_\mu(t). \tag{3.13}$$

The numerical solution is based on dividing the time axis into intervals with the length Δt_i, where only the values of hidden variables at time t_{i-1} have to be known in order to get the values at time t_i. In the first step, these values are equal to zero. Assuming that at the beginning of the i-th interval (t_{i-1}, t_i), the strain $\varepsilon(t_{i-1})$ is known then the hidden variables $\gamma_\mu(t_{i-1})$ for each element of the Kelvin-Voigt chain (Equation (3.10)) can be numerically integrated under certain assumptions. Denoting $\overline{D}_\mu = D_\mu(t_{i-1} + \frac{\Delta t_i}{2})$, after some manipulations $\gamma_\mu(t_i)$ can be expressed as:

$$\gamma_\mu(t_i) = \gamma_\mu(t_{i-1}) e^{-\Delta y_\mu} + \frac{1}{\overline{D}_\mu} \frac{(1 - e^{-\Delta y_\mu})}{\Delta y_\mu} \Delta\sigma. \tag{3.14}$$

The strain increment in the μ-th element of the chain can be expressed as

$$\Delta\varepsilon_\mu = \frac{\Delta\sigma}{\overline{D}_\mu}(-\gamma_\mu(t_i)) = \gamma_\mu(t_{i-1}) \frac{\Delta\sigma}{\overline{D}_\mu} \left(1 - \frac{(1 - e^{-\Delta y_\mu})}{\Delta y_\mu}\right) + \gamma_\mu(t_{i-1})(1 - e^{-\Delta y_\mu}). \tag{3.15}$$

The increments of strains, hidden variables and stresses can be written in the contracted form as

$$\begin{aligned} \Delta\varepsilon_\mu &= \varepsilon_\mu(t_i) - \varepsilon_\mu(t_{i-1}), \\ \Delta\gamma_\mu &= \varepsilon_\mu(t_i) - \gamma_\mu(t_{i-1}), \\ \Delta\sigma_\mu &= \sigma_\mu(t_i) - \sigma_\mu(t_{i-1}). \end{aligned} \tag{3.16}$$

The total strain increment is obtained by the sum of individual contributions from links of the chain

$$\Delta\varepsilon_{\mathrm{tot}} = \Delta\sigma \sum_{\mu=1}^{M} \frac{1}{\overline{D}_\mu} \left(1 - \frac{(1 - e^{-\Delta y_\mu})}{\Delta y_\mu}\right) + \sum_{\mu=1}^{M} \gamma_\mu(t_{i-1})(1 - e^{-\Delta y_\mu}) + \Delta\varepsilon_0. \tag{3.17}$$

Setting the stiffness $\overline{E}_i$ for the i-th interval $\langle t_{i-1}, t_i \rangle$

$$\frac{1}{\overline{E}_i} = \sum_{\mu=1}^{M} \frac{1}{\overline{D}_\mu} \left(1 - \frac{(1 - e^{-\Delta y_\mu})}{\Delta y_\mu} \right) \tag{3.18}$$

and

$$\Delta\varepsilon_c = \sum_{\mu=1}^{M} \gamma_\mu(t_{i-1})(1 - e^{-\Delta y_\mu}) \tag{3.19}$$

allows for the conversion of Equation (3.17) into the final expression for the incremental constitutive relation based on the Dirichlet-Prony series

$$\Delta\sigma = \overline{E}_i \left(\Delta\varepsilon_{\text{tot}} - \Delta\varepsilon_c - \Delta\varepsilon_0 \right), \tag{3.20}$$

which can be generalized into 3D

$$\Delta\boldsymbol{\sigma} = \overline{E}_i \widehat{\boldsymbol{D}} \left(\Delta\boldsymbol{\varepsilon}_{\text{tot}} - \Delta\boldsymbol{\varepsilon}_c - \Delta\boldsymbol{\varepsilon}_0 \right), \tag{3.21}$$

where

$$\widehat{\boldsymbol{C}} = \widehat{\boldsymbol{D}}^{-1} = \begin{pmatrix} 1 & -\nu & -\nu & 0 & 0 & 0 \\ & 1 & -\nu & 0 & 0 & 0 \\ & & 1 & 0 & 0 & 0 \\ & & & 2(1+\nu) & 0 & 0 \\ & & & & 2(1+\nu) & 0 \\ & & & & & 2(1+\nu) \end{pmatrix}. \tag{3.22}$$

3.1.2 Continuous model

As mentioned in the previous section, the total strain is calculated as a sum of individual strains corresponding to the Kelvin-Voigt chain's links. A very efficient method for computer simulations is to introduce the continuous Kelvin chain model with an infinite number of units and retardation times with infinite close spacing [Bažant and Xi, 1995]. This approach was proposed by [Baweja and Bažant, 1995] for B3 compliance function with log-power law

$$J(t, \tau) = q_1 + C(\xi), \tag{3.23}$$

where

$$C(\xi) = q_3 \ln \left[1 + \left(\frac{\xi}{\lambda_0} \right)^n \right], \tag{3.24}$$

with parameters q_3, $\lambda_0 = 1$ and n, is given by the Dirichlet series

$$C(\xi) = \sum_{\mu=1}^{M} B_\mu \left(1 - e^{-\xi/\tau_\mu} \right), \qquad B_\mu = \frac{1}{D_\mu}, \tag{3.25}$$

where $\xi = t - \tau$; t = time (age of concrete); τ = time when the loading was applied and D_μ is the elastic modulus of the μ-th Kelvin unit. Creep compliance function $C(\xi)$ defined by relation (3.24) can be approximated in the continuous form

$$C(\xi) \approx \int_0^\infty L^*(\tau)(1 - e^{-\xi/\tau_\mu})\mathrm{d}\tau. \tag{3.26}$$

Setting $L^*(\tau) = L(\tau)/\tau$, Equation (3.26) reads

$$C(\xi) = \int_0^\infty L(\tau)(1 - e^{-\xi/\tau_\mu})\mathrm{d}(\ln\tau), \tag{3.27}$$

where $L(\tau)$ denotes the continuous retardation spectrum. It has the same meaning in the logarithmic scale as B_μ in the actual time scale. Derivation of $L(\tau)$ from the known compliance function of the material originates from a very efficient general method developed by [Tschoegl, 1971] and later improved by [Tschoegl, 1989].

Using Equations (3.26) and (3.27) and setting $\tau = 1/\zeta$ with $\mathrm{d}(\ln\tau) = -\mathrm{d}(\ln\zeta)$, the creep compliance function has the form of

$$\begin{aligned} C(\xi) &= \int_0^\infty L(\zeta^{-1})(1 - e^{-\xi\zeta})\zeta^{-1}\mathrm{d}\zeta = \\ C(\xi) &= \int_0^\infty L(\zeta^{-1})\zeta^{-1}\mathrm{d}(\zeta) - \int_0^\infty L(\zeta^{-1})e^{-\xi\zeta}\zeta^{-1}\mathrm{d}\zeta. \end{aligned} \tag{3.28}$$

Equation (3.28) can be condensed in the form

$$C(\xi) = f(0) - f(\xi), \tag{3.29}$$

where $f(\xi)$ represents

$$f(\xi) = \int_0^\infty L(\zeta^{-1})e^{-\xi\zeta}\zeta^{-1}\mathrm{d}\zeta, \tag{3.30}$$

where $f(\xi)$ is the Laplace transform of the function $L(\zeta^{-1})\zeta^{-1}$, and ξ is the transformed variable. According to Bazant's recommendation [Bažant and Xi, 1995], the Laplace transform is inverted by using the inversion operator

$$F_{k,\zeta}[f(\xi)] = \frac{(-1)^k}{k!}\left(\frac{k}{\zeta}\right)^{k+1} f^{(k)}\left(\frac{k}{\zeta}\right) \tag{3.31}$$

with the property

$$\lim_{k\to\infty} F_{k,\zeta}[f(\xi)] = \lim_{k\to\infty}\left[\frac{(-1)^k}{k!}\left(\frac{k}{\zeta}\right)^{k+1} f^{(k)}\left(\frac{k}{\zeta}\right)\right] = L(\zeta^{-1})\zeta^{-1}, \tag{3.32}$$

where $f^{(k)}$ is k-th derivative of function f ($f(0)$ is constant). For $k \geq 1$,

$$L(\tau) = -\lim_{k\to\infty}\frac{(-k\tau)^k}{(k-1)!}C^{(k)}(k\tau). \tag{3.33}$$

The approximate spectrum of k-th order is obtained by using a finite value of k. Employing Equations (3.30), (3.29) and (3.24), the transform is written as

$$f(\xi) = q_3 \ln(1+\xi^n) - \int_0^\infty L(\zeta^{-1})\zeta^{-1} \mathrm{d}\zeta, \tag{3.34}$$

Assuming $k = 3$, Equations (3.33) yields the approximation

$$\begin{aligned} L(\tau) &= \left[\frac{-2n^2(3\tau)^{2n-3}[n-1-(3\tau)^n]}{[1+(3\tau)^n]^3}\right]\frac{(3\tau)^3}{2}q_3 \\ &+ \left[\frac{n(n-2)(3\tau)^{n-3}[n-1-(3\tau)^n] - n^2(3\tau)^{2n-3}}{[1+(3\tau)^n]^2}\right]\frac{(3\tau)^3}{2}q_3. \end{aligned} \tag{3.35}$$

For numerical computations, $\ln(\tau)$ is subdivided into time intervals $\Delta\ln(\tau) = \ln 10 \Delta(\log(\tau_\mu))$ and the finite sum approximates the integral in Equations (3.26) and (3.27)

$$C(\xi) = \sum_{\mu=1}^{M} L(\tau_\mu)\left(1 - e^{-\xi/\tau_\mu}\right)\ln 10 \Delta(\log(\tau_\mu)), \quad \text{or} \quad C(\xi) = \sum_{\mu=1}^{M} B_\mu \left(1 - e^{-\xi/\tau_\mu}\right), \tag{3.36}$$

where

$$B_\mu = L(\tau_\mu)\ln 10 \Delta(\log(\tau_\mu)). \tag{3.37}$$

$L(\tau_\mu)$ is given by relation (3.35) and $\Delta(\log(\tau_\mu)$ is equal to time interval between two adjacent Kelvin units in the logarithmic scale [Bažant and Xi, 1995]. It is recommended using high order approximation with high order derivatives of function $C^k(k\tau)$ for more complex expression of the compliance function.

Comparison of discrete and continuous creep model

The continuous retardation spectrum has a significant contribution to the speedup of numerical computations. Assuming the variable character of loading is applied to a structure, it is necessary to find a minimum of function (3.4) in every step for each integration point. It leads to the solution of the high number of equation systems, and consequently, the calculation is slowed down according to the increasing number of elements.

Table 3.1 summarizes computational times of elastic modulus for rectangular 2D finite element mesh with the various number of finite elements for the discrete and continuous model, respectively. The constant speed up of computational time is evident from the table.

Number of elements (num. of int. points)	100(400)	1000(4000)	10000(40000)
Discrete Kelvin chain model	0.69s	6.95s	69.37s
Continuous Kelvin chain model	0.03s	0.33s	3.33s
Speed up	23 times	21 times	21 times

Table 3.1: Speed up of computer calculation for finite element meshes with various number of elements

3.1.3 B3 creep model

As the most popular, Bazant's B3 model with logarithmic-power law was selected for implementation in SIFEL package

$$J(t,\tau) = q_1 + q_2 Q(t,\tau) + q_3 \ln\left[1 + \left(\frac{t-\tau}{\lambda_0}\right)^n\right] + q_4 \ln\left(\frac{t}{\tau}\right), \tag{3.38}$$

where $J(t,\tau)$ is the compliance function at time t due to a unit stress $\sigma = 1$ applied at time τ. The material parameter q_1 is the instantaneous strain due to unit stress. The term with the coefficient q_2 represents the aging viscoelastic compliance, q_3 is the non-aging viscoelastic compliance, and q_4 stands for flow compliance. The coefficient λ_0 is almost equal to 1.0, and $Q(t,\tau)$ is a binomial integral. A detailed description of all coefficients can be found, e.g., in [Baweja and Bažant, 1995].

Moisture and temperature effects

Proper modeling of concrete structures exposed to temperature and moisture changes should cover three complex phenomena in concrete creep (solidification theory model [Bažant et al., 2004]):

- The aging of concrete, which is manifested by a significant decrease of creep with the age at loading is of two types:
  - Short-term chemical aging, which ceases at room temperature after about a year. It is caused by the fact that new solids are produced by the slowly advancing chemical reactions of cement hydration and deposit (in an essentially stress-free) on the walls of capillary pores.
  - Long-term non-chemical aging, manifested by the fact that the decrease of creep with the age at loading continues unabated even for many years after the degree of hydration of cement ceased to grow.
- The drying creep effect, also called the stress-induced shrinkage or Picket effect. It is a transient effect based on the fact that the apparent creep during drying is much larger than the basic creep while the creep after drying is much smaller than basic creep. There is an apparent mechanism manifested by apparent additional creep due to microcracking and a true mechanism that resides in the nanostructure.
- The transitional creep, which represents a transient increase of creep after a temperature change, both heating and cooling. In the case of cooling, the transient increase is of the opposite sign than the final change in creep rate after a steady-state lower temperature has been regained. Similarly to drying creep effect, there are two analogous mechanisms:
  - An apparent macroscopic mechanism, due to thermally induced microcracking and similar to drying creep; and
  - A nanoscale mechanism due to changes in the level of microprestress caused by change of chemical potential of nanopore water with a temperature change.

The effect of temperature on concrete creep is twofold [Bažant et al., 2004], generated by two different mechanisms:

- A temperature increase accelerates the bond breakages and restorations causing creep, increasing the creep rate.
- The higher the temperature accelerates the chemical process of cement hydration and, thus, the aging of concrete, which reduces the creep rate.

Usually, the former effect prevails, and the overall effect of temperature rises in an increase of creep.

Moisture changes have a similar effect on the aging of concrete [Bažant et al., 2004]. The rate of hydration and creep decrease with decreasing relative humidity φ, and when φ approaches 0.3, the rate of aging is almost zero.

The special time quantities are applied to the creep model:

- Reduced time t_r characterizing the changes in the rate of bond breakages and restoration on the microstructural level:

$$t_r(t) = \int_0^t \psi(\tau)\mathrm{d}\tau \leq t, \tag{3.39}$$

where

$$\begin{aligned} \psi(t) &= \psi_T(t)\psi_\varphi(t), & (3.40)\\ \psi_T(t) &= \exp\left[\frac{Q_v}{R}\left(\frac{1}{T_0}-\frac{1}{T}\right)\right], & (3.41)\\ \psi_\varphi(t) &= \alpha_\varphi + (1-\alpha_\varphi)\varphi^2(t), & (3.42) \end{aligned}$$

where T is the absolute temperature, T_0 denotes the reference temperature, φ is the relative humidity in the pores of cement paste, R stands for the gas constant, Q_v is the activation energy for the viscous processes, and α_φ is a material parameter that has to be determined experimentally. Concerning a large set of experiments, Bazant ([Bažant et al., 2004]) determined the following parameters $T_0 = 294$ K, $Q_v/R = 5000$ K and $\alpha_\varphi = 0.1$.

- Equivalent time t_e (equivalent hydration period or maturity), which indirectly characterizes the degree of hydration ($t_e \geq t$):

$$t_e(t) = \int_0^t \beta(\tau)\mathrm{d}\tau, \tag{3.43}$$

where

$$\begin{aligned} \beta(t) &= \beta_T(t)\beta_\varphi(t), & (3.44)\\ \beta_T(t) &= \exp\left[\frac{Q_h}{R}\left(\frac{1}{T_0}-\frac{1}{T}\right)\right], & (3.45)\\ \beta_\varphi(t) &= \{1+[a_\varphi - a_\varphi\varphi(t)]^4\}^{-1}, & (3.46) \end{aligned}$$

where Q_h is the activation energy, $Q_h/R = 2700$ K, and $a_\varphi = 5$.

The effect of temperature and humidity changes (structural thermal expansion and shrinkage) at zero stress can be expressed in strain rates:

- thermal expansion rate

$$\dot{\boldsymbol{\varepsilon}}_t = \boldsymbol{\alpha}\dot{T}, \tag{3.47}$$

- drying shrinkage rate

$$\dot{\boldsymbol{\varepsilon}}_{sh} = \boldsymbol{k}\dot{\varphi} \tag{3.48}$$

where $\boldsymbol{k} = \{k_{11}, k_{22}, k_{33}, k_{23}, k_{31}, k_{12}\}^{\mathrm{T}}$ is the incremental shrinkage coefficient vector, which depends on φ, T and t_e, and $\boldsymbol{\alpha} = \{\alpha_{11}, \alpha_{22}, \alpha_{33}, \alpha_{23}, \alpha_{31}, \alpha_{12}\}^{\mathrm{T}}$ is the thermal expansion coefficient vector.

Providing that shrinkage and thermal expansion are independent of stress, they are assumed in the form

$$\boldsymbol{k} = \varepsilon^0_{sh}\psi\boldsymbol{m}^{\mathrm{T}}, \quad \boldsymbol{\alpha} = \alpha^0\boldsymbol{m}^{\mathrm{T}}, \tag{3.49}$$

where $(-\varepsilon^0_{sh}) = 0.0002 \div 0.001$ and α^0 are empirical constants, and $(-\psi) = E(t_0)/E(t_e)3\varphi^2$ for relative humidity $0.4 \leq \varphi \leq 0.98$.

In the presence of stress, the shrinkage and thermal expansion coefficient vectors are approximated as linear functions of the stress vector [Bažant and Chern, 1985],
$\boldsymbol{\sigma} = \{\sigma_{11}, \sigma_{22}, \sigma_{33}, \sigma_{23}, \sigma_{31}, \sigma_{12}\}^{\mathrm{T}}$ as

$$\boldsymbol{k} = \varepsilon^0_{sh}\psi(\boldsymbol{m}^{\mathrm{T}} + r\boldsymbol{\sigma}\mathrm{sign}(\dot{H})), \quad \boldsymbol{\alpha} = \alpha^0(\boldsymbol{m}^{\mathrm{T}} + \rho\boldsymbol{\sigma}\mathrm{sign}(\dot{H})), \tag{3.50}$$

where $\dot{H} = \dot{\varphi} + c\dot{T}$ (c being a non-negative constant). Empirical coefficients normally attain the values $r = (0.1 \div 0.6)/f_t$ (MPa^{-1}), $\rho = (1 \div 2)/f_t$ (MPa^{-1}), where f_t is the tensile strength. In [Bažant, 1988], Equations (3.50) are simplified by considering $c \to 0$ in case of $\boldsymbol{k}$, to get $\mathrm{sign}(\dot{H}) = \mathrm{sign}(\dot{\varphi})$, and by setting $c \to \infty$ in case of $\boldsymbol{\alpha}$, thus yielding $\mathrm{sign}(\dot{H}) = \mathrm{sign}(\dot{T})$. A general linear dependence (3.50) would also include terms proportional to $\sigma_{\mathrm{mean}} = \frac{1}{3}\boldsymbol{\sigma}^{\mathrm{T}}\boldsymbol{m}^{\mathrm{T}}$.

Generalization into 3D and including incremental form of shrinkage $\Delta\boldsymbol{\varepsilon}_{\mathrm{sh}} = \boldsymbol{k}\Delta\varphi$ and thermal dilatation $\Delta\boldsymbol{\varepsilon}_t = \boldsymbol{\alpha}\Delta T$, the incremental constitutive equation based on the Dirichlet - Prony series is obtained

$$\Delta\boldsymbol{\sigma} = \overline{E}_i\widehat{\boldsymbol{D}}\big(\Delta\boldsymbol{\varepsilon} - \boldsymbol{k}\Delta\varphi - \boldsymbol{\alpha}\Delta T - \Delta\boldsymbol{\varepsilon}_{\mathrm{c}} - \Delta\boldsymbol{\varepsilon}_{\mathrm{d}}\big). \tag{3.51}$$

3.2 Damage Models

Concrete belongs to quasi-brittle materials. In such materials, exceeding a certain strain level leads to the evolution of defects such as microcracks and microvoids. If the growth of strains continues, microcracks can localize into a large discrete crack while the progression of the rest microcracks stops. The process is called the localization of inelastic strains. It can be described by a variety of models depending on the concept of yielding.

3.2.1 Scalar isotropic damage model

The scalar isotropic damage model is one of the simplest models of continuum damage mechanics. More details about the model can be found in [Lemaitre and Chaboche, 1994] and [Skrzypek and Ganczarski, 1999]. The damage models consist in concepts of virgin, damaged and pseudo-undamaged states of material. The material is assumed to be at virgin state when no defects are present which corresponds to elastic state. In a one-dimensional problem, the bar element is subjected to increasing uniaxial stress. The evolution of defects starts at a certain level of strain. A bar element's cross-section area is denoted by A at the virgin state, and let A_d denote the area of defects. In the damaged state, the nominal stress σ is assumed acting on the original cross-section area A while in the pseudo-undamaged state, the effective stress $\tilde{\sigma}$ acts on the undamaged area $\tilde{A} = A - A_d$. The equivalence condition on the bar element can be written in the form

$$\sigma A = \tilde{\sigma}\tilde{A} \tag{3.52}$$

and dimensionless damage parameter ω can is defined

$$\omega = \frac{A_d}{A}. \tag{3.53}$$

Using Equations (3.52) and (3.53), the stress-strain relation for the one-dimensional case can be written

$$\sigma = (1-\omega)E\varepsilon_e = E(\varepsilon_e - \varepsilon_d), \tag{3.54}$$

where

$$\varepsilon_d = \omega\varepsilon. \tag{3.55}$$

In the general three-dimensional case, the stress-strain relation is obtained similarly

$$\boldsymbol{\sigma} = (1-\omega)\boldsymbol{D}_e\boldsymbol{\varepsilon}, \tag{3.56}$$

where $\boldsymbol{\varepsilon}$ represents strain vector without irreversible strains in the form

$$\boldsymbol{\varepsilon} = \boldsymbol{\varepsilon}_{tot} - \boldsymbol{\varepsilon}_p - \boldsymbol{\varepsilon}_c - \boldsymbol{\varepsilon}_{ag} - \boldsymbol{\varepsilon}_{sh} - \boldsymbol{\varepsilon}_t. \tag{3.57}$$

Additionally, the evolution law for damage parameter ω has to be established, and it depends on the type of the modeled material. The evolution law suitable for concrete was proposed in [Papa and Taliercio, 1996], and has the form

$$\omega = \frac{a(\varepsilon - \varepsilon_0)^b}{1 + a(\varepsilon - \varepsilon_0)^b}, \tag{3.58}$$

where ε_0 is the strain threshold, a and b are material parameters controlling the peak value and slope of the softening branch. The damage evolves after the strains exceed the limit value of ε_0.

It is well known ([Lemaitre and Chaboche, 1994]), that damage models are mesh-sensitive. It is connected with the dissipated energy, which depends on the characteristic size of a damaged element, and it leads to physically unrealistic results. Dissipated energy tends to zero with decreasing the characteristic size of the element. The so-called method of the variable softening modulus was developed to avoid the spurious mesh dependency [Pietruszczak and Mróz, 1981].

The method consists in involving the characteristic element length into the damage evolution law. The stress can be expressed for one-dimension in the form

$$\sigma = f_t \exp\left(-\frac{w_{cr}}{w_{cr0}}\right), \tag{3.59}$$

where f_t is the tensile strength in [Pa], w_{cr} [m] is the crack opening, and w_{cr0} [m] is the material parameter controlling the initial slope of the softening branch, see Figure 3.2. The crack opening can be smeared over the element using the following equation

$$\varepsilon - \varepsilon_e = \frac{w_{cr}}{h}, \tag{3.60}$$

where h is the characteristic element length. When combining Equations (3.54), (3.60), and (3.59), the resulting nonlinear equation for the damage parameter ω yields

$$(1-\omega)E\varepsilon = f_t \exp\left(-\frac{\omega h \varepsilon}{w_{cr0}}\right). \tag{3.61}$$

In the case of two-dimensional and three-dimensional models, strain ε has to be substituted by equivalent strain κ. There are many definitions of the equivalent strain κ, but in the case of concrete modeling, the most used definition is the Mazars' norm ([Mazars and Pijaudier-Cabot, 1989]) which has the form

$$\kappa = \sqrt{\langle\varepsilon_\alpha\rangle\langle\varepsilon_\alpha\rangle}, \tag{3.62}$$

where ε_α denotes the principal values of the strain tensor $\boldsymbol{\varepsilon}$ and the symbol $\langle\rangle$ denotes the selection of positive components (Macaulay brackets).

3.2.2 Anisotropic damage model

The main drawback of the scalar isotropic damage model is that it uses only one damage parameter for all principle directions regardless of tension or compression. Once the damage parameter caused by exceeding limit strain in one principle direction evolves, it reduces stiffness in all remaining principal directions even though they should not be influenced. This drawback is not significant in the case of one-dimensional stress state such as tension/compression, but it becomes more important, especially for three-dimensional stress state.

That led to the development of the more advanced damage model, which can better describe the 3D problems. In the paper [Papa and Taliercio, 1996], the authors proposed a general anisotropic model for concrete, which contains nine material parameters. The anisotropic damage model was implemented similarly to the approach proposed in [Papa and Taliercio, 1996] returning zero stresses for the full damage evolution. The model is derived from the Helmholtz free energy written in tensorial notation

$$\begin{aligned}\rho\psi^{\mathrm{el}} &= \frac{1}{2}\left(K-\frac{2}{3}G\right)\left(\varepsilon_V^2 - d\varepsilon_V^2\right) + G\mathrm{tr}\left[\left(\boldsymbol{I}-\boldsymbol{\omega}^t\right)^{1/2}\boldsymbol{e}^t\left(\boldsymbol{I}-\boldsymbol{\omega}^t\right)^{1/2}\boldsymbol{e}^t\right] + \\ &\quad + G\mathrm{tr}\left[\left(\boldsymbol{I}-\boldsymbol{\omega}^c\right)^{1/2}\boldsymbol{e}^c\left(\boldsymbol{I}-\boldsymbol{\omega}^c\right)^{1/2}\boldsymbol{e}^c\right]\end{aligned} \tag{3.63}$$

where ρ is the material density, K is the bulk modulus, G is the shear modulus, ε_V stands for the volumetric strain, indices t and c denote tension and compression. $\boldsymbol{I}$ is the second-order

identity tensor. Additionally, d stands for volumetric damage, $\boldsymbol{\omega}^t$ represents the damage tensor for tension, and $\boldsymbol{\omega}^c$ represents the damage tensor for compression. The strain vector $\boldsymbol{\varepsilon}$ is rewritten to the tensorial form $\boldsymbol{e}$, and decomposed to the tensile and compressive components

$$\boldsymbol{e} = \boldsymbol{e}^t + \boldsymbol{e}^c, \tag{3.64}$$

where $\boldsymbol{e}^t$ and $\boldsymbol{e}^c$ are tensor having the same positive and negative eigenvalues as the tensor $\boldsymbol{e}$, respectively, and zero for possible remaining eigenvalues.

Damage driving forces conjugated to volumetric damage d, damage tensor for tension $\boldsymbol{\omega}^t$ and damage tensor for compression $\boldsymbol{\omega}^c$ can be derived from the relation (3.63) by its derivatives with respect to damage parameters

$$\boldsymbol{Y}^t = -\frac{\partial(\rho\psi^{\mathrm{el}})}{\partial\boldsymbol{\omega}^t} = G\boldsymbol{e}^t \cdot \boldsymbol{e}^t, \tag{3.65}$$

$$\boldsymbol{Y}^c = -\frac{\partial(\rho\psi^{\mathrm{el}})}{\partial\boldsymbol{\omega}^c} = G\boldsymbol{e}^c \cdot \boldsymbol{e}^c, \tag{3.66}$$

$$y = -\frac{\partial(\rho\psi^{\mathrm{el}})}{\partial d} = \frac{1}{2}\left(K - \frac{2}{3}G\right)(\varepsilon_V)^2 \tag{3.67}$$

The tensors $\boldsymbol{Y}^c$ and $\boldsymbol{Y}^t$ have the same principal directions as $\boldsymbol{e}^c$ or $\boldsymbol{e}^t$, respectively. Both $\boldsymbol{\omega}^c$ and $\boldsymbol{\omega}^t$ also have the same directions. Principal stresses can be derived from Equation (3.63) by derivatives with respect to strains, and the following relation can be obtained

$$\sigma_\alpha = \left(K - \frac{2}{3}G\right)\left[1 - dH(\varepsilon_V)\right]\varepsilon_V + 2G\left[1 - H(\varepsilon_\alpha)\omega_\alpha^t - H(-\varepsilon_\alpha)\omega_\alpha^c\right]\varepsilon_\alpha, \tag{3.68}$$

where α represents the index of principal direction, and H stands for the Heaviside function.

The model has three sets of material parameters controlling damage evolution for volumetric and deviatoric damage. The authors of the model proposed the following damage evolution laws

$$\omega_\alpha^\beta = \frac{A_\beta\left(\bar{Y}_\alpha^\beta - \bar{Y}_0^\beta\right)^{B_\beta}}{1 + A_\beta\left(\bar{Y}_\alpha^\beta - \bar{Y}_0^\beta\right)^{B_\beta}}, \tag{3.69}$$

and

$$d = \frac{a\left(\bar{y} - \bar{y}_0\right)^b}{1 + a(\bar{y} - \bar{y}_0)^b}, \tag{3.70}$$

where β represents indices t and c, which are used for tension and compression, respectively. The parameters $\bar{Y}_0^\beta$ and $\bar{y}_0$ stand for initial damage threshold, and parameters A, B, a and b controls the stress peak and slope of the softening branch. The dimensionless conjugated driving forces $\bar{Y}^\beta$ and $\bar{y}$ are defined as $\bar{Y}_\alpha^\beta = Y_\alpha^\beta/E$ and $\bar{y} = y/E$.

3.2.3 Orthotropic damage model

In the case of the anisotropic damage model, laboratory measurements of required material parameters have to be performed, but they cause difficulties in some cases. Additionally, the model requires a significant number of internal variables that have to be stored. These difficulties led to

the development of a simplified version of the model, which is based on six material parameters - three for tension and another three parameters for compression.

The model is based on the following stress-strain relation

$$\sigma_\alpha = \left(1 - H(\varepsilon_\alpha)\omega_\alpha^t - H(-\varepsilon_\alpha)\omega_\alpha^c\right)\left[\left(K - \frac{2}{3}G\right)\varepsilon_V + 2G\varepsilon_\alpha\right], \tag{3.71}$$

where the index α stands for the index of principal components of the given quantity. The model defines two sets of damage parameters ω_α^t and ω_α^c for tension and compression.

Many evolution laws can be used for ω_α^t and ω_α^c description. The two evolution laws for the damage parameters are used similar to the laws used in the scalar isotropic damage model. The first law gives better results for compression, but the material parameters' determination is more complicated. It can be written in the form

$$\omega_\alpha^\beta = \frac{A_\beta\left(|\varepsilon_\alpha^\beta| - \varepsilon_0^\beta\right)^{B_\beta}}{1 + A_\beta\left(|\varepsilon_\alpha^\beta| - \varepsilon_0^\beta\right)^{B_\beta}}, \tag{3.72}$$

where $|\varepsilon_\alpha^\beta|$ is the maximum principal strain in the loading history, equivalent to in Equations (3.61) and (3.62). A_β, B_β, ε_0^β are material parameters with the same meaning as in the similar law defined by Equation (3.58). The second law involves the correction of the dissipated energy concerning the size of elements, and it describes tension better. It is defined by the nonlinear Equation (3.73) which can be solved using the Newton method

$$\left(1 - \omega_\alpha^\beta\right) E|\varepsilon_\alpha^\beta| = f_\beta \exp\left(-\frac{\omega_\alpha^\beta h|\varepsilon_\alpha^\beta|}{w_{cr0}^\beta}\right). \tag{3.73}$$

In the above equation, f_β represents the tensile or compressive strength, and w_{cr0}^β controls the initial slope of the softening branches. More details about the implemented models can be found in [Koudelka and Krejčí, 2008], [Krejčí et al., 2009] and [Koudelka et al., 2009].

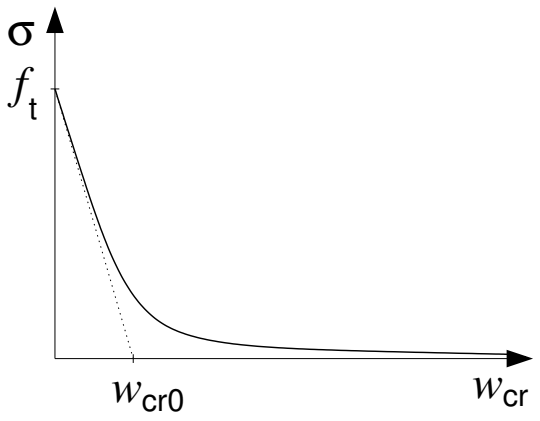

Figure 3.2: One-dimensional traction separation law.

3.3 Computer simulation of reactor containment

The reliability and durability of reactor containments depend directly on the prestressing system. General results from in-situ measurements during the operation show the increase of deformations and the increase of prestress losses since the onset of service. Many measurements explain these phenomena, e.g., at Swedish nuclear reactor containments with non-injected (non-bounded) prestress tendons [Anderson, 2005]. An example of such time evolution of the tendon force in 5 years is plotted in the logarithmic scale in Figure 3.3. Most of the measurements also indicate that the temperature significantly influences prestress losses. This fact is also supported by two gradients of the tendon force losses observed in the nuclear power plant in Temelın in the Czech Republic. It is documented by 6.5 years of measurements of the tendon force depicted in Figure 3.4. This section presents a computer simulation of the nuclear power plant containment in Temelın (Figure 3.5) under cyclic temperature loading during service when stages of service and planned stops are changed. For this study, the well-known fact that the increase in temperature influences the rate of concrete creep is accepted. It is also responsible for the prestress losses of the structure. Simultaneously, increasing deformations can be observed, and additional cracks could occur.

The presented computer simulation as a local model is a part of a complex two-level, global and local, model predicting the prestress losses and the structure response. The global model aims the evolution of prestress forces changed by temperature and climatic loading while the local model is loaded by the mechanical and thermal loading determined from the global model to explain several peculiarities in the containment behavior, mainly the increase of radial strains, which began to show after the service onset. It was verified that the global model results agree very well with the measurement by a magneto-elastic method (MEM). This is mainly the capturing of the prestress force fluctuation caused by temperature decrease and increase during the cyclic reactor shutdown and restart [Bittnar et al., 2008]. The central part of the local model is a staggered coupled thermo-mechanical analysis, where the heat transfer analysis runs in parallel with the mechanical analysis. The fundamental models in the mechanical part are Bažant's B3 model defined in material point with microprestress-solidification theory describing the temperature effect on concrete creep and the orthotropic damage model. The presented computation attempts to model and explain the increase of radial deformation and decreasing of tendon forces since the onset of power plant service. Regarding [Anderson, 2005] and discussions in theoretical studies [Bažant et al., 2004] and [Hellmich, 1999], it can be concluded that the increase of temperature influences creep acceleration. Every change of temperature, moisture content, and loading causes changes in creep rate [Bažant et al., 2004]. There is no doubt that the temperature is one of the sources of prestress losses increase.

3.3.1 Geometry of the local model and basic data

The containment of the nuclear power plant in Temelín in the Czech Republic is a monolithic post-tensioned structure made from reinforced concrete (Figure 3.5). It consists of two parts - the lower cylindrical part and the upper dome. The cylinder has an internal diameter of 45.00 m, and the wall is 1.20 m thick. The dome is fixed into a massive girder. The scheme of the structure is in Figure 3.6. The leak-proofness of the containment is secured by the 8 mm thick steel lining placed inside the structure. Unbounded tendons are placed in three parallel layers in the containment wall.

The local model, one cylindrical segment, represents a periodic unit cell (PUC) from the

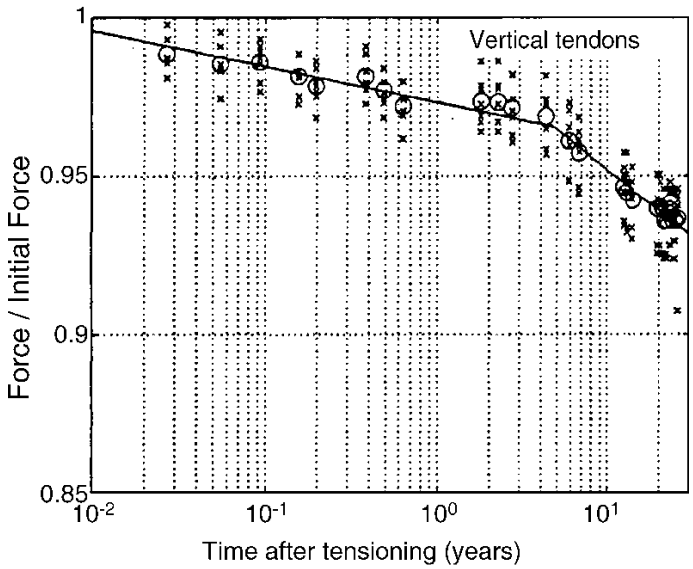

Figure 3.3: Change of tendon force gradient since service time for Swedish nuclear reactor containment [Anderson, 2005].

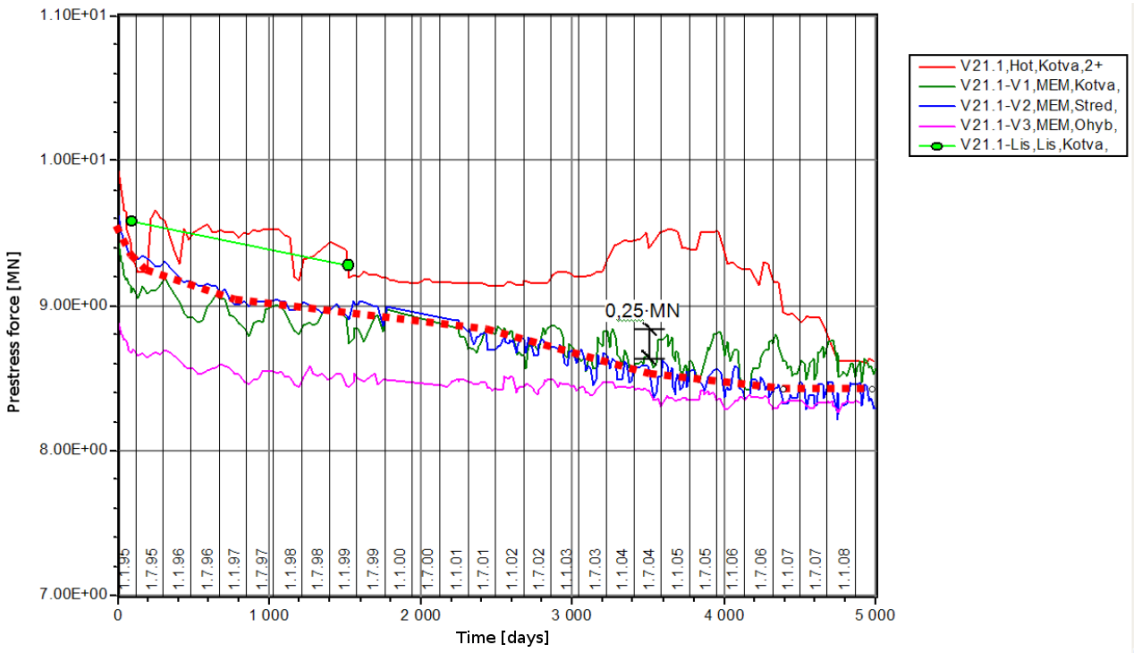

Figure 3.4: Change of tendon force gradient since the service time of reactor containment in Temelín [Štěpán, 2005], measurements by a magneto-elastic method (MEM) and by Hottinger sensors.

cylindrical part of the containment with channels for prestressing tendons and vertical, radial and horizontal reinforcement. It is captured in Figures 3.7 and 3.8. The height of PUC is 2.12 m, and it covers the section of the angle of 7.5°. The prestressing tendons are not modeled. Their effect is introduced as mechanical loading applied through the anchorage system on the top surface of the cylindrical segment, and on the surface of the tendon channels.

The finite element mesh was generated by the mesh generator T3D [Rypl, 2021]. It contains

Figure 3.5: Containments in Temelín (source virtualniprohlidky.cez.cz)[CEZ, 2021].

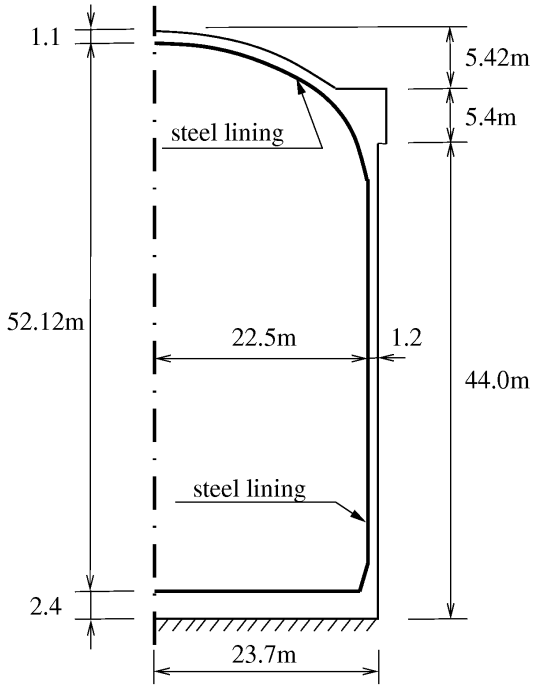

Figure 3.6: Geometry - section view of the containment.

1064171 nodes, 334078 tetrahedral elements with linear approximation functions for concrete and 1685 linear bar elements for steel reinforcement. The model was computed in SIFEL computer code as a thermo-mechanical coupled analysis using a staggered algorithm. The partially coupled

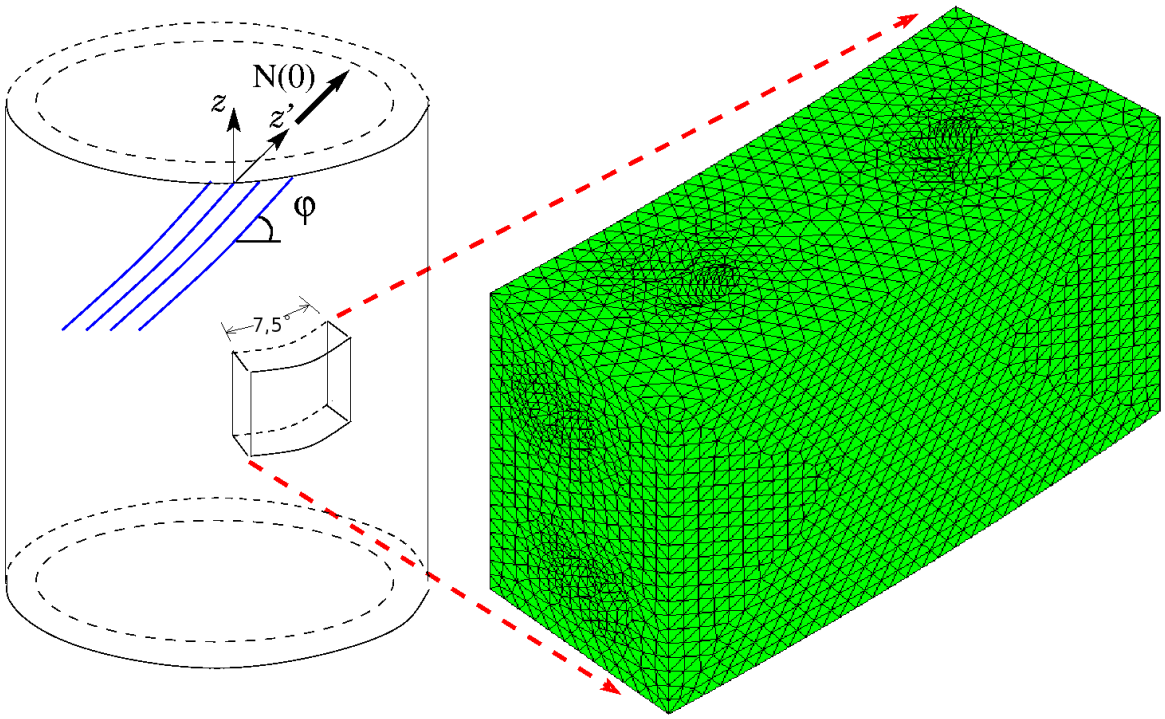

Figure 3.7: Scheme of PUC.

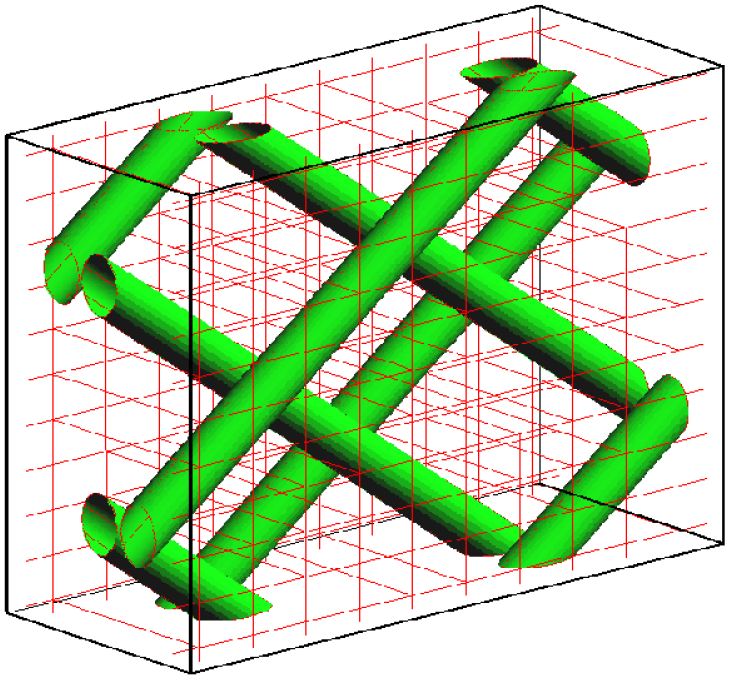

Figure 3.8: Tendon channels and reinforcement.

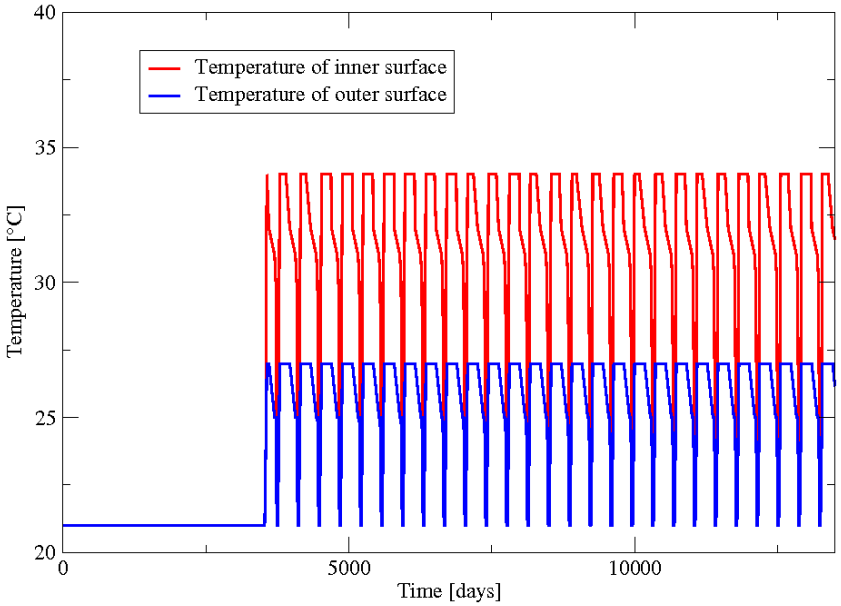

Figure 3.9: Temperatures of inner and outer surface considered in the computer simulation since the end of construction.

concept solves the system of Equations (2.55) for heat transfer in the transport part

$$\boldsymbol{K}_T \boldsymbol{d}_T + \boldsymbol{C}_T \dot{\boldsymbol{d}}_T = \boldsymbol{f}_T$$

and the system of Equations (2.30) in the incremental form in the mechanical part

$$\boldsymbol{K}_u \Delta \boldsymbol{d}_u = \Delta \boldsymbol{f}_{ext} + \Delta \boldsymbol{f}_0.$$

3.3.2 Temperature loading

The Dirichlet boundary conditions represent the impact of temperature, and temperatures from in-situ measurements (inner and outer surface) are applied. The temperature cycle loading depicted in Figure 3.9 was considered in one-year intervals. Applied Dirichlet conditions have been obtained from the idealized course of measured temperatures [Štěpán, 2005], where one cycle operation-stop per year was assumed. The maximal temperature difference about 11°C is applied at the inner surface and about 5°C at the outer surface, see. Figure 3.10.

3.3.3 Mechanical loading

Mechanical loading of the cylindrical segment is considered as a combination of four types of loading:

- Self-weight of the segment.
- Self-weight of the containment over the segment is considered as loading on the top surface.
- Vertical loading of the prestress forces is also considered as loading on the top surface. It is computed from the reactions of the anchorage system decreased by prestressing losses caused by friction in tendon channels.

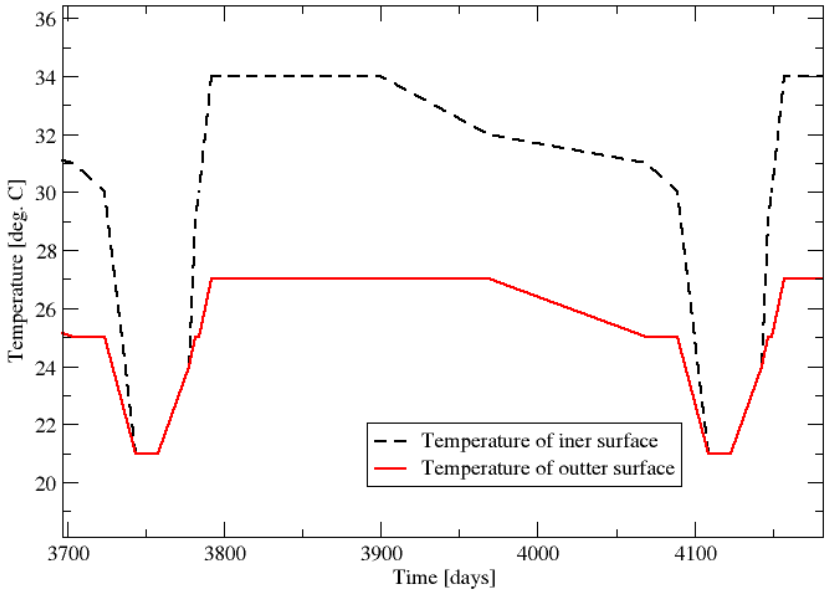

Figure 3.10: Temperatures of inner and outer surface considered in one year cycle.

- Loading prescribed directly in tendon channels consists of radial and tangential components (Figure 3.11).

The first two loadings are instantaneous. The latter two loadings are calculated as a multiple of prestressing forces in tendons in place of the anchorage system. The prestress forces' values are obtained from in-situ measurements by a magneto-elastic method (MEM) [Štěpán, 2005], and they are displayed in Fig. 3.12. The data were approximated by a logarithmic regression method. In the graph, jumps in the prestress force, which simulate the cycle service time - the planned stop (Fig. 3.13), are obtained from the global model [Bittnar et al., 2008].

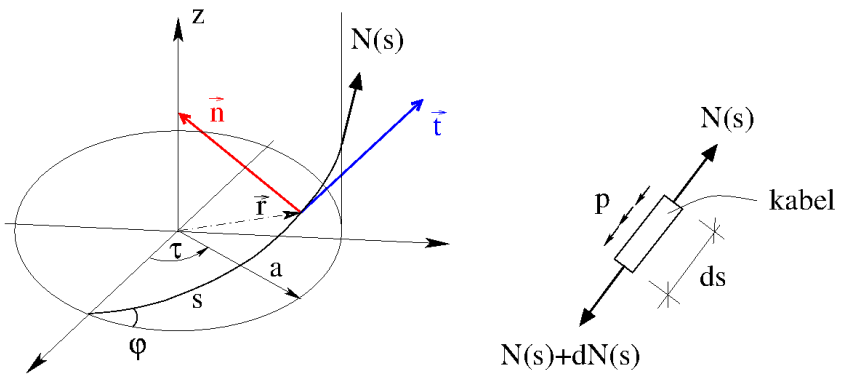

Figure 3.11: Radial and tangential components of loading in tendon channels.

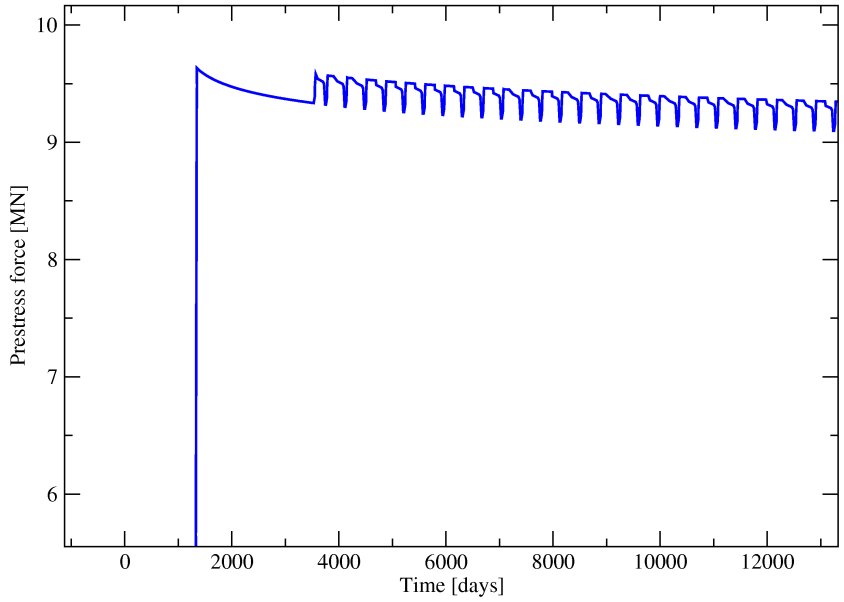

Figure 3.12: Change of the prestress force in the anchorage system since the end of construction.

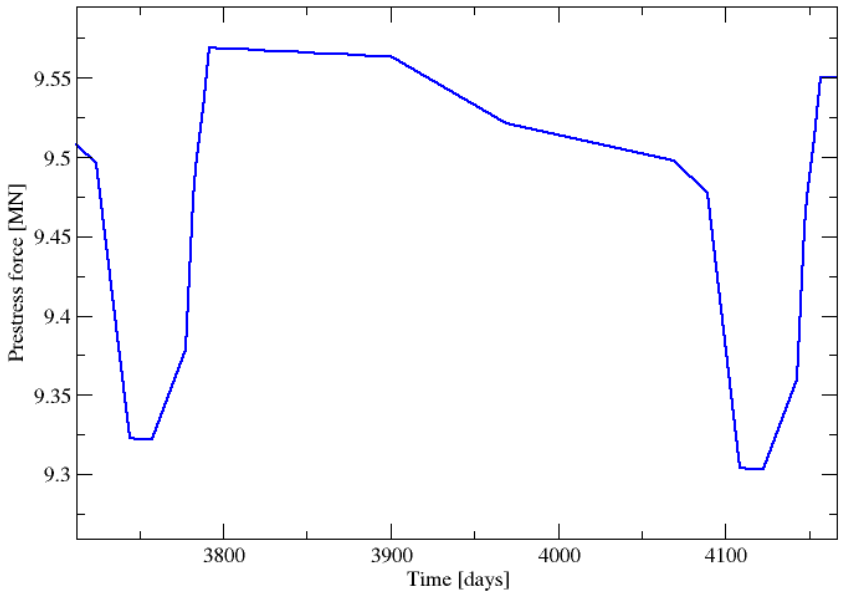

Figure 3.13: Change of the prestress force in the anchorage system in one year cycle.

3.3.4 Material properties and models

In the transport part of the problem, the linear and non-stationary heat transport was solved, assuming constant material parameters. The mechanical part of the computation considered four

types of constitutive material models: creep, damage, plasticity, and the thermal dilatation. The concrete behavior is described by the combination of the B3 creep model influenced by temperature changes and by a suitable damage model. Moisture effects were not taken into account due to the concrete's maturity and due to inner and outer surface structure isolation. Several damage models were used in the computer simulation. The local and non-local versions of the scalar isotropic damage model were tested first. Then the model was extended by anisotropic and orthotropic damage models.

The scalar isotropic damage model showed that tensile strength plays a key role. Several analyzes with different values of the tensile concrete strength were performed. The results obtained for the tensile strength lower than 3.7 MPa give unrealistic behavior due to the extensive damage evolution. In contrast, no damage was observed on the containment structure in situ. It should be noted, the value of the tensile strength was not measured experimentally. Only the compressive strength was determined to value 60 MPa from laboratory tests [Štěpán, 2005]. For this compressive strength, the approximate value of the tensile strength 3.5 MPa can be set according to Czech Technical Standards. It can be recommended for such an important structure the necessity of experiments with concrete specimens created during containment construction to obtain other reliable material parameters for advanced modeling, e.g., the tensile strength and fracture energy in case of damage models.

The scalar isotropic damage model provides the highest limit of structure damage estimation due to the global stiffness reduction. Then the anisotropic and orthotropic damage models appear to be preferable for 3D problems loaded by temperature changes. Calculations using these models give a similar response for the lower level of tensile strength - in the range 2.0-2.8 MPa. The setup of the anisotropic damage model's material parameters was more difficult and time-consuming. Therefore, the orthotropic model, combined with the B3 concrete creep model, was finally used. The basic material parameters setup is summarized in Tables 3.2 and 3.3.

The model of the containment should exhibit good agreement with measured strains in the radial reinforcement. From this point of view, the most important outputs for comparison are damage distribution and the time evolution of the strains in radial steel reinforcement. The steel reinforcement was modeled by the finite bar elements with the plasticity model using the Huber-Misses-Hencky yield criterion, where the yield stress 490 MPa was assumed. The thermal dilatation coefficient was supposed to be $12 \times 10^{-6}\mathrm{K}^{-1}$ in both materials (concrete and reinforcement). Material parameters of steel reinforcement are listed in Table 3.4.

The sequential computation of the containment segment was very time and memory consuming. It should be noted that many calculations had to be performed due to the setup of material parameters. Although the small segment was modeled instead of the complete containment, the single processor computation was suffered by large memory requirements and the computational time was unacceptably long. Therefore, the parallelization of the problem based on the domain decomposition method was adopted.

Volume weight	$\rho = 2600$ kg.m^{-3}
Thermal conductivity coefficient	$\lambda = 2.0$ W.(m.K)$^{-1}$
Specific heat capacity	$C = 800$ J.(kg.K)$^{-1}$

Table 3.2: Thermal material parameters for concrete.

Young's modulus in 28 days	$E_b = 30500$ MPa
Poisson's ratio	$\nu = 0.2$
Cement PC 475	499 kg/m^3
aggregate size 0-4 mm	710 kg/m^3
aggregate size 8-16 mm	460 kg/m^3
aggregate size 16-22 mm	530 kg/m^3
Ligoplast SF	4.9 kg/m^3
Water content	215 kg/m^3
Cubic compressive stregth in 28 days	$R_b = 44.0$ MPa
Beginning of prestressing	$t_0 = 1260$ days

Table 3.3: Parameters for B3 concrete creep model.

Young's modulus	$E_o = 210000$ MPa
Poisson's ratio	$\nu = 0.3$
Yield stress	$f_y = 490$ MPa

Table 3.4: Parameters of steel reinforcement.

3.3.5 Parallelization of the problem

The number of unknowns in the mechanical analysis was 190000 and 63000 unknowns in the heat transport analysis. The analysis was performed on a single processor computer with the processor AMD Athlon 64 X2 6400+ equipped with 8 GB of memory. Concerning extremely high memory requirements, the matrix of the system of equations was stored in the compressed storage scheme, and 2.5 GB of memory was consumed. Because of the storage scheme, the conjugate gradient method was used. The system of algebraic equations was solved in each increment and each inner iteration loop of the Newton-Raphson method. The solution of one system of equations took about two minutes.

The problem was decomposed into eight subdomains to speed up the computation (Fig. 3.14). The average number of unknowns on one subdomain in the mechanical analysis was about 25000, and about 8300 unknowns in the transport analysis, respectively. The parallel computation was performed on a heterogeneous PC cluster where five computers were based on the Intel E6850 processors with the frequency 3 GHz, and 3.3 GB of memory and three computers were based on the Intel E6600 processors with the frequency 2.4 GHz and 3 GB of memory. The Schur complement method was used with the factorization of the subdomain matrices, and the reduced problem was solved using the $\boldsymbol{LDL}^{\mathrm{T}}$ factorization. The factorization of the subdomain matrices took about 17 minutes, and the reduced problem's factorization took 5.5 minutes. The modified Newton-Raphson method was used, then the factorizations were performed only once. The solution of new systems with different right-hand side vectors took about 5 seconds only. The analysis exploited 1.5 GB of memory on slave processors and 2.1 GB on the master processor.

In comparison, both single processor and parallel computations were executed within 93 hours. The parallel algorithm performed 39000-time steps; on the other hand, the single processor algorithm did only 3590-time steps. From this point of view, the parallel code was more than ten times faster than the single processor one. The results of both computations were thoroughly compared

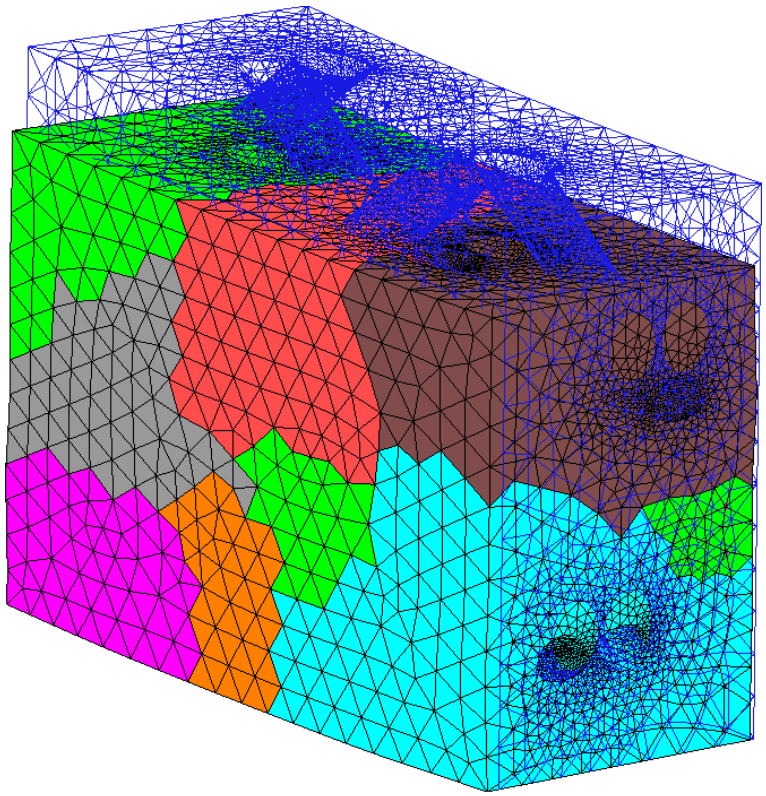

Figure 3.14: Decomposition into subdomains, deformed shape of the mesh (blue).

because they used different methods of the solution of the equation system.

3.3.6 Results of computation. Validation and verification of the model

The relation between the local model response and the tensile strength of concrete in damage models was observed during the computer simulation. Hence, several calculations were performed with different tensile strengths to verify the damage evolution. As expected, the scalar isotropic damage model gives the higher estimate than the orthotropic damage model because the damage parameter in the scalar one influences all principal directions.

Fig. 3.15 - left captures the damage parameter distribution for the scalar isotropic damage model. The concrete tensile strength was assumed 3.75 MPa, and the results were obtained after applying 100% of prestressing. The damage parameter ω attained the maximum value of 0.97. In comparison, the state at the beginning of operation can be seen in the same figure Fig. 3.15 - right. In this case, the maximum attained value of the damage parameter ω was 0.98. For both states, the maximum values of the damage parameter are represented by the dark red color, while the blue areas are undamaged. The distribution of the corresponding crack opening, w, is shown in Fig. 3.16. The damage evolution can be observed during the prestressing phase, especially. The increase of damage parameter can also be observed at the beginning of the operation, but during particular cycles of shutdowns and operations, the damage remains almost unchanged. The maximum value of the crack opening width, w, is 0.088 mm at the end of the prestressing phase and 0.113 mm at the beginning of the operation. Note that in these figures, the same color scheme is used for the damage parameter, ω.

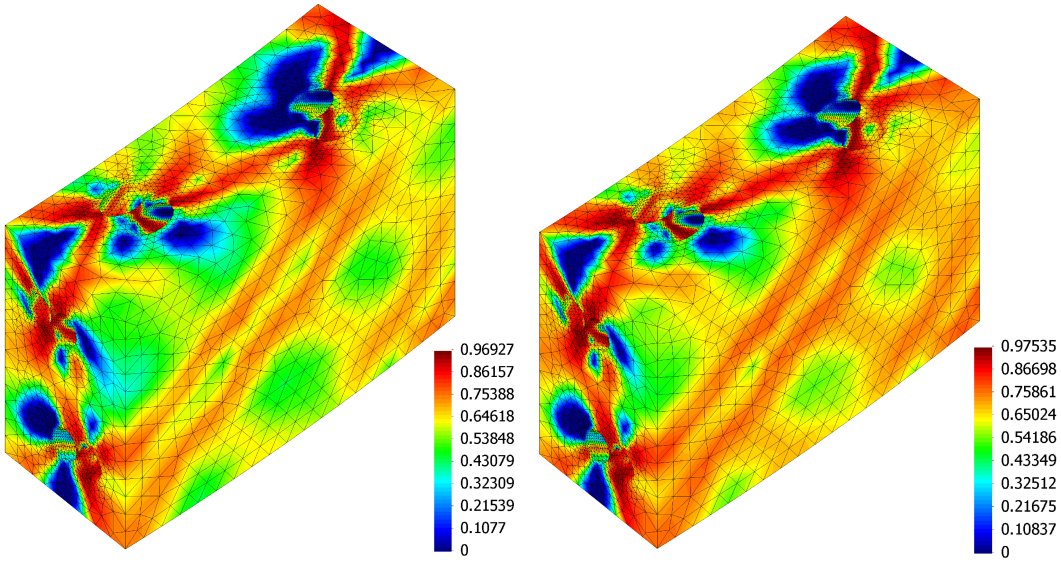

Figure 3.15: Distribution of the damage parameter ω for 100% of prestressing (left) and at the beginning of operation (right) - scalar isotropic damage model.

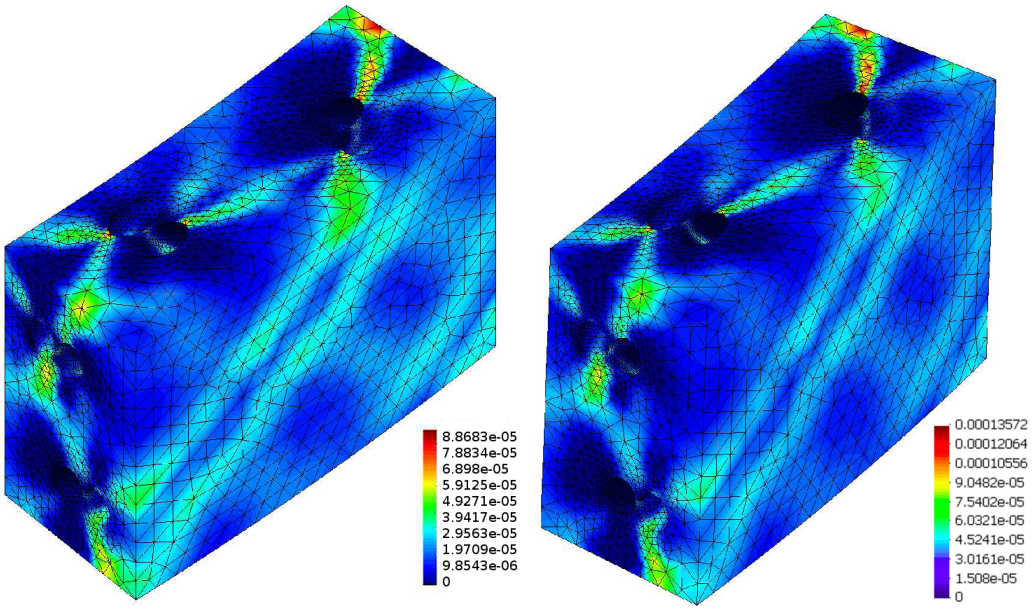

Figure 3.16: Distribution of the crack opening width w [m] for 100% of prestressing (left) and at the beginning of operation (right) - scalar isotropic damage model.

The following results were obtained using the orthotropic damage model for the lower tensile strength $f_t = 2.0$ MPa. Fig. 3.17 (left) illustrates the distribution of the tensile damage parameter in the first principal direction, which corresponds to the radial direction and Fig. 3.18 shows the distribution of the tensile damage parameter in the second principal direction, which corresponds to the tangential direction, for the level of 100% of prestressing. The maximum value of the damage parameter in the radial direction ω^t is 0.93 and 0.93 in the tangential direction. The same color scheme is used as previous for the scalar isotropic damage model. The damage parameters in the third principal direction have zero or negligible values.

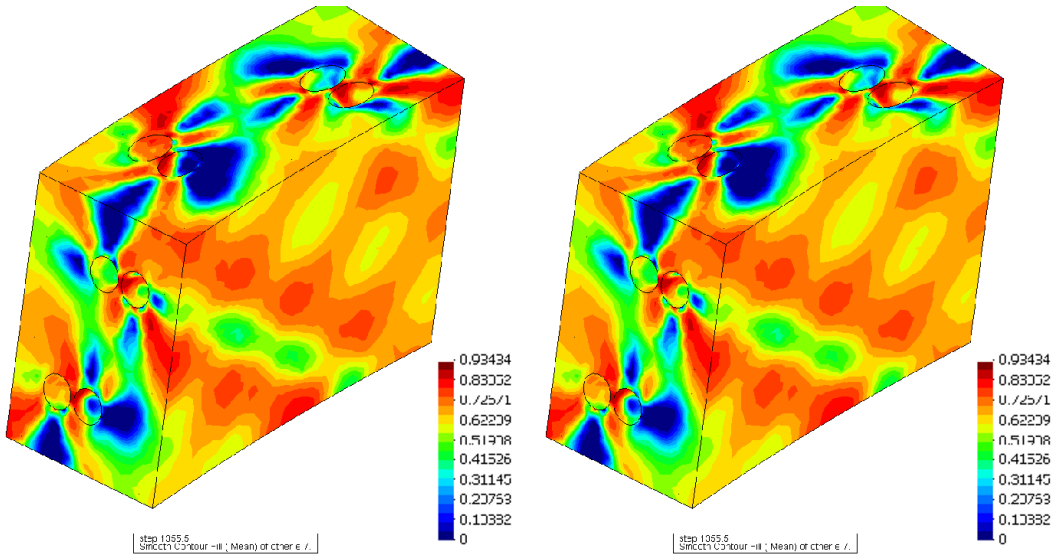

Figure 3.17: Distribution of the damage parameter ω^t in the radial direction for 100% of prestressing (left) and the corresponding crack opening width w^t [m] in the radial direction - orthotropic damage model.

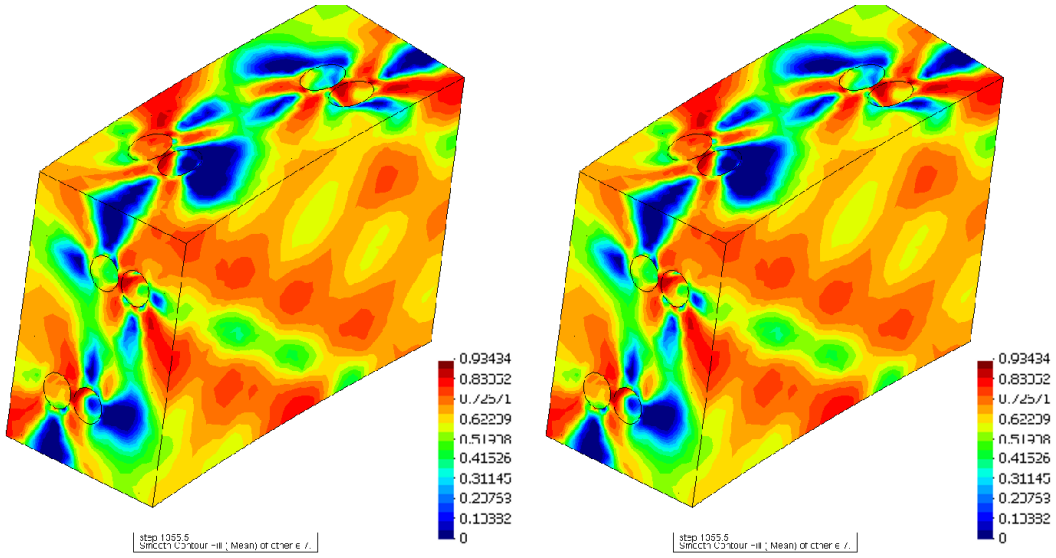

Figure 3.18: Distribution of the damage parameter ω^t in the tangential direction for 100% of prestressing (left) and the corresponding crack opening width w^t [m] in the radial direction - orthotropic damage model.

The validation of the presented numerical model against in situ measurements was carried out by comparing strains in radial reinforcement in the place of sensors Hottinger. The main aim was capturing the trend of the strain evolution during the construction and operation time. The development of the strain in the most loaded bar of radial reinforcement can be seen in Fig. 3.19 (above). Due to output data reduction, each two operation/shutdown cycles have been merged and printed. In the diagram, the dashed red line represents measured strain in the radial reinforcement, and the black line represents the computed results, respectively. The course of the measured strains was simplified, and this red dashed line connected only peak values. These

results are not acceptable because they differ from the measurements significantly since the end of the prestressing phase. Additionally, unrealistic tensile strength 3.75 MPa was used, and the scalar isotropic damage model seems to be less accurate for this analysis. On the contrary, the second diagram in Fig. 3.19 (lower), which corresponds to the orthotropic damage model with the tensile strength 2.0 MPa, exhibits better coincidence with the measured data. However, the evolution of strains still differs from measurements in later times (from the time 4000 days).

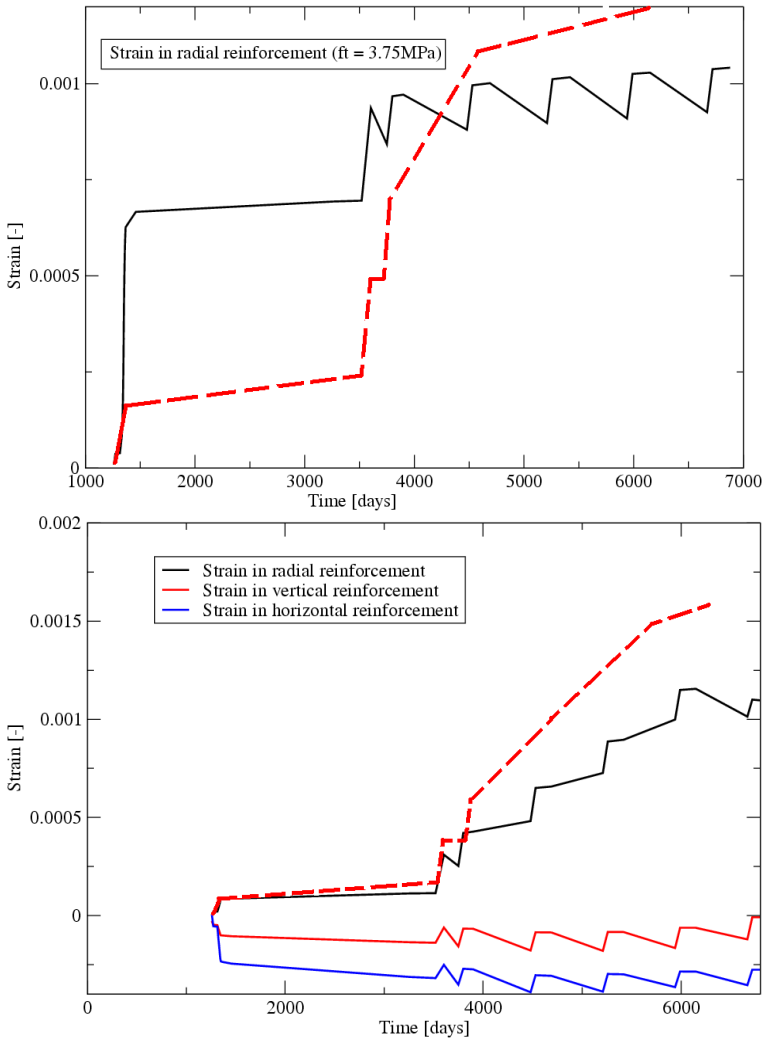

Figure 3.19: Diagram of the strain evolution in the radial reinforcement - isotropic damage model (above) and orthotropic damage model (lower).

3.3.7 Results of computation and conclusions

It can be concluded from the data of the analysis that the temperature effect, which increases concrete creep, is vanishing in time. In the case of accompanying effects due to cracking strain evolution, the increase of radial deformation and decrease of tendon forces during service life can be observed.

The following conclusions can be made from the obtained results:

- The explanation of the increase of radial strains and decrease of tendon forces since the onset of service is based on the theoretical knowledge in concrete creep influenced by the temperature changes and partly on the prestress losses measurements mainly at Swedish nuclear reactor containments. The influence of the temperature increase during the service was proved.
- The results obtained from the combination of the simplified global model and the local model show relatively good coincidence with in-situ measurements.
- For the best coincidence between the computer simulation and the measurements, calibration of all appearing material models and their parameters should be performed and compared with laboratory and in-situ measurements. Especially, the tensile strength, which is the fundamental property for monitoring the possible damage of the containment, has to be determined.

From the computational point of view, it can also be concluded that the parallelization of the problem helped significantly to reduce computational time. Achieved speed up of the parallel code stems from two facts. First, more processors were used compared to the sequential version. Second, the sequential code had to use a solution of the system of equations based on the conjugate gradient method due to huge memory requirements, while the parallel implementation was based on matrix factorization. Therefore, only the back substitution was performed in each loop of the Newton method.

Chapter 4

Thermo-hygro-mechanical analysis of Charles bridge

The second numerical example is the study of the current stress and damage state of the masonry Charles bridge influenced by climatic loading. The Charles bridge belongs to the most prominent European historical structures. It is highly esteemed not only for its historical magnitude but also for the economic contributions, caused namely by the attention of tourists. In this study, the thermo-hygro-mechanical analysis follows the staggered coupling algorithm connecting the heat and moisture transfer model, which was extended by climatic loading and mechanical damage models.

4.1 Künzel and Kiessl's coupled heat and moisture transfer approach

The coupled heat and moisture transfer can in porous materials be easily simulated by a model proposed by Künzel and Kiessl's [Künzel and Kiessl, 1997]. It is a phenomenological approach suitable for concrete and masonry structures under common climatic conditions. Advantage of this approach is its straightforward application to the analysis of building structures in normal climatic conditions and easy and quick determination of physical material properties obtained from laboratory measurements. This popular model is summarized in the following section.

Two unknowns are introduced in the model for each material point, relative humidity φ [-] and temperature T [K]. The model divides the over-hygroscopic region into two subranges - capillary water region and supersaturated region, where different conditions for water and water vapor transport are considered. For the description of simultaneous water and water vapor transport, the relative humidity φ is chosen as the only moisture potential for both hygroscopic and over-hygroscopic ranges. Although the model uses certain simplifications, it describes all substantial phenomena, and the predicted results comply well with experimentally obtained data, which is the main advantage of the model together with the effortless and quick determination of the material properties measured in a laboratory.

4.1.1 Transport equations

Künzel proposed that the moisture transport mechanisms are just water vapor diffusion and liquid transpor which is relevant to numerical analysis in building physics [Künzel and Kiessl, 1997]. Vapor diffusion is the most important for large pores, whereas fluid transport occurs place on pore surfaces and in small capillaries.

Vapor diffusion in porous media is described in the model by the Fick's diffusion and effusion in the form

$$\boldsymbol{J}_v = -\delta_p \boldsymbol{\nabla} p = -\frac{\delta}{\mu} \boldsymbol{\nabla} p, \tag{4.1}$$

where δ_p [kg m s^{-1} Pa^{-1}] is the vapor permeability of the porous material, p denotes vapor pressure [Pa], the vapor diffusion resistance number, μ [-], is a material property, and δ [kg m s^{-1} Pa^{-1}] is the vapor diffusion coefficient in air.

The liquid transport mechanism includes fluid flow in the layer absorbed (surface diffusion) and in the water-filled capillaries (capillary transport). The driving potential in both cases is capillary pressure (suction stress) or relative humidity φ. The flux of liquid water is described by

$$\boldsymbol{J}_w = -D_\varphi \boldsymbol{\nabla} \varphi, \tag{4.2}$$

where the liquid conductivity, D_φ [kg m s^{-1}], is the product of the liquid diffusivity, D_w [m^2 s^{-1}], and the derivative of water retention function $D_\varphi = D_w \cdot \mathrm{d}w/\mathrm{d}\varphi$.

The heat flux is proportional to the thermal conductivity of the moist material and the temperature gradient (Fourier's law)

$$\boldsymbol{q} = -\lambda \boldsymbol{\nabla} T, \tag{4.3}$$

where λ [W m^{-1} K^{-1}] is the effective thermal conductivity of the wet material. The enthalpy flows through moisture movement and phase transition is taken into account in the form of source

terms in the heat balance equation. In Equations (4.1) to (4.3), permeability, liquid, and thermal conductivities are assumed as tensors for general three-dimensional problems.

4.1.2 Balance equations

The heat and moisture balance equations are closely coupled because the moisture content depends on the total enthalpy and thermal conductivity, while the temperature depends on moisture flow. The resulting set of differential equations for the description of simultaneous heat and moisture transfer, expressed in terms of temperature, T, and relative humidity, φ, has the form of partial differential equations defined on a domain Ω

$$\frac{\partial w}{\partial \varphi}\frac{\partial \varphi}{\partial t} = \boldsymbol{\nabla}^{\mathrm{T}}\big(D_\varphi \boldsymbol{\nabla}\varphi + \delta_p \boldsymbol{\nabla}(\varphi p_{\mathrm{sat}})\big), \qquad \boldsymbol{x} \in \Omega, \tag{4.4}$$

$$\Big(\rho C + \frac{\partial H_w}{\partial T}\Big)\frac{\partial T}{\partial t} = \boldsymbol{\nabla}^{\mathrm{T}}\big(\lambda\, \boldsymbol{\nabla} T\big) + h_v \boldsymbol{\nabla}^{\mathrm{T}}\big(\delta_p \boldsymbol{\nabla}(\varphi p_{\mathrm{sat}})\big), \qquad \boldsymbol{x} \in \Omega, \tag{4.5}$$

where H_w [J m^{-3}] is the enthalpy of the material moisture, w [kg m^{-3}] represents the water content of the material, h_v [J kg^{-1}] is the evaporation enthalpy of the water, p_{sat} [Pa] denotes the water vapor saturation pressure, ρ [kg m^{-3}] is the material density, C [J kg^{-1} K^{-1}] is the specific heat capacity, and t [s] denotes time. The boundary of the domain Ω is split into several parts Γ_T, Γ_φ, Γ_{qpT}, $\Gamma_{Jp\varphi}$, Γ_{qcT} and $\Gamma_{Jc\varphi}$ which are disjoint and their union is the whole boundary Γ.

4.1.3 Boundary conditions

Three types of boundary conditions accompany the system of equations (4.4) and (4.5):

- Dirichlet boundary conditions for prescribed temperature and relative humidity

$$T(\boldsymbol{x}, t) = \overline{T}(\boldsymbol{x}, t), \qquad \boldsymbol{x} \in \Gamma_T \tag{4.6}$$

$$\varphi(\boldsymbol{x}, t) = \overline{\varphi}(\boldsymbol{x}, t), \qquad \boldsymbol{x} \in \Gamma_\varphi \tag{4.7}$$

- Neumann boundary conditions for prescribed fluxes

$$q_n(\boldsymbol{x}, t) = \overline{q}(\boldsymbol{x}, t), \qquad \boldsymbol{x} \in \Gamma_{qpT}, \tag{4.8}$$

$$J_n(\boldsymbol{x}, t) = \overline{J}(\boldsymbol{x}, t), \qquad \boldsymbol{x} \in \Gamma_{Jp\varphi}, \tag{4.9}$$

- Cauchy boundary conditions

$$q_n(\boldsymbol{x}, t) = \alpha(T(\boldsymbol{x}, t) - T_\infty(\boldsymbol{x}, t)), \qquad \boldsymbol{x} \in \Gamma_{qcT}, \tag{4.10}$$

$$J_n(\boldsymbol{x}, t) = \beta(p(\boldsymbol{x}, t) - p_\infty(\boldsymbol{x}, t)), \qquad \boldsymbol{x} \in \Gamma_{Jc\varphi}, \tag{4.11}$$

where $\overline{T}(\boldsymbol{x}, t)$ is the prescribed temperature, $\overline{\varphi}(\boldsymbol{x}, t)$ is the prescribed relative humidity, $\overline{q}(\boldsymbol{x}, t)$ represents the value of heat boundary flux in the direction of normal vector $\boldsymbol{n}$, $\overline{J}(\boldsymbol{x}, t)$ is the value of moisture boundary flux in the direction of normal vector $\boldsymbol{n}$, α [W m^{-2} K^{-1}] and β [kg s^{-1} Pa^{-1}] are the heat and mass transfer coefficient, T_∞ denotes the ambient temperature, and p_∞ stands for the ambient water vapor pressure.

4.1.4 Discretisation of the differential equations

The finite element method is used for spatial discretisation of the partial differential equations Eq. (4.4) and (4.5). The weighted residual method is applied to the mass balance equation assuming $\delta T = 0$ on Γ_T and $\delta\varphi = 0$ on Γ_φ

$$\int_\Omega \delta\varphi\Big(\frac{\partial w}{\partial \varphi}\frac{\partial \varphi}{\partial t} - \boldsymbol{\nabla}^{\mathrm{T}}\big(D_\varphi \boldsymbol{\nabla}\varphi + \delta_p \boldsymbol{\nabla}(\varphi p_{\mathrm{sat}})\big)\Big)\mathrm{d}\Omega = 0 \tag{4.12}$$

and also to the energy balance equation

$$\int_\Omega \delta T\left(\left(\rho C \ + \frac{\partial H_w}{\partial T}\right)\frac{\partial T}{\partial t} - \boldsymbol{\nabla}^{\mathrm{T}}\left(\lambda\ \boldsymbol{\nabla} T\right) - h_v \boldsymbol{\nabla}^{\mathrm{T}}\left(\delta_p \boldsymbol{\nabla}(\varphi p_{\mathrm{sat}})\right)\right)\mathrm{d}\Omega = 0. \tag{4.13}$$

Applying Green's theorem the weak formulation for mass transfer yields

$$\begin{aligned}\int_\Omega \delta\varphi\Big(\frac{\partial w}{\partial \varphi}\frac{\partial \varphi}{\partial t}\Big)\mathrm{d}\Omega + \int_\Omega \boldsymbol{\nabla}\delta\varphi\cdot\Big(D_w\frac{\mathrm{d}w}{\mathrm{d}\varphi} + \delta_p p_{\mathrm{sat}}\Big)\boldsymbol{\nabla}\varphi\mathrm{d}\Omega + \int_\Omega \boldsymbol{\nabla}\delta\varphi\cdot\Big(\delta_p\varphi\frac{\mathrm{d}p_{\mathrm{sat}}}{\mathrm{d}T}\Big)\nabla T\mathrm{d}\Omega \\ - \int_{\Gamma_J}\delta\varphi\Big(D_w\frac{\mathrm{d}w}{\mathrm{d}\varphi} + \delta_p p_{\mathrm{sat}}\Big)\frac{\partial\varphi}{\partial\vec{n}}\mathrm{d}\Gamma - \int_{\Gamma_q}\delta\varphi\Big(\delta_p\varphi\frac{\mathrm{d}p_{\mathrm{sat}}}{\mathrm{d}T}\Big)\frac{\partial T}{\partial\vec{n}}\mathrm{d}\Gamma = 0\end{aligned} \tag{4.14}$$

and the weak formulation for heat transfer

$$\begin{aligned}\int_\Omega \delta T\Big(\rho C \ + \frac{\partial H_w}{\partial T}\Big)\frac{\partial T}{\partial t}\mathrm{d}\Omega + \int_\Omega \boldsymbol{\nabla}\delta T\Big(\lambda + h_v\delta_p\varphi\frac{\mathrm{d}p_{\mathrm{sat}}}{\mathrm{d}T}\Big)\boldsymbol{\nabla}T\mathrm{d}\Omega + \\ \int_\Omega \boldsymbol{\nabla}\delta T\Big(h_v\delta_p p_{\mathrm{sat}}\Big)\boldsymbol{\nabla}\varphi\mathrm{d}\Omega - \int_{\Gamma_{Jp\varphi}}\delta T\Big(h_v\delta_p p_{\mathrm{sat}}\Big)\frac{\partial\varphi}{\partial\vec{n}}\mathrm{d}\Gamma \\ - \int_{\Gamma_{qpT}}\delta T\Big(\lambda + h_v\delta_p\varphi\frac{\mathrm{d}p_{\mathrm{sat}}}{\mathrm{d}T}\Big)\frac{\partial T}{\partial\vec{n}}\mathrm{d}\Gamma \ = \ 0.\end{aligned} \tag{4.15}$$

In the finite element method, the temperature T and relative humidity φ are approximated in the form

$$T \approx \boldsymbol{N}_T(\boldsymbol{x})\boldsymbol{d}_T, \qquad \varphi \approx \boldsymbol{N}_\varphi(\boldsymbol{x})\boldsymbol{d}_\varphi, \tag{4.16}$$

and the gradients of temperature and relative humidity are also needed

$$\boldsymbol{\nabla}T \approx \boldsymbol{B}_T(\boldsymbol{x})\boldsymbol{d}_T, \qquad \boldsymbol{\nabla}\varphi \approx \boldsymbol{B}_\varphi(\boldsymbol{x})\boldsymbol{d}_\varphi. \tag{4.17}$$

In the previous equations, $\boldsymbol{d}_T$ denotes the vector of nodal temperatures, and $\boldsymbol{d}_\varphi$ is the vector of nodal relative humidities. Matrices of approximation functions for temperature and relative humidity $\boldsymbol{N}_T(\boldsymbol{x})$, $\boldsymbol{N}_\varphi(\boldsymbol{x})$ are usually identical. Then the identity also follows for their gradients $\boldsymbol{B} = \boldsymbol{B}_T(\boldsymbol{x}) = \boldsymbol{B}_\varphi(\boldsymbol{x})$. The same rule is adopted for the weight functions δT and $\delta\varphi$.

Approximations (4.16) and (4.17) are introduced in Equations (4.14) and (4.15). It leads to a set of first-order differential equations written in the matrix form

$$\begin{pmatrix} \boldsymbol{K}_{\varphi\varphi} & \boldsymbol{K}_{\varphi T} \\ \boldsymbol{K}_{T\varphi} & \boldsymbol{K}_{TT} \end{pmatrix}\begin{pmatrix} \boldsymbol{d}_\varphi \\ \boldsymbol{d}_T \end{pmatrix} + \begin{pmatrix} \boldsymbol{C}_{\varphi\varphi} & \boldsymbol{C}_{\varphi T} \\ \boldsymbol{C}_{T\varphi} & \boldsymbol{C}_{TT} \end{pmatrix}\begin{pmatrix} \dot{\boldsymbol{d}}_\varphi \\ \dot{\boldsymbol{d}}_T \end{pmatrix} = \begin{pmatrix} \boldsymbol{J}_\varphi \\ \boldsymbol{q}_T \end{pmatrix}. \tag{4.18}$$

The matrices $\boldsymbol{K}_{\varphi\varphi}$, $\boldsymbol{K}_{\varphi T}$, $\boldsymbol{K}_{T\varphi}$ and $\boldsymbol{K}_{TT}$ create the conductivity matrix of the problem, and they have the form

$$\boldsymbol{K}_{\varphi\varphi} = \int_\Omega \boldsymbol{B}^T \boldsymbol{D}_{\varphi\varphi} \boldsymbol{B} \mathrm{d}\Omega, \quad \boldsymbol{K}_{\varphi T} = \int_\Omega \boldsymbol{B}^T \boldsymbol{D}_{\varphi T} \boldsymbol{B} \mathrm{d}\Omega, \tag{4.19}$$

$$\boldsymbol{K}_{T\varphi} = \int_\Omega \boldsymbol{B}^T \boldsymbol{D}_{T\varphi} \boldsymbol{B} \mathrm{d}\Omega, \quad \boldsymbol{K}_{TT} = \int_\Omega \boldsymbol{B}^T \boldsymbol{D}_{TT} \boldsymbol{B} \mathrm{d}\Omega, \tag{4.20}$$

where the conductivity matrices of material $\boldsymbol{D}_{\varphi\varphi}$, $\boldsymbol{D}_{\varphi T}$, $\boldsymbol{D}_{T\varphi}$, and $\boldsymbol{D}_{TT}$ are diagonal matrices. The diagonal entries are equal to following conductivities

$$k_{\varphi\varphi} = D_w \frac{\mathrm{d}w}{\mathrm{d}\varphi} + \delta_p p_{\mathrm{sat}}, \quad k_{\varphi T} = \delta_p \varphi \frac{\mathrm{d}p_{\mathrm{sat}}}{\mathrm{d}T}, \tag{4.21}$$

$$k_{T\varphi} = h_v \delta_p p_{\mathrm{sat}}, \quad k_{TT} = \lambda + h_v \delta_p \varphi \frac{\mathrm{d}p_{\mathrm{sat}}}{\mathrm{d}T}. \tag{4.22}$$

The matrices $\boldsymbol{C}_{\varphi\varphi}$, $\boldsymbol{C}_{\varphi T}$, $\boldsymbol{C}_{T\varphi}$, and $\boldsymbol{C}_{TT}$ create the capacity matrix of the problem

$$\boldsymbol{C}_{\varphi\varphi} = \int_\Omega \boldsymbol{N}^T \boldsymbol{H}_{\varphi\varphi} \boldsymbol{N} \mathrm{d}\Omega, \quad \boldsymbol{C}_{\varphi T} = \int_\Omega \boldsymbol{N}^T \boldsymbol{H}_{\varphi T} \boldsymbol{N} \mathrm{d}\Omega, \tag{4.23}$$

$$\boldsymbol{C}_{T\varphi} = \int_\Omega \boldsymbol{N}^T \boldsymbol{H}_{T\varphi} \boldsymbol{N} \mathrm{d}\Omega, \quad \boldsymbol{C}_{TT} = \int_\Omega \boldsymbol{N}^T \boldsymbol{H}_{TT} \boldsymbol{N} \mathrm{d}\Omega, \tag{4.24}$$

where capacity matrices of material $\boldsymbol{H}_{\varphi\varphi}$, $\boldsymbol{H}_{\varphi T}$, $\boldsymbol{H}_{T\varphi}$ and $\boldsymbol{H}_{TT}$ are also diagonal matrices with the following diagonal entries corresponding to capacities

$$c_{\varphi\varphi} = \frac{\partial w}{\partial \varphi}, \quad c_{\varphi T} = 0, \tag{4.25}$$

$$c_{T\varphi} = 0, \quad c_{TT} = \rho C \ + \frac{\partial H_w}{\partial T}. \tag{4.26}$$

The vectors $\boldsymbol{J}_\varphi$ and $\boldsymbol{q}_T$ contain prescribed nodal fluxes

$$\boldsymbol{J}_\varphi = \int_{\Gamma_{Jp\varphi}} \boldsymbol{N}^T \overline{J} \mathrm{d}\Gamma, \quad \boldsymbol{q}_T = \int_{\Gamma_{qpT}} \boldsymbol{N}^T \overline{q} \mathrm{d}\Gamma \ . \tag{4.27}$$

There are several extensions and modifications of Künzel and Kiessl's model, improving the model's features or the computational stability of numerical solutions. One such extension by climatic conditions effect is implemented into SIFEL code according to [Grunewald, 2000], and it is briefly described, e.g., in [Maděra and Černý, 2005]. Another modification of the model is presented in [Maděra et al., 2017]. The driving equations are changed for two basic unknowns - partial vapor pressure p_v and temperature T to obtain better stability near a fully saturated state. A general moisture storage function replaces the sorption isotherm, and the derivative $\frac{\partial w}{\partial \varphi}$ in Equation (4.4) reaches the high values out of proportion.

4.2 Thermo-hygro-mechanical analysis of Charles bridge

Charles bridge in Prague is one of the most prominent historical structures in the Czech Republic (Figure 4.1 and 4.2).

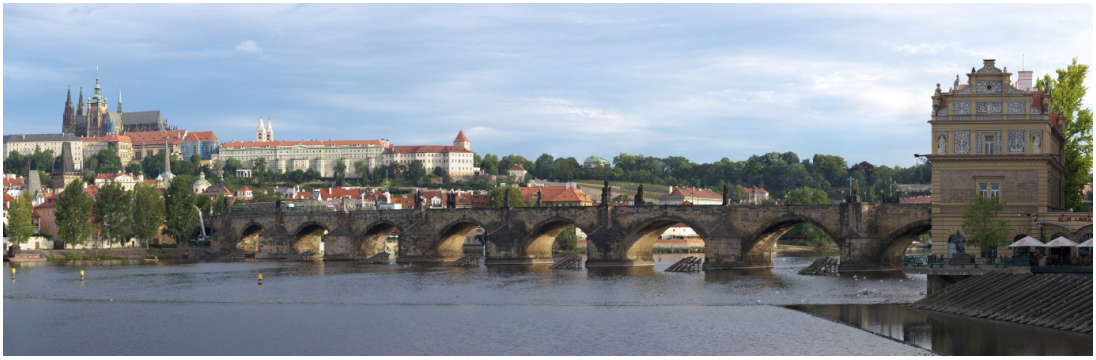

Figure 4.1: Charles bridge, St. Vitus cathedral and the Castle on the background.

Figure 4.2: Detail of Charles bridge in Prague.

The foundation stone was laid down on 9th July 1357, and the bridge itself was completed around 1406. In the past, the bridge has suffered a lot of disastrous states, mostly due to floods and water erosion. Fortunately, after the last flood in August 2002, the bridge sustained without notable damage. The bridge also went through a variety of reconstructions. The previous two strongly influenced the actual structure. In the last century (the 1960s - 1970s), it was grouting, the introduction of the water-proofing layer, installation of stabilizing reinforced concrete slab, replacement of facing masonry, and more recent actions. In July 2007 - June 2010, the last work included the repair of parapets, hydroisolation of the pavement, and the rehabilitation of the foundations. The reconstruction was based on a series of computational and experimental

studies described in [Zeman et al., 2008], [Šťastná et al., 2009], [Přikryl and Šťastná, 2010] and [Přikryl et al., 2011]. The complex underlying model was multi-scale due to the heterogeneity of the bridge on different levels. It was able to reflect non-linear material properties, multi-physical and transient phenomena covering climatic effects, and the interaction of the bridge with water and colliding vessels. The analyses established that climatic loading should be considered most dangerous for the bridge as it is responsible for the nucleation and further development of cracks in the bridge.

The thermo-hygro-mechanical analysis performed could be the first thing when contemplating any actions such as, e.g., designing further stages of the bridge repair. In the case of Charles bridge, it is the retrofit of the bridge's sandstone cladding scheduled for the near future.

The numerical model presented was three dimensional, taking into account the voluminous proportion of the bridge. The most important part was the simulation of coupled heat and moisture transfer in the stone masonry of Charles Bridge, which represented the first phase of the thermo-hygro-mechanical analysis with the comparison of computer results with experimentally obtained data. The second phase of the study - the prediction of damage evolution, was carried out in a staggered-coupled format to keep the model complexity manageable. It means that transport phenomena served as inputs for the mechanical part in each time step.

Such simulations of the evolution of temperature and moisture fields and their impact on the mechanical response are very arduous tasks, especially when sequential computations of coupled problems are both time and memory consuming. Therefore, the parallelization of the problem based on the domain decomposition method was adopted. This method speeded up not only the solution of the system of algebraic equations but also the evaluation of constitutive equations and assembling the system matrices.

4.2.1 History and current state

Charles bridge links both banks of the Vltava river, connecting the Old Town and the Lesser Town in Prague. It was the second arch masonry bridge in Prague, built to substitute the collapsed Judith's bridge.

The bridge is 516.7 m long and 9.1 - 9.7 m wide, with 16 arches whose span varies from 16.6 to 23.4 m. It stands on 17 piers (each shielded by an ice guard) with a cross-section ranging from 6.3 - 10.8 m by 24 - 25 m. Founded initially on millstones (either supported by oaken grillages or boxes anchored to the bed of the river), the piers have heads sharpened at an angle of 65°, to protect it against water stream and drifting ice. The subsoil is formed by a 5 - 10 m layer of coarse grained gravel (with the particle size of up to 0.5 m) that lies on a rock massif consisting of Ordovic shales and quartzite [Toesca, 2014]. The bridge has been a vital trade route for five centuries, but since 1966 it only serves pedestrians.

The bridge was damaged many times, mainly from floods and water erosion that caused periodic reconstructions, rehabilitations, or strengthening, giving to the monument a significant variability of materials and construction technologies in its different parts. The floods happened several times during the construction, as well as after the completion. The last catastrophic event was in 1890, which brought to the collapse three bridge spans (5th, 6th, and 7th vault). Due to the floods, the original foundations (millstones) were gradually replaced, and some foundation of piers were rebuilt on concrete caissons, see [Zeman et al., 2008].

4.2.2 Materials and structural elements

The bridge is mainly built up of Bohemian sandstone masonry. There are main three mesoscopic heterogeneity patterns distinguished in the body [Zeman et al., 2008]:

- Regular periodic sandstone (upper Cretaceous quartz sandstone and carboniferous arkoses) ashlars (opus quadratum) facing of vaults (Figure 4.3 left), bound on lime mortar from sandstone stucco and hydraulic lime [Witzany et al., 2008].
- Sandstone masonry (opus quadratum) with a non-periodic arrangement of blocks used in the facing of breast walls (Figure 4.3 in the middle).
- Filling irregular quarry masonry (opus caementicium) consisting of arenaceous marl blocks and mortar made of sand and black hydraulic lime (Figure 4.3 right). Classified as structural mortared rubble masonry [Přikryl and Šťastná, 2010] according to the different granulometry (from 5 to 50 cm) and the coarse particles. The aggregates are macroscopically very fine grained (aleuropelitic) sedimentary rock of light beige to ochre color. Despite the numerous interventions, the fill masonry is considered as gothic original, since it is preserved in 13 out of 15 pillars and in 13 arches out of 16 [Přikryl and Šťastná, 2010].

Figure 4.3: Periodic sandstone, non-periodic sandstone and filling masonry in the Charles bridge [Toesca, 2014].

Charles bridge is constructed as a traditional masonry arch bridge, where massive piers support arches - vaults. An internal infill (Figure 4.5 part C), laterally covered by breast walls, makes the proper level for the flooring, which includes concrete slab, gravity concrete layers, today hydroisolation, and granite paving. The breast walls (Figure 4.5 part B) stand on the bridge arches (Figure 4.5 part A); in the lower part, they are 0.9 m thick, while in the upper one, the thickness is 0.4 m. They were built without expansion joints and are reinforced at the connection with piers by masonry pillars that are also pedestals for statues (Figure 4.6). As the breast walls, even piers and vault arches, are built using bush-hammered blocks. The pier masonry is made up of granite blocks up to the level of the Vltava river, above it, the sandstone is used [Witzany et al., 2008].

4.2.3 Last interventions

The last two reconstructions mainly influence the present state of the bridge. In 1966 - 1975, the bridge was strengthened by high-pressure grouting and by a reinforced concrete slab (without

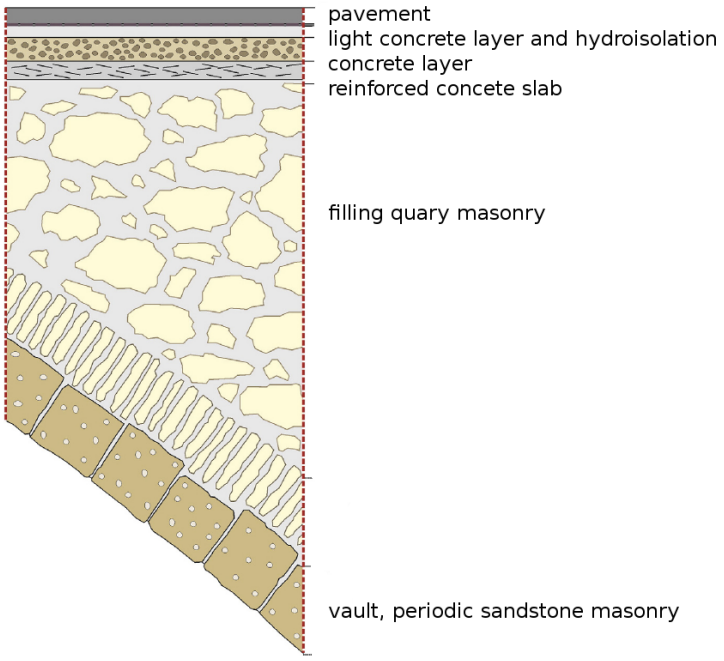

Figure 4.4: Cross-section through the fill masonry of arch XIV [Přikryl and Šťastná, 2010].

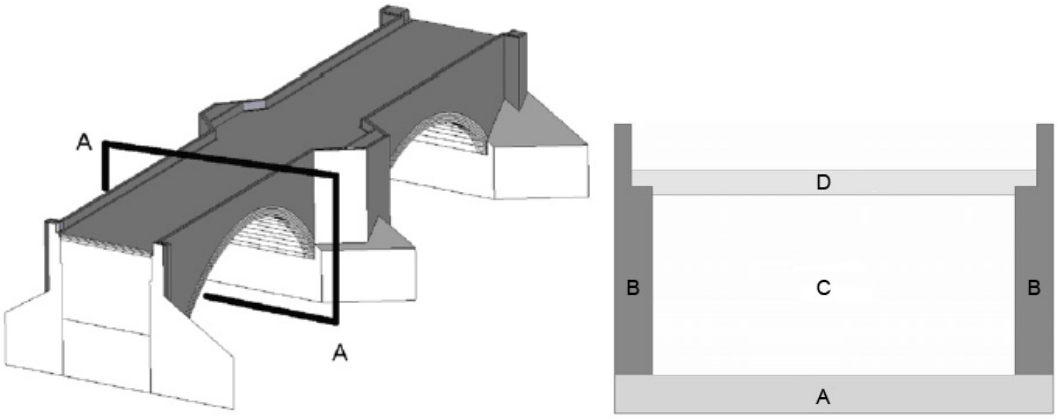

Figure 4.5: Schematic 3D view of Charles bridge with A-A section.

expansion joints), covered by a bituminous waterproofing layer. The most degraded stone blocks were replaced. The passage to vehicles was excluded. It was later shown that some interventions during the reconstruction were made very callous. This erroneous interventions of the 1960s-1970s brought problems with chemical, biochemical, and physical degradation of the bridge. They also strongly influenced the interaction of bridge structural elements (e.g., body filler with the stone structure) and harmed the overall behavior, contributing to the gradual mechanical disintegration of the structure. Most of the mentioned problems are described in references [Přikryl et al., 2011], [Witzany and Zigler, 2007] and [Witzany et al., 2008].

A new intervention was performed in 2007 - 2010 to solve problems in a compatible way, not only created by the 1960's - 1970's repair. It consisted of the rehabilitation of foundations as

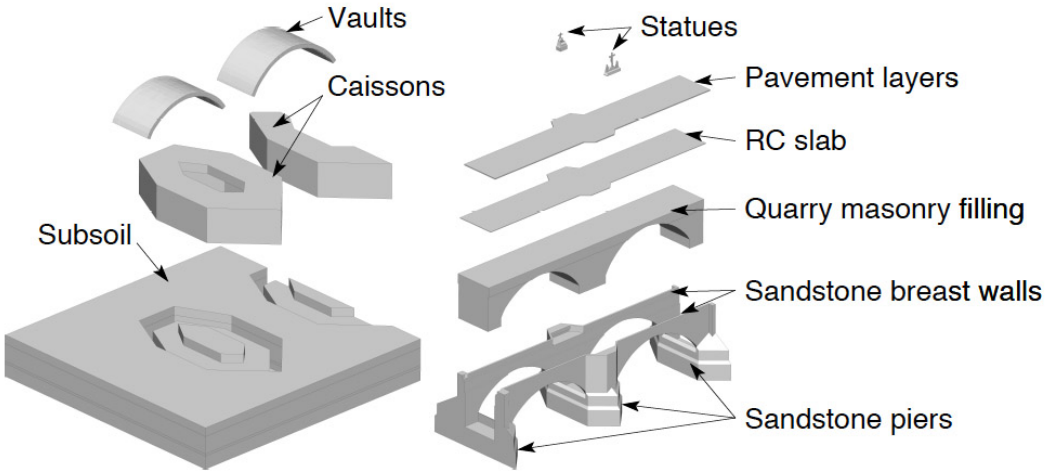

Figure 4.6: Schematization of the bridge elements [Zeman et al., 2008].

the first step, followed by the pavement's hydroisolation. Then the replacement of parapets, new navigation signs, and gaslighting followed to end of the work. The existing concrete slab was cut and dilated in the middle and in the borders to create expansion joints to reduce the stresses related to its dilatation. Now, the expansion joint in contact with the breast wall is 150 mm thick, and it is filled with gravel, while the one in the middle of the slab has thickness 20 cm, and it is formed by extruded polystyrene [MottMacDonald, 2011].

Dilatation joints have been made in the stone railing masonry in correspondence with vault/pier intersection to prevent cracks evolution in the parapets and breast walls caused by temperature changes. They are filled with a plastic mortar mixed with stone fragments (Figure 4.7). It was proven the parapets are the most affected by the up/down movements of the vault related to summer/winter changes and by the non-uniform temperature profile of the bridge body.

And finally, the most degraded stone blocks were replaced in parapets and breast walls. Despite all the efforts, the replacement was sharply criticized because the new stones do not match the old ones aesthetically in their vicinity. All mentioned interventions are summarized in [Toesca, 2014].

4.2.4 Current damage state and possible causes

As for mechanical degradation, there are visible cracks (thickness of millimeters) in vaults, breast walls, and parapets. In the vaults, the cracks are aligned and located approximately 1 m from the breast wall (Figure 4.8). They are also present in buttresses, near the pedestals for statues, and in the corners between buttress and breast wall. Even in the monument, many minor cracks are present, but they do not represent a menace for structural stability.

Recent studies explained the leading causes of crack development. It is assumed, thanks to the previous repair, the damage is not related to the movements of the foundation [Zeman et al., 2008]. The non-stress effects are considered causing the interaction of stone bridge structure, bridge body filler, and breast walls prominently affecting the vertical deformations of the bridge vaults. The gradient of the non-uniform temperature changes of individual bridge parts (spatial distribution of temperature field) causes deformation and permanent strain. It leads to a gradual disintegration of the stone masonry, e.g., growing tilt of the breast walls [Witzany and Zigler, 2007], shear

Figure 4.7: Dilatation joint and contrast between old and new blocks [Toesca, 2014].

stresses development close to the external surfaces and in layers along with the interface between sandstone masonry and irregular quarry masonry [Zeman et al., 2008]. The shear stresses caused by differences in temperature are balanced by tensile stresses which cause the crack nucleation and development in the breast wall faces and vaults [Krejčí and Šejnoha, 2015]. In the parapets, which have been recently repaired (2007 - 2010), cracks are expected to show again due to the periodic shear stresses action related to the temperature gradient between the upper and lower parts and due to the vertical movements of the vaults (upwards in summer and downwards in winter). It is considered that, in the long period, the mechanism will bring to the ultimate damage the horizontal joints, and consequently, the repair of the parapet will be needed again. The above mentioned vertical joints have been filled with deformable plastic mortar during the last reconstruction to reduce this effect (Figure 4.7).

4.2.5 Installation of measuring system and monitoring of temperature and moisture fields

During the last intervention, a measuring system was installed to monitor the temperature and moisture content. The continuous monitoring of temperature and moisture fields required a sufficiently dense network of reliable sensors. To this end, four bridge cross-sections were selected, and they are plotted together with the logger's position for illustration in Figure 4.9.

The control system has been allocated under the twelfth vault on the Lesser Town's side of the bridge. Cross-sections 1 and 2 situated in arch No. XI are 36 m and 34 m away from the logger's position, respectively. The distance of cross-sections 3 and 4 (arch VIII) from the logger is 128 m and 137 m, respectively. Several gauge points are located in the selected cross-sections 1 through 4 (C.S. 1 - 11pts., C.S. 2 - 13 pts., C.S. 3 - 11 pts., C.S. 4 - 15 pts.). Each measuring point has been fitted with three temperature sensors and with one moisture sensor. To cope with demanding simulations, just one segment of the bridge, one half of arch VIII, was examined in computer experiments. The corresponding set-up in cross-sections 3 and 4 is displayed in Figures 4.11 and

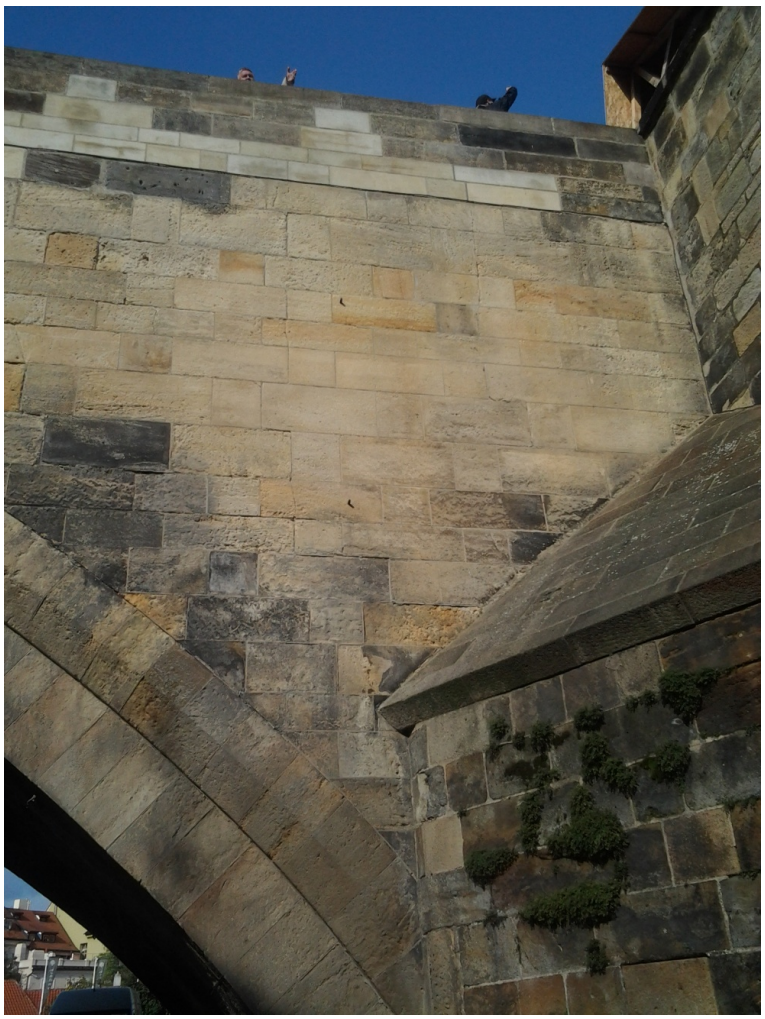

Figure 4.8: Visible vertical cracks in the southern breast wall of arch No. XI near pillar No. 10.

4.10.

Each measuring point has been fitted with three temperature sensors and with one moisture sensor. To cope with demanding simulations, just one segment of the bridge, one half of arch VIII, was examined in computer experiments. The corresponding set-up in cross-sections 3 and 4 is displayed in BT 3D1:1, BT 3D1:2, and BT 3D1:3 sstand subsequently for temperature sensors 1, 2, and 3, respectively, while the moisture sensor situated at the same point is denoted as BH 3D1:4. Selected data are stored under this notation in the Information System [CTU, 2010].

The Pt1000 thermometers performed temperature measuring, imbedded in a special resin in a stainless casing, 6 mm in diameter. Four strands of shielded conductors were delivered with no interconnections because of the system's reliability. The sensors were subjected to accelerated aging in a climatic chamber (cycling between 30 - 100°C and with samples submerged in warm acid, alkali, and water). Moisture sensors were also imbedded in unique porous ceramics and connected with an electric resistivity-voltage transducer made to order. Calibrating was provided using the gravimetric method exploiting samples extracted from the test pit.

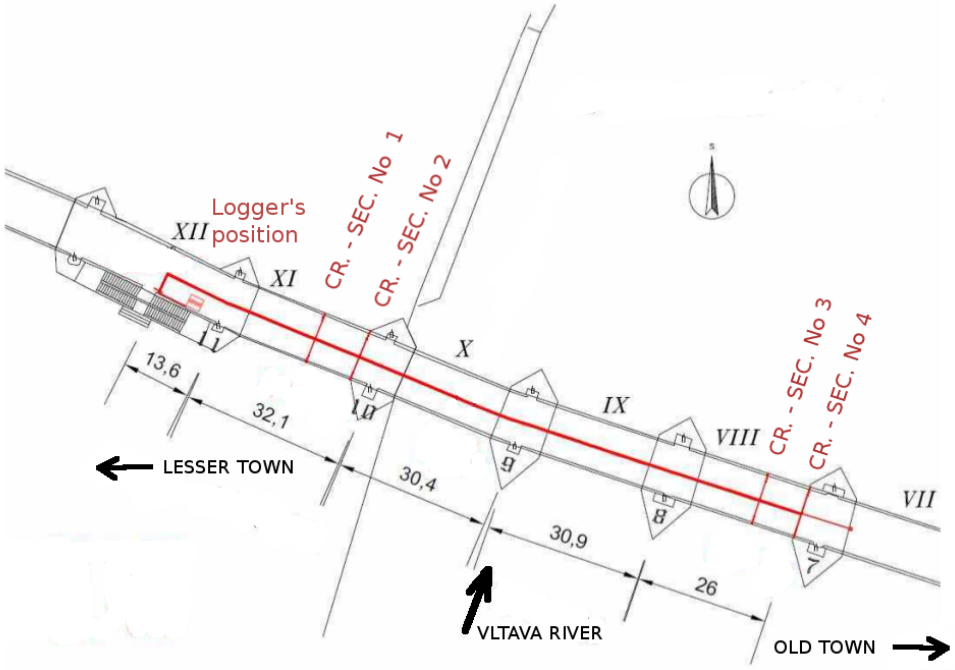

Figure 4.9: Layout of cross-sections selected for sensors instalment.

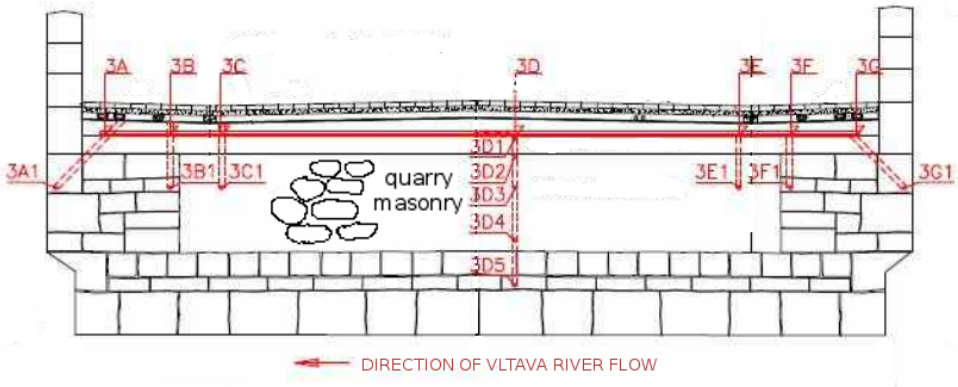

Figure 4.10: Cross-section 3 - gauge points (11 points, i.e. 33 temperature sensors and 11 moisture sensors).

4.2.6 Computational model

The numerical model of Charles bridge simulated the coupled heat and moisture transfer and mechanical response of one half of arch III in the course of two years, 2011 - 2012. The finite element mesh was created using tetrahedron elements with linear approximation functions in an academic version of GiD modeler [GiD, 2021]. It had 73749 nodes and 387773 elements (Figure 4.12).

The numerical model was based on two theoretical approaches and material models. The first approach was the heat and moisture transport model, according to Künzel and Kiessl's theory described in section 4.1. And the second one, describing the mechanical response, was the orthotropic damage model (Sec. 3.2.3) which is suitable for three dimensional analyses of quasi-

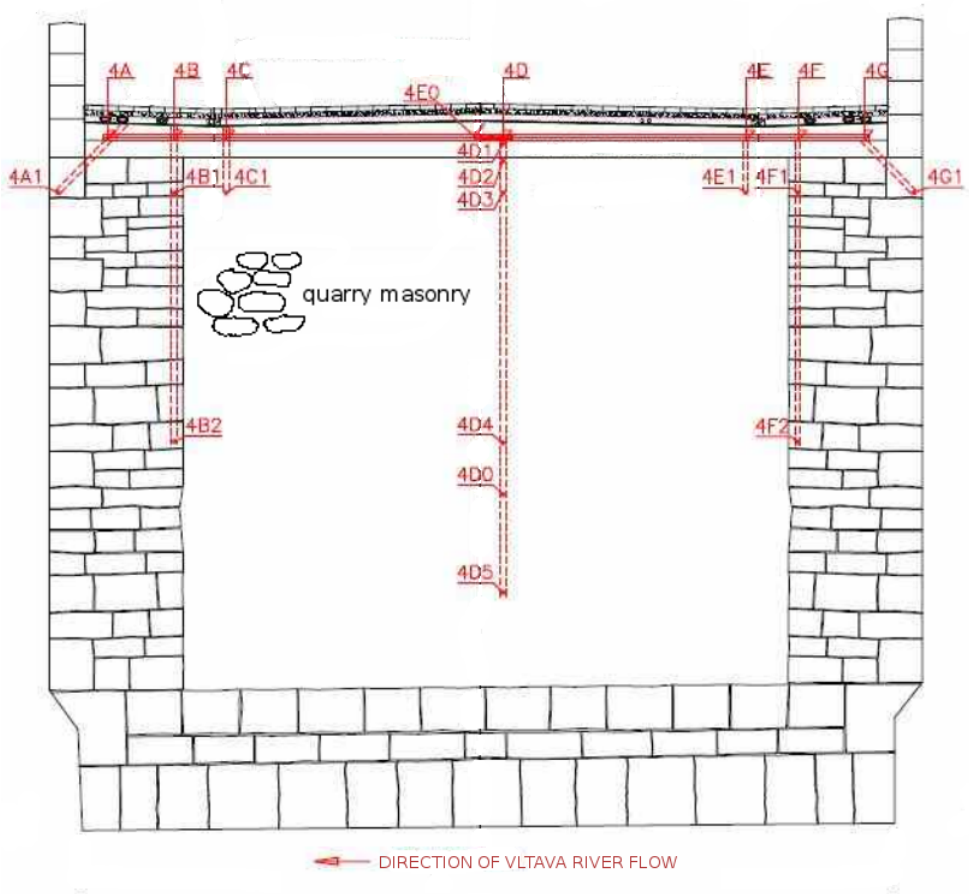

Figure 4.11: Cross-section 4 - gauge points (15 points, i.e. 45 temperature sensors and 15 moisture sensors).

brittle materials like concrete and masonry influenced by temperature and moisture changes. The partially coupled thermo-hygro-mechanical leads to the system of Equations (4.18) for heat and moisture transfer in the transport part

$$\begin{pmatrix} \boldsymbol{K}_{\varphi\varphi} & \boldsymbol{K}_{\varphi T} \\ \boldsymbol{K}_{T\varphi} & \boldsymbol{K}_{TT} \end{pmatrix} \begin{pmatrix} \boldsymbol{d}_{\varphi} \\ \boldsymbol{d}_{T} \end{pmatrix} + \begin{pmatrix} \boldsymbol{C}_{\varphi\varphi} & \boldsymbol{C}_{\varphi T} \\ \boldsymbol{C}_{T\varphi} & \boldsymbol{C}_{TT} \end{pmatrix} \begin{pmatrix} \dot{\boldsymbol{d}}_{\varphi} \\ \dot{\boldsymbol{d}}_{T} \end{pmatrix} = \begin{pmatrix} \boldsymbol{J}_{\varphi} \\ \boldsymbol{q}_{T} \end{pmatrix}$$

and the system of Equations (2.30) in the incremental form in the mechanical part:

$$\boldsymbol{K}_u \Delta \boldsymbol{d}_u = \Delta \boldsymbol{f}_{ext} + \Delta \boldsymbol{f}_0.$$

The parallelization of the problem based on the domain decomposition method was inevitable concerning computer memory requirements. A parallel version of the SIFEL computer code was used with the distributed memory scheme and the MPI communication library. The Schur complement method was applied due to a non-linear and non-symmetric final system of Equations (2.94). The technique was built on the factorization, and the non-linear system was solved using the modified Newton-Raphson method, which used the initial Jacobi matrix, and the factorization of the matrix was performed only once in each step. The segment analyzed was split into 12 sub-domains (Figure 4.13). The average number of nodes and elements on one sub-domain was 7000 and 32000,

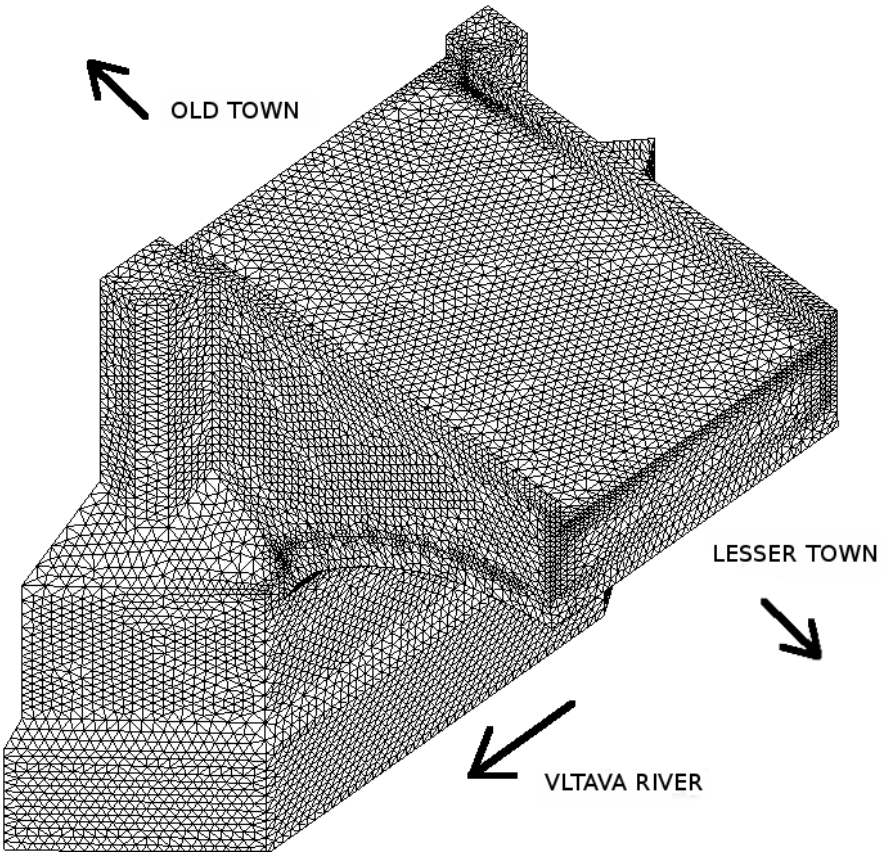

Figure 4.12: 3D finite element mesh model of one half of the arch III.

respectively. The parallel computation was performed on a heterogeneous PC cluster equipped by 32 bit Intel E6850 processors with different frequencies (2.4 to 3 GHz) and the memory from 3GB to 3.3 GB. The parallel algorithm performed 7596 time steps. A time step was set to cover two hours (7200 seconds). The overall consumption of the computation (CPU) time was one month.

The staggered algorithm was chosen for the thermo-hygro-mechanical analysis, where data (temperature and moisture fields) are transferred from the transport part to the mechanical one. The finite element model for the mechanical analysis corresponds to the current state after the last reconstruction in 2007 - 2010. The mesh was divided in several different elements and material groups - the pier masonry, the infill of the pier, vault, the infill of the vault, the northern breast walls and the southern breast walls, the concrete slab, the first layer upon the concrete slab, the second layer upon the concrete slab, the pavement with dilatation, and expansion joints (plastic mortar and extruded polystyrene), see Fig. 4.14.

4.2.7 Validation of simulations against monitoring

The first step of the thermo-hygro-mechanical analysis was the verification and validation of the heat and moisture transfer model and its material parameters. The boundary conditions for this part of the study were specified concerning representative climatic data, including the effect of solar radiation, wind, rain, heat conditions, and the structure's orientation [Ďurana et al., 2013]. Subsequently, after estimating the extreme surface temperatures of the annual cycle at -15 ^{0}C and

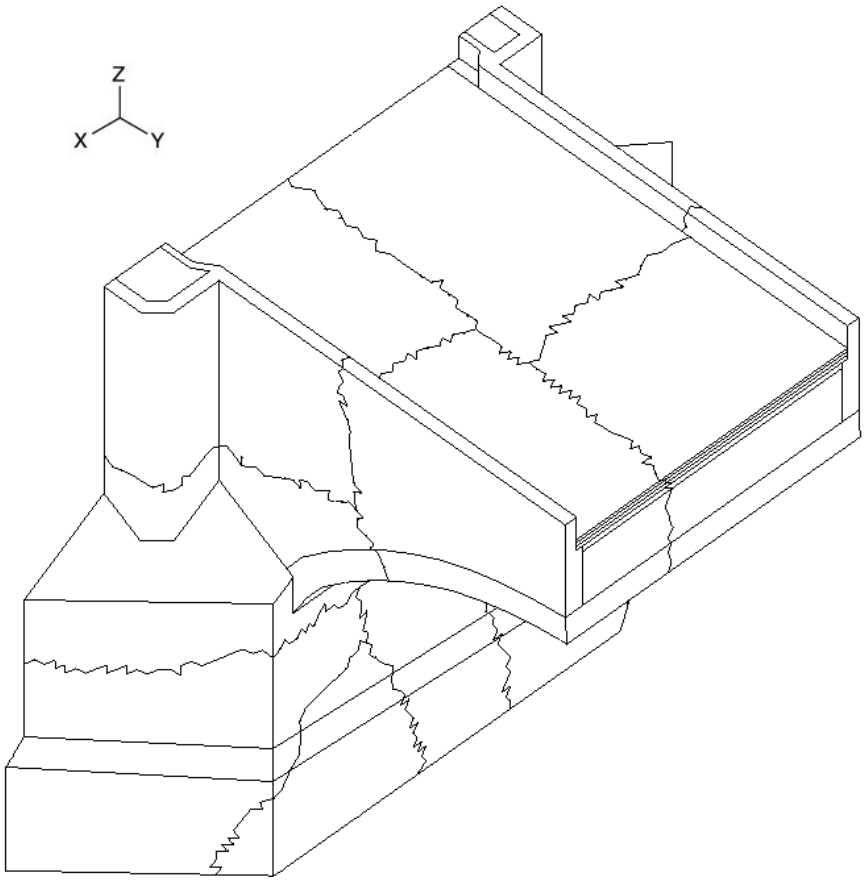

Figure 4.13: Domain decomposition of 3D finite element model of one half of the arch III.

52 ^{0}C for the winter and summer season, respectively, a three dimensional temperature field was analyzed solving linear steady-state heat transfer problems implementing homogenized material parameters and the surface and interior temperatures obtained from two-dimensional data. The 3D non-stationary evolution of temperature and moisture fields in Charles Bridge was analyzed in conjunction with its last repair ([Krejčí and Šejnoha, 2015] and [Toesca, 2014]), when a measuring system was installed in the bridge, and the temperature and moisture content at selected gauge points have been continuously monitored for two years. The only simplification was applied to the moisture field. As evident from the monitoring, see Figure 4.15, the moisture content evolves insignificantly within the scrutinized period.

The additional fully coupled heat and moisture transfer approach was carried out in a shorter period to assess a three dimensional distribution of the moisture field which was then considered to remain stationary, as the difference between the evolution of the moisture content predicted on the one hand by simulation and on the other by monitoring seems to be inessential. It was experimentally ascertained that the percentage increase of the moisture content varies from 5 to 12%, see selected curves in Figure 4.15. These curves confirm the assumption of nearly stationary moisture content at individual material points (it varies in space, but hardly in time). Some of the sensors are adversely affected by disturbances coming from the environment (e.g., induced voltage), which is evident in the end parts of the graphs in Figure 4.15 (lower). In any case, the reliability of the temperature sensors is much higher in comparison to the sensors monitoring the

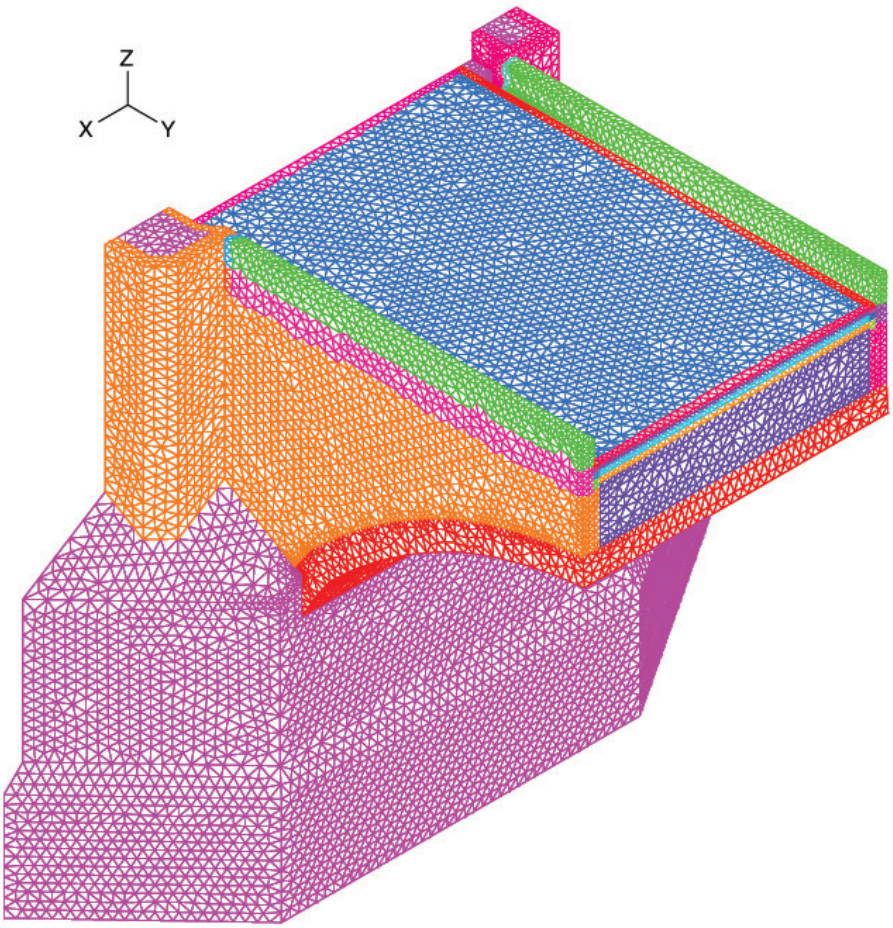

Figure 4.14: 3D finite element mesh - material groups and dilatation joints.

moisture content.

This finding allowed us to account for the dependence of the heat transport parameters on the moisture content and assume the temperature as the only problem unknown. The boundary and initial conditions were formulated in the same way as in the above described simplified approach. Two hours were set for the integration step so that twelve values a day were simulated to cover local fluctuations. Just one value of a daily set was collected and displayed in graphs to spare printing time. Moreover, it facilitates discerning the simulated temperature courses from the monitored data (delivered every ten minutes, i.e., 144 values a day).

The selected comparison of evolutions of the monitored and computed temperatures at individual gauge points are shown in Figures 4.16 and 4.17. In the early period of the calculation, a noticeable disproportion is apparent between the simulated and monitored data. This phenomenon is due to the incorrectly predicted distribution of the initial temperature field. Fortunately, this spurious phenomenon vanishes soon afterward, say within three months, and does not devalue the relevant results.

Two findings draw attention going through these figures in detail. First, the temperature maxima in summer on the southern surface are higher by roughly 7 - 8°C Two findings draw attention going through these figures in detail. First, the temperature maxima in summer on the southern surface are higher by roughly 4°C. The second finding shows a specific shift between the

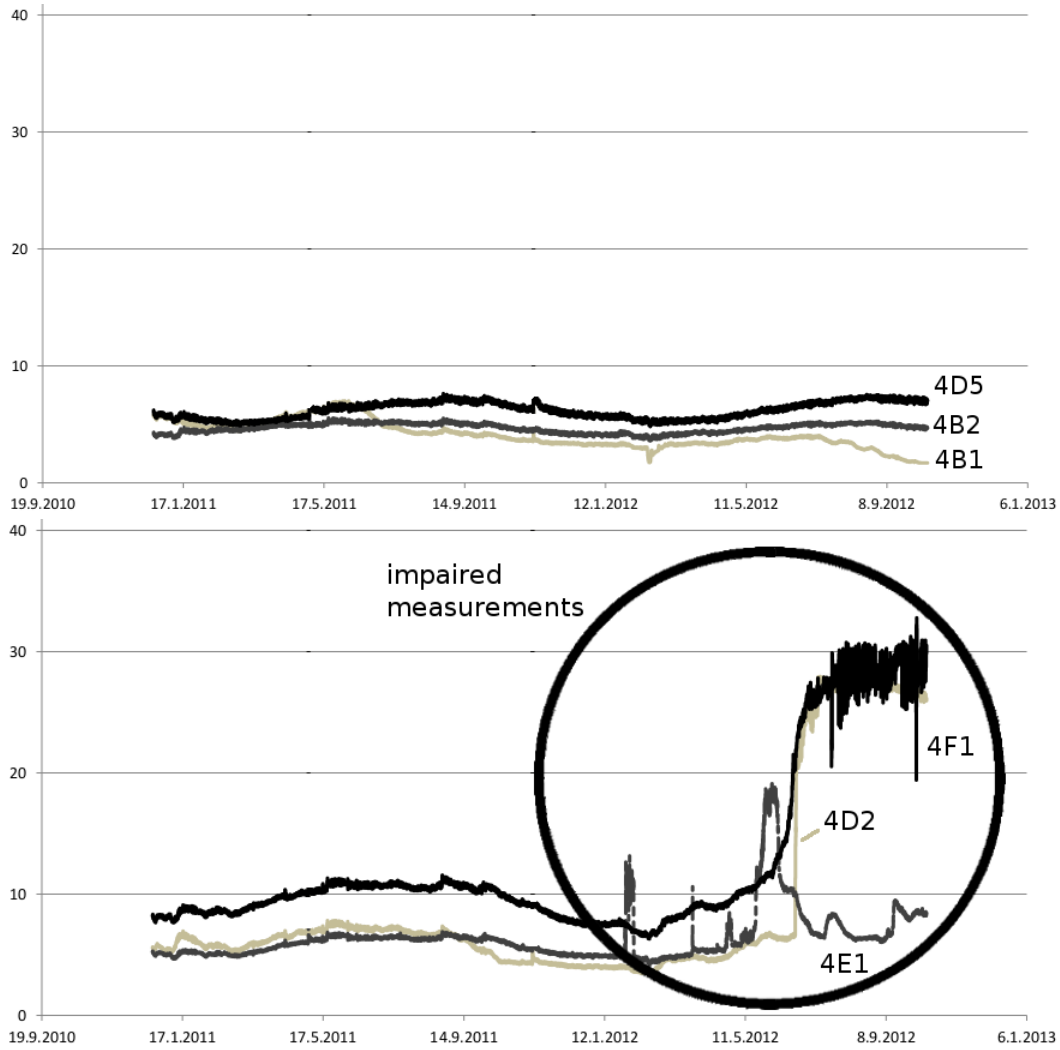

Figure 4.15: Measurement of the percentage increase of moisture content at gauge points 4D5, 4B2, 4B1 (above) and 4F1, 4D2, 4E1 (lower) [%].

simulated and monitored data in time, which becomes more perceptible at the points approaching the surface of the vault. As was discovered by direct measurement of surface temperature, such an undesirable discrepancy was brought about by improperly specified boundary conditions on the lower surface of arch VIII. The exterior temperature was influenced not only by the shielding against solar radiation but also by the temperature of the water flowing under the bridge, which should be accounted for as well. Another reason for the lag between the simulated and monitored data could be attributed to the imperfect homogenized transport parameters of strongly heterogeneous material.

It is also interesting that the daily fluctuations become higher with a decreasing distance from the bridge's surface, whereas they are smoother in the internal regions of the bridge. The temperature of water affects the surface temperature of the bridge foundations. In this case study, the water table was considered steady and equal to the average year level [Krejčí and Šejnoha, 2015].

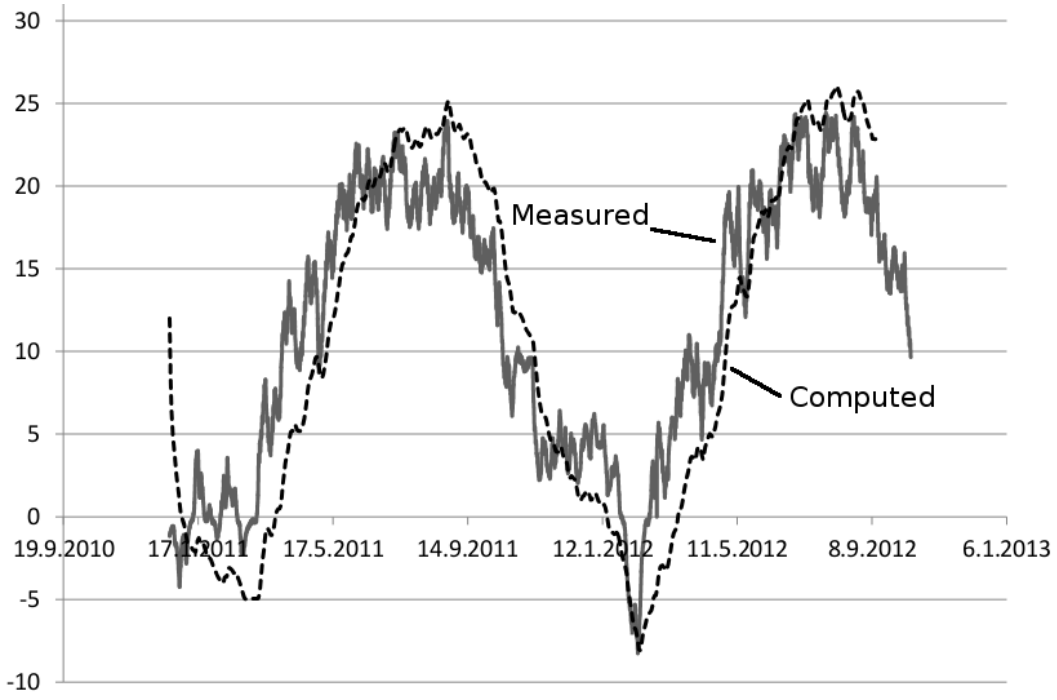

Figure 4.16: Distribution of temperature at gauge points 3A1 [°C].

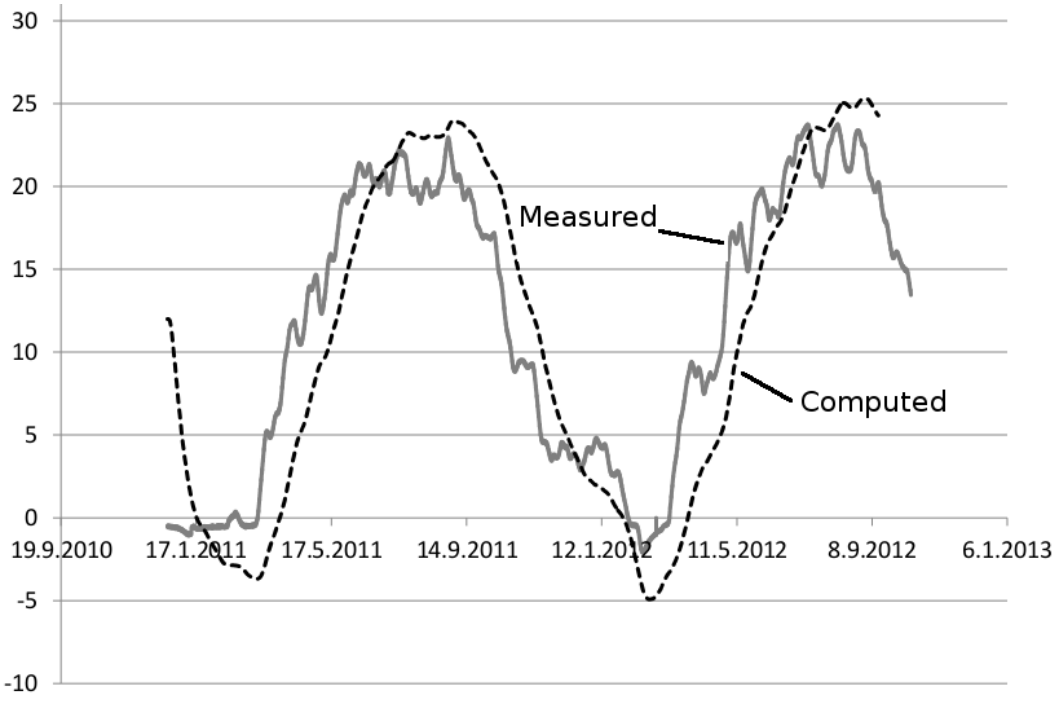

Figure 4.17: Distribution of temperature at gauge points 3B1 [°C].

4.2.8 Results of computation and prediction of the bridge behaviour

Because moisture content is not varying significantly during the annual cycle, the thermo-mechanical analysis was then performed with the staggered algorithm. The computation covered

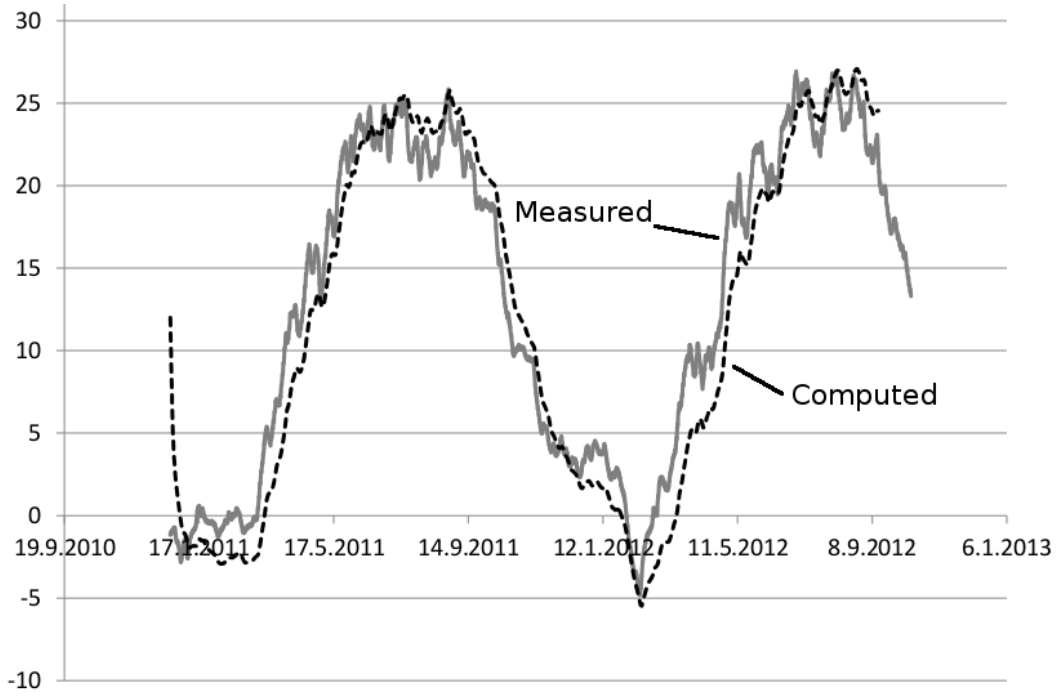

Figure 4.18: Distribution of temperature at gauge points 3D5 [°C].

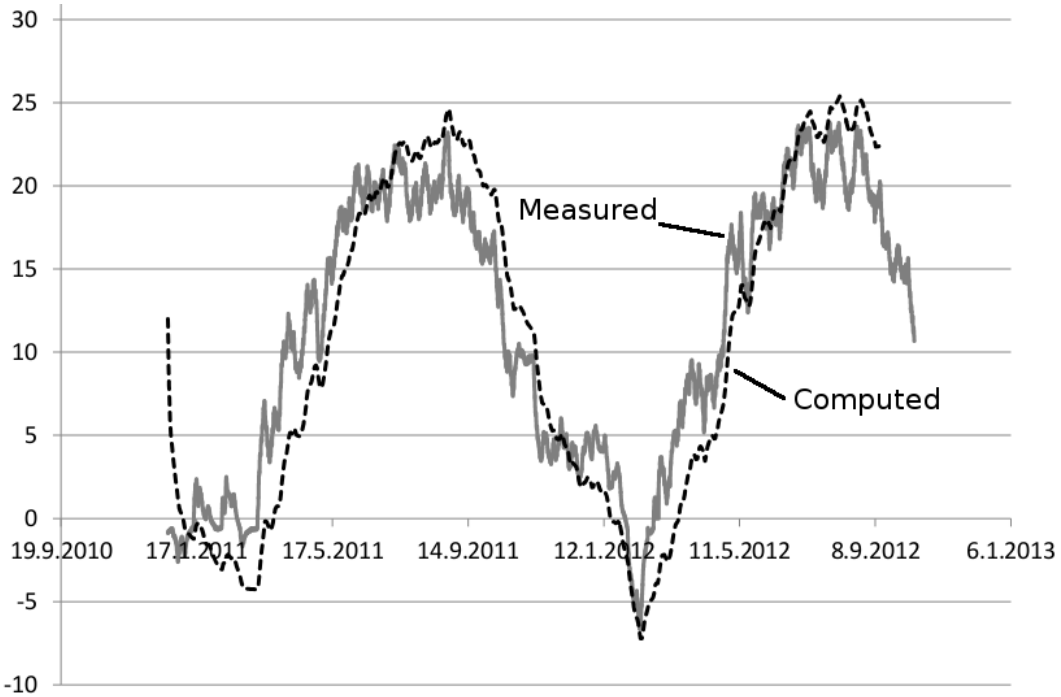

Figure 4.19: Distribution of temperature at gauge points 4A1 [°C].

the period from April 2011 to October 2012. The boundary conditions and the homogenized material parameters for the heat transport were taken over from the previous coupled heat and

moisture transfer problem validated against in situ measurements. The initial temperature field was set just in April 2011 as the average values for the oscillating annual temperatures. Due to the computational time and memory and CPU requirements, the time step was set to two hours (7200 seconds) for the heat transport part and to one week (604800 seconds) for the mechanical analysis.

Two mechanical loadings were added to the FE model apart from the temperature loading entering the mechanical part of the analysis. The first one was the self weight. The second one was the pedestrian live load of 5 kN/m^2 on the pavement prescribed according to Eurocodes. Material parameters entering the thermo-mechanical computation were chosen from references [Krejčí and Šejnoha, 2015] and [Toesca, 2014], and they are listed in Tables 4.1 - 4.3.

Quantity	Sandstone masonry	Filling masonry	Concrete	Granit pavement
ρ [kg/m^3]	1787.89	1841.66	2600.0	2600.0
C [J kg^{-1} K^{-1}]	696.91	1007.3	800.0	900.0
λ_{dry} [W m^{-1} K^{-1}]	0.449	0.547	1.5	3.5
λ_{sat} [W m^{-1} K^{-1}]	0.802	1.281	1.5	3.5

Table 4.1: Material parameters for the heat transfer model [Krejčí and Šejnoha, 2015]. Homogenized (overall) values were estimated using SEPUC [Sýkora et al., 2009].

The deformed shape demonstrates the mechanical response of the structure with the displacements, the stress state, the damage parameters (in three principal directions), and the corresponding crack opening width. The bridge arch moving during a one year cycle, upwards in summer and downwards in winter, is regarded as a bridge breathing. The maximum vertical displacement is about +3 mm and -2 mm in summer and winter, respectively. Due to the non-uniform temperature distribution and differences between southern and northern surface temperatures, the arch also twists and bends in a horizontal direction. The maximum horizontal displacement is approximately 1.5 mm. Moreover, both parapets, along with the upper parts of breast walls, twist and deflect from the vertical plane. The displacements of parapets in horizontal direction reach 1 mm.

The maximum values of compression stress remain in the elastic range, while the tensile stress reaches its limit value in the regions, where damage develops. The damage parameter and mainly the corresponding crack opening width provide necessary information about possible damage evolution in the bridge. The damage parameters in two principal directions (in tension) are approaching one in the most stressed parts of the bridge. In contrast, in the third principal direction (in compression), it equals to zero. The first principal direction coincides with the horizontal axis y of the bridge axis (see Figure 4.13). The second principal direction corresponds to the horizontal axis x perpendicular to the longitudinal bridge axis.

Material	Element	Young's modulus E [GPa]	Poisson's ratio ν	Volume weight ρ [kg/m^3]	Therm. dilat. coeff. α [1/K]
Periodic sandstone masonry	Arch, pier	20.2	0.15	2700	$7{\cdot}10^{-6}$
Non-periodic sandstone masonry	Breast wall	20.2	0.17	2700	$8{\cdot}10^{-6}$
Quarry masonry	Infill	10.4	0.17	2500	$8{\cdot}10^{-6}$
Reinforced concrete	Concrete slab	27.5	0.2	2600	$1.2{\cdot}10^{-5}$
Granite pavement and lime mortar	Paving	1.0	0.2	2600	$5{\cdot}10^{-6}$
Light concrete and hydroisolation	1st layer	19.0	0.2	2000	$8{\cdot}10^{-6}$
Concrete (with steel net, geotextile)	2nd layer	16.0	0.2	2000	$8{\cdot}10^{-6}$
Extruded polystyrene	Joint in slab	3.0	0.3	35	$6{\cdot}10^{-5}$
Crushed gravel	Joint slab-wall	0.6	0.35	1500	$5{\cdot}10^{-6}$
Plastic mortar	Joint in railing	2.0	0.37	1300	$1{\cdot}10^{-6}$

Table 4.2: Homogenized mechanical parameters [Toesca, 2014], [Zeman et al., 2008].

Material	Fracture energy G_f [N/m]	Tensile strength $\sigma_{t,\max}$ [MPa]	Limit displacement in tension $u_{t,\max}$ [mm]	Compressive strength $\sigma_{c,\max}$ [MPa]	Limit displacement in compression $u_{c,\max}$ [mm]
Periodic sandstone	80	0.50	0.16000	-7.40	0.01081
Non-periodic sandstone	80	0.50	0.16000	-7.40	0.01081
Quarry masonry	40	0.30	0.13333	-3.10	0.01290
Granite pav. (lime mortar)	10	0.75	0.01333	-4.00	0.00250
Light concrete + hydr.	36	1.40	0.02571	-12.75	0.00282
Concrete with steel net	36	1.50	0.02400	-12.75	0.00282
Extruded polystyrene	10	$1.00{\cdot}10^{10}$	$1.00{\cdot}10^{-15}$	$-1.00{\cdot}10^{10}$	$1.00{\cdot}10^{-15}$
Crushed gravel	10	$1.00{\cdot}10^{10}$	$1.00{\cdot}10^{-15}$	$-1.00{\cdot}10^{10}$	$1.00{\cdot}10^{-15}$
Plastic mortar	10	$1.00{\cdot}10^{10}$	$1.00{\cdot}10^{-15}$	$-1.00{\cdot}10^{10}$	$1.00{\cdot}10^{-15}$

Table 4.3: Material properties for stress-strain relation in orthotropic damage model.

Figure 4.20 illustrates the distribution of damage parameters in the body of arch III. There

are distinct damage zones in the quarry masonry filling and the transition zone between the filling and the sandstone masonry of the breast walls. These distributions are underpinned with the spatial distributions of the temperature field in cross-sections 3 and 4 plotted in 4.21 and 4.22, respectively. They show the regions where damage might be anticipated. Namely, the strong temperature gradients, accentuated in these figures with a sudden variation of colors, give rise to shear stresses in the proximity of the surfaces of the bridge and, consequently, originate massive damage in the layers localized along with the interface between the quarry and sandstone masonry. The shear stresses are balanced out by tensile stresses, which then initiate the nucleation and further development of cracks in the vault and on the breast wall faces.

Figures 4.23 and 4.24 show damage parameters distributions and Figures 4.25 and 4.26 display the corresponding crack opening width. There are three main distinct zones of possible damage evolution in parapets and breast walls. The first zone is situated near the connection of the breast wall and pillar (Figure 4.25). The tensile stress characterizes this zone due to the bridge bending. The second damage zone (Figure 4.26) is in the middle part of the breast wall under the bed joints of the parapet. This sort of damage is probably caused by shear stresses arising due to the differences in the temperature field. The third zone is in the breast wall in the lower part of the pillar (Figure 4.26), and it is probably brought about by the tensile and shear stresses resulting from the differences in temperature. Even the variations in temperature in the mere vertical direction and in the cross-section of the bridge arch give rise to the deformation of parapets and breast walls working against the adjacent bridge body. This effect then provokes the tensile and shear stresses evolution. The maximum crack opening width in the first principal direction reaches $1.0 \cdot 10^{-1}$ mm, and the maximum crack opening width in the second principal direction is about $1.5 \cdot 10^{-2}$ mm. There is one other visible damage zone (Figure 4.25) in concrete layers under the pavement, which is caused mainly by the differences in temperature in conjunction with the different thermal dilatation coefficient of materials.

The significant finding is that the damage in the vault appears only in perpendicular (horizontal) direction, not in the direction of the bridge and vault axis, and its crack opening width reaches a maximum value of $1.0 \cdot 10^{-3}$ mm, so the vault is almost undamaged.

It should be pointed out that the one year cycle analysis was subsequently extended by further annual cycles to explore the effect of cyclic temperature loading and to obtain a prediction of the bridge behavior in the near future. The slight progress of displacements, the evolution of existing damage zones, and the development of new small damage zones during the second year of simulation (an increase is about 10%) were discovered when analyzing the results. This state of the bridge has remained unchanged since.

This analysis underlays the claim that the structure is currently stable and safe and that the thermal loading has the maximum impact on the bridge's behavior. Precisely, decreasing temperatures toward winter provoke the highest tensile stress state and, therefore, the most significant damage. As already underlined in [Zeman et al., 2008], considering the temperature cycle, it can be noticed that this loading is not a threat to the stability of the structure (according to the model used, the maximum displacement (deflection) is about 3 mm).

The results imply the tendency of the structure to damage in agreement with the real crack distribution observed on site, mainly on arches 5, 6, 10, 11 and 12 where the damage state is higher than in arch 3 (the one used in the model because of its known geometry).

The results imply the tendency of the structure to damage in agreement with the real crack distribution observed on-site, mainly on arches 5, 6, 10, 11 and 12 where the damage state is higher than in arch 3 (the one used in the model because of its known geometry). The last

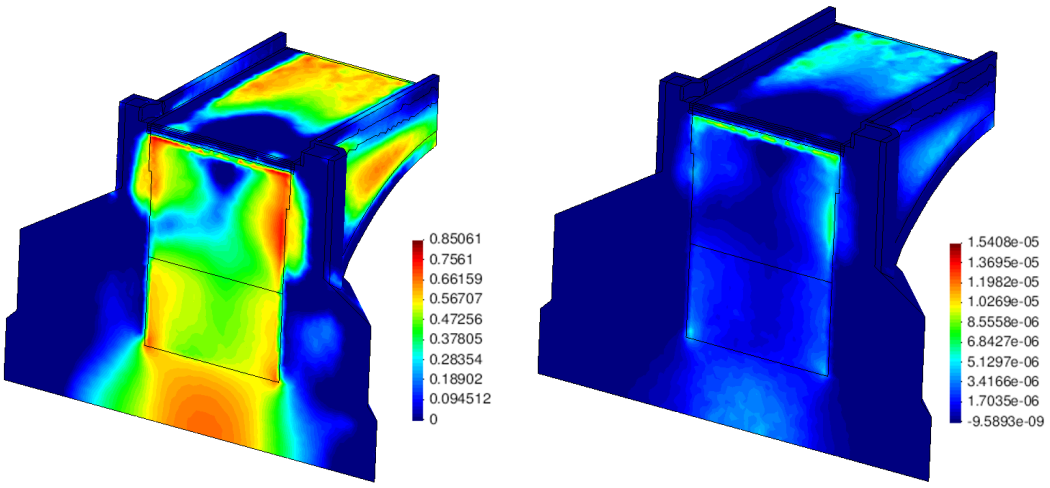

Figure 4.20: Spatial distribution of damage parameter in the bridge structure in summer time after one year cycle in the first principal direction (left) and corresponding width of cracks openings (right).

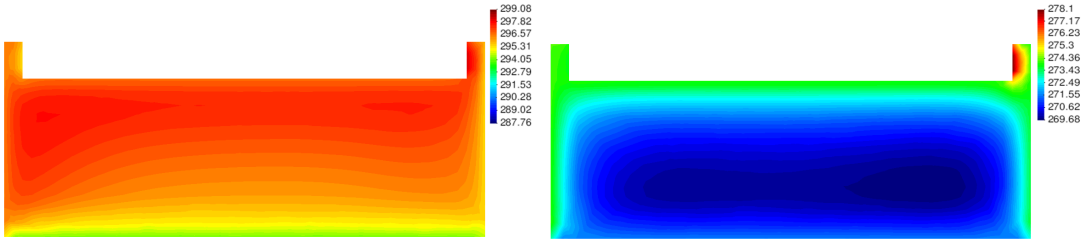

Figure 4.21: Spatial distribution of temperature [Kelvins] in cross-section 3 in summer (left) and in winter (right).

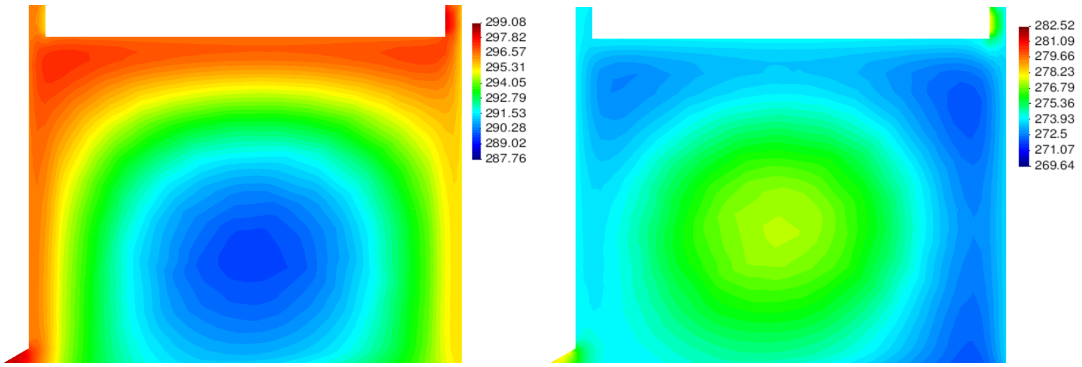

Figure 4.22: Spatial distribution of temperature [Kelvins] in cross-section 4 in summer (left) and in winter (right).

rehabilitation deserves to be commented in the light of FE model. The release of the connection between the breast walls and concrete slab undoubtedly prevents the breasts from damage. The

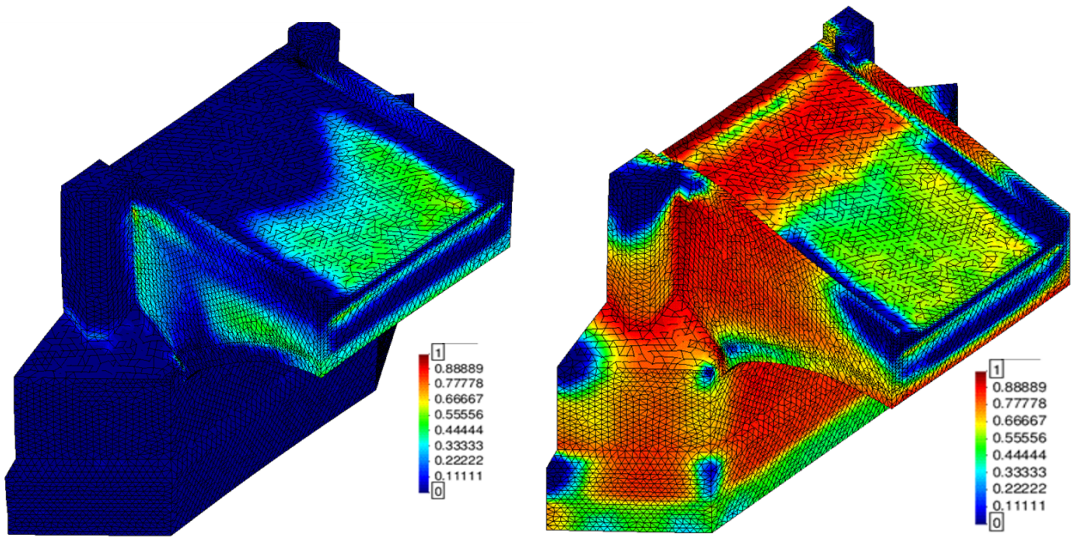

Figure 4.23: Deformed shape and damage parameter after two year cycles in the first principal direction in summer 2011 (left); in winter 2012 (right).

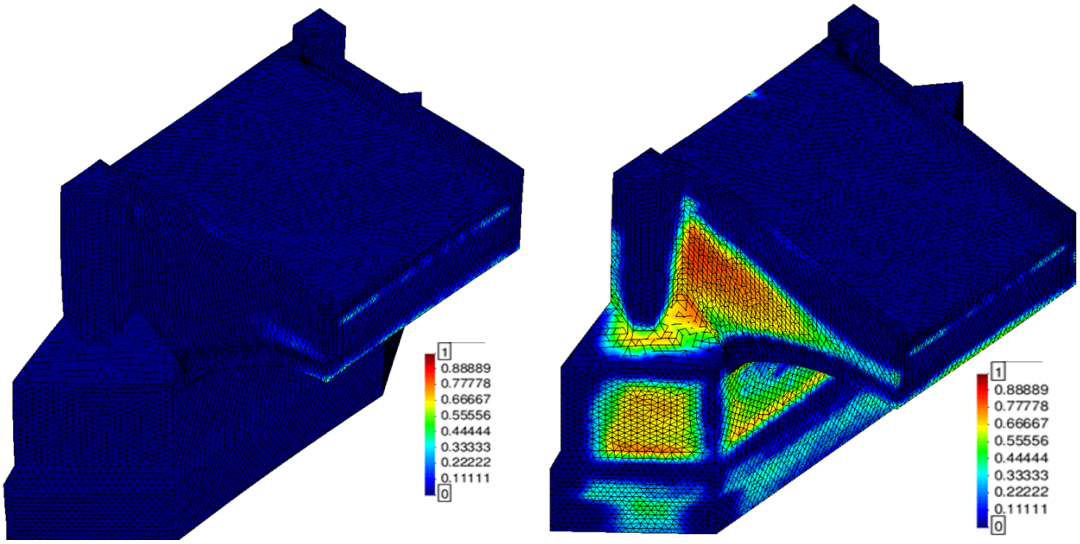

Figure 4.24: Deformed shape and damage parameter after two year cycles in the second principal direction in summer 2011 (left); in winter 2012 (right).

vertical dilatation joints (filled with plastic mortar) spare the damage on parapets, though they cannot avoid the propagating cracks into breast walls underneath the joints. The conclusion is that the damage related to thermal loading in the massive structure cannot be avoided. It is possible to change its distribution, trying to move it from the weakest structural parts or just from the eye (as achieved with the last intervention). On the other hand, the low maximum crack width computed for the actual bridge configuration implies that the problem is mainly aesthetic. Only the repetition of cycles with exceptional temperatures, combined with the presence of low-quality blocks or mortar, can subsequently lead to clearly visible damage. The reliability of the

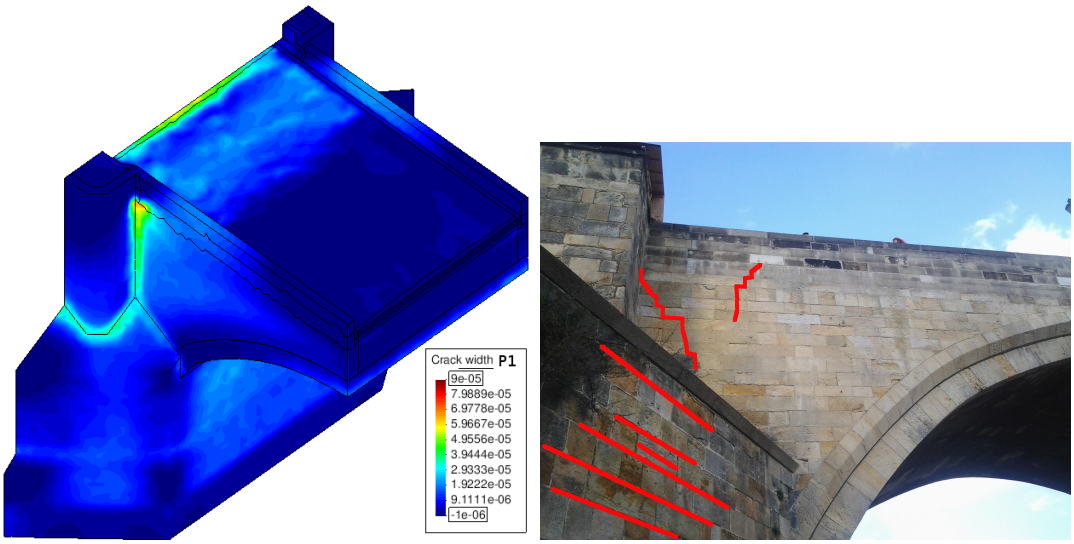

Figure 4.25: Distribution of the width of crack openings computed from tensile damage tensor after two year cycles in the first principal direction (left) in winter 2012; red highlighted visible cracks in breast walls (right) of arch X.

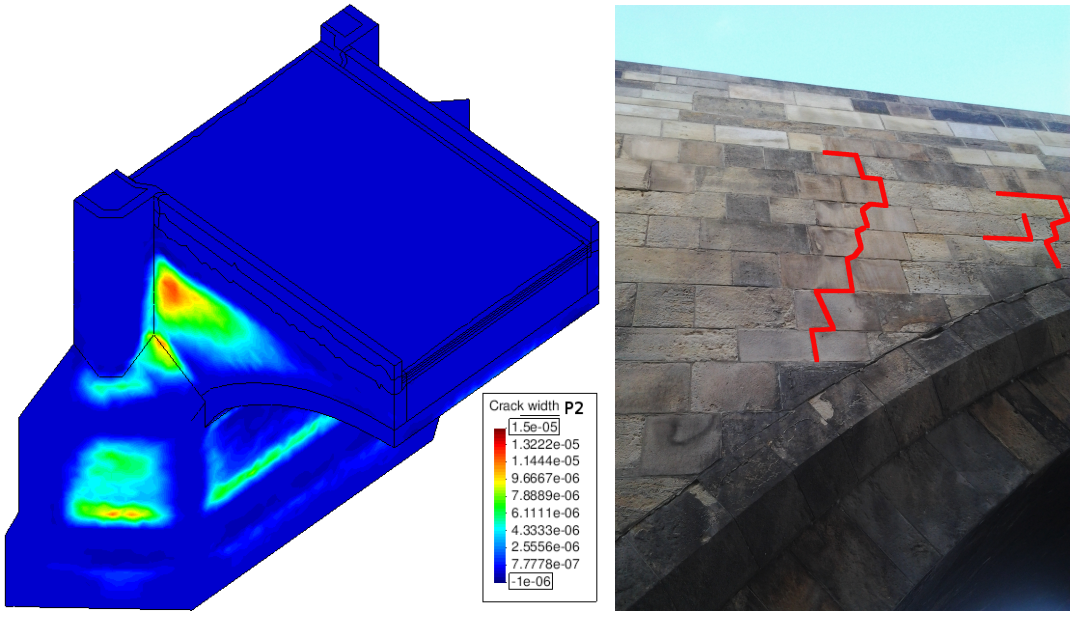

Figure 4.26: Distribution of the width of crack openings computed from tensile damage tensor after two year cycles in the second principal direction (left) in winter 2012; red highlighted visible cracks in breast walls (right) of arch X.

model cannot be admitted without reservations, because the initial condition of the FE model (absence of damage) slightly deviates from reality, where some small cracks were still visible even after rehabilitation and replacement of blocks.

4.2.9 Conclusions about Charles bridge thermo-hygro-mechanical analysis

The presnted is thermo-hygro-mechanical analysis of Charles bridge had two aims. The first aim was to demonstrate a reliable approach to the description of a coupled heat and moisture transport in large stone masonry structures, such as Charles bridge in Prague, using computer simulations. To this end, the well-tried material (constitutive) model by Künzel and Kiessl was addressed. The study presented the evolution of both temperature and moisture fields obtained by continuous monitoring of these quantities at selected gauge points in the bridge. Eventually, the results of computer simulations were validated against those obtained experimentally. A detailed investigation of computed results manifested a lag of heat transfer at internal points compared to the ones in the vicinity of the bridge surface. Whereas this phenomenon is thermodynamically correct, a slight discrepancy between the computational prediction and the measurement was, in the first place, ascribed to an imperfect prior estimate of transport parameters. It can be deduced that the thermal conductivities of individual phases (and subsequently of masonry as a whole) were under-estimated, while the phase heat capacities could likely be over-estimated. Another phenomenon observed is the decrease in the daily temperature fluctuations passing inside the bridge. The smoothed out simulated courses correspond to taking only one value a day when drawing individual courses. As for the moisture content, it is worth noting that this quantity varies rather slowly over time. This finding was somewhat disappointing after the expensive hydroisolation of the bridge deck had been implemented. Nevertheless, the moisture content appeared to be plausible.

The second aim of this analysis was to obtain a notion about the current mechanical state of Charles bridge. The results presented could serve as a basis for providing a reliable estimate of real states of stress and damage in Charles bridge. As has already been mentioned, climatic loading is the most serious for stone bridges as it is responsible for the nucleation and further development of cracks. The 3D simulations using the SIFEL computer code implicated two causes of periodic damage in the parapets: shear stresses due to the temperature differences between the upper and lower parts of the parapets (roughly 2 - 3°C) and the vertical movements of the vaults (upwards in summer and downwards in winter) - the breathing of the bridge. There is no doubt that after a certain period, both reiterating mechanisms will lead to the ultimate damage in the horizontal joint and the need for maintenance and a complete repair of the parapets. On the other hand, the damage state and cracks evolution do not influence the stability and bearing capacity of the bridge distinctly.

Chapter 5

Thermo-hygro-mechanical analysis of bentonite in engineered barrier

The third example presented is the numerical simulation of bentonite in an engineered barrier for the nuclear waste repository. Compacted expansive clays and mainly bentonite are widely used in sealing geological structures because of their high swelling capacity, low permeability, and favorable retardation properties. The bentonites are tested as a part of engineered barriers in high-level radioactive waste storage and disposals in many countries and including the Czech Republic. Nuclear waste repositories are planned as complex structures with very high demands on safety and reliability. They will be placed deep in the stable rock host environment with a system of galleries with chambers created to store radioactive waste surrounded by the engineered barrier. The barriers will be composed of the special metallic canister enclosing the waste and a bentonite layer, which should stop the radionuclides migration in the case of container failure. The canisters will be placed in horizontal drifts or vertical boreholes in a host rock mass [Gens et al., 2009].

The bentonite backfill will be subjected to hydration from the surrounding rock, the nuclear waste's heating up, and various mechanical effects that interact in a complex coupled thermo-hygro-mechanical (THM) phenomena. It is necessary to understand the processes in the near mass and their time evolution to design a safe and reliable repository. Recent research proved the need to perform large-scale or medium-scale heating tests simulating repository conditions in underground laboratories. A lot of facilities are being used around the world. Several of them are presented, e.g., in [Šťástka et al., 2018], [Gens et al., 2009], [Dixon et al., 2002], [Selvadurai, 1997], [Alonso et al., 1996], and [Pusch et al., 1985]. Such experiments require long time testing, measured in years, to obtain relevant results. The understanding of the involved phenomena and their interaction can be supported by suitable numerical models able to reproduce the main feature of the tests, where coupled THM formulations are inevitably required.

In-situ tests in underground laboratories are generally intensively instrumented. A large amount of data obtained are required to define the appropriate parameters of coupled THM numerical models. From the soil mechanics point of view, in-situ experiments provide the opportunity to examine the behavior of swelling clays under controlled conditions and validate coupled THM formulations and associated computer codes.

This chapter presents the numerical analysis of in-situ interaction physical models at the Bukov Underground Research Facility (URF) in the Czech Republic [SÚRAO, 2021]. The aim of in-situ interaction physical models at the Bukov URF is to compare several bentonite materials and their interactions under deep geological repository conditions using several in-situ experiments in a hard

rock mass. The results of these studies will support the decision of usability of materials and their combinations in the future deep geological repository [Svoboda et al., 2019a].

The numerical simulation is the auxiliary analysis accompanying the in-situ test. Verification of the suitable instruments setup, the number of sensors, their type, and the location is essential for the construction of further tests. Moreover, the simulation helps to predict long-term experiment behavior for bentonite sampling. The main part of the analysis consists of the coupled thermo-hygro-mechanical analysis of the bentonite layer, surrounding the metallic canister. This analysis follows the staggered coupling algorithm combining a hypoplastic mechanical model for expansive clays with an extended micromechanical based model for heat and moisture transfer in deforming medium. The numerical results are compared with measured data, and the model is subsequently validated.

5.1 Hypoplastic model for expansive clays

Mechanical models for clayed soils can be sorted into two groups. The first group is characterized by the theory of elastoplasticity described by the stress-strain relation in the form

$$\boldsymbol{\sigma} = \boldsymbol{D}_e : (\boldsymbol{\varepsilon} - \boldsymbol{\varepsilon}_p), \tag{5.1}$$

where $\boldsymbol{\sigma}$ is the second-order stress tensor, $\boldsymbol{D}_e$ is the fourth-order elastic stiffness tensor, $\boldsymbol{\varepsilon}$ is the second-order total strain tensor, and $\boldsymbol{\varepsilon}_p$ is the second-order plastic strain tensor. Symbol ":" denotes the double contraction. The plastic strains $\boldsymbol{\varepsilon}_p$ represents an irreversible part of the total strains $\boldsymbol{\varepsilon}$, which can be defined by the associated plastic flow rule given by

$$\dot{\boldsymbol{\varepsilon}}_p = \dot{\gamma} \frac{\partial f(\boldsymbol{\sigma}, \boldsymbol{h})}{\partial \boldsymbol{\sigma}}, \tag{5.2}$$

where $f(\boldsymbol{\sigma}, \boldsymbol{h})$ denotes a selected yield function, $\boldsymbol{h}$ is the vector of hardening parameters, and γ is the consistency parameter. The Cam-clay model is one of the most popular elastoplastic models [Roscoe et al., 1963]. It involves pressure-dependent modulus for loading and associated flow rule with isotropic hardening. It was originally developed for fully saturated soils. A model extension for the partially saturated states was proposed in [Gallipoli et al., 2003]. An additional hardening parameter depends on the suction pressure, shifting the yield surface along the hydrostatic axis. The model's advantages are the pressure-dependent loading, incorporation of the state boundary surface (SBS), and the influence of the suction pressure. On the other hand, there are also significant shortcomings related to the elastic unloading, which does not agree with the observed soil behavior.

The second group comprises advanced hygro-mechanical and thermo-hygro-mechanical models based on the hypoplastic approach. Hypoplastic models involve different loading/unloading moduli directly in the rate form of stress-strain relation

$$\dot{\boldsymbol{\sigma}} = \mathcal{M}(\boldsymbol{\sigma}, \dot{\varepsilon}, \boldsymbol{p}) : \dot{\varepsilon}. \tag{5.3}$$

$\mathcal{M}$ is the fourth-order generalized stiffness tensor, which depends on the actual stresses $\boldsymbol{\sigma}$, strain rate $\Delta\boldsymbol{\varepsilon}$, and other state variables denoted by vector $\boldsymbol{p}$.

One of the most promising models has been proposed in [Mašín, 2013]. The model is composed of a mechanical part based on hypoplasticity coupled with the hydraulic part. It assumes the double structure of the aggregated soils supported by the experimental evidence of the pore size distribution (Figure 5.1). The dual structure approach exploits separated formulation of macro and micro behavior according to well-evaluated models presented in [Alonso et al., 2011], [Sánchez et al., 2005], and [Romero et al., 2011]. The extension of the model includes the dependence of water retention on volumetric deformation and the influence of temperature changes. Coupling between macro and microstructure levels depends on the size of macropores (interaggregate pores). It is assumed that the shear strength of the soil is attributed to the macrostructure, and it is given by effective stress measure independent of microstructural quantities. Hydraulic equilibrium is assumed between both structure levels, too.

In the model, the deformation of the macroskeleton and the aggregates' deformation fully contribute to the overall deformation. The possibility that the aggregates occlude into macropores are expressed in the following equation describing the additive decomposition of the total strain rate $\dot{\boldsymbol{\varepsilon}}$

$$\dot{\boldsymbol{\varepsilon}} = \dot{\boldsymbol{\varepsilon}}^M + f_m \dot{\boldsymbol{\varepsilon}}^m, \qquad 0 \leq f_m \leq 1, \tag{5.4}$$

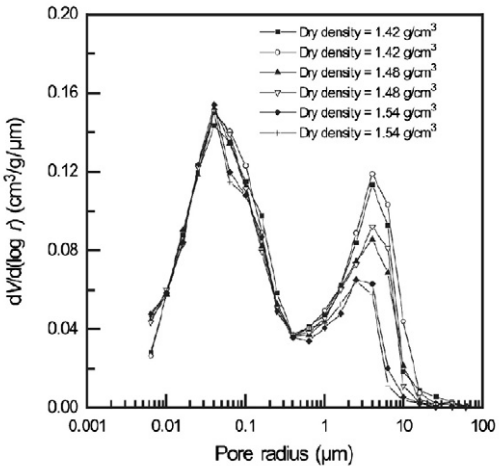

Figure 5.1: Distribution of pore size density [Mašín, 2013].

where f_m stands for the factor quantifying macroporosity occlusion by aggregates ranging from 0 to 1, the superscript index ^{M} denotes the macro-structural behavior. In contrast, superscript index ^{m} represents quantities related to the microstructural level. The dot $\dot{()}$ means the time derivative.

The total void ratio e together with the consistent definition of the double porosity measures for particular structural levels are defined by

$$e = e^M + e^m + e^M e^m, \tag{5.5}$$

$$\frac{\dot{e}}{1+e} = \varepsilon_V, \tag{5.6}$$

$$\frac{\dot{e}^M}{1+e^M} = \varepsilon_V^M + (f_m - 1)\varepsilon_V^m, \tag{5.7}$$

$$\frac{\dot{e}^m}{1+e^m} = \varepsilon_V^m. \tag{5.8}$$

In Equations (5.5)-(5.8), the volumetric strains for macro and micro levels are denoted by ε_V^M and ε_V^m respectively, while the total volumetric strain is denoted by ε_V. The total degree of saturation S_w describing the water volume fractions of the two-pore system can be written in terms degree of saturation of macro (S_w^M) and micro (S_w^m) structures by

$$S_w = S_w^M + \frac{e^m}{e}(S_w^m - S_w^M). \tag{5.9}$$

Two different mechanical models for macro and microstructure are defined under the assumption of individual behavior of the two structural levels. Assuming local hydraulic equilibrium $s^m = s^M$ and $\boldsymbol{\sigma}^{net} = \boldsymbol{\sigma}^{netM} = \boldsymbol{\sigma}^{netm}$ and the effective stresses concept for unsaturated media [Bishop, 1959], the following terms for the effective stresses at macro and micro levels are given

$$\boldsymbol{\sigma}^M = \boldsymbol{\sigma}^{net} - \boldsymbol{I} s\chi^M, \tag{5.10}$$

$$\boldsymbol{\sigma}^m = \boldsymbol{\sigma}^{net} - \boldsymbol{I} s\chi^m, \tag{5.11}$$

where $\boldsymbol{I}$ is the second-order identity tensor, χ denotes the effective stress parameter, and the effective stress vector $\boldsymbol{\sigma}^{\text{eff}}$ in unsaturated soils, the net stress vector $\boldsymbol{\sigma}^{net}$, and suction s are in the forms

$$\begin{aligned} \boldsymbol{\sigma}^{\text{eff}} &= \boldsymbol{\sigma}^{tot} + \boldsymbol{I}p^{w}\chi + \boldsymbol{I}p^{g}(1-\chi), && (5.12)\\ \boldsymbol{\sigma}^{net} &= \boldsymbol{\sigma}^{tot} + \boldsymbol{I}p_{g}, && (5.13)\\ s &= p_{g} - p_{w}, && (5.14) \end{aligned}$$

where $\boldsymbol{\sigma}^{tot}$ is the total stress vector, p_g and p_w stand for the air and water pressures, respectively. It should be noted that p_g and p_w are assumed to be positive in compression. The hydraulic (water retention) model for macro-level reads

$$\chi^{M} = S_{w}^{M} = \chi = \begin{cases} 1, & s < s_{e} \\ \left(\dfrac{s_{e}}{s}\right)^{\gamma}, & s \geq s_{e}, \end{cases} \tag{5.15}$$

where parameter γ represents the macrostructural water retention curve slope, and it is usually assumed $\gamma = 0.55$. s_e is the suction level at air-entry or air-expulsion defined to be $s_e = s_{en}$ for the drying branch of the macrostructural water retention curve and $s_e = a_e\, s_{en}$ for the wetting branch. The quantity s_{en} is defined by

$$s_{en} = s_{e0}\frac{e_{0}^{M}}{e^{M}}, \tag{5.16}$$

where model parameter s_{e0} expresses the air entry value of suction for the reference macrostructural void ratio e_0^M, and the parameter a_e is the ratio between the air expulsion and entry values of suction, which controls the difference between the wetting and drying branches of water retention curves. On the micro-level, the fully saturated state in the micropore system is assumed

$$\chi^{m} = S_{w}^{m} = 1, \tag{5.17}$$

The following equation gives the hysteretic water retention relationship

$$\dot{S}_{w}^{M} = -\gamma_{a}\frac{S_{w}^{M}}{s}\dot{s} - \gamma\frac{S_{w}^{M}}{e^{M}}\dot{e}^{M}, \tag{5.18}$$

where parameter γ_a defines the slope of drying/wetting curves. Introducing Equations (5.18) and (5.17) in Equations (5.10) and (5.11), the following rate forms of the macrostructural and microstructural effective stresses are obtained

$$\begin{aligned} \dot{\boldsymbol{\sigma}}^{M} &= \dot{\boldsymbol{\sigma}}^{net} + \boldsymbol{I}\chi^{M}\left[(\gamma_{a}-1)\dot{s} + \gamma\, s\,\frac{\dot{e}^{M}}{e^{M}}\right], && (5.19)\\ \dot{\boldsymbol{\sigma}}^{m} &= \dot{\boldsymbol{\sigma}}^{net} - \boldsymbol{I}\dot{s}. && (5.20) \end{aligned}$$

The mechanical behavior of macroskeleton described by the hypoplastic model [Mašín, 2013] can be defined in the rate form of the macrostructure effective stress

$$\dot{\boldsymbol{\sigma}}^{M} = f_{s}\left(\boldsymbol{\mathcal{L}} : \dot{\boldsymbol{\varepsilon}}^{M} + f_{d}\boldsymbol{N}\|\dot{\boldsymbol{\varepsilon}}^{M}\|\right) + f_{u}\boldsymbol{H}_{s}, \tag{5.21}$$

where $\|\dot{\boldsymbol{\varepsilon}}^{M}\|$ is the Euclidean norm of strain rate tensor, f_s, f_d, and f_u, are three scalar factors, and $\boldsymbol{\mathcal{L}}$ stands for the hypoelastic fourth-order tensor defined by

$$\boldsymbol{\mathcal{L}} = 3\left(c_{1}\boldsymbol{\mathcal{I}} + c_{2}\,a^{2}\,\hat{\boldsymbol{\sigma}}^{M}\otimes\hat{\boldsymbol{\sigma}}^{M}\right). \tag{5.22}$$

In previous Equation (5.22), symbol $\otimes$ denotes the dyadic product of two tensors, $\hat{\boldsymbol{\sigma}}^M$ represents dimensionless stress tensor given by $\hat{\boldsymbol{\sigma}}^M = \dfrac{\boldsymbol{\sigma}^M}{\mathrm{tr}(\boldsymbol{\sigma}^M)}$, where symbol tr defines the tensor trace ($\mathrm{tr}(\boldsymbol{\sigma}) = \sigma_{ii}$). Parameters c_1, c_2, and a are scalar factors defined as:

$$c_1 = \frac{2\left(3 + a^2 - 2^\alpha\, a\,\sqrt{3}\right)}{9\,r}, \tag{5.23}$$

$$c_2 = 1 + (1 - c_1)\frac{3}{a^2}, \tag{5.24}$$

$$a = \frac{\sqrt{3}(3 - \sin\phi_c)}{2\sqrt{2}\sin\phi_c}, \tag{5.25}$$

where r is the parameter controlling stiffness in shear, and α is the function of material parameters ϕ_c, λ^* and κ^*

$$\alpha = \frac{1}{\ln 2}\ln\left[\frac{\lambda^* - \kappa^*}{\lambda^* + \kappa^*}\left(\frac{3 + a^2}{a\sqrt{3}}\right)\right]. \tag{5.26}$$

ϕ_c is the critical state friction angle, λ^* denotes the slope of the normal compression line, and κ^* stands for the slope of the macrostructural isotropic unloading line.

The second-order tensor $\boldsymbol{N}$ can be defined according to failure condition in the form

$$\boldsymbol{N} = \boldsymbol{\mathcal{L}}\left(Y\frac{\boldsymbol{M}}{\|\boldsymbol{M}\|}\right), \tag{5.27}$$

where Y represents the failure criterion in the form

$$Y = \left(\frac{\sqrt{3}\,a}{3 + a^2} - 1\right)\frac{(I_1 I_2 + 9I_3)\left(1 - \sin^2\phi_c\right)}{8I_3\,\sin^2\phi_c} + \frac{\sqrt{3}\,a}{3 + a^2}, \tag{5.28}$$

where I_1, I_2 and I_3 stands for the first, second, and third stress invariants defined as follows

$$I_1 = \mathrm{tr}(\boldsymbol{\sigma}^M), \quad I_2 = \frac{1}{2}\left(\boldsymbol{\sigma}^M : \boldsymbol{\sigma}^M - \mathrm{tr}(\boldsymbol{\sigma}^M)\right), \quad I_3 = \det(\boldsymbol{\sigma}^M). \tag{5.29}$$

The direction of 'hypoplastic flow' is given by the second-order tensor $\boldsymbol{M}$

$$\boldsymbol{M} = -\frac{a}{F}\left[\hat{\boldsymbol{\sigma}}^M + \mathrm{dev}(\hat{\boldsymbol{\sigma}}^M) - \frac{\hat{\boldsymbol{\sigma}}^M}{3}\left(\frac{6\,\hat{\boldsymbol{\sigma}}^M : \hat{\boldsymbol{\sigma}}^M - 1}{(F/a)^2 + \hat{\boldsymbol{\sigma}}^M : \hat{\boldsymbol{\sigma}}^M}\right)\right], \tag{5.30}$$

with factor F defined by

$$F = \sqrt{\frac{1}{8}\tan^2\psi_h + \frac{2 - \tan^2\psi_h}{2 + \sqrt{2}\tan\psi_h\cos 3\theta}} - \frac{1}{2\sqrt{2}}\tan\psi_h, \tag{5.31}$$

where

$$\tan\psi_h = \sqrt{3}\|\mathrm{dev}(\hat{\boldsymbol{\sigma}}^M)\|, \quad \cos 3\theta = -\sqrt{6}\frac{\mathrm{tr}\left(\hat{\boldsymbol{\sigma}}^M \cdot \hat{\boldsymbol{\sigma}}^M \cdot \hat{\boldsymbol{\sigma}}^M\right)}{\left[\mathrm{dev}(\hat{\boldsymbol{\sigma}}^M) : \mathrm{dev}(\hat{\boldsymbol{\sigma}}^M)\right]^{3/2}}. \tag{5.32}$$

The barotropy factor f_s introduces the pressure dependency of the model response according to the mean stress level attained

$$f_s = \frac{3\,p^M}{\lambda^*(s)}\left(3 + a^2 - 2^\alpha\, a\sqrt{3}\right)^{-1}, \tag{5.33}$$

while the pyknotropy factor f_d is rather connected with specific volume influence

$$f_d = \left(\frac{2p^M}{p_e}\right)^{\alpha}, \quad p_e = p_r \exp\left[\frac{N(s) - \ln(1+e)}{\lambda^*(s)}\right], \tag{5.34}$$

where p^M is the mean stress at the macrolevel, and p_r is the reference pressure.

The model adopts a concept of the normal compression line similar to the one in Cam-Clay model, where the compression line is being defined with the influence of suction pressure s as

$$\ln(1+e) = N(s) - \lambda^*(s) \ln\left(\frac{p^M}{p_r}\right), \tag{5.35}$$

with the mentioned slope of normal consolidation (compression) line λ^* and position of the normal consolidation line $N(s)$ defined by

$$N(s) = N + n_s \ln\left(\frac{s}{s_e}\right), \tag{5.36}$$

$$\lambda^*(s) = \lambda^* + l_s \ln\left(\frac{s}{s_e}\right), \tag{5.37}$$

$$s_e = s(S_w^M)^(1/\gamma), \tag{5.38}$$

where N, n_s, and l_s are model parameters.

The second-order tensor $\boldsymbol{H}_s$ and factor f_u introduce the wetting-induced collapse of the clay and the following terms give them

$$\boldsymbol{H}_s = -c_i \frac{\hat{\boldsymbol{\sigma}}^M}{s\,\lambda^*(s)} \left[n_s - l_s \ln\frac{p_e}{p_r}\right](-\dot{s}) \quad \text{for } s > s_{exp} \text{ and } S_w < 1, \tag{5.39}$$

$$\boldsymbol{H}_s = \boldsymbol{0} \quad \text{otherwise}, \tag{5.40}$$

$$f_u = \left(\frac{f_d}{f_d^{SBS}}\right)^{m/\alpha}, \tag{5.41}$$

where s_{exp} is the suction at air expulsion value, f_d^{SBS} is the value of pyknotropy factor for stress states at the state boundary surface (SBS), and factor c_i is defined as

$$c_i = \frac{3 + a^2 - f_d\, a\sqrt{3}}{3 + a^2 - f_d^{SBS} a\sqrt{3}}. \tag{5.42}$$

On the microstructure level, the reversible behavior linear in $\ln p^m$ vs. $\ln(1+e^m)$ plot is adopted, and the stresses are defined as follows

$$\dot{\boldsymbol{\sigma}^m} = \boldsymbol{I}\frac{p^m}{\kappa_m}\dot{\varepsilon}_V^m, \tag{5.43}$$

where p^m denotes the mean stress at the micro-level, and κ_m is the model parameter. There is an explicit formulation of void ratio on the microstructural level given by the term

$$e^m = \exp\left[\kappa_m \ln\frac{s_r}{p^m} + \ln(1+e_r^m)\right] - 1, \tag{5.44}$$

where e_r^m and s_r are the material parameters representing an arbitrary reference value of void ratio at the micro-level for suction reference value. The state variable vector of the model is given by $\boldsymbol{v} = \{e, s, S_w, e^M, e^m, S_w^M, a_s, r_e\}^T$ where all state variables are defined in the rate form similarly to the stress-strain relation.

Recall that the total stress $\boldsymbol{\sigma}^{tot}$ is defined by equations (5.10), (5.11), (5.13), (5.21) and (5.43). The total stress is consequently substituted into the linear momentum balance equation (equation of equilibrium) that can be expressed in terms of the total stresses in the form

$$\operatorname{div} \boldsymbol{\sigma}^{tot} + \boldsymbol{b} = \boldsymbol{0} \quad \text{in } \Omega, \quad \boldsymbol{u} = \bar{\boldsymbol{u}} \quad on\ \Gamma_u, \quad \boldsymbol{l}\,\boldsymbol{\sigma}^{tot} = \bar{\boldsymbol{t}} \quad on\ \Gamma_t, \tag{5.45}$$

where $\boldsymbol{u}$ is the displacement vector, $\boldsymbol{b}$ is the body force vector, $\boldsymbol{0}$ is the zero vector, $\boldsymbol{l}$ contains components of the unit outer normal vector of the surface Γ_t, $\boldsymbol{t}$ is the vector of tractions, and $\bar{\boldsymbol{u}}$ is the vector of prescribed displacements on the surface Γ_u. Additionally, it holds that $\Gamma = \Gamma_t \cup \Gamma_u$ and $\Gamma_u \cap \Gamma_t = 0$ where Γ represents the surface of the space domain Ω. The total strains $\boldsymbol{\varepsilon}$ and displacement vector $\boldsymbol{u}$ are linked by the strain-displacement operator matrix $\boldsymbol{\partial}$ (see Equation (2.5)).

It should be noted, the numerical solution of hypoplastic models requires the application of a suitable time integration method. The performance evaluation of different techniques, including the simple forward Euler method, Crank-Nicolson scheme, Runge-Kutta-Fehlberg (RKF) methods with substepping, was investigated, e.g., in references [Tamagnini et al., 2000], [Conti et al., 2013], and [Janda, 2013]. The detailed comparison of the time integration method, including implicit backward Euler and Crank-Nicholson scheme and explicit high order RKF Dormand-Prince scheme with substepping, was presented in [Ding et al., 2015]. Implicit integration methods were considered, e.g., in [Zhang et al., 2001], but generally, there are difficulties with the residual Jacobian expression for the Newton-Raphson iterative approach. Concerning experiences and conclusions in the above-listed papers, the explicit integration RKF algorithm with substepping has been selected and implemented in SIFEL computer code [Koudelka et al., 2017], where several RKF schemes have been implemented and compared for the time integration of the model. It was concluded that the scheme proposed by Bogacki-Shampine [Bogacki and Shampine, 1989] performed better than the standard Runge-Kutta-Fehlberg approach, and it can be considered as an excellent alternative integration scheme for the presented thermo-hygro-mechanical model [Koudelka et al., 2018].

Thermo-mechanical extension to saturated and unsaturated soils

Plenty of laboratory tests showed the phenomenon that the temperature does not change the qualitative response of unsaturated soil to a change in suction. That suction does not alter the qualitative response of the soil exposed to a change in temperature. The constitutive models for the effects of unsaturation and temperature can be combined in a hierarchical way, which is presented, e.g., in [Mašín, 2017]. The model parameters controlling the position and slope of the normal compression line (NCL) N and λ^* in Equation (5.36) are considered to be dependent also on temperature

$$\ln(1+e) = N(s,T) - \lambda^*(s,T) \ln\left(\frac{p^M}{p_r}\right), \tag{5.46}$$

with

$$N(s,T) = N + n_s \ln\left(\frac{s}{s_e}\right) + n_T \ln\left(\frac{T}{T_0}\right) \tag{5.47}$$

$$\lambda^*(s,T) = \lambda^* + l_s \ln\left(\frac{s}{s_e}\right) + l_T \ln\left(\frac{T}{T_0}\right) \tag{5.48}$$

Recall, the parameters n_s and l_s describe the effect of suction on the position and slope of NCL, while n_T and l_T are additional parameters controlling the influence of temperature. T_0 is the reference temperature, and model parameters $N = N(0,T_0)$ and $\lambda^* = \lambda^*(0,T_0)$ correspond to the reference temperature. According to the experimental evidence, the slope of the NCL for most practical problems may be taken as independent of temperature (thus $l_T = 0$). This means that n_T should be negative to predict a decrease of the preconsolidation pressure with increasing temperature.

The heating-induced collapse for the states at the SBS is introduced by an additional tensorial term $\boldsymbol{H}_T$ in the general model formulation for macrostructure effective stress (5.21)

$$\dot{\boldsymbol{\sigma}}^M = f_s \left(\boldsymbol{\mathcal{L}} : (\dot{\boldsymbol{\varepsilon}}^M - \dot{\boldsymbol{\varepsilon}}_T^M) + f_d \boldsymbol{N} \|\dot{\boldsymbol{\varepsilon}}^M - \dot{\boldsymbol{\varepsilon}}_T^M\|\right) + f_{us}\boldsymbol{H}_s + f_{uT}\boldsymbol{H}_T, \tag{5.49}$$

where the thermal macroscopic strain rate is assumed for a thermally isotropic material

$$\dot{\boldsymbol{\varepsilon}}_T^M = \frac{\alpha_s \dot{T}}{3}\boldsymbol{I} \tag{5.50}$$

with the overall thermal expansion coefficient equal to the thermal expansion coefficient of the solid constituent α_s. Note that the thermal expansion is independent of the void ratio, does not affect the void ratio, and is fully reversible.

The factor f_u in Equation (5.49) is split into two parts, one controlling the wetting-induced collapse f_{us}, and the second controlling the thermally induced collapse f_{uT}

$$f_{us} = \left[f_d \| f_s A^{-1} : \boldsymbol{N}\|\right]^{m_s/\alpha}, \qquad f_{uT} = \left[f_d \| f_s A^{-1} : \boldsymbol{N}\|\right]^{m_T/\alpha} \tag{5.51}$$

with two model parameters m_s and m_T. The derivation of the $\boldsymbol{H}_T$ term follows conceptually the same approach as the derivation of the term $\boldsymbol{H}_s$ in relations (5.39) with the same factor c_i (5.42):

$$\boldsymbol{H}_T = -c_i \frac{\hat{\boldsymbol{\sigma}}^M}{T\,\lambda^*_{\text{act}}} \left(n_T - l_T \ln\frac{p_e}{p_r}\right)\dot{T}, \tag{5.52}$$

where λ^*_{act} is the actual tangent value of the compression index differing from the compression index $\lambda^*(s,T)$. The derivation of λ^*_{act} together and the detailed description of the hypoplastic model with all parameters are presented in reference [Mašín, 2017].

5.2 Extended saturated-unsaturated non-isothermal air and water flow model for deforming soil medium

The coupled heat and moisture transfer in deforming porous media such as soils can be successfully decribed by a micromechanical-based model presented in [Schrefler and Lewis, 1998]. This approach uses an averaging process assuming that dry air, vapor, and moist air occupy the same

volume fraction in the volume together with the solid phase and the liquid water. Three primary unknowns are defined in the material point - pore water pressure, p^w, pore gas pressure, p^g, and temperature, T for the transport part. Generally, three unknown displacements u, v, w are defined for the mechanical part. A choice of primary unknowns with pore capillary pressure, p^c, instead of pore water pressure, p^w, is recommended in literature dealing with the modeling of concrete loaded by high temperatures. To name several references, e.g., [Gawin et al., 1999], [Schrefler et al., 2002], and [Pesavento, 2000].

This model in connection with the principle of effective stresses is briefly discussed and extended by an effect of volume changes on the global moisture accumulation function (suction curve) observed mainly in expansive soils.

5.2.1 Constitutive and transport equations

The moist air in the pore system is usually assumed to be a perfect mixture of two ideal gases dry air and water vapor. The ideal gas law is applied to dry air (ga), water vapor (gw), and moist air (g)

$$p^{ga} = \rho^{ga} TR/M_a, \qquad p^{gw} = \rho^{gw} TR/M_w, \tag{5.53}$$

$$\rho^g = \rho^{ga} + \rho^{gw}, \qquad p^g = p^{ga} + p^{gw}, \tag{5.54}$$

$$M_g = \left(\frac{\rho^{gw}}{\rho^g} \frac{1}{M_w} + \frac{\rho^{ga}}{\rho^g} \frac{1}{M_a} \right)^{-1}, \tag{5.55}$$

where R is the universal gas constant, M_a, M_w, and M_g, denote the molar masses of individual constituents. Densities ρ^g, ρ^{ga}, and ρ^{gw} stand for the density of moist air, dry air, and water vapor, respectively. The second Equation (5.54) expresses Dalton's law [Moran et al., 2018].

In soils, the water is usually present as a condensed liquid that is separated from its vapor by a concave meniscus (capillary water) because of the surface tension. The capillary pressure is defined as the pressure difference between the gas phase and the liquid phase, by the capillary pressure equation

$$p^c = p^g - p^w. \tag{5.56}$$

The relationship between the relative humidity, φ, and the capillary pressure, p^c, in the pores can be defined by the Kelvin-Laplace law

$$\varphi = \frac{p^{gw}}{p^{gws}} = \exp\left(\frac{p^c M_w}{\rho^w RT} \right) \tag{5.57}$$

The water vapor saturation pressure p^{gws}, which is a function of the temperature only, can be obtained from the Clausius-Clapeyron equation or from empirical formulas proposed, e.g., in [ASHRAE, 1993].

The moisture retention curve is an alternative representation of the pore size distribution. It demonstrates the connection between the suction stress, s, and the water accumulated. The suction stress rapidly decreases from the upward hygroscopic moisture as the large pores are filled with water. In soil mechanics, the moisture retention curves are mostly substituted by the material relationship between capillary pressure p_c, saturation degree S_w and temperature T [Schrefler and Lewis, 1998]

$$p^c = p^c(S_w, T). \tag{5.58}$$

In the case of expansive soils, the volume changes are significant phenomena influencing also the capability of absorbing moisture from an environment. The degree of saturation S_w depends on suction stress s, void ratio, and the suction-loading path [Mašín, 2010]. The previous relationship can be expressed in an inverse form with the dependence on the mentioned volume changes

$$S_w = S_w(p^c, T, \varepsilon_V), \tag{5.59}$$

where ε_V is the volume strain measured from a reference state. Is should be noted the equality $s = p^c = p^g - p^w$.

A similar description of moisture retention is the retention of enthalpy in materials having heat capacities which can be simply expressed as

$$H = H(T), \tag{5.60}$$

where H is the the mass-specific enthalpy [J·kg^{-1}]. The changes of enthalpy are usually described in a differential way, which leads to the definition of the specific heat capacity

$$C_p = \left(\frac{\partial H}{\partial T}\right)_{p=\text{const}}. \tag{5.61}$$

The heat capacity varies insignificantly with temperature. It is customary, however, to correct this term for all phases (solid, water, gas) to introduce the effective heat capacity as

$$(\rho C_p)_{\text{eff}} = \rho_s C_p^s + \rho_w C_p^w + \rho_g C_p^g, \tag{5.62}$$

were phase average densities are expresed via volume fractions $\rho_\pi = nS_\pi\rho^\alpha$ with index π standing for water, w, and gas, g. For solid $\pi = s$, the phase average density is $\rho_s = (1-n)\rho^s$. Recall, the curves reflecting material properties of porous media and their descriptions are commonly known as the state equations. The equation of state for water was presented, e.g., in [Fernandez, 1972]. The linearized form is:

$$\rho^w = \rho^{w0}\left[1 - \beta_w T + \alpha_w(p^w - p^{w0})\right] \tag{5.63}$$

and its time derivative is obtained from the mass conservation equation

$$\frac{\mathrm{D}^w(\rho^w V^w)}{\mathrm{D}t} = 0, \tag{5.64}$$

$$\frac{1}{\rho^{w0}}\frac{\mathrm{D}^w\rho^w}{\mathrm{D}t} = \frac{1}{K_w}\frac{\mathrm{D}^w p^w}{\mathrm{D}t} - \beta_w\frac{\mathrm{D}^w T}{\mathrm{D}t}, \tag{5.65}$$

where $K_w = 1/\alpha_w$ is the bulk modulus of water with the compressibility coefficient α_w, and β_w is the thermal expansion coefficient. The density ρ^{w0} and the pressure p^{w0} indicate an initial steady-state at standard conditions.

For the slow phenomena in soils, the moisture convection is not assumed, and the liquid and gas transport and vapor diffusion taking place in the gas are the remaining driving phenomena. The generalized form of Darcy's law is assumed for the water and gas transport:

$$\boldsymbol{J}_s^\pi = nS_\pi\rho^\pi\boldsymbol{v}^{\pi s} = \frac{k^{r\pi}\boldsymbol{k}\rho^\pi}{\mu^\pi}\left(-\mathrm{grad}p^\pi + \rho^\pi\boldsymbol{g}\right). \tag{5.66}$$

The subscript or superscript $\pi = w$ is for the liquid phase and $\pi = g$ for the gaseous phase. $k^{r\pi}$ denotes dimensionless relative permeability, usually as a function of saturation degree. In Equation (5.66), $\boldsymbol{k}$ [m^2] is the intrinsic permeability matrix, and μ^π [kg.m^{-1}s^{-1}] is the dynamic viscosity. To avoid misunderstanding, note that the so-called permeability matrix, or hydraulic conductivity, commonly used in the geotechnical literature, is defined as

$$\boldsymbol{K}^w = \frac{k^{rw}\boldsymbol{k}\rho^w g}{\mu^w}, \qquad [\mathrm{m}\cdot\mathrm{s}^{-1}], \tag{5.67}$$

where g is the gravity acceleration. The second driving mechanism is the diffusive-dispersive mass flux of the water vapor in the gas described by Fick's law

$$\boldsymbol{J}_g^{gw} = nS_g\rho^{gw}\left(\boldsymbol{v}^{gw} - \boldsymbol{v}^g\right) = -\rho^g\boldsymbol{D}_g\mathrm{grad}\left(\frac{\rho^{gw}}{\rho^g}\right), \tag{5.68}$$

where $\boldsymbol{D}_g$ [m^2.s^{-1}] is the effective dispersive tensor, which is a function of the tortuosity factor accounting for the tortuous nature of the pathway in soil. The flux in Equation (5.68) can be modified into the following equation

$$\boldsymbol{J}_g^{gw} = -\rho^g\frac{M_aM_w}{M_g^2}\boldsymbol{D}_g\mathrm{grad}\left(\frac{p^{gw}}{p^g}\right) = \rho^g\frac{M_aM_w}{M_g^2}\boldsymbol{D}_g\mathrm{grad}\left(\frac{p^{ga}}{p^g}\right) = -\boldsymbol{J}_g^{ga}, \tag{5.69}$$

where $\boldsymbol{J}_g^{ga}$ is the diffusive-dispersive mass flux of dry air in the gas. It should be noted, diffusion of physically adsorbed water is neglected.

When considering the solid phase as compressible, a relationship for the material time derivative of the solid density can be obtained from the mass conservation equation in differential form

$$\frac{\mathrm{D}^s(\rho^sV^s)}{\mathrm{D}t} = 0. \tag{5.70}$$

By assuming that the solid density is a function of pore pressure p^s

$$p^s = S_wp^w + S_gp^g, \tag{5.71}$$

temperature, and the first invariant of the effective stress, the above derivative (5.70) reads

$$\frac{1}{\rho^s}\frac{\mathrm{D}^s\rho^s}{\mathrm{D}t} = -\frac{1}{V^s}\frac{\mathrm{D}^sV^s}{\mathrm{D}t} = -\frac{1}{K_s}\frac{\mathrm{D}^sp^s}{\mathrm{D}t} - \beta_s\frac{\mathrm{D}^sT}{\mathrm{D}t} - \frac{1}{3(n-1)K_s}\frac{\mathrm{D}^s\mathrm{tr}(\boldsymbol{\sigma}^{\mathrm{eff}})}{\mathrm{D}t}. \tag{5.72}$$

In the above equation, the individual derivatives follow

$$\begin{aligned}
\frac{1}{\rho^s}\frac{\mathrm{D}^s\rho^s}{\mathrm{D}p^s} &= \frac{1}{K_s}\\
\frac{1}{\rho^s}\frac{\mathrm{D}^s\rho^s}{\mathrm{D}T} &= -\beta_s\\
\frac{1}{\rho^s}\frac{\mathrm{D}^s\rho^s}{\mathrm{D}\boldsymbol{I}_1'} &= -\frac{1}{3(n-1)K_s}
\end{aligned} \tag{5.73}$$

with K_s, the bulk modulus of the grain material. β_s is the thermal expansion coefficient for the solid, and $\mathrm{tr}(\boldsymbol{\sigma}^{\mathrm{eff}}) = \boldsymbol{I}_1'$ is the first stress invariant.

It is essential to introduce the constitutive relationship for the first stress invariant

$$\frac{\mathrm{D}^s(\mathrm{tr}\boldsymbol{\sigma}^{\mathrm{eff}})}{\mathrm{D}t} = 3K_T\left(\mathrm{div}\boldsymbol{v}^s + \frac{1}{K_s}\frac{\mathrm{D}^s p^s}{\mathrm{D}t} - \beta_s\frac{\mathrm{D}^s T}{\mathrm{D}t}\right), \tag{5.74}$$

where K_T is the bulk modulus of the skeleton, different from that of the grain material, and

$$\frac{1}{K_s}\frac{\mathrm{D}^s p^s}{\mathrm{D}t} \tag{5.75}$$

represents an overall volumetric strain rate caused by uniform compression of particles (as opposed to the skeleton) by the average pressure p_s . In soils, this volumetric strain is relatively insignificant. It can be ignored, but it is crucial in rock mechanics and concrete modeling, for which the compressibility of the solid phase is comparable to that of the skeleton.

Including the definition of the Biot's constant

$$1 - \alpha = \frac{K_T}{K_s} \tag{5.76}$$

in Equation (5.72), the final relation for solid skeleton density is obtained

$$\frac{1}{\rho^s}\frac{\mathrm{D}^s\rho^s}{\mathrm{D}t} = \frac{1}{(1-n)}\left((\alpha-n)\frac{1}{K_s}\frac{\mathrm{D}^s p^s}{\mathrm{D}t} - \beta_s(\alpha-n)\frac{\mathrm{D}^s T}{\mathrm{D}t} - (1-\alpha)\mathrm{div}\boldsymbol{v}^s\right). \tag{5.77}$$

For incompressible grain material $1/K_s = 0$ and $\alpha = 1$. This does not imply that the solid skeleton is rigid because of rearrangements of grains and voids.

The generalized Fourier's Law for the average heat flux of the multiphase medium must complete constitutive equations

$$\boldsymbol{q}_T = \boldsymbol{\lambda}_{\mathrm{eff}}\mathrm{grad}T \tag{5.78}$$

with the effective thermal conductivity tensor $\boldsymbol{\lambda}_{\mathrm{eff}}$.

5.2.2 Mass and energy balance equations

The macroscopic mass balance equations start from the equation for solid phase

$$\frac{\mathrm{D}^s\rho_s}{\mathrm{D}t} + \mathrm{div}\left(\rho_s\boldsymbol{v}^s\right) = 0. \tag{5.79}$$

The superscript s denotes the solid fraction, $\boldsymbol{v}^s$ expresses the mass averaged solid velocity. Recall, the operator $\mathrm{D}^s/\mathrm{D}t$ is the time derivative taken with the moving solid (s) phase. The solid phase average density corresponds to the volume fraction approach $\rho_s = (1-n)\rho^s$, where ρ^s is the intrinsic solid phase averaged density and n is the average porosity.

The mass balance for the liquid phase (liquid water) includes the relative velocity and the material time derivative with respect to the moving solid:

$$\frac{\mathrm{D}^s\rho_w}{\mathrm{D}t} + \boldsymbol{v}^{ws}\cdot\mathrm{grad}\rho_w + \rho_w\mathrm{div}\left(\boldsymbol{v}^s + \boldsymbol{v}^{ws}\right) = -\dot{m}_{\mathrm{vap}}, \tag{5.80}$$

where $\boldsymbol{v}^{ws} = \boldsymbol{v}^w - \boldsymbol{v}^s$ is the relative velocity of the liquid phase related to the solid phase, $\dot{m}_{vap}$ stands for the mass rate of evaporation. The liquid phase averaged density is expressed via volume

fraction $\rho_w = nS_w\rho^w$, where S_w is the water saturation degree, and ρ^w is the water density. The subscript or superscript w denotes the liquid phase (water).

The macroscopic mass balance equation for gas (g) as a mixture of dry air (ga) and water vapor (gw) is written in a similar way

$$\frac{\mathrm{D}^s\rho_g}{\mathrm{D}t} + \boldsymbol{v}^{gs}\cdot\mathrm{grad}\rho_g + \rho_g\mathrm{div}\big(\boldsymbol{v}^s + \boldsymbol{v}^{gs}\big) = \dot{m}_{\mathrm{vap}}, \tag{5.81}$$

where $\boldsymbol{v}^{gs} = \boldsymbol{v}^g - \boldsymbol{v}^s$ is the relative velocity of the gaseous phase related to the solid phase, and $\rho_g = nS_g\rho^g$. The gas density includes dry air density and vapor density $\rho^g = \rho^{ga} + \rho^{gw}$. The degree of gas saturation S_g follow the expression

$$S_g + S_w = 1. \tag{5.82}$$

The macroscopic energy balance equation for the multiphase system is written with the assumption that the phases of partially saturated porous medium are locally in a thermodynamic equilibrium state. It means that averaged temperatures of all phases are assumed equal at each point in the multiphase system, and they are equal to macroscopic average temperature T:

$$\begin{aligned}\big(\rho C_p\big)_{\mathrm{eff}}\frac{\partial T}{\partial t} = \big(\rho_s C_p^s\boldsymbol{v}^s + \rho_w C_p^w\boldsymbol{v}^w + \rho_g C_p^g\boldsymbol{v}^g\big)\cdot\mathrm{grad}T \\ -\mathrm{div}\big(\boldsymbol{\lambda}_{\mathrm{eff}}\mathrm{grad}T\big) = -\dot{m}_{\mathrm{vap}}\Delta H_{\mathrm{vap}},\end{aligned} \tag{5.83}$$

where the effective specific heat capacity of multiphase medium includes all phases in (5.62), as well as the effective heat conductivity.

In soil mechanics, the energy balance equation usually does not consider heat source terms. Moreover, the solid phase's convective heat flux $\rho_s C_p^s\boldsymbol{v}^s$ is usually insignificant and neglected. In the Equation (5.83), $\rho_w C_p^w\boldsymbol{v}^w = (1-n)\rho^w C_p^w\boldsymbol{v}^w$ is the convective heat flux in the liquid phase, $\rho_g C_p^g\boldsymbol{v}^g = (1-n)\rho^g C_p^g\boldsymbol{v}^g$ is the convective heat flux in the gaseous phase, and $\Delta H_{\mathrm{vap}} = H^{gw} - H^w$ is the latent heat of evaporation.

The linear momentum balance equation for the whole multiphase medium is based on the concept of effective stresses [Schrefler and Lewis, 1998], where the total stress vector can be expressed as

$$\boldsymbol{\sigma}^{\mathrm{eff}} = \boldsymbol{\sigma}^{\mathrm{tot}} + (S_w p^w + S_g p^g)\boldsymbol{m}^{\mathrm{T}}. \tag{5.84}$$

The stress vector $\boldsymbol{\sigma}^{\mathrm{eff}}$ expresses the effective stress between grains, the identity tensor is replaced by the unit vector $\boldsymbol{m} = (1,1,1,0,0,0)$. In generalized form, the total stress vector reads

$$\boldsymbol{\sigma}^{\mathrm{eff}} = \boldsymbol{\sigma}^{\mathrm{tot}} + \chi(S_w p^w + S_g p^g)\boldsymbol{m}^{\mathrm{T}}. \tag{5.85}$$

with the effective stress parameter χ being usually a function of saturation degree S_w, see, e.g., Equation (5.15), or Biot's constant α, see, e.g. [Schrefler and Lewis, 1998]. The linear momentum balance equation assuming slow phenomena is then written in the following form

$$\mathrm{div}\left(\boldsymbol{\sigma}^{\mathrm{eff}} - \alpha(S_w p^w + S_g p^g)\boldsymbol{m}^{\mathrm{T}}\right) + \rho\boldsymbol{g} = 0. \tag{5.86}$$

Density $\rho = (1-n)\rho^s + nS_w\rho^w + nS_g\rho^g$ is the average density of the multiphase system, the vector $\boldsymbol{g}$ stands for the gravity acceleration. The Biot's constant is usually $\alpha = 1$ for cohesive soils assuming as an incompressible grain material ($1/K_s = 0$).

Introduction of intrinsic phase-average density with the appropriate volume fraction, the mass balance equation for the solid phase (5.79) can be rewritten in this form

$$\frac{(1-n)}{\rho^s}\frac{\mathrm{D}^s\rho^s}{\mathrm{D}t} - \frac{\mathrm{D}^s n}{\mathrm{D}t} + (1-n)\mathrm{div}\boldsymbol{v}^s = 0. \tag{5.87}$$

The use of vector identity for water

$$\mathrm{div}(\rho_w \boldsymbol{v}^w) = \rho_w \mathrm{div}\boldsymbol{v}^w + \mathrm{grad}\rho_w \cdot \boldsymbol{v}^w, \tag{5.88}$$

and division by $S_w\rho^w$, the continuity equation for water (5.80) is tranformed

$$\frac{\mathrm{D}^s n}{\mathrm{D}t} + \frac{n}{\rho^w}\frac{\mathrm{D}^s\rho^w}{\mathrm{D}t} + \frac{n}{S_w}\frac{\mathrm{D}^s S_w}{\mathrm{D}t} + \frac{1}{S_w\rho^w}\mathrm{div}(nS_w\rho^w\boldsymbol{v}^{ws}) + n\mathrm{div}\boldsymbol{v}^s = -\frac{\dot{m}_{\mathrm{vap}}}{S_w\rho^w}. \tag{5.89}$$

Summation with (5.87), to eliminate $\mathrm{D}^s n/\mathrm{D}t$, gives

$$\frac{(1-n)}{\rho^s}\frac{\mathrm{D}^s\rho^s}{\mathrm{D}t} + \mathrm{div}\boldsymbol{v}^s + \frac{n}{\rho^w}\frac{\mathrm{D}^s\rho^w}{\mathrm{D}t} + \frac{n}{S_w}\frac{\mathrm{D}^s S_w}{\mathrm{D}t} + \frac{1}{S_w\rho^w}\mathrm{div}(nS_w\rho^w\boldsymbol{v}^{ws}) = -\frac{\dot{m}_{\mathrm{vap}}}{S_w\rho^w}. \tag{5.90}$$

Introduction of (5.64) and (5.70) for the material derivatives of the water and solid densities along with (5.71) gives

$$\begin{aligned}\frac{(\alpha-n)}{K^s}\frac{\mathrm{D}^s}{\mathrm{D}t}(S_w p^w + S_g p^g) - \beta_s(\alpha-n)\frac{\mathrm{D}T}{\mathrm{D}t} + \alpha\mathrm{div}\boldsymbol{v}^s + \\ +n\left(\frac{1}{K_w}\frac{\mathrm{D}^s p^w}{\mathrm{D}t} - \beta_w\frac{\mathrm{D}^s T}{\mathrm{D}t}\right) + \frac{n}{S_w}\frac{\mathrm{D}^s S_w}{\mathrm{D}t} + \frac{1}{S_w\rho^w}\mathrm{div}(nS_w\rho^w\boldsymbol{v}^{ws}) = -\frac{\dot{m}_{\mathrm{vap}}}{S_w\rho^w}.\end{aligned} \tag{5.91}$$

Carrying out derivatives p^w and p^g, collecting term and employing $\mathrm{D}^s S_g/\mathrm{D}t = -\mathrm{D}^s S_w/\mathrm{D}t$ yields

$$\begin{aligned}\left(\frac{(\alpha-n)}{K_s}S_w^2 + \frac{nS_w}{K_w}\right)\frac{\mathrm{D}^s p^w}{\mathrm{D}t} + \frac{(\alpha-n)}{K_s}S_w S_g\frac{\mathrm{D}^s p^g}{\mathrm{D}t} + \alpha S_w\mathrm{div}\boldsymbol{v}^s + \\ -\beta_{sw}\frac{\mathrm{D}^s T}{\mathrm{D}t} + \left(\frac{(\alpha-n)}{K_s}S_w p^w - \frac{(\alpha-n)}{K_s}S_w p^g + n\right)\frac{\mathrm{D}^s S_w}{\mathrm{D}t} + \frac{1}{\rho^w}\mathrm{div}(nS_w\rho^w\boldsymbol{v}^{ws}) = -\frac{\dot{m}_{\mathrm{vap}}}{\rho^w},\end{aligned} \tag{5.92}$$

where

$$\beta_{sw} = S_w\left[(\alpha-n)\beta_s + \beta_w\right]. \tag{5.93}$$

The mass balance equation for gas (5.81) as a mixture of dry air and vapor is derived in a similar way applying the vector identity (5.88) formulated for gas and carrying out of material time derivative of the first term, and the equation is divided by $\rho^g S_g$ yields

$$\frac{\mathrm{D}^s n}{\mathrm{D}t} + \frac{n}{\rho^g}\frac{\mathrm{D}^s\rho^g}{\mathrm{D}t} + \frac{n}{S_g}\frac{\mathrm{D}^s S_g}{\mathrm{D}t} + \frac{1}{S_g\rho^g}\mathrm{div}(nS_g\rho^g\boldsymbol{v}^{gs}) + n\mathrm{div}\boldsymbol{v}^s = \frac{\dot{m}_{\mathrm{vap}}}{S_g\rho^g}. \tag{5.94}$$

Eliminating $\mathrm{D}^s n/\mathrm{D}t$ by summation with the mass balance equation of the solid (5.87)

$$\frac{(1-n)}{\rho^s}\frac{\mathrm{D}^s\rho^s}{\mathrm{D}t} + \mathrm{div}\boldsymbol{v}^s + \frac{n}{\rho^g}\frac{\mathrm{D}^s\rho^g}{\mathrm{D}t} + \frac{n}{S_g}\frac{\mathrm{D}^s S_g}{\mathrm{D}t} + \frac{1}{S_g\rho^g}\mathrm{div}(nS_g\rho^g\boldsymbol{v}^{gs}) = \frac{\dot{m}_{\mathrm{vap}}}{S_g\rho^g}. \tag{5.95}$$

Introduction of Eq. (5.53) and (5.54) gives

$$\frac{(1-n)}{\rho^s}\frac{\mathrm{D}^s\rho^s}{\mathrm{D}t} + \mathrm{div}\boldsymbol{v}^s + \frac{n}{\rho^g}\frac{\mathrm{D}^s}{\mathrm{D}t}\left[\frac{1}{TR}(p^{ga}M_a + p^{gw}M_w)\right] + \\ + \frac{n}{S_g}\frac{\mathrm{D}^s S_g}{\mathrm{D}t} + \frac{1}{S_g\rho^g}\mathrm{div}(nS_g\rho^g\boldsymbol{v}^{gs}) = \frac{\dot{m}_{\mathrm{vap}}}{S_g\rho^g}. \tag{5.96}$$

Similarly, the introduction of (5.64) and (5.70) for the material derivatives of the water and solid densities along with (5.71) gives

$$\frac{(\alpha-n)}{K_s}S_wS_g\frac{\mathrm{D}^s p^w}{\mathrm{D}t} + \frac{(\alpha-n)}{K_s}S_g^2\frac{\mathrm{D}^s p^g}{\mathrm{D}t} + \alpha S_g\mathrm{div}\boldsymbol{v}^s + \\ -\beta_s(\alpha-n)S_g\frac{\mathrm{D}^s T}{\mathrm{D}t} + \left(\frac{(\alpha-n)}{K_s}S_gp^g - \frac{(\alpha-n)}{K_s}S_gp^w + n\right)\frac{\mathrm{D}^s S_w}{\mathrm{D}t} + \\ + \frac{nS_g}{\rho^g}\frac{\mathrm{D}^s}{\mathrm{D}t}\left[\frac{1}{TR}(p^{ga}M_a + p^{gw}M_w)\right] + \frac{1}{\rho^g}\mathrm{div}(nS_g\rho^g\boldsymbol{v}^{gs}) = \frac{\dot{m}_{\mathrm{vap}}}{\rho^g}, \tag{5.97}$$

For the coupled thermo-hygro analysis in partially saturated porous media, it is more convenient to consider the mass balance equation for dry air separately from that of vapor and sum the mass balance equation of water species - liquid water and water vapor [Schrefler and Lewis, 1998]. The advantage of this approach is that the water evaporation $\dot{m}_{\mathrm{vap}}$ disappears from these mass balance equations. The mass balance equation for dry air in connection with the dry air flux relation gives the following equation

$$\frac{\mathrm{D}^g}{\mathrm{D}t}(nS_g\rho^{ga}) + \mathrm{div}\boldsymbol{J}_g^{ga} + nS_g\rho^{ga}\mathrm{div}\boldsymbol{v}^g = 0. \tag{5.98}$$

This relation is transformed as the mass balance equation for gas, where material time derivatives for the moving solid and relative velocities are introduced

$$\frac{\mathrm{D}^g f^s}{\mathrm{D}t} = \frac{\mathrm{D}^s f^s}{\mathrm{D}t} + \mathrm{grad}f^s\cdot\boldsymbol{v}^{gs} \tag{5.99}$$

$$\boldsymbol{v}^{gs} = \boldsymbol{v}^g - \boldsymbol{v}^s. \tag{5.100}$$

The vector identity (5.88) is applied to gas phase, and together with previous relationships (5.99) and (5.100) is used in mass balance equation for dry air (5.98). Moreover, the resulting equation is divided by $\rho^{ga}S_g$ and summed with (5.87). After introduction of (5.71) and (5.77), the following equation is obtained

$$\frac{(\alpha-n)}{K_s}S_wS_g\frac{\mathrm{D}^s p^w}{\mathrm{D}t} + \frac{(\alpha-n)}{K_s}S_g^2\frac{\mathrm{D}^s p^g}{\mathrm{D}t} + \alpha S_g\mathrm{div}\boldsymbol{v}^s + \\ -\beta_s(\alpha-n)S_g\frac{\mathrm{D}^s T}{\mathrm{D}t} + \left(\frac{(\alpha-n)}{K_s}S_gp^g - \frac{(\alpha-n)}{K_s}S_gp^w + n\right)\frac{\mathrm{D}^s S_w}{\mathrm{D}t} + \\ + \frac{nS_g}{\rho^{ga}}\frac{\mathrm{D}^s\rho^{ga}}{\mathrm{D}t} + \frac{1}{\rho^{ga}}\mathrm{div}\boldsymbol{J}_g^{ga} + \frac{1}{\rho^{ga}}\mathrm{div}(nS_g\rho^{ga}\boldsymbol{v}^{gs}) = 0. \tag{5.101}$$

Constitutive equations for ρ^{ga} (5.53) and for the flux $\boldsymbol{J}_g^{ga}$ (5.69) are then introduced into the previous Equation (5.101) to obtain

$$\begin{aligned}\frac{(\alpha-n)}{K_s}S_wS_g\frac{\mathrm{D}^s p^w}{\mathrm{D}t}+\frac{(\alpha-n)}{K_s}S_g^2\frac{\mathrm{D}^s p^g}{\mathrm{D}t}+\alpha S_g\mathrm{div}\boldsymbol{v}^s+\\ -\beta_s(\alpha-n)S_g\frac{\mathrm{D}^s T}{\mathrm{D}t}-\left(\frac{(\alpha-n)}{K_s}S_gp^g-\frac{(\alpha-n)}{K_s}S_gp^w+n\right)\frac{\mathrm{D}^s S_w}{\mathrm{D}t}+\\ +\frac{nS_g}{\rho^{ga}}\frac{\mathrm{D}^s}{\mathrm{D}t}\left(\frac{M_a}{TR}p^{ga}\right)+\frac{1}{\rho^{ga}}\mathrm{div}\left[\rho^g\frac{M_aM_w}{M_g^2}\boldsymbol{D}_g\mathrm{grad}\left(\frac{p^{gw}}{p^g}\right)\right]+\frac{1}{\rho^{ga}}\mathrm{div}(nS_g\rho^{ga}\boldsymbol{v}^{gs})=0.\end{aligned}\tag{5.102}$$

The derivation of the mass balance equation for vapor is identical to that of dry air. By the change ga to gw of indices, it results in

$$\begin{aligned}\frac{(\alpha-n)}{K_s}S_wS_g\frac{\mathrm{D}^s p^w}{\mathrm{D}t}+\frac{(\alpha-n)}{K_s}S_g^2\frac{\mathrm{D}^s p^g}{\mathrm{D}t}+\alpha S_g\mathrm{div}\boldsymbol{v}^s+\\ -\beta_s(\alpha-n)S_g\frac{\mathrm{D}^s T}{\mathrm{D}t}-\left(\frac{(\alpha-n)}{K_s}S_gp^g-\frac{(\alpha-n)}{K_s}S_gp^w+n\right)\frac{\mathrm{D}^s S_w}{\mathrm{D}t}+\frac{nS_g}{\rho^{gw}}\frac{\mathrm{D}^s}{\mathrm{D}t}\left(\frac{M_w}{TR}p^{gw}\right)+\\ \frac{1}{\rho^{gw}}\mathrm{div}\left[-\rho^g\frac{M_aM_w}{M_g^2}\boldsymbol{D}_g\mathrm{grad}\left(\frac{p^{gw}}{p^g}\right)\right]+\frac{1}{\rho^{gw}}\mathrm{div}(nS_g\rho^{gw}\boldsymbol{v}^{gs})=\frac{\dot{m}_{\mathrm{vap}}}{\rho^{gw}}.\end{aligned}\tag{5.103}$$

This equation is multiplied by ρ^{gw} and added to the mass balance equation of liquid water (5.92) (multiplied by ρ^w). This leads to the mass balance equation for water species (liquid and water), without the mass rate of water evaporation as

$$\begin{aligned}\left(\rho^w\frac{(\alpha-n)}{K_s}S_w^2+\rho^w\frac{nS_w}{K_w}+\rho^{gw}\frac{(\alpha-n)}{K_s}S_wS_g\right)\frac{\mathrm{D}^s p^w}{\mathrm{D}t}+\\ +\left(\rho^w\frac{(\alpha-n)}{K_s}S_wS_g+\rho^{gw}\frac{(\alpha-n)}{K_s}S_g^2\right)\frac{\mathrm{D}^s p^g}{\mathrm{D}t}+\left(\rho^w\alpha S_w+\rho^{gw}\alpha S_g\right)\mathrm{div}\boldsymbol{v}^s-\beta_{swg}\frac{\mathrm{D}^s T}{\mathrm{D}t}+\\ +\left(\rho^w\frac{(\alpha-n)}{K_s}S_w(p^w+p^g)+\rho^{gw}\frac{(\alpha-n)}{K_s}S_g(p^g-p^w)+(\rho^w+\rho^{gw})n\right)\frac{\mathrm{D}^s S_w}{\mathrm{D}t}+\\ +nS_g\frac{\mathrm{D}^s}{\mathrm{D}t}\left(\frac{M_w}{TR}p^{gw}\right)+\mathrm{div}\left[-\rho^g\frac{M_aM_w}{M_g^2}\boldsymbol{D}_g\mathrm{grad}\left(\frac{p^{gw}}{p^g}\right)\right]+\\ +\mathrm{div}(nS_g\rho^{gw}\boldsymbol{v}^{gs})+\mathrm{div}(nS_w\rho^w\boldsymbol{v}^{ws})=0,\end{aligned}\tag{5.104}$$

where

$$\beta_{swg}=(\alpha-n)\beta_s\left(S_g\rho^{gw}+S_w\rho^w\right)+n\beta_wS_w\rho^w.\tag{5.105}$$

5.2.3 Summary of governing equations

The final form of the governing equations is obtained by the introduction of transport equations - Darcy's law (5.66), Fick's law (5.68), into the mass balance equations for dry air (5.102) and water species (5.104) together with an assumption of slow phenomena with inertia forces neglected [Krejčí et al., 2001]. Assuming small displacements and heat and moisture fluxes related to the solid phase, material derivatives $\mathrm{D}^s/\mathrm{D}t$ can be replaced by spatial derivatives $\partial/\partial T$. For the expansive soil modeling, the premises of incompressible grains and incompressible water are

adopted ($\alpha = 1$, $1/K_s = 0$, and $1/K_w = 0$). It has to be mentioned that saturation degree is also the function of the volume changes, so its derivative reads

$$\frac{\partial S_w}{\partial t} = \frac{\partial S_w}{\partial p^c}\frac{\partial p^g}{\partial t} - \frac{\partial S_w}{\partial p^c}\frac{\partial p^w}{\partial t} + \frac{\partial S_w}{\partial T}\frac{\partial T}{\partial t} + \frac{\partial S_w}{\partial \varepsilon_{\mathrm{V}}}\frac{\partial \varepsilon_{\mathrm{V}}}{\partial t}, \tag{5.106}$$

where

$$\frac{\partial \varepsilon_{\mathrm{V}}}{\partial t} = \boldsymbol{m}\frac{\partial \boldsymbol{\varepsilon}}{\partial t} = \boldsymbol{m}\boldsymbol{\partial}\frac{\partial \boldsymbol{u}}{\partial t} = \mathrm{div}\boldsymbol{v}^s. \tag{5.107}$$

Note that

$$\frac{\partial S_w}{\partial t} = -\frac{\partial S_g}{\partial t}. \tag{5.108}$$

The final balance equations are summarized below:

Mass conservaton of dry air

$$\begin{aligned} S_g \mathrm{div}\boldsymbol{v}^s - \beta_s(1-n)S_g\frac{\partial T}{\partial t} - n\frac{\partial S_w}{\partial t} + \frac{nS_g}{\rho^{ga}}\frac{\partial}{\partial t}\left(\frac{M_a}{TR}p^{ga}\right) \quad + \\ \frac{1}{\rho^{ga}}\mathrm{div}\left[\rho^g\frac{M_aM_w}{M_g^2}\boldsymbol{D}_g\mathrm{grad}\left(\frac{p^{gw}}{p^g}\right)\right] + \frac{1}{\rho^{ga}}\mathrm{div}\left[\frac{k^{rg}\boldsymbol{k}\rho^{ga}}{\mu^g}\left(-\mathrm{grad}p^g + \rho^g\boldsymbol{g}\right)\right] \quad = \quad 0. \end{aligned} \tag{5.109}$$

Mass conservaton of water species - liquid water and vapor

$$\begin{aligned} \left(\rho^w S_w + \rho^{gw}S_g\right)\mathrm{div}\boldsymbol{v}^s - \beta_{swg}\frac{\partial T}{\partial t} \quad + \\ +(\rho^w + \rho^{gw})n\frac{\partial S_w}{\partial t} + nS_g\frac{\partial}{\partial t}\left(\frac{M_w}{TR}p^{gw}\right) + \mathrm{div}\left[-\rho^g\frac{M_aM_w}{M_g^2}\boldsymbol{D}_g\mathrm{grad}\left(\frac{p^{gw}}{p^g}\right)\right] \quad + \\ +\mathrm{div}\left[\frac{k^{rg}\boldsymbol{k}\rho^{gw}}{\mu^g}\left(-\mathrm{grad}p^g + \rho^g\boldsymbol{g}\right)\right] + \mathrm{div}\left[\frac{k^{rw}\boldsymbol{k}\rho^w}{\mu^w}\left(-\mathrm{grad}p^w + \rho^w\boldsymbol{g}\right)\right] \quad = \quad 0. \end{aligned} \tag{5.110}$$

Enthalpy conservation equation of the multiphase medium

$$\left(\rho C_p\right)_{\mathrm{eff}}\frac{\partial T}{\partial t} + \left(\rho_w C_p^w\boldsymbol{v}^w + \rho_g C_p^g\boldsymbol{v}^g\right)\cdot\mathrm{grad}T - \mathrm{div}\left(\boldsymbol{\lambda}_{\mathrm{eff}}\mathrm{grad}T\right) = -\dot{m}_{\mathrm{vap}}\Delta H_{\mathrm{vap}}, \tag{5.111}$$

where $\dot{m}_{\mathrm{vap}}$ is obtained from mass balance equation for liquid water

$$\dot{m}_{\mathrm{vap}} = -\alpha S_w\rho^w\mathrm{div}\boldsymbol{v}^s + \rho^w\beta_{sw}\frac{\partial^s T}{\partial t} - \rho^w n\frac{\partial^s S_w}{\partial t} - \mathrm{div}(nS_w\rho^w\boldsymbol{v}^{ws}), \tag{5.112}$$

and convective heat fluxes read

$$\begin{aligned} \rho_w C_p^w\boldsymbol{v}^w &= n\rho^w C_p^w\frac{k^{rw}\boldsymbol{k}\rho^w}{\mu^w}\left(-\mathrm{grad}p^w + \rho^w\boldsymbol{g}\right), \\ \rho_g C_p^g\boldsymbol{v}^g &= n\rho^g C_p^g\frac{k^{rg}\boldsymbol{k}\rho^{gw}}{\mu^g}\left(-\mathrm{grad}p^g + \rho^g\boldsymbol{g}\right). \end{aligned} \tag{5.113}$$

Linear momentum balance equation of the multiphase medium

$$\mathrm{div}\left(\boldsymbol{\sigma}^{\mathrm{eff}} - \alpha(S_w p^w + S_g p^g)\boldsymbol{m}^{\mathrm{T}}\right) + \rho\boldsymbol{g} = 0. \tag{5.114}$$

The balance equations must be completed by initial and boundary conditions

Initial conditions

The initial conditions specify the field of displacements, pore water and gas pressures, and temperature at time $t = 0$

$$\boldsymbol{u} = \boldsymbol{u}_0, \qquad p^w = p_0^w, \qquad p^g = p_0^g, \qquad T = T_0, \qquad \text{in } \Omega \text{ and on } \Gamma, \tag{5.115}$$

where Ω is the domain of interest and Γ its boundary.

Boundary conditions

The boundary conditions for displacements and stresses (2.6) and (2.7) in the mechanical part are completed by Dirichlet boundary conditions with prescribed values

$$\begin{aligned} \boldsymbol{u} &= \boldsymbol{u}_0, && \text{on } \Gamma_u, \\ \boldsymbol{n}\boldsymbol{\sigma} &= \boldsymbol{t}, && \text{on } \Gamma_t, \\ p^w &= \overline{p}^w, && \text{on } \Gamma_w, \\ p^g &= \overline{p}^g, && \text{on } \Gamma_g, \\ T &= \overline{T}, && \text{on } \Gamma_T, \end{aligned} \tag{5.116}$$

and the flux boundary conditions for fluxes of gas, water, and heat

$$\begin{aligned} J^{ga} &= \left[\frac{k^{rg}\boldsymbol{k}\rho^{ga}}{\mu^g}\left(-\mathrm{grad}p^g + \rho^g\boldsymbol{g}\right) + \rho^g\frac{M_a M_w}{M_g^2}\boldsymbol{D}_g\mathrm{grad}\left(\frac{p^{gw}}{p^g}\right)\right]\cdot\boldsymbol{n}, && \text{on } \Gamma_{qg}, \\ J^w &+ J^{gw} + \beta(\rho^{gw} - \rho_\infty^{gw}) = \left[\frac{k^{rw}\boldsymbol{k}\rho^w}{\mu^w}\left(-\mathrm{grad}p^w + \rho^w\boldsymbol{g}\right)\right]\cdot\boldsymbol{n} \\ &+ \left[\frac{k^{rg}\boldsymbol{k}\rho^{gw}}{\mu^g}\left(-\mathrm{grad}p^g + \rho^g\boldsymbol{g}\right)\right]\cdot\boldsymbol{n} - \left[\rho^g\frac{M_a M_w}{M_g^2}\boldsymbol{D}_g\mathrm{grad}\left(\frac{p^{gw}}{p^g}\right)\right]\cdot\boldsymbol{n}, && \text{on } \Gamma_{qw}, \\ q^T &+ \beta_T(T - T_{ext}) + e\sigma_0(T^4 - T_\infty^4) = \left[-\boldsymbol{\lambda}_{\mathrm{eff}}\mathrm{grad}T\right]\cdot\boldsymbol{n} \\ &+ \left[\frac{k^{rw}\boldsymbol{k}\rho^w}{\mu^w}\left(-\mathrm{grad}p^w + \rho^w\boldsymbol{g}\right)\Delta H_{\mathrm{vap}}\right]\cdot\boldsymbol{n}, && \text{on } \Gamma_{qT}. \end{aligned} \tag{5.117}$$

The domain boundary Γ is split into parts Γ_u, Γ_t, Γ_w, Γ_g withs conditions of the first type and parts of the second type conditions, Γ_{qg}, Γ_{qw}, Γ_{qT}.

Variational formulation and FE discretisation of the model in space domain

The weighted residual method and Green's theorem are applied to obtain the governing equations in weak form. Discretisation in the space of the governing equations in their weak form is performed using the finite element method (FEM). As usual, the primary variables are expressed by their nodal values and shape functions. In the standard Galerkin procedure, the weight functions are

replaced by the corresponding shape functions. The detailed derivation of the final system of equations via the weighted residual method and the standard Galerkin procedure is presented in Appendix A. The final non-linear system of equation can be expressed in the matrix form:

$$\begin{pmatrix} \boldsymbol{K}_{uu} & \boldsymbol{K}_{uw} & \boldsymbol{K}_{ug} & \boldsymbol{K}_{uT} \\ \boldsymbol{K}_{wu} & \boldsymbol{K}_{ww} & \boldsymbol{K}_{wg} & \boldsymbol{K}_{wT} \\ \boldsymbol{K}_{gu} & \boldsymbol{K}_{gw} & \boldsymbol{K}_{gg} & \boldsymbol{K}_{gT} \\ \boldsymbol{K}_{Tu} & \boldsymbol{K}_{Tw} & \boldsymbol{K}_{Tg} & \boldsymbol{K}_{TT} \end{pmatrix} \begin{pmatrix} \boldsymbol{d}_u \\ \boldsymbol{d}_w \\ \boldsymbol{d}_g \\ \boldsymbol{d}_T \end{pmatrix} + \\ + \begin{pmatrix} \boldsymbol{C}_{uu} & \boldsymbol{C}_{uw} & \boldsymbol{C}_{ug} & \boldsymbol{C}_{uT} \\ \boldsymbol{C}_{wu} & \boldsymbol{C}_{ww} & \boldsymbol{C}_{wg} & \boldsymbol{C}_{wT} \\ \boldsymbol{C}_{gu} & \boldsymbol{C}_{gw} & \boldsymbol{C}_{gg} & \boldsymbol{C}_{gT} \\ \boldsymbol{C}_{Tu} & \boldsymbol{C}_{Tw} & \boldsymbol{C}_{Tg} & \boldsymbol{C}_{TT} \end{pmatrix} \begin{pmatrix} \dot{\boldsymbol{d}}_u \\ \dot{\boldsymbol{d}}_w \\ \dot{\boldsymbol{d}}_g \\ \dot{\boldsymbol{d}}_T \end{pmatrix} = \begin{pmatrix} \boldsymbol{f}_{ext} \\ \boldsymbol{f}_w \\ \boldsymbol{f}_g \\ \boldsymbol{f}_T \end{pmatrix}, \tag{5.118}$$

where the subscript u denotes the displacements, and the subscripts w, g, T represent pore water pressure, p^w, pore gas pressure, p^g, and temperature, T. The vectors $\boldsymbol{d}_u$, $\boldsymbol{d}_w$, $\boldsymbol{d}_g$, and $\boldsymbol{d}_T$ stand for their unknown nodal variables, and the vectors $\boldsymbol{f}_{ext}$, $\boldsymbol{f}_w$, $\boldsymbol{f}_g$, and $\boldsymbol{f}_T$ denote nodal forces and fluxes prescribed in boundary conditions in (5.117) (usually marked $\boldsymbol{J}$ and $\boldsymbol{q}$ in transport part). The matrices $\boldsymbol{K}$ with subscripts represent the generally non-linear non-symmetric stiffness, conductivity, permeability, and coupling matrices, and $\boldsymbol{C}$ denotes the capacity and coupling matrix. The time integration of this system of equations follows the procedure previously described in Sec. 2.2.

5.3 Computer implementation of hypoplastic model and test benchmarks

5.3.1 Isothermal water flow in deforming medium

The system of equations (5.118) describes the fully coupled thermo-hygro-mechanical approach. It is convenient to simplify the model assuming the liquid water transfer as the only driving mechanism for isothermal saturation processes in soils. All parts with pore gas pressure and temperature are neglected in the governing system of Equations (5.109) to (5.117). The final matrix form in Equations (5.118) is simplified into the following fully-coupled form

$$\begin{pmatrix} \boldsymbol{K}_{uu} & \boldsymbol{K}_{uw} \\ \boldsymbol{0} & \boldsymbol{K}_{ww} \end{pmatrix} \begin{pmatrix} \boldsymbol{d}_u \\ \boldsymbol{d}_w \end{pmatrix} + \begin{pmatrix} \boldsymbol{0} & \boldsymbol{0} \\ \boldsymbol{C}_{wu} & \boldsymbol{C}_{ww} \end{pmatrix} \begin{pmatrix} \dot{\boldsymbol{d}}_u \\ \dot{\boldsymbol{d}}_w \end{pmatrix} = \begin{pmatrix} \boldsymbol{f}_{ext} \\ \boldsymbol{f}_w \end{pmatrix}, \tag{5.119}$$

where off-diagonal coupling blocks are

$$\boldsymbol{K}_{uw} = -\int_\Omega \boldsymbol{B}_u^{\mathrm{T}} \boldsymbol{m}^{\mathrm{T}} (\alpha S_w) \boldsymbol{N}_w \mathrm{d}\Omega, \qquad \boldsymbol{C}_{wu} = \int_\Omega \boldsymbol{N}_w^{\mathrm{T}} (\alpha S_w) \boldsymbol{m}^{\mathrm{T}} \boldsymbol{B}_u \mathrm{d}\Omega. \tag{5.120}$$

Mašín in [Mašín, 2017] developed the fully-coupled model determined for a material point with suction and temperature as input parameters. The implementation and coupling of this model, together with Lewis and Schrefler's approach, was then implemented as a staggered algorithm. The transport and mechanical parts run separately with data transfer; see Sec. 2.3.1 and Sec. 2.4.

In this concept, the transport part runs first before the mechanical part. The system of equations (5.119) is modified for the partially coupled approach for transport and mechanical parts separately with the mechanical system of equation rewritten in incremental form

- *Transport part*

$$\boldsymbol{K}_{ww}\boldsymbol{d}_w + \boldsymbol{C}_{ww}\dot{\boldsymbol{d}}_w = \boldsymbol{f}_w + \boldsymbol{f}_{wu}, \tag{5.121}$$

- *Mechanical part*

$$\boldsymbol{K}_{uu}\Delta\boldsymbol{d}_u = \Delta\boldsymbol{f}_u + \Delta\boldsymbol{f}_{uw}, \tag{5.122}$$

where

$$\boldsymbol{f}_{wu} = -\boldsymbol{C}_{wu}\boldsymbol{d}_u = -\int_\Omega \boldsymbol{N}_w^{\mathrm{T}}(\alpha S_w)\boldsymbol{m}^{\mathrm{T}}\boldsymbol{B}_u \mathrm{d}\Omega\boldsymbol{d}_u = -\int_\Omega \boldsymbol{N}^{\mathrm{T}}(\alpha S_w)\Delta\boldsymbol{\varepsilon}_V \mathrm{d}\Omega. \tag{5.123}$$

Vector $\Delta\boldsymbol{\varepsilon}_V$ contains nodal increments of volumetric strains computed from the previous time step. In the presented notation, the right-hand side vector $\Delta\boldsymbol{f}_{uw}$ expresses the forces caused by changes of pore water pressure computed only in the mechanical part from pore water pressure (or suction) increments taken from the transport part

$$\Delta\boldsymbol{f}_{uw} = -\boldsymbol{K}_{uw}\Delta\boldsymbol{d}_w = -\int_\Omega \boldsymbol{B}_u^{\mathrm{T}}\boldsymbol{m}^{\mathrm{T}}(\alpha S_w)\boldsymbol{N}_w \mathrm{d}\Omega\Delta\boldsymbol{d}_w. \tag{5.124}$$

Vector $\Delta\boldsymbol{d}_w$ is the vector of pore water pressure increments. In the hypoplastic model, the vector $\Delta\boldsymbol{f}_{uw}$ is computed from the total stress definition. The vector of total stress $\boldsymbol{\sigma}^{\mathrm{tot}}$, which is previously defined by equations (5.13), (5.21), and (5.43) can be expressed in the form of vector function

$$\boldsymbol{\sigma}^{\mathrm{tot}} = \boldsymbol{g}(\boldsymbol{\varepsilon}(\boldsymbol{u}), p^w). \tag{5.125}$$

The time derivative of the stress vector has the form

$$\dot{\boldsymbol{\sigma}}^{\mathrm{tot}} = \frac{\partial \boldsymbol{g}}{\partial \boldsymbol{\varepsilon}}\dot{\boldsymbol{\varepsilon}} + \frac{\partial \boldsymbol{g}}{\partial p^w}\dot{p}^w = \boldsymbol{D}_u\dot{\boldsymbol{\varepsilon}} + \boldsymbol{h}\dot{p}^w. \tag{5.126}$$

The stiffness matrix $\boldsymbol{D}_u$ and vector $\boldsymbol{h}$ are derived from Equations (5.12) and (5.21). The rate of the total stress has to satisfy the equilibrium equation in the form

$$\boldsymbol{\partial}^T\left(\boldsymbol{D}_u\dot{\boldsymbol{\varepsilon}} + \boldsymbol{h}\dot{p}^w\right) + \dot{\boldsymbol{b}} = \boldsymbol{0}. \tag{5.127}$$

Recall, $\dot{\boldsymbol{b}}$ is the time derivative of the body force vector. Additionally, the hypoplastic model involves state variables given by vector $\boldsymbol{p}$ that can also be formulated in the rate form and thus generally, the stress rate can be defined by

$$\dot{\boldsymbol{\tau}} = \boldsymbol{M}\dot{\boldsymbol{\varepsilon}} = \boldsymbol{\Psi}\left(\boldsymbol{\tau}(t), \Delta\boldsymbol{\varepsilon}(t)\right), \tag{5.128}$$

where $\boldsymbol{\tau}$ is the generalized stress vector $\boldsymbol{\tau} = \{\boldsymbol{\sigma}, \boldsymbol{p}\}^T$, $\boldsymbol{M}$ represents the generalized stiffness matrix and $\boldsymbol{\varepsilon}$ is the generalized strain vector $\boldsymbol{\varepsilon} = \{\boldsymbol{\varepsilon}, p^w\}^T$ and $\boldsymbol{\Psi}$ represents the model response function on the given input of strain increment $\Delta\boldsymbol{\varepsilon}$ of the actual time step and attained stress level

$\boldsymbol{\tau}$. The explicit integration RKF algorithm with substepping has been selected and implemented in SIFEL. (5.128) represents the initial value problem given by the set of ordinary differential equations. These equations can be written in generic substep k at time interval $[t_n; t_{n+1}]$ formally as follows

$$\boldsymbol{\tau}_{k+1} = \boldsymbol{\tau}_k + \Delta t_k \sum_{i=1}^{s} b_i \, \boldsymbol{k}_i \left(\boldsymbol{\tau}_k, \Delta\boldsymbol{\varepsilon}(t_{n+1}), \Delta t_k \right), \tag{5.129}$$

where $\boldsymbol{k}_i \left(\boldsymbol{\tau}_k, \Delta\boldsymbol{\varepsilon}(t_{n+1}), \Delta t_k \right)$ represents the function $\boldsymbol{\Psi}$ evaluated for the given strain increment of the actual time step $\Delta\boldsymbol{\varepsilon}(t_{n+1}) = \boldsymbol{\varepsilon}(t_{n+1}) - \boldsymbol{\varepsilon}(t_n)$ and attained stress levels at the prescribed points of the time interval. In Equation (5.129), dimensionless step length $\Delta t_k \in (0; 1]$ has been introduced with the following definition

$$\Delta t_k = \frac{t_{k+1} - t_k}{t_{n+1} - t_n}. \tag{5.130}$$

A detailed description of the integration by Runge-Kutta-Fehlberg methods is presented in the reference [Koudelka et al., 2017].

5.3.2 Benchmark tests

The computer implementation of the hypoplastic model in connection with Lewis and Schrefler's approach was tested on several examples and benchmarks. Suitable benchmarks can be laboratory tests presented in [Hausmannová and Vašíček, 2014] and [Hausmannová, 2017]. These studies focus on the impact of using high hydraulic gradients on combined measurements of hydraulic conductivity and swelling pressure. The hydraulic conditions are supposed to be consistent with possible water pressures in a deep repository. Both parameters are determined in a full saturation state. Measuring these parameters in such a low-permeable bentonite material requires much time. Therefore, the high hydraulic gradients may accelerate the determination of these parameters. Experiments with the Czech bentonite 75 (B75) from Černý vrch deposit were selected for numerical simulations. The material was uniaxially compacted in the laboratory to reach the required dry density $\rho_d = 1200$ to 1750 kg/m^3. The tested samples have a diameter of 30 mm, and a height of 20 mm. The initial values of hydraulic conductivity and swelling pressure were evaluated using a saturation pore water pressure $p^w = 1$ MPa corresponding to the gradient of grad$p^w = 50$ MPa/m (hydraulic gradient 5000) [Hausmannová and Vašíček, 2014]. A unique device was used to measure the hydraulic conductivity and the swelling pressure (Figure 5.2). The setup of this device is described in detail in the reference [Hausmannová and Vašíček, 2014].

The finite element mesh consists of 20 axisymmetric quadrilateral elements in the vertical direction. Linear approximation functions are used in the transport part and quadratic in the mechanical part. The watering process was modeled as a prescribed pore water pressure from the bottom with the values taken from the measurements. Two switching boundary conditions model the top permeable surface. For the first, the water flux is prescribed zero on the boundary until the water head reaches the closest material point, equal to zero water pressure. Then, the conditions are changed to the Dirichlet boundary condition with prescribed zero water pressure. This procedure is commonly used for free soil surface modeling. The initial pore water pressure p_0^w = -100 MPa is set for all benchmarks. The soil parameters used in the simulations are used from the recent calibration for bentonite B75 [Sun et al., 2021]. The sample is fixed to avoid its

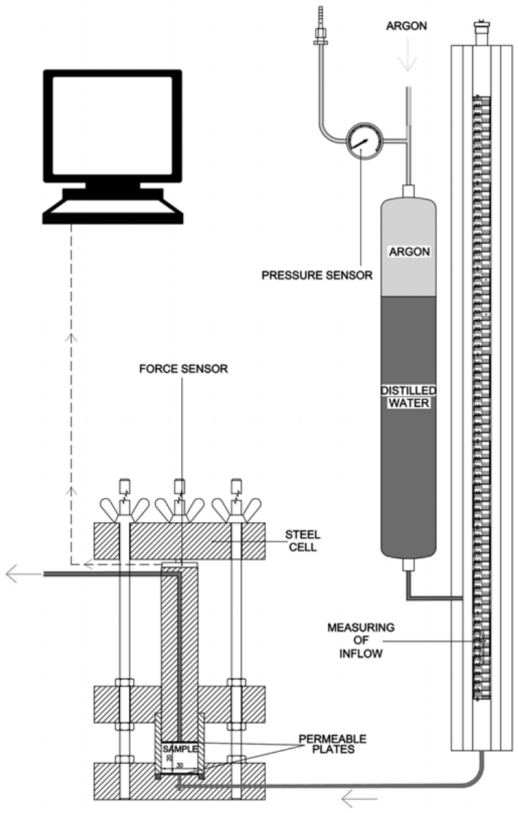

Figure 5.2: Scheme of the measuring device [Hausmannová and Vašíček, 2014].

swelling, and no friction between bentonite material and the steel structure of the testing device is neglected.

Three tests with dry density ρ_d=1298 kg/m^3, ρ_d = 1498 kg/m^3, and ρ_d = 1743 kg/m^3 were used for verification and validation of coupling of mentioned material models in SIFEL computer code and setup of their parameters. A comparison of selected results for different configurations of dry density and hydraulic conductivity is presented. Figures 5.3 and 5.4 show the history of swelling stress for bentonite samples of dry densities ρ_d = 1498 kg/m^3 and ρ_d = 1743 kg/m^3, respectively. From the considerable amount of computations, the best results closed to the measurements are obtained by using of Bogacki-Shampine integration scheme [Koudelka et al., 2017] for the hypoplastic model in connection with the smoothed water retention curve [Sun et al., 2021] and for maximum time step t$_{max}$=1000 s [Scaringi et al., 2022]. It has to be mentioned that such numerical simulations are strongly non-linear, time step length-dependent, and time-consuming. Most of them took from 10 to 20 hours, despite the use of multithreading architecture via OpenMP system.

Attained levels of swelling pressure at full saturation depend only on the setup of initial dry densities. This fact corresponds to the previous experiments and hypoplastic model calibration. The swelling stress for bentonite with ρ_d = 1498 kg/m^3 is about 3 MPa, and for ρ_d = 1743 kg/m^3 is 10.5 MPa, respectively. The initial swelling pressures growth is influenced by the sample saturation rate, related to intrinsic permeability (or hydraulic conductivity). The permeability was assumed constant for all benchmarks. For better compliance with the measurements in the initial phase, the application of a relationship dependent on saturation degree can be successfully

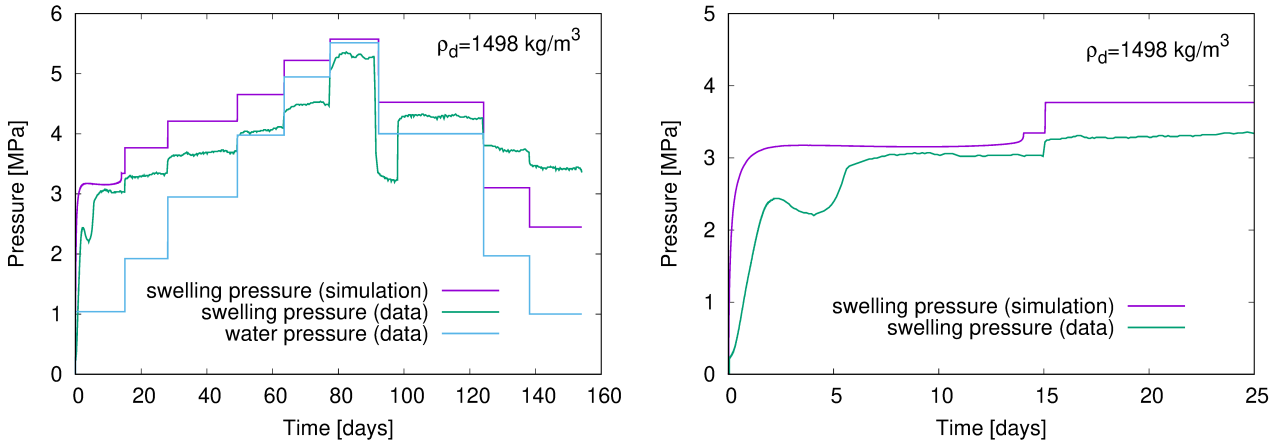

Figure 5.3: History of water pressure and swelling pressure for bentonite B75 $\rho_d = 1498$ kg/m^3 and $K^w = 2.0{\cdot}10^{-13}$ m/s [Scaringi et al., 2022] (left), and zoom of the initial phase (right).

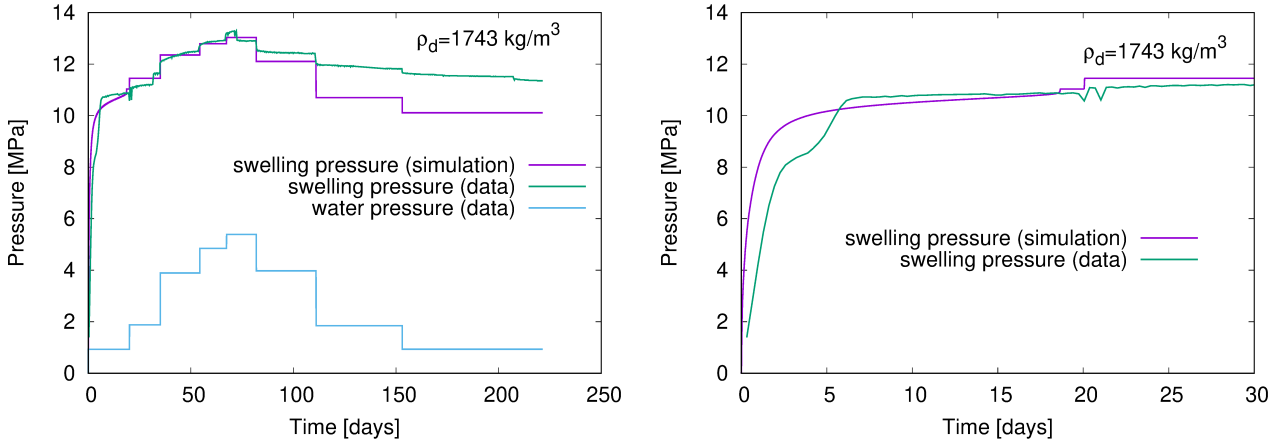

Figure 5.4: History of water pressure and swelling pressure for bentonite B75 $\rho_d = 1743$ kg/m^3 and $K^w = 1.0{\cdot}10^{-13}$ m/s [Scaringi et al., 2022], and zoom of the initial phase (right).

used. The coincidence between simulations and measurements is validated as relatively good. The trends of watering with loading water pressure jumps are captured well.

From the analysis of the results, it can be concluded that coupling the hypoplastic model in connection with Lewis and Schrefler's approach in a staggered scheme works well. However, the model response is primarily dependent on the hypoplastic model setup.

5.4 THM model of Interaction experiments at the Bukov URF

The thermo-hygro-mechanical (THM) model of the physical model (PM) is a part of the project "In-situ interaction physical models at the Bukov Underground Research Facility (URF)" solved with the cooperation of the Czech technical university in Prague (CTU), Radioactive waste repository authority (SÚRAO), and Nuclear research institute Řež (ÚJV Řež, a. s.) [SÚRAO, 2021]. The project aims to compare several bentonite materials and their interactions under deep geological repository conditions using the results of several in-situ experiments in a hard rock mass. The results of these studies will support the decision of usability of materials and their combinations in the future deep geological repository. The mathematical THM model comprises two analyses. The first analysis is the 3D global model of heat transfer in the rock mass analyzing the thermal interaction of the physical models. The main criterion is the temperature profile and its evolution in the surrounding rock mass.

The second analysis is the detailed thermo-hygro-mechanical (THM) model of two selected physical models. The computed results are validated against in-situ measurements. The study is further extended by a parametric study of the mathematical model of PM No. 4. Various input values of material density and permeability have been investigated to establish their influence on the model performance, focusing on getting a close fit to the measured data. The validated mathematical model will be used to interpret physical model behavior [Krejčí et al., 2020].

Figure 5.5: Installation of physical models in the test chamber ZK-3S at Bukov URF, heated models on the left and unheated models on the right [Svoboda et al., 2019a].

Ten physical models simulating a bentonite barrier in a radioactive waste repository were installed in the test chamber of the rock mass at the Bukov URF in the Czech republic. Five

Figure 5.6: Installation and instrumentation of the physical model No. 5 [Svoboda et al., 2019a].

PMs are heated, No. 1 - 4 to 100 °C, No. 5 to 200 °C, in the left wall in Figure 5.5, and five PMs are unheated placed in the opposite wall of the test chamber, the right wall in Figure 5.5. Each PM was constructed as an individual cylindrical cartridge inserted into the prepared 2 m deep borehole, see Figure 5.6. The diameter is 25 cm for heated PMs and 10 cm for unheated, respectively. The heater simulates the canister with radioactive material, a surrounding bentonite barrier, and concrete plugs on both sides. The bentonite material is used from Černý vrch deposit in the north-western region of the Czech Republic selected as the primary buffer material by the Czech nuclear waste agency SURAO. The bentonite is named BCV 2017. PMs were filled with modified bentonite in pellets, blocks, or as a bulk and compacted material. The initial dry density and thus initial porosity were different for each PM. The values were in the range of 1267 kg/m^3 to 1455 kg/m^3 [Svoboda et al., 2019b]. The PMs are thoroughly instrumented by temperature, moisture, and pressure sensors for continuous monitoring. Moreover, temperature sensors are also installed into surrounding rock mass to observe models' thermal interaction (Figure 5.7 and Figure 5.8). For a better temperature distribution image, each borehole has temperature sensors at several levels, usually 0.1 m, 1 m, 2 m, and 3 m deep from the chamber surface.

5.4.1 3D global model of heat transfer in the rock mass

Blind Model

The purpose of the global model was to support the design and the placement of the physical models in the test chamber and the prognosis of the heat transfer in the rock mass with the subsequent validation against measured data. The first phase of the model consists of two 3D numerical models with inclined boreholes in 45 degrees from the horizontal plane and horizontal boreholes, see Figure 5.9. In these supporting models, the analyses simulate only heat transfer for three years since the start of heating [Krejčí et al., 2019]. This period is supposed as a working life of the experiments. The finite element analysis is based on the system of Equations (2.55)

$$\boldsymbol{K}_T \boldsymbol{d}_T + \boldsymbol{C}_T \dot{\boldsymbol{d}}_T = \boldsymbol{f}_T.$$

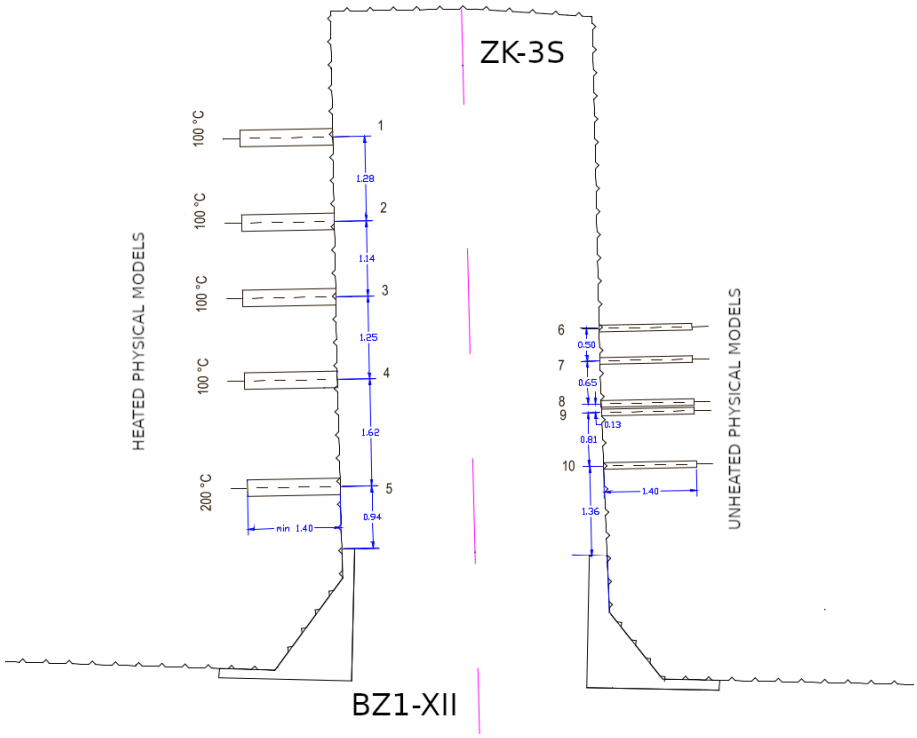

Figure 5.7: Situation of the physical models in the test chamber, heated models on the left and nonheated models on the right.

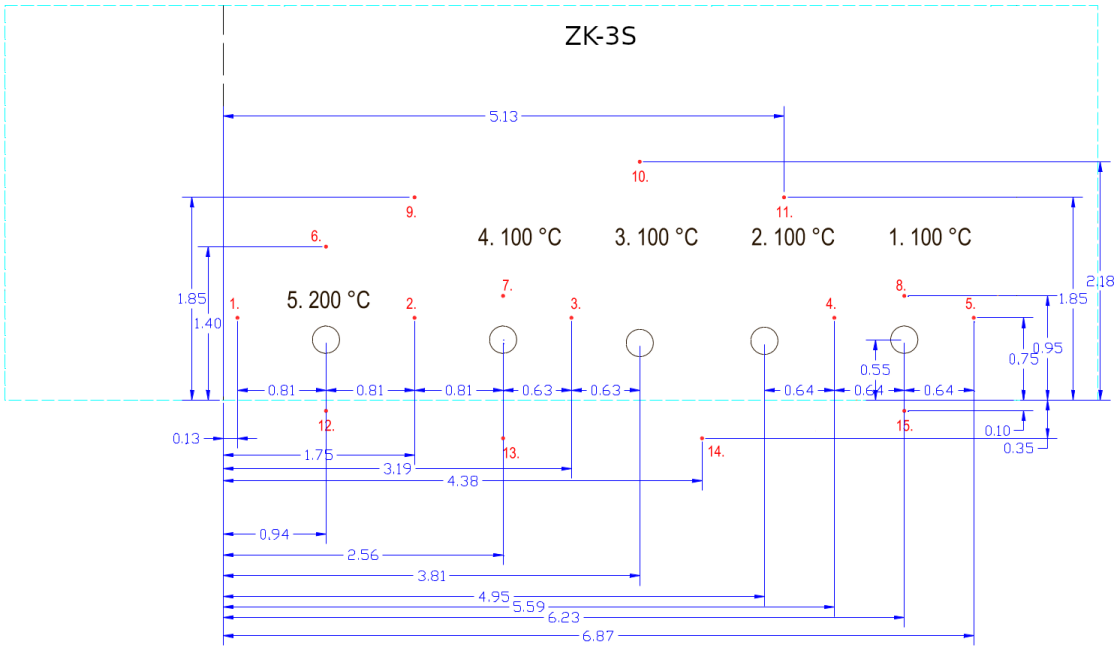

Figure 5.8: Front view of the wall with the heated physical models (black circles) and boreholes for temperature sensors No. 1-15 (red dots).

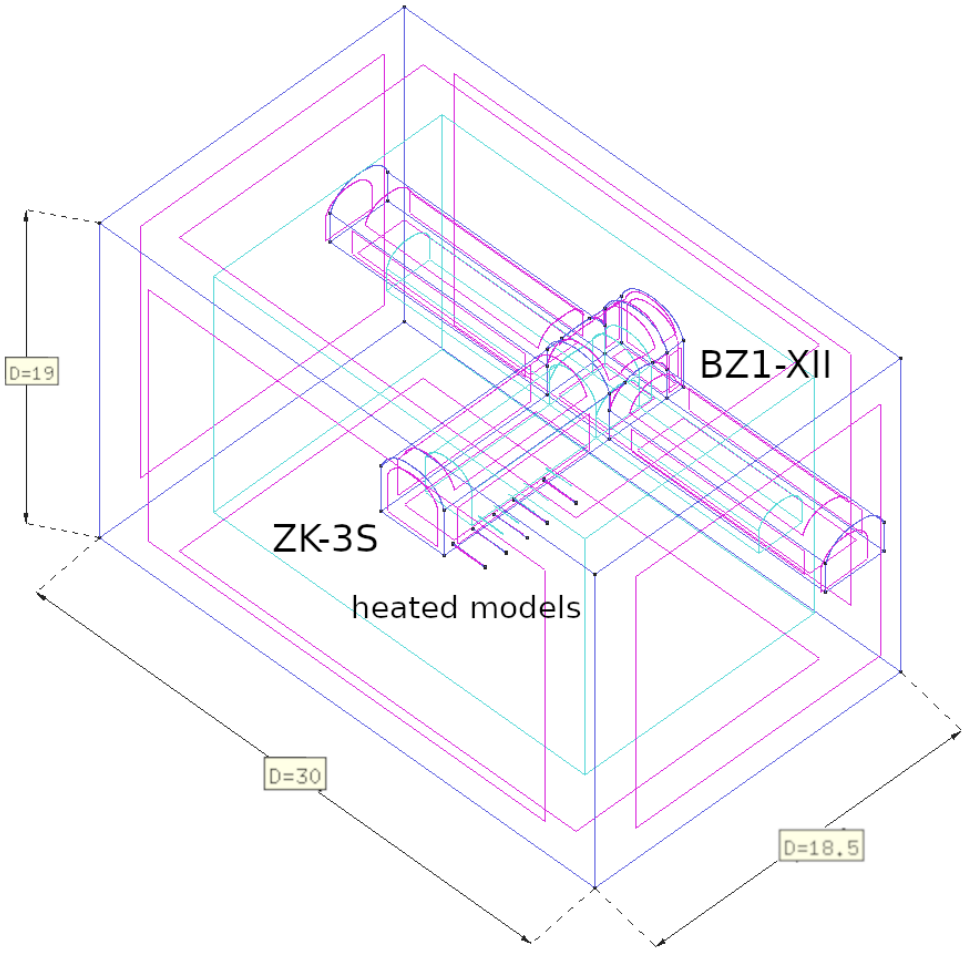

Figure 5.9: Geometry of 3D model of rock mass with horizontal PMs created in GiD mesh modeler.

Dirichlet boundary conditions were prescribed on the boreholes internal surfaces of PMs No. 1 - 4 with a constant temperature 100°C and PM No. 5 with 200°C. The layout of the heated PMs' for the model with horizontal boreholes is illustrated in Figures 5.7 and 5.8. The finite element mesh consists of 870 404 tetrahedral elements with linear approximation functions and 158 054 nodes created in an academic version of GiD modeler [GiD, 2021]. The Newton boundary condition for heat transmission was prescribed for external surfaces in the test chamber (denoted ZK-3S) and in the main gallery (denoted BZ1-XII). The temperature of ambient air was initially set to 16°C. The Dirichlet boundary condition with a prescribed temperature of 16°C was also assumed for the model external surfaces. These surfaces belong to the rock mass block of the dimensions 30 m x 18.6 m x 19 m, which is supposed to be sufficient surrounding mass volume. Considering the PM's dimensions to the rock mass, the bentonite material, heater, and surrounding concrete material were not modeled. This assumption is supposed to give a little higher temperatures than in reality. The time increment of the numerical analysis was set initially to one hour, increasing to one month at the end of the computation. Material parameters of the rock mass were set for granite rock and are listed in Table 5.1.

The analysis leads to conclusion, the heated physical models cause a temperature increase of about 3°C in unheated models. Figures 5.10 and 5.11 illustrate the temperature distribution around the heated PMs after one day and after three years, respectively. The visual control of

Quantity		Value
Volume weight	ρ	2871 kg/m^3
Specific heat	C_{eff}	748 J$\cdot$ kg$^{-1}\cdot$ K^{-1}
Thermal conductivity	λ_{eff}	2.15 W$\cdot$ m$^{-1}\cdot$ K^{-1}

Table 5.1: Material parameters of the granite rock for the global 3D heat transfer model [Krejčí et al., 2020].

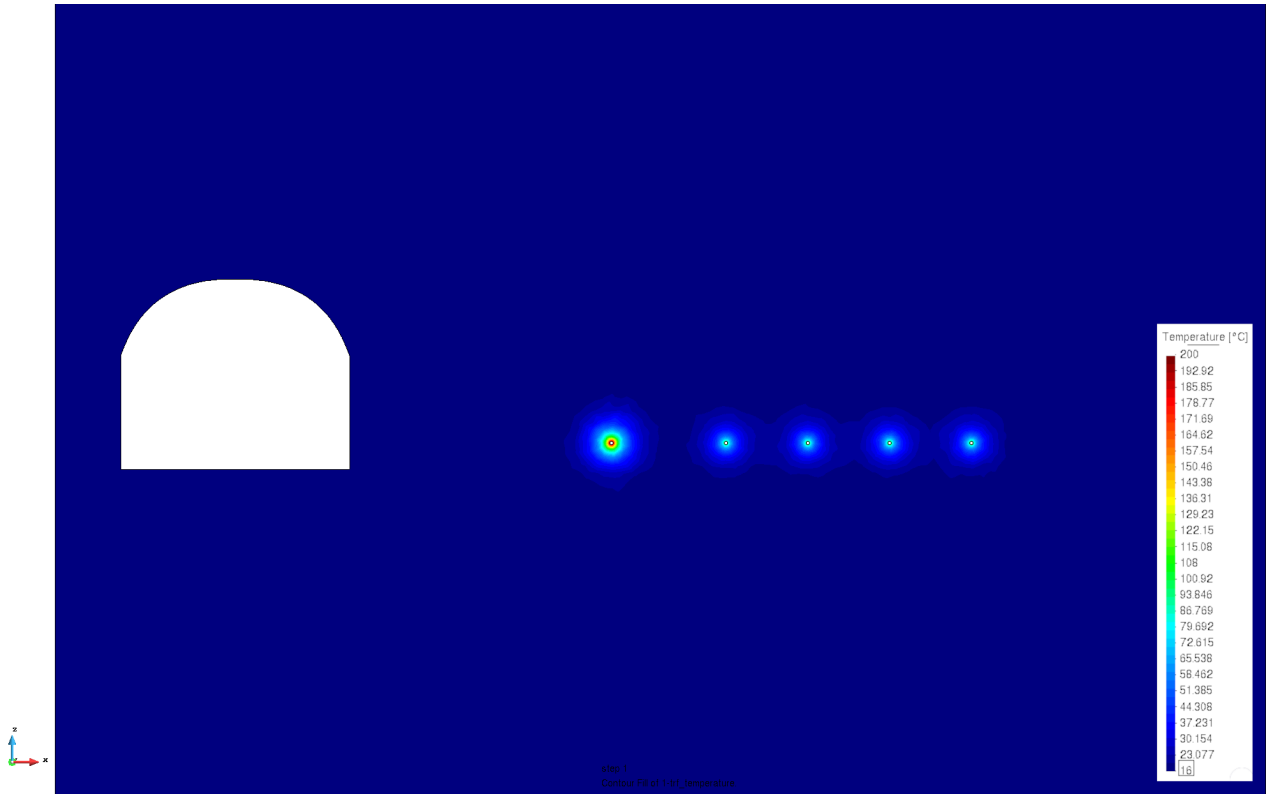

Figure 5.10: Detail of temperature distribution after one day around the heated PMs in °C.

animated temperature results found no rise in temperatures after three years of simulation. Heat is transferred mainly by conduction in the rock mass. Convection and radiation in the test chamber are not assumed in the model. A slight temperature elevation is registered on the floor, over and around the test chamber. The notable increase in temperatures is happening in the first year of computation. The calculated heating powers 2382 W and 5027 W were necessary for the start phase of the heating process to warm up PMs to temperatures 100°C and 200°C, respectively. For the subsequent temperatures maintenance, the heating powers 587 W and 1504 W were required.

Model validation

An augmented numerical model was created to check material parameters obtained from samples taken from the rock mass and to support the presumed minor influence of the elevated temperatures on the unheated physical models. This model comes out from the previous 3D model with

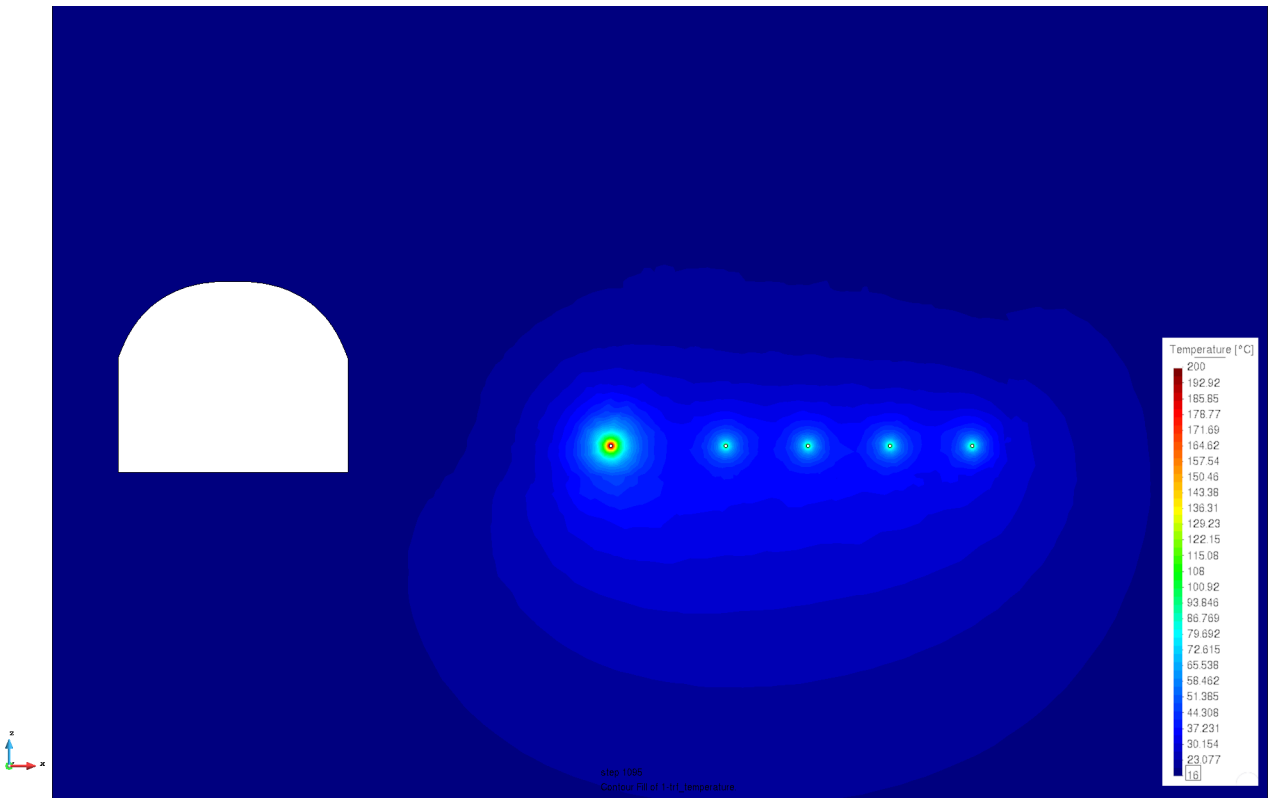

Figure 5.11: Detail of temperature distribution after three years around the heated PMs in °C.

horizontal heated PMs. The initial and boundary conditions were mainly improved based on the measured data. The initial temperature was set to 13.8°C. The external temperatures in the test chamber and in the main gallery were improved concerning measurements. Values for heaters were taken directly from thermometers on the heater-bentonite interface of each PM. The Dirichlet boundary conditions in PM boreholes were changed to Newton's heat transfer conditions. The heat transfer parameter $\beta = 18.2$ W$\cdot$ m$^{-2}\cdot$ K^{-1} was optimized from a simple 1D analysis in order to match temperatures in sensors on the bentonite-rock interface [Krejčí et al., 2019]. The model geometry was not changed. Only the finite element mesh, which has 308121 nodes and 1607404 tetrahedral elements, was generated and refined around PMs (Figure 5.12).

Figure 5.13 illustrates the temperature profile in the rock mass of the PMs section in the depth of 1m in time 230 days from the measurement onset, which was 11/02/2019 at 8:10 am. Figure 5.14 shows temperature around the PM1 also in 230 days. The computed and measured temperatures for the selected thermometers always in depths 1 m and 2 m are depicted in Figures 5.15 to 5.17. The differences between 1°C to 6°C validate the correct setup of initial and boundary conditions derived from the in situ measured data. Results analysis verifies the negligible effect of rock mass warming in the area of unheated PMs, which is also supported by measurements.

5.4.2 THM model of physical model No. 4 (100 °C)

The second part of the THM analysis concentrates on detailed models of two selected PMs, No. 4 heated to 100°C and No. 5 heated to 200°C. These models simulate only the cartridges inserted

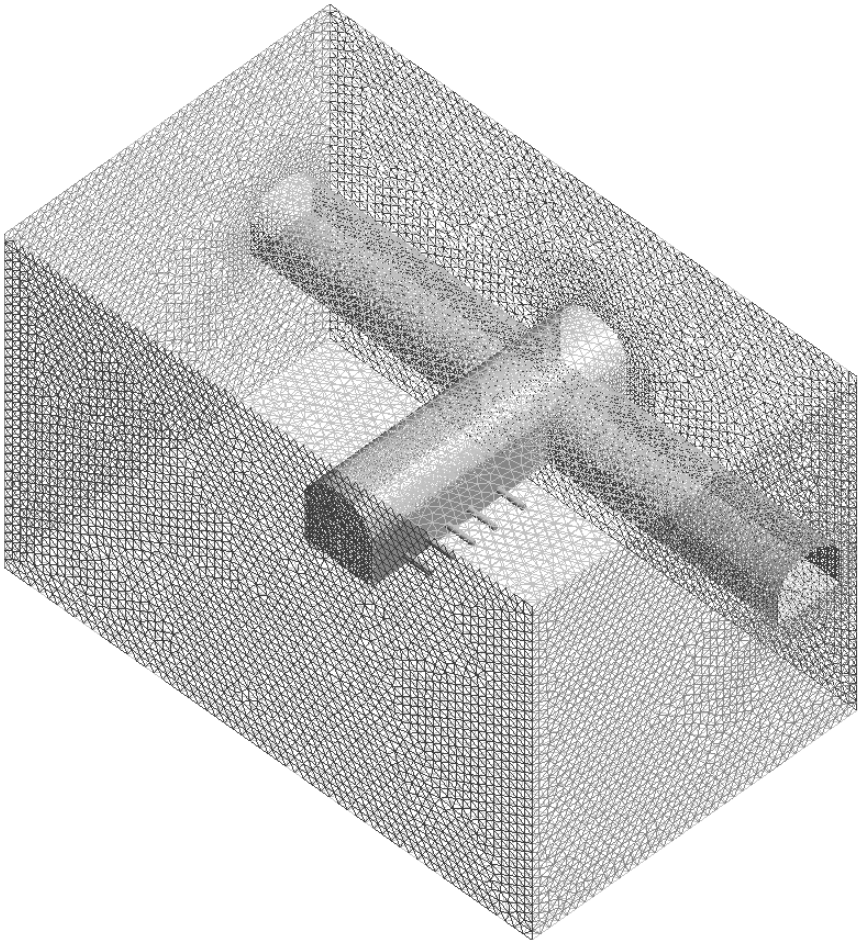

Figure 5.12: Finite element mesh of augmented 3D model of the rock mass.

into the stiff surrounding rock, see Figure 5.18. The finite element mesh discretizes only one upper half of bentonite and concrete plugs on both sides as an axisymmetric domain with the horizontal axis of symmetry in the heater, which was not modeled. Bentonite material was modeled by the complex hypoplastic model (Sec. 5.1). While the concrete was modeled only as an elastic material with thermal dilatation effect in mechanical part and as a fully saturated material enabling the only heat conduction in transport part. The finite element mesh built in the GiD academic version consists of 8163 nodes and 2620 quadrilateral axisymmetric elements with linear approximation functions in the transport part and quadratic in the mechanical part. Boundary conditions were set as Dirichlet with temperature interpolated and extrapolated from thermometers data on both interfaces heater-bentonite (denoted 4.13 and 4.13) and bentonite-rock (denoted 4.11 and 4.12) which is illustrated by Figure 5.19. The watering process was modeled as a prescribed pore water pressure on the whole external surface on the bentonite-rock interface (sensor 4.51). The initial temperature was set to 13.8°C, initial pore water pressure was set to -100 MPa corresponding to a suction negative value, and gas pore pressure was equal to ambient air pressure 101 kPa. The initial porosity was set according to the initial dry density 1600 kg/m^3 for bentonite blocks. The computation simulates 230 days of running experiment starting also at 11/02/2019 at 8:10 am. According to the hypoplastic model implementation (Sec. 5.3) as an individual material module in

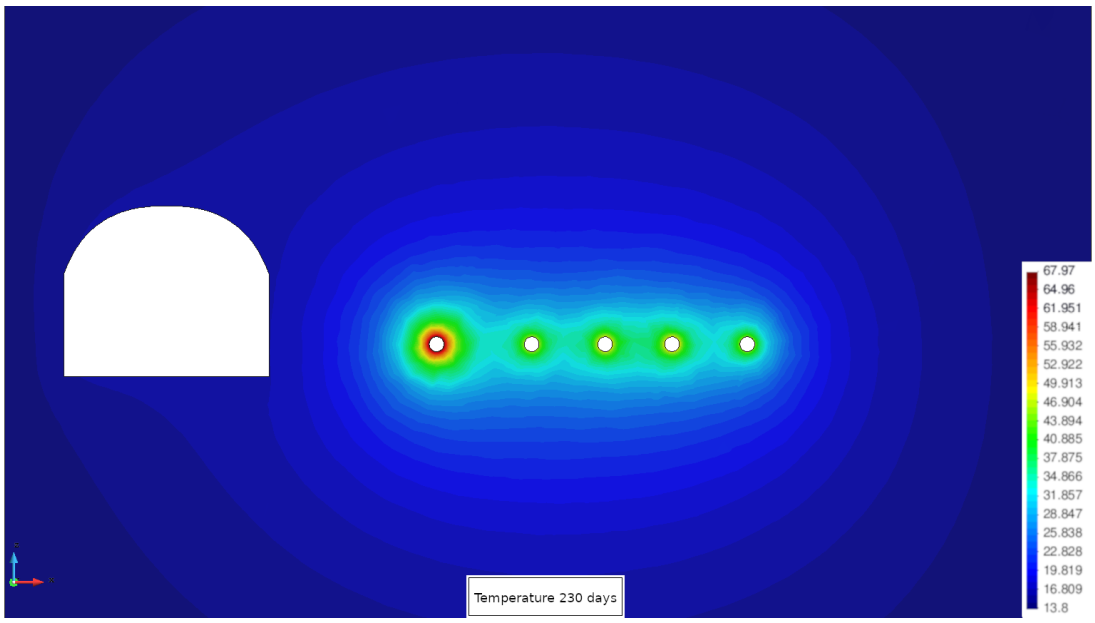

Figure 5.13: Temperature profile in the vertical section after 230 days in °C.

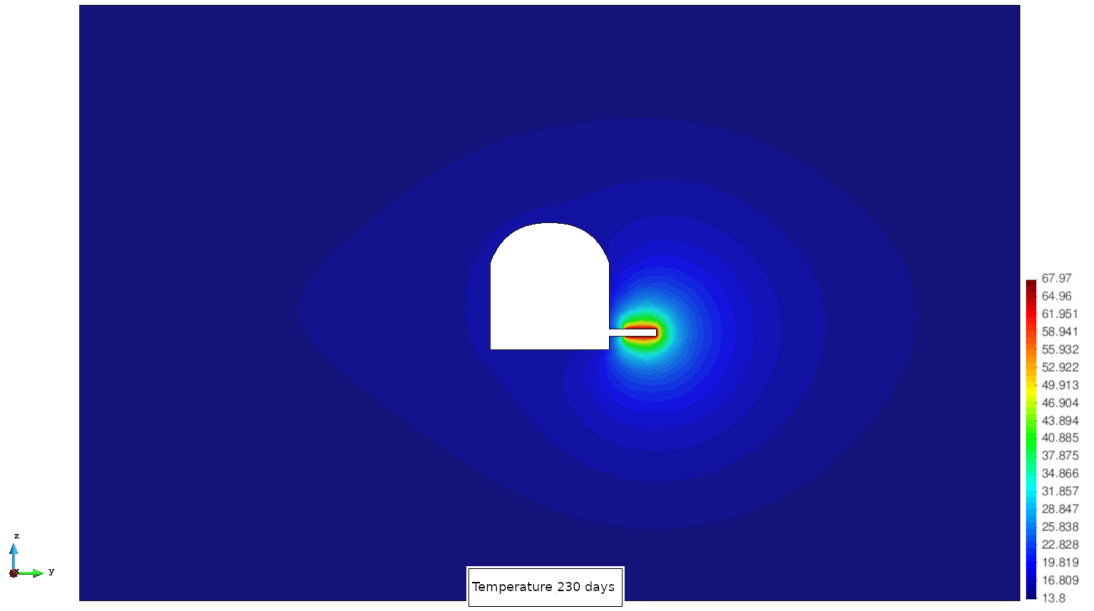

Figure 5.14: Temperature profile in the vertical section of the borehole PM5 after 230 days in °C.

the MEFEL part, the staggered algorithm scheme solves the non-linear system of Equations (5.118) in transport part

$$\begin{pmatrix} \boldsymbol{K}_{ww} & \boldsymbol{K}_{wg} & \boldsymbol{K}_{wT} \\ \boldsymbol{K}_{gw} & \boldsymbol{K}_{gg} & \boldsymbol{K}_{gT} \\ \boldsymbol{K}_{Tw} & \boldsymbol{K}_{Tg} & \boldsymbol{K}_{TT} \end{pmatrix} \begin{pmatrix} \boldsymbol{d}_w \\ \boldsymbol{d}_g \\ \boldsymbol{d}_T \end{pmatrix} + \begin{pmatrix} \boldsymbol{C}_{ww} & \boldsymbol{C}_{wg} & \boldsymbol{C}_{wT} \\ \boldsymbol{C}_{gw} & \boldsymbol{C}_{gg} & \boldsymbol{C}_{gT} \\ \boldsymbol{C}_{Tw} & \boldsymbol{C}_{Tg} & \boldsymbol{C}_{TT} \end{pmatrix} \begin{pmatrix} \dot{\boldsymbol{d}}_w \\ \dot{\boldsymbol{d}}_g \\ \dot{\boldsymbol{d}}_T \end{pmatrix} = \begin{pmatrix} \boldsymbol{f}_w \\ \boldsymbol{f}_g \\ \boldsymbol{f}_T \end{pmatrix},$$

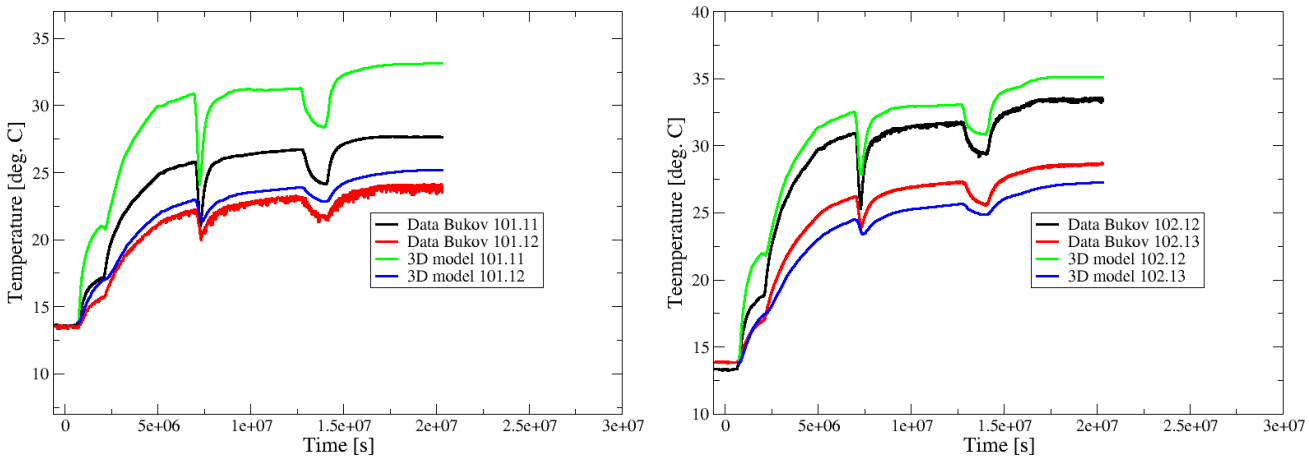

Figure 5.15: Temperature history in borehole No. 1 - sensors No. 101.11 and 101.12 (left), and in borehole No. 2 - in sensors No. 102.12 and 102.13 (right).

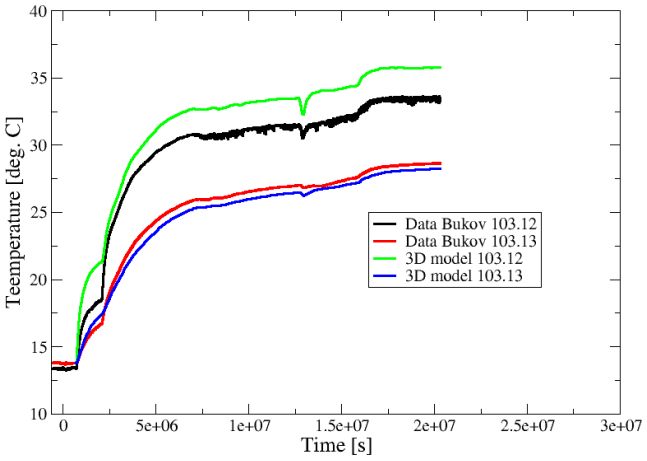

Figure 5.16: Temperature history in borehole No. 3 - sensors No. 103.12 and 103.13.

and the system of Equations (2.30) in the incremental form in mechanical part:

$$\boldsymbol{K}_u \Delta \boldsymbol{d}_u = \Delta \boldsymbol{f}_{ext} + \Delta \boldsymbol{f}_0.$$

Material parameters for the transport part with the coupled hygro-thermal model are listed in Table 5.2 and the mechanical part with the hypoplastic model in Table 5.3. The following figures illustrate the results of selected quantities in the bentonite material. Figures 5.20 and 5.21 show profiles of temperature, saturation, and pore pressure. Horizontal and radial stresses are depicted in Figure 5.22. It can be seen that the bentonite barrier is fully saturated after 160 days. The maximal horizontal and radial stresses are around 3500 kPa, appropriate to swelling pressure obtained for bentonite material with dry density 1600 kg/m^3. The comparison of temperature history in the location of selected thermometers depicted in Figure 5.23 shows good agreement

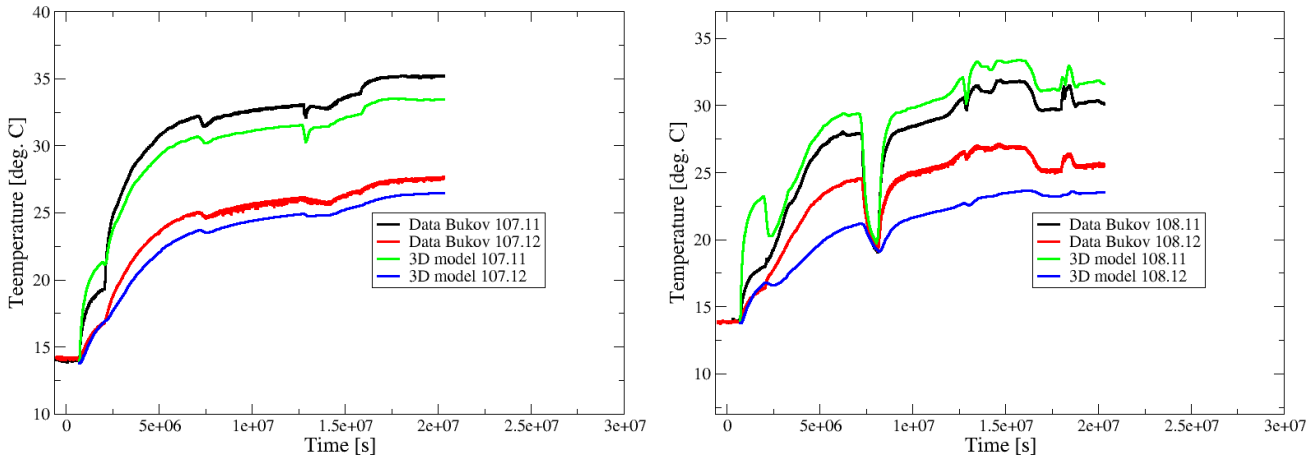

Figure 5.17: Temperature history in borehole No. 7 - sensors No. 107.11 and 107.12 (left), and borehole No. 8 - sensors No. 108.11 and 108.12 (right).

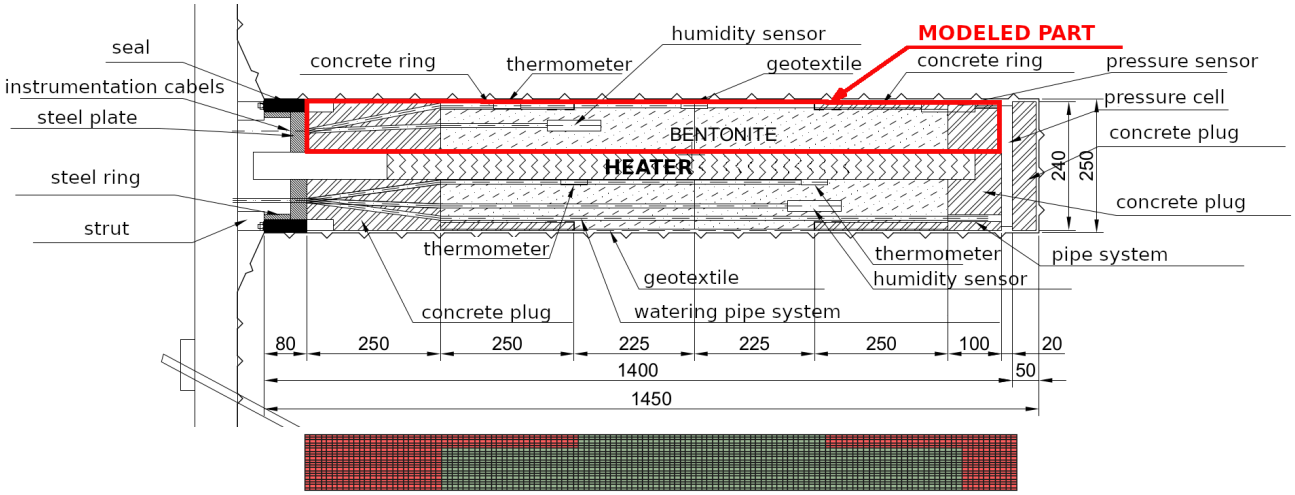

Figure 5.18: Geometry of the physical model No. 4 (up), and finite element mesh of the numerical model (down).

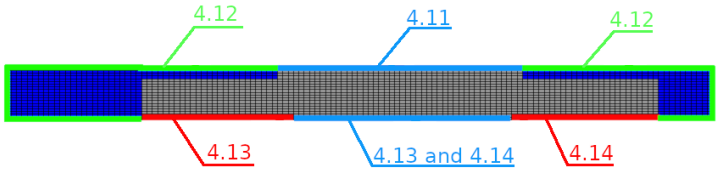

Figure 5.19: Scheme of thermometers included to boundary conditions.

between computed and measured values. It should be pointed out, resulting temperatures come from average data from temperature sensors placed on opposite sides. Time evolutions of satura-

Parameter	Description	Value
n_0	initial porosity	0.4425
k_{intr}	intrinsic permeability	$1.0{\cdot}10^{-20}$ m^2
K^w	hydraulic conductivity (corresponding to intrinsic permability)	$1.0{\cdot}10^{-13}$ m$\cdot$s^{-1}
ρ_s	skeleton volume weight	2870 kg/m^3
ρ_d	dry density	1600 kg/m^3
C_{eff}	Effective specific heat	1000.0 J$\cdot$kg$^{-1}\cdot$K^{-1}
λ_{dry}	Dry effective thermal conductivity	0.6 W$\cdot$m$^{-1}\cdot$K^{-1}
λ_{wet}	Wet effective thermal conductivity	1.35 W$\cdot$m$^{-1}\cdot$K^{-1}

Table 5.2: Parameters of the bentonite material for transport part.

tion degree and horizontal stress are in Figure 5.24. In comparison with measurements, computed saturation degree has slower growth. A jump growth of in situ data can be explained by faster water convection between pellets and bentonite blocks, while the numerical model assumes homogeneous material. The horizontal pressure computed from reactions in the left side nodes reaches the maximal value of 3000 kPa, which is much higher than the measured value of about 850 kPa in the pressure cell (Figure 5.24) It leads to the decision that initial dry density $\rho_d = 1600$ kg/m^3 is somewhat overrated in the analysis.

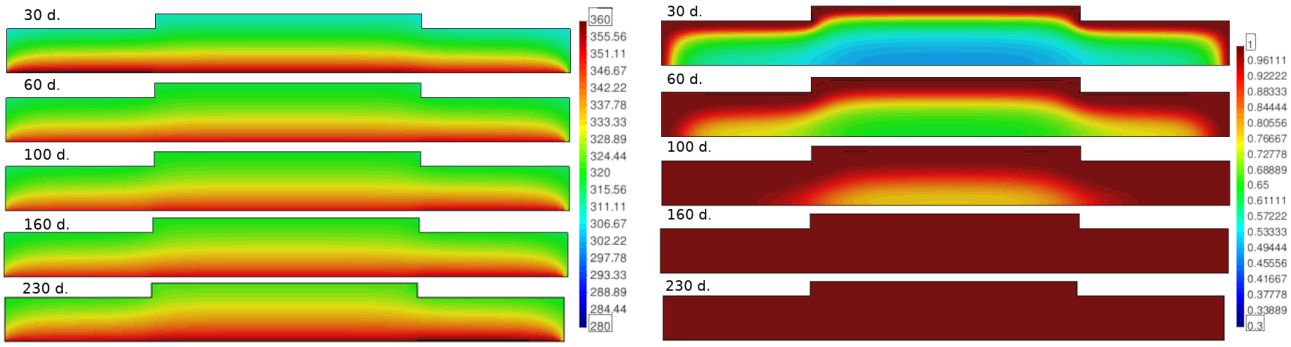

Figure 5.20: Temperature [in Kelvins] (left) and saturation (right) profiles in model No. 4.

5.4.3 THM model of physical model No. 5 (200 °C)

The hot PM No. 5 is modeled in the same manner as PM No. 4. In this case, the boundary conditions for temperature are taken from thermometers 5.11 to 5.13 located in the same positions. The watering of this PM is similar, and the pore pressure values are taken from sensor 5.51. Results of the computation are presented in the same way as in the previous analysis. Unfortunately, the comparison of measured and computed horizontal pressure is missing due to the damage of pressure cells caused by high temperatures. For this PM, there is observed a little slower saturation process than in previous PM No. 4. The fully saturation state is reached later than in 160 days. Horizontal and radial stresses have nearly the same profiles and maximal values of

Parameter	Description	Value
φ_c	Critical state friction angle of macrostructure in a standard soil-mechanics context	25°
λ^*	Slope of isotropic normal compression line in $\ln(p^M/p_r)$ versus $\ln(1+e)$ space	0.13
κ^*	Macrostructural volume strain in p^M (unloading)	0.06
N	Position of isotropic normal compression line in $\ln(p^M/p_r)$ versus $\ln(1+e)$ space	1.73
ν	Parameter controlling stiffness in shear	0.25
n_s	Dependency of position of isotropic normal compression line on suction	0.012
l_s	Dependency of slope of isotropic normal compression line on suction	-0.005
n_T	Dependency of position of isotropic normal compression line on temperature	-0.07
l_T	Dependency of slope of isotropic normal compression line on temperature	0.0
m	(1) Control of and thus dependency of wetting-heating-induced compaction on distance from state boundary surface; (2) control of double-structure coupling function and thus response to wetting-drying and heating-cooling cycles[Mašín, 2013]	1.0
α_s	Dependency of microstructural volume strains on temperature	0.00015 K^{-1}
κ_m	Dependency of microstructural volume strains on p^m	0.07
e^m_{r0}	Reference microstructural void ratio for reference temperature T_r reference suction s_r, and zero total stress	0.45
c_{sh}	Value of f_m for compression	0.002
s_{e0}	Air-entry value of suction for reference macrostructural void ratio e^M_0	-2700 kPa
a	Dependency of macrostructural air-entry value of suction on temperature	0.118 $N{\cdot}m^{-1}$
b	Dependency of macrostructural air-entry value of suction on temperature	-0.000154 $N{\cdot}m^{-1}{\cdot}K^{-1}$
a_e	Ratio of air entry and air expulsion values of suction for macrostructure water retention model	1.0
s_r	Reference suction for e^m_{r0}	-2000.0 kPa
e^M_0	Reference macrostructural void ratio for air-entry value of suction of macrostructure	0.7
T_r	Reference temperature	286 K

Table 5.3: Parameters of the bentonite material for mechanical part [Mašín, 2017].

about 3500 kPa. Figures 5.25 and 5.26 illustrate profiles of temperature, saturation, and pore pressure. Horizontal and radial stresses are depicted in Figure 5.27. The history of temperature, pore pressure, and saturation degree in selected sensors represents graphs in Figures 5.28 and 5.29.

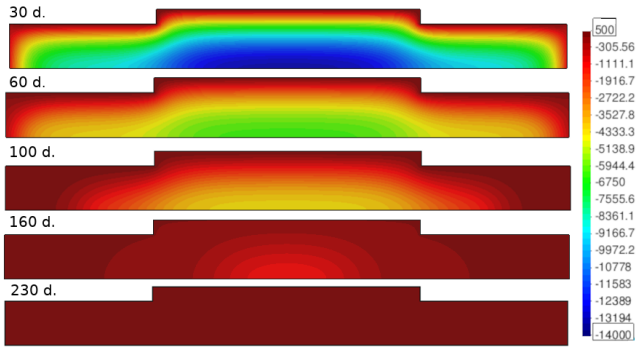

Figure 5.21: Pore pressure profile in model No. 4 [kPa].

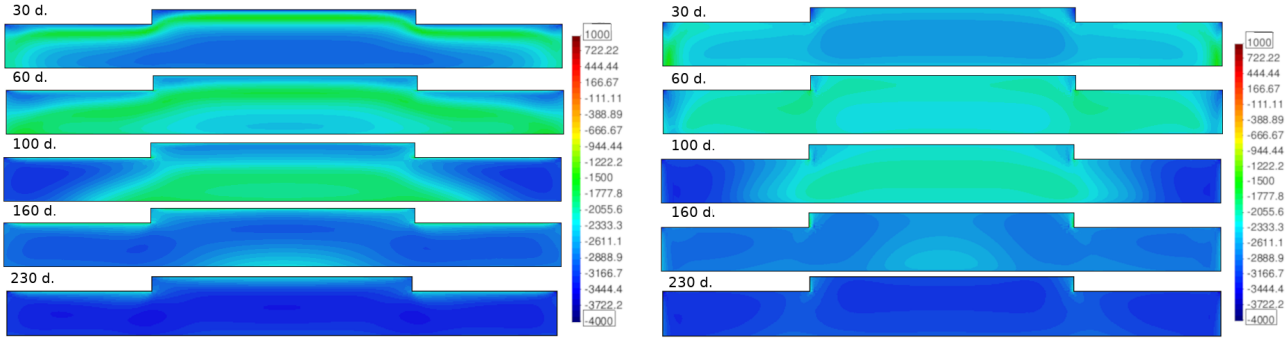

Figure 5.22: Horizontal stress (left) and radial stress (right) profiles in model No. 4 [kPa].

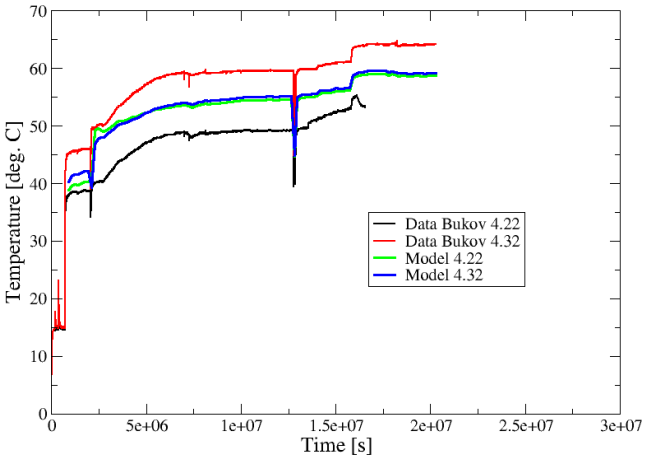

Figure 5.23: Temperature history in sensors No. 4.22 and 4.32.

The differences between computation and measurements are obvious, mainly for pore pressure. While the computation shows a gradual saturation process in homogenous material, the moisture sensor (piezometer) cannot measure negative values of pore pressure. Moreover, the watering process can also be strongly influenced by fast water convection in voids and gaps between pellets

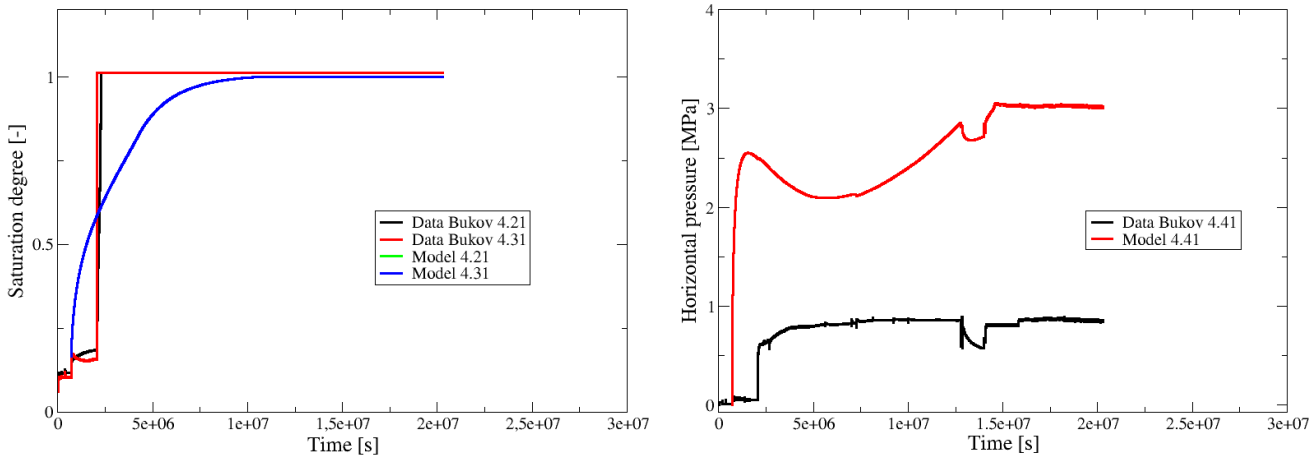

Figure 5.24: Saturation degree history in sensors No. 4.21 and 4.31 (left) and horizontal pressure history in sensor No. 4.41 (right).

and bentonite blocks.

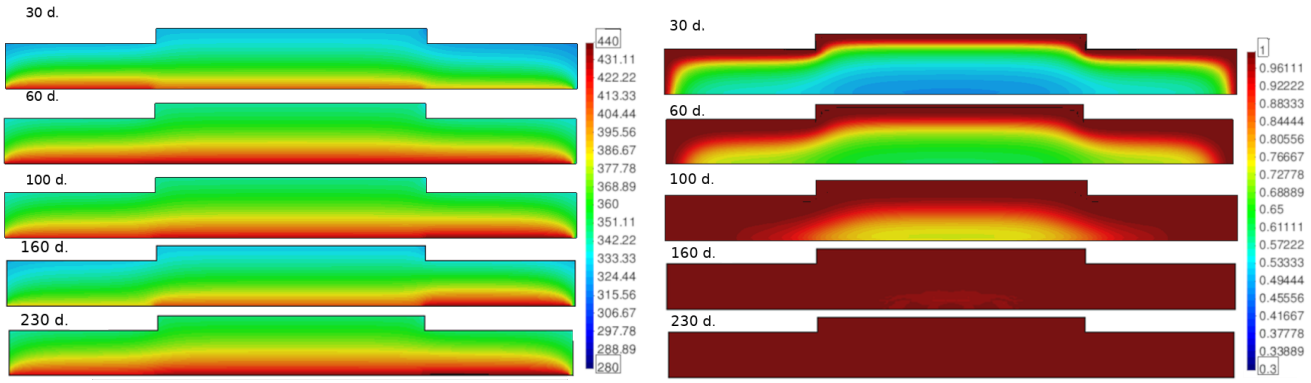

Figure 5.25: Temperature [in Kelvins] (left) and saturation (right) profiles in model No. 5.

5.4.4 Validation of THM model of physical model No. 4 (100 °C) and parametrical study

The presented simulations show significant differences versus measured data in the initial watering phase, where the measurements have a faster saturation increase. However, the significant disparity is evident in horizontal pressure, which is overestimated in the numerical model. The attained level of swelling pressure can be affected by the initial dry density and permeability values. For this purpose, the parametric study with various setups (Table 5.4) was performed for PM No. 4. In this section, the parametrical study aimed to validate material parameters and to obtain responses closer to experimental measurements. Selected results of computer simulations with various combinations of dry density, ρ_d, and hydraulic conductivity, K^w, are then presented

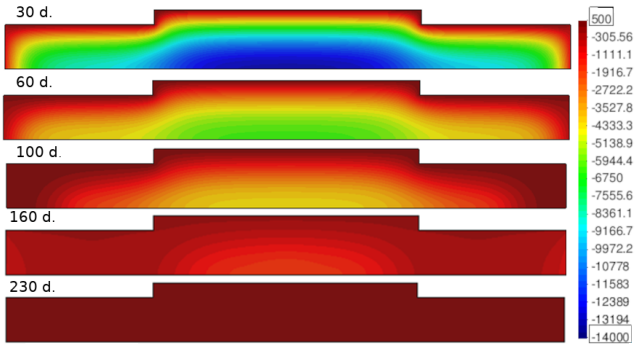

Figure 5.26: Pore pressure profile in model No. 5 [kPa].

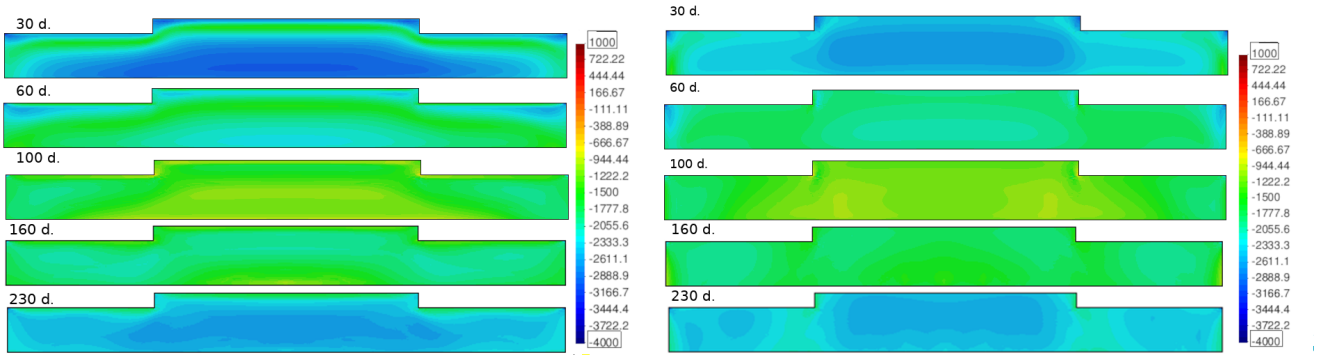

Figure 5.27: Horizontal stress (left) and radial stress (right) profiles in model No. 5 [kPa].

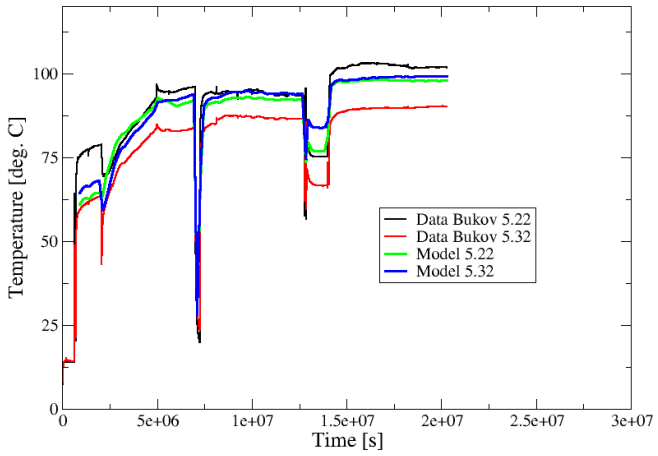

Figure 5.28: Temperature history in sensors No. 5.22 and 5.32.

in Figure 5.30. The main criterion for comparison is the horizontal pressure (swelling pressure) and the history of saturation degree. It is evident the last combination gives the best match to the measurements in PM4, where the dry density was determined $\rho_d = 1371$ kg/m^3.

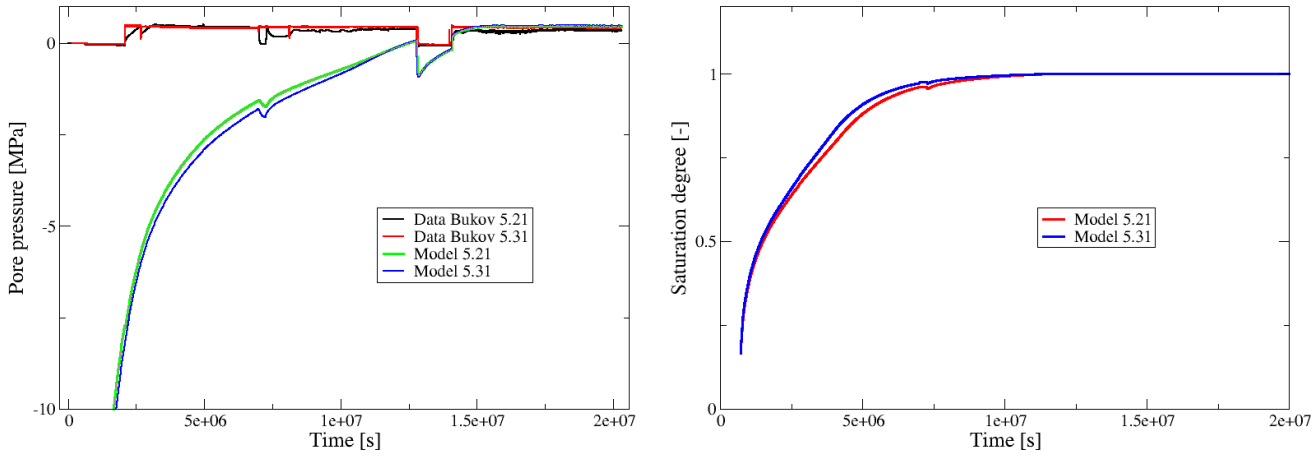

Figure 5.29: Pore pressure history in sensors No. 5.21 and 5.31 (left) and computed saturation degree history (right).

	Dry density ρ_d [kg/m^3]	Hydraulic conductivity K^w [m·s^{-1}]
1.	1600	$1.0{\cdot}10^{-13}$
2.	1500	$3.75{\cdot}10^{-13}$
3.	1400	$5.0{\cdot}10^{-13}$
4.	1300	$7.75{\cdot}10^{-13}$
5.	1300	$2.0{\cdot}10^{-12}$

Table 5.4: Combinations of material parameters for the parametric study.

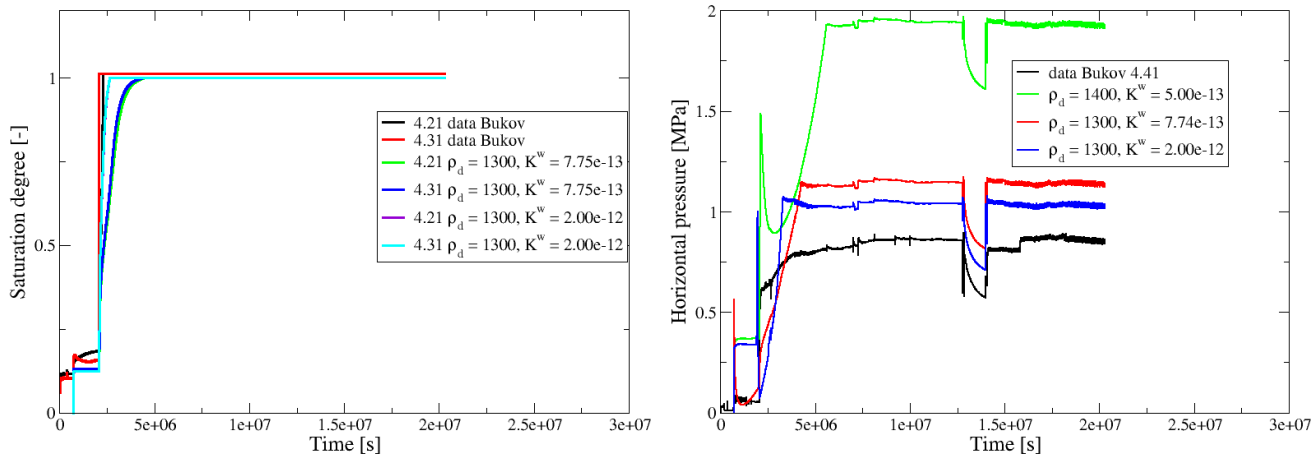

Figure 5.30: Saturation degree history in sensors No. 4.21 and 4.31 (left) and horizontal pressure history in sensor No. 4.41 (right).

5.4.5 Conclusions about THM model of Interaction experiments at the Bukov URF

In the first phase, the aim of the thermo-hygro-mechanical model of interaction experiments at the Bukov URF was to verify the thermal influence of heated physical models to unheated models located on the opposite side of the test chamber. The heat transfer analysis proved no significant thermal influence. It was concluded slow warming of surrounding rock mass and slight temperature increase around unheated PMs. This fact was also supported by a model validation against in situ measurements with improved boundary conditions. Moreover, the setup of correct material parameters was validated.

The second phase of the THM model was the computational prediction of the physical models' behavior. The numerical analysis was solved as a coupled thermo-hygro-mechanical problem by staggered algorithm combining the hypoplastic model for expansive soils in mechanical part and the micromechanical based model of hygro-thermal transfer in a porous medium in transport part. The experiment was modeled as an axisymmetric domain. The computation with the initial material parameters setup gives results differing in the initial phase of watering in the saturation rate and the reached value of swelling pressure. This effect is explained by the fact that the mathematical model assumes homogeneous and isotropic material, whereas the physical model contains voids and gaps between pellets and bentonite blocks. The following model validation against in situ measurements better captures the effects mentioned above. The evolution and temperature profiles are simulated very well, as well as the reached steady state with jumps in values connected with outages of experiments. Conclusions made from numerical simulations provide valuable information not only for the setup of the numerical model but mainly for the production of the physical model, which brings several uncertainties. It can be stated, the numerical model using the hypoplastic model for expansive soils in connection with the micromechanical-based approach for hygro-thermal transport appears to be very promising in modeling interaction experiments and engineered barriers [Krejčí et al., 2020].

Chapter 6

Conclusions

This thesis was motivated by the research in coupled thermo-hygro-mechanical problems and their applications to real structures and practical issues. The work presented two primary approaches of the coupled problem solution, fully coupled algorithm and partially coupled system with the staggered algorithm. The main principles were explained by the simple thermo-mechanical problem and its discretisation by the finite element method. These coupled algorithms were implemented into the open-source computer code SIFEL (Simple Finite Elements), which architecture was briefly described. The implementation was illustrated by three selected numerical analyses created in collaboration with the partner industrial companies and institutions. The presented studies were performed from the multiphysics point of view. Therefore, each study described used material models and approaches and their combinations in the final model. Moreover, the results of the analyses were discussed and validated against in situ measurements.

The first analysis dealt with the thermo-mechanical simulation of the behavior of the nuclear power plant containment. The reliability and durability of reactor containments depend directly on the prestressing system. General results from in situ measurements during the operation showed the increase of deformations and the increase of prestress losses since the onset of service. Most measurements also indicated that the temperature has a significant influence on the prestress losses. The containment was studied under cyclic temperature loading during service life when stages of service and planned stops are changed. An advanced two-level model was used for predicting the prestress losses and the structure response. The global macro-level model aimed to model the evolution of prestress forces changed by the temperature and climatic loading. Consequently, the local meso-model was created, and it was loaded by the mechanical and thermal loading from the global model. The staggered coupled thermo-mechanical analysis was the local model's main part, which had to explain the time-dependent processes in the containment wall. The core of the used mechanical model consists of Bažant's B3 creep model based on the microprestress-solidification theory with ageing effect influenced by moisture and temperature changes. The original discrete model was extended by continuous retardation spectrum due to speed up the computation. The creep model was supplemented with the damage model in the isotropic and orthotropic formulation. The combination of models was achieved under the assumption of small strains when the additive strain decomposition was adopted. The heat transfer analysis run in parallel with the mechanical analysis. The analysis results obtained from the connection of the simplified global model and the local model showed relatively good coincidence with in situ measurements. The explanation of the increase of radial strains and decrease of tendon forces since the onset of service was based on the theoretical knowledge in concrete

creep influenced by the temperature changes and partly on the prestress losses measurements. The influence of the temperature on the mechanical response during the service was proved.

The second analysis concerned the thermo-hygro-mechanical analysis of climatic conditions' impact on the current state of Charles bridge. For this purpose, Künzel and Kiessl's phenomenological model suitable for structures under the typical conditions was described and used in the analysis. The model can be used right for the study of building structures under the standard climatic conditions, and its parameters can be simply determined from laboratory measurements. The final model was completed by the orthotropic damage model, which is suitable for three-dimensional analyses of quasi-brittle materials like concrete and masonry influenced by temperature and moisture changes. Homogenized and averaged material parameters were used for the masonry. The staggered algorithm was also used for this partially coupled thermo-hygro-mechanical analysis. This analysis aimed to obtain a notion about the current mechanical state of the Charles bridge. The results presented could serve as a severe basis for providing a reliable estimate of real states of stress and damage in Charles bridge. It was shown that climatic loading is the most serious for stone bridges as it is responsible for the nucleation and further development of cracks. The results analysis concluded that shear stresses due to the temperature differences between the upper and lower parts of the parapets and the vertical movements of the vaults lead to the ultimate damage in the horizontal joint and the need for a complete repair of parapets. Fortunately, it seems the damage state and cracks evolution do not influence the stability and bearing capacity of the bridge distinctly.

The last analysis dealt with the thermo-hygro-mechanical analysis of interaction experiments, physical models (PMs) at the Bukov Underground Research Facility in the Czech Republic. In the first phase, the goal of the analysis was to verify the thermal influence of heated physical models on unheated models located on the opposite side of the test chamber. The heat transfer analysis proved no significant thermal influence. It was concluded slow warming of surrounding rock mass and slight temperature increase around unheated PMs. A numerical model validation also supported it against in situ measurements with improved boundary conditions. The second phase of the THM analysis was the computational prediction of the physical models' behavior. The well-instrumented physical models simulating a bentonite barrier in a radioactive waste repository were installed in the test chamber of the host rock mass. For the solution, the coupled heat and moisture transfer based on micromechanical approaches of porous media was selected. It is suitable, e.g., for simulation of soils or concrete structures exposed to fire. This model was described in detail and extended by the influence of volume changes on the water retention curve. The bentonite behavior was described by the complex hypoplastic model for expansive clays presented in [Mašín, 2017]. The staggered algorithm also solved the numerical analysis as a coupled thermo-hygro-mechanical problem. The PMs were modeled as axisymmetric domains. Results of the analysis were also subsequently validated against in situ measurements. The evolution and temperature profiles were simulated very well, and they reached a steady state with jumps in values connected with outages of experiments. Conclusions made from numerical simulations provide valuable information not only for the setup of the numerical model but mainly for the production of the physical model, which brings several uncertainties. It can be stated, the numerical model using the hypoplastic model for expansive soils in connection with the micromechanical-based approach for hygro-thermal transport appears to be very promising in modeling interaction experiments and engineered barriers.

All results were obtained with the help of the in-house open-source FEM software SIFEL, which is based on the modular architecture enabling the solution of mechanical and transport, hygro-

thermal, problems. For the coupled thermo-hygro-mechanical problems, two basic algorithms were implemented, the staggered algorithm for partially coupled problems and the fully coupled algorithm for complex coupled problems, respectively. Despite the complexity of the fully coupled scheme, the staggered algorithm is preferred to solve the real issues. This fact is supported by the analyses presented in this thesis, where the used mathematical models were developed individually. They were extended and combined in the staggered scheme, which is easier and more effective for computer implementation. However, the derivation and development of the fully coupled approach is still a big challenge for the author for future work.

Appendix A

Variational formulation and FE solution

A.1 Extended saturated-unsaturated non-isothermal air and water flow model for deforming soil medium

The discretization of mass and energy conservation equations (5.109) to (5.111) via the finite element method is derived in this appendix. For this purpose, the final balance equations with initial and boundary conditions are summarized again:

Mass conservaton of dry air

$$\begin{aligned} S_g \mathrm{div}\boldsymbol{v}^s - \beta_s(1-n)S_g\frac{\partial T}{\partial t} - n\frac{\partial S_w}{\partial t} + \frac{nS_g}{\rho^{ga}}\frac{\partial}{\partial t}\left(\frac{M_a}{TR}p^{ga}\right) \quad + \\ \frac{1}{\rho^{ga}}\mathrm{div}\left[\rho^g\frac{M_aM_w}{M_g^2}\boldsymbol{D}_g\mathrm{grad}\left(\frac{p^{gw}}{p^g}\right)\right] + \frac{1}{\rho^{ga}}\mathrm{div}\left[\frac{k^{rg}\boldsymbol{k}\rho^{ga}}{\mu^g}\left(-\mathrm{grad}p^g + \rho^g\boldsymbol{g}\right)\right] \quad = \quad 0. \end{aligned} \tag{A.1}$$

Mass conservaton of water species - liquid water and vapor

$$\begin{aligned} \left(\rho^w S_w + \rho^{gw}S_g\right)\mathrm{div}\boldsymbol{v}^s - \beta_{swg}\frac{\partial T}{\partial t} \quad + \\ +(\rho^w + \rho^{gw})n\frac{\partial S_w}{\partial t} + nS_g\frac{\partial}{\partial t}\left(\frac{M_w}{TR}p^{gw}\right) + \mathrm{div}\left[-\rho^g\frac{M_aM_w}{M_g^2}\boldsymbol{D}_g\mathrm{grad}\left(\frac{p^{gw}}{p^g}\right)\right] \quad + \\ +\mathrm{div}\left[\frac{k^{rg}\boldsymbol{k}\rho^{gw}}{\mu^g}\left(-\mathrm{grad}p^g + \rho^g\boldsymbol{g}\right)\right] + \mathrm{div}\left[\frac{k^{rw}\boldsymbol{k}\rho^w}{\mu^w}\left(-\mathrm{grad}p^w + \rho^w\boldsymbol{g}\right)\right] \quad = \quad 0. \end{aligned} \tag{A.2}$$

Enthalpy conservation equation of the multiphase medium

$$\begin{aligned} \left(\rho C_p\right)_{\mathrm{eff}}\frac{\partial T}{\partial t} + n\rho^w C_p^w\frac{k^{rw}\boldsymbol{k}\rho^w}{\mu^w}\left(-\mathrm{grad}p^w + \rho^w\boldsymbol{g}\right)\cdot\mathrm{grad}T \quad + \\ +n\rho^g C_p^g\frac{k^{rg}\boldsymbol{k}\rho^{gw}}{\mu^g}\left(-\mathrm{grad}p^g + \rho^g\boldsymbol{g}\right)\cdot\mathrm{grad}T \quad + \\ -\mathrm{div}\left(\boldsymbol{\lambda}_{\mathrm{eff}}\mathrm{grad}T\right) \quad + \\ +\Delta H_{\mathrm{vap}}\left(-\alpha S_w\rho^w\mathrm{div}\boldsymbol{v}^s + \rho^w\beta_{sw}\frac{\partial T}{\partial t} - \rho^w n\frac{\partial S_w}{\partial t} - \mathrm{div}\left[\frac{k^{rw}\boldsymbol{k}\rho^w}{\mu^w}\left(-\mathrm{grad}p^w + \rho^w\boldsymbol{g}\right)\right]\right) \quad = \quad 0. \end{aligned} \tag{A.3}$$

Linear momentum balance equation of the multiphase medium

$$\operatorname{div}\left(\boldsymbol{\sigma}^{\mathrm{eff}} - \alpha(S_w p^w + S_g p^g)\boldsymbol{m}^{\mathrm{T}}\right) + \rho\boldsymbol{g} = 0. \tag{A.4}$$

Initial conditions at time $t = 0$

$$\boldsymbol{u} = \boldsymbol{u}_0, \qquad p^w = p_0^w, \qquad p^g = p_0^g, \qquad T = T_0, \qquad \text{in } \Omega \text{ and on } \Gamma, \tag{A.5}$$

Boundary conditions of type I

$$\begin{aligned} \boldsymbol{u} &= \boldsymbol{u}_0, && \text{on } \Gamma_u, \\ \boldsymbol{n}\boldsymbol{\sigma} &= \boldsymbol{t}, && \text{on } \Gamma_t, \\ p^w &= \overline{p}^w, && \text{on } \Gamma_w, \\ p^g &= \overline{p}^g, && \text{on } \Gamma_g, \\ T &= \overline{T}, && \text{on } \Gamma_T, \end{aligned} \tag{A.6}$$

Boundary conditions of type II

$$\begin{aligned} J^{ga} &= \left[\frac{k^{rg}\boldsymbol{k}\rho^{ga}}{\mu^g}\left(-\mathrm{grad}p^g + \rho^g\boldsymbol{g}\right) + \rho^g\frac{M_a M_w}{M_g^2}\boldsymbol{D}_g\mathrm{grad}\left(\frac{p^{gw}}{p^g}\right)\right]\cdot\boldsymbol{n}, && \text{on } \Gamma_{qg}, \\ J^w &+ J^{gw} + \beta(\rho^{gw} - \rho_\infty^{gw}) = \left[\frac{k^{rw}\boldsymbol{k}\rho^w}{\mu^w}\left(-\mathrm{grad}p^w + \rho^w\boldsymbol{g}\right)\right]\cdot\boldsymbol{n} \\ &+ \left[\frac{k^{rg}\boldsymbol{k}\rho^{gw}}{\mu^g}\left(-\mathrm{grad}p^g + \rho^g\boldsymbol{g}\right)\right]\cdot\boldsymbol{n} - \left[\rho^g\frac{M_a M_w}{M_g^2}\boldsymbol{D}_g\mathrm{grad}\left(\frac{p^{gw}}{p^g}\right)\right]\cdot\boldsymbol{n}, && \text{on } \Gamma_{qw}, \\ q^T &+ \beta_T(T - T_{ext}) + e\sigma_0(T^4 - T_\infty^4) = \left[-\boldsymbol{\lambda}_{\mathrm{eff}}\mathrm{grad}T\right]\cdot\boldsymbol{n} \\ &+ \left[\frac{k^{rw}\boldsymbol{k}\rho^w}{\mu^w}\left(-\mathrm{grad}p^w + \rho^w\boldsymbol{g}\right)\Delta H_{\mathrm{vap}}\right]\cdot\boldsymbol{n}, && \text{on } \Gamma_{qT}. \end{aligned} \tag{A.7}$$

The Galerkin method is applied to obtain the governing equations in weak form. The weight functions δp^w, δp^g, δT, and $\delta\boldsymbol{u}$ have to satisfy the boundary conditions of type I (A.6) and boundary conditions of type II (A.7). Furthermore, the weight functions are, in general arbitrary. For convenience, their choice is limited only in such a way that

$$\begin{aligned} \delta\boldsymbol{u} &= \boldsymbol{0}, && \text{on } \Gamma_u, \\ \delta p^w &= 0, && \text{on } \Gamma_w, \\ \delta p^g &= 0, && \text{on } \Gamma_g, \\ \delta T &= 0, && \text{on } \Gamma_T, \end{aligned} \tag{A.8}$$

Assuming the following relationships

$$\begin{aligned} \frac{\partial}{\partial t}\left(\frac{M_a}{TR}p^{ga}\right) &= \frac{\partial}{\partial t}\left(\frac{M_a}{TR}(p^g - p^{gw})\right) = \frac{M_a}{TR}\frac{\partial p^g}{\partial t} - \frac{M_a}{T^2R}\frac{\partial T}{\partial t} \\ &- \frac{M_a}{TR}\frac{\partial p^{gw}}{\partial p^c}\left(\frac{\partial p^g}{\partial t} - \frac{\partial p^w}{\partial t}\right) - \frac{M_a}{TR}\left(\frac{\partial p^{gw}}{\partial T} - \frac{p^{gw}}{T}\right)\frac{\partial T}{\partial t}, \end{aligned} \tag{A.9}$$

$$\frac{\partial}{\partial t}\left(\frac{M_w}{TR}p^{gw}\right) = \frac{M_w}{TR}\frac{\partial p^{gw}}{\partial p^c}\left(\frac{\partial p^g}{\partial t} - \frac{\partial p^w}{\partial t}\right) + \frac{M_w}{TR}\left(\frac{\partial p^{gw}}{\partial T} - \frac{p^{gw}}{T}\right)\frac{\partial T}{\partial t}, \tag{A.10}$$

$$\mathrm{grad}\left(\frac{p^{gw}}{p^g}\right) = \frac{\mathrm{grad}p^{gw}}{p^g} - \frac{p^{gw}}{(p^g)^2}\mathrm{grad}p^g = \frac{1}{p^g}\frac{\partial p^{gw}}{\partial p^c}\left(\mathrm{grad}p^g - \mathrm{grad}p^w\right) - \frac{p^{gw}}{(p^g)^2}\mathrm{grad}p^g, \tag{A.11}$$

and applying the derivative from Equation (5.106)

$$\frac{\partial S_w}{\partial t} = \frac{\partial S_w}{\partial p^c}\frac{\partial p^g}{\partial t} - \frac{\partial S_w}{\partial p^c}\frac{\partial p^w}{\partial t} + \frac{\partial S_w}{\partial T}\frac{\partial T}{\partial t} + \frac{\partial S_w}{\partial \varepsilon_\mathrm{V}}\frac{\partial \varepsilon_\mathrm{V}}{\partial t} \tag{A.12}$$

with the relationship of the volume strain rate (5.107)

$$\frac{\partial \varepsilon_\mathrm{V}}{\partial t} = \boldsymbol{m}\frac{\partial \boldsymbol{\varepsilon}}{\partial t} = \boldsymbol{m}\boldsymbol{\partial}\frac{\partial \boldsymbol{u}}{\partial t} = \mathrm{div}\boldsymbol{v}^s, \tag{A.13}$$

the governing Equations (A.1) to (A.7) in their variational form are the following:

Mass conservaton of dry air

$$\begin{aligned}
&\int_\Omega \delta p^g \left[\rho^{ga}(1-S_w)\boldsymbol{m}\boldsymbol{\partial}\frac{\partial \boldsymbol{u}}{\partial t}\right]\mathrm{d}\Omega \;+\\
&-\int_\Omega \delta p^g \left[\rho^{ga} n\left(\frac{\partial S_w}{\partial p^c}\frac{\partial p^g}{\partial t} - \frac{\partial S_w}{\partial p^c}\frac{\partial p^w}{\partial t} + \frac{\partial S_w}{\partial T}\frac{\partial T}{\partial t} + \frac{\partial S_w}{\partial \varepsilon_\mathrm{V}}\boldsymbol{m}\boldsymbol{\partial}\frac{\partial \boldsymbol{u}}{\partial t}\right)\right]\mathrm{d}\Omega \;+\\
&-\int_\Omega \delta p^g \left[\rho^{ga}\beta_s(1-n)(1-S_w)\frac{\partial T}{\partial t}\right]\mathrm{d}\Omega \;+\\
&+\int_\Omega \delta p^g \left[n(1-S_w)\left(\frac{M_a}{TR}\frac{\partial p^g}{\partial t} - \frac{M_a}{T^2R}\frac{\partial T}{\partial t} - \frac{M_a}{TR}\frac{\partial p^{gw}}{\partial p^c}\left(\frac{\partial p^g}{\partial t} - \frac{\partial p^w}{\partial t}\right)\right)\right]\mathrm{d}\Omega \;+\\
&-\int_\Omega \delta p^g \left[n(1-S_w)\left(\frac{M_a}{TR}\left(\frac{\partial p^{gw}}{\partial T} - \frac{p^{gw}}{T}\right)\frac{\partial T}{\partial t}\right)\right]\mathrm{d}\Omega \;+\\
&+\int_\Omega \delta p^g \mathrm{div}\left[\rho^g \frac{M_a M_w}{M_g^2}\boldsymbol{D}_g\left(\frac{1}{p^g}\frac{\partial p^{gw}}{\partial p^c}\left(\mathrm{grad}p^g - \mathrm{grad}p^w\right) - \frac{p^{gw}}{(p^g)^2}\mathrm{grad}p^g\right)\right]\mathrm{d}\Omega \;+\\
&+\int_\Omega \delta p^g \mathrm{div}\left[\frac{k^{rg}\boldsymbol{k}\rho^{ga}}{\mu^g}\left(-\mathrm{grad}p^g + \rho^g\boldsymbol{g}\right)\right]\mathrm{d}\Omega \;=\; 0.
\end{aligned} \tag{A.14}$$

Mass conservaton of water species - liquid water and vapor

$$\begin{aligned}
\int_\Omega \delta p^w \left[(\rho^w S_w + \rho^{gw}(1-S_w))\, \boldsymbol{m}\boldsymbol{\partial} \frac{\partial \boldsymbol{u}}{\partial t} \right] \mathrm{d}\Omega - \int_\Omega \delta p^w \left[\beta_{swg} \frac{\partial T}{\partial t} \right] \mathrm{d}\Omega \; + \\
+ \int_\Omega \delta p^w \left[(\rho^w + \rho^{gw}) n \left(\frac{\partial S_w}{\partial p^c}\frac{\partial p^g}{\partial t} - \frac{\partial S_w}{\partial p^c}\frac{\partial p^w}{\partial t} + \frac{\partial S_w}{\partial T}\frac{\partial T}{\partial t} + \frac{\partial S_w}{\partial \varepsilon_\mathrm{V}} \boldsymbol{m}\cdot\boldsymbol{\partial}\frac{\partial \boldsymbol{u}}{\partial t} \right) \right] \mathrm{d}\Omega \; + \\
+ \int_\Omega \delta p^w \left[n(1-S_w) \left(\frac{M_w}{TR}\frac{\partial p^{gw}}{\partial p^c} \left(\frac{\partial p^g}{\partial t} - \frac{\partial p^w}{\partial t} \right) + \frac{M_w}{TR} \left(\frac{\partial p^{gw}}{\partial T} - \frac{p^{gw}}{T} \right) \right) \frac{\partial T}{\partial t} \right] \mathrm{d}\Omega \; + \\
- \int_\Omega \delta p^w \mathrm{div} \left[\rho^g \frac{M_a M_w}{M_g^2} \boldsymbol{D}_g \left(\frac{1}{p^g}\frac{\partial p^{gw}}{\partial p^c} (\mathrm{grad} p^g - \mathrm{grad} p^w) - \frac{p^{gw}}{(p^g)^2} \mathrm{grad} p^g \right) \right] \mathrm{d}\Omega \; + \\
+ \int_\Omega \delta p^w \mathrm{div} \left[\frac{k^{rg}\boldsymbol{k}\rho^{gw}}{\mu^g} (-\mathrm{grad} p^g + \rho^g \boldsymbol{g}) \right] \mathrm{d}\Omega \; + \\
+ \int_\Omega \delta p^w \mathrm{div} \left[\frac{k^{rw}\boldsymbol{k}\rho^{w}}{\mu^w} (-\mathrm{grad} p^w + \rho^w \boldsymbol{g}) \right] \mathrm{d}\Omega \; = \; 0.
\end{aligned} \tag{A.15}$$

Enthalpy conservation equation of the multiphase medium

$$\begin{aligned}
\int_\Omega \delta T \left[\left(\rho C_p\right)_{\mathrm{eff}} \frac{\partial T}{\partial t} \right] \mathrm{d}\Omega \; + \\
+ \int_\Omega \delta T \left[n\rho^w C_p^w \frac{k^{rw}\boldsymbol{k}\rho^w}{\mu^w} (-\mathrm{grad} p^w + \rho^w \boldsymbol{g}) \cdot \mathrm{grad} T \right] \mathrm{d}\Omega \; + \\
+ \int_\Omega \delta T \left[n\rho^g C_p^g \frac{k^{rg}\boldsymbol{k}\rho^{gw}}{\mu^g} (-\mathrm{grad} p^g + \rho^g \boldsymbol{g}) \cdot \mathrm{grad} T \right] \mathrm{d}\Omega \; + \\
- \int_\Omega \delta T \mathrm{div} \left[\boldsymbol{\lambda}_{\mathrm{eff}} \mathrm{grad} T \right] \mathrm{d}\Omega \; + \\
- \int_\Omega \delta T \Delta H_{\mathrm{vap}} \left[\alpha S_w \rho^w \boldsymbol{m}\boldsymbol{\partial} \frac{\partial \boldsymbol{u}}{\partial t} \right] \mathrm{d}\Omega + \int_\Omega \delta T \Delta H_{\mathrm{vap}} \left[\rho^w \beta_{sw} \frac{\partial T}{\partial t} \right] \mathrm{d}\Omega \; + \\
- \int_\Omega \delta T \Delta H_{\mathrm{vap}} \left[\rho^w n \left(\frac{\partial S_w}{\partial p^c}\frac{\partial p^g}{\partial t} - \frac{\partial S_w}{\partial p^c}\frac{\partial p^w}{\partial t} + \frac{\partial S_w}{\partial T}\frac{\partial T}{\partial t} + \frac{\partial S_w}{\partial \varepsilon_\mathrm{V}} \boldsymbol{m}\boldsymbol{\partial}\frac{\partial \boldsymbol{u}}{\partial t} \right) \right] \mathrm{d}\Omega \; + \\
- \int_\Omega \delta T \Delta H_{\mathrm{vap}} \mathrm{div} \left[\frac{k^{rw}\boldsymbol{k}\rho^{w}}{\mu^w} (-\mathrm{grad} p^w + \rho^w \boldsymbol{g}) \right] \mathrm{d}\Omega \; = \; 0.
\end{aligned} \tag{A.16}$$

Linear momentum balance equation of the multiphase medium

$$\int_\Omega \delta \boldsymbol{u}\, \mathrm{div} \left[\boldsymbol{\sigma}^{\mathrm{eff}} - \alpha (S_w p^w + S_g p^g) \boldsymbol{m}^{\mathrm{T}} \right] \mathrm{d}\Omega + \int_\Omega \delta \boldsymbol{u} \rho \boldsymbol{g} \mathrm{d}\Omega = 0. \tag{A.17}$$

To the divergence operator in the set of Equations A.14 to A.16, Green's theorem is applied in the form

$$\int_\Omega \Phi \boldsymbol{\nabla}^{\mathrm{T}} \boldsymbol{\Psi} \mathrm{d}\Omega = - \int_\Omega (\boldsymbol{\nabla}\Phi)^{\mathrm{T}} \cdot \boldsymbol{\Psi} \mathrm{d}\Omega + \int_\Gamma \Phi \boldsymbol{\Psi} \cdot \boldsymbol{n} \mathrm{d}\Gamma, \tag{A.18}$$

where Φ is a scalar function and $\boldsymbol{\Psi} = \{\Psi_x, \Psi_y, \Psi_z\}$ is a vector. Remind $\boldsymbol{\nabla}^{\mathrm{T}}$ stands for the divergence operator, div, and $\boldsymbol{\nabla}$ denotes the gradient operator, grad. In the governing equations,

the weighting functions and the terms of the gradient of primary variables are the scalars and the vector functions, respectively, in Green's theorem. With the application of A.18, new integral terms on the boundary related to fluxes arise in the equations. They will be partly eliminated employing the boundary conditions type II in Equation A.7.

In the linear momentum conservation equation, the term of the differential operator div $= \boldsymbol{\partial}$ gives the stress tensor $\boldsymbol{\sigma}$, so Green's theorem is presented in the following form

$$\int_{\Omega} \Phi \boldsymbol{\partial}^{\mathrm{T}} \boldsymbol{\sigma} \mathrm{d}\Omega = -\int_{\Omega} (\boldsymbol{\nabla}\Phi)^{\mathrm{T}} \boldsymbol{\sigma} \mathrm{d}\Omega + \int_{\Gamma} \Phi \boldsymbol{l} \boldsymbol{\sigma} \mathrm{d}\Gamma. \tag{A.19}$$

Applying A.18 and A.19, keeping in mind the form of boundary conditions, the weak form of governing equations is obtained:

Mass conservaton of dry air

$$\begin{aligned}
&\int_{\Omega} \delta p^g \left[\rho^{ga}(1-S_w) \boldsymbol{m}\boldsymbol{\partial} \frac{\partial \boldsymbol{u}}{\partial t} \right] \mathrm{d}\Omega \quad + \\
&- \int_{\Omega} \delta p^g \left[\rho^{ga} n \left(\frac{\partial S_w}{\partial p^c}\frac{\partial p^g}{\partial t} - \frac{\partial S_w}{\partial p^c}\frac{\partial p^w}{\partial t} + \frac{\partial S_w}{\partial T}\frac{\partial T}{\partial t} + \frac{\partial S_w}{\partial \varepsilon_{\mathrm{V}}} \boldsymbol{m}\boldsymbol{\partial}\frac{\partial \boldsymbol{u}}{\partial t} \right) \right] \mathrm{d}\Omega \quad + \\
&- \int_{\Omega} \delta p^g \left[\rho^{ga} \beta_s (1-n)(1-S_w) \frac{\partial T}{\partial t} \right] \mathrm{d}\Omega \quad + \\
&+ \int_{\Omega} \delta p^g \left[n(1-S_w) \left(\frac{M_a}{TR}\frac{\partial p^g}{\partial t} - \frac{M_a}{T^2 R}\frac{\partial T}{\partial t} - \frac{M_a}{TR}\frac{\partial p^{gw}}{\partial p^c} \left(\frac{\partial p^g}{\partial t} - \frac{\partial p^w}{\partial t} \right) \right) \right] \mathrm{d}\Omega \quad + \\
&- \int_{\Omega} \delta p^g \left[n(1-S_w) \left(\frac{M_a}{TR} \left(\frac{\partial p^{gw}}{\partial T} - \frac{p^{gw}}{T} \right) \frac{\partial T}{\partial t} \right) \right] \mathrm{d}\Omega \quad + \\
&- \int_{\Omega} (\boldsymbol{\nabla}\delta p^g)^{\mathrm{T}} \left[\rho^g \frac{M_a M_w}{M_g^2} \boldsymbol{D}_g \left(\frac{1}{p^g}\frac{\partial p^{gw}}{\partial p^c} (\boldsymbol{\nabla} p^g - \boldsymbol{\nabla} p^w) - \frac{p^{gw}}{(p^g)^2} \boldsymbol{\nabla} p^g \right) \right] \mathrm{d}\Omega \quad + \\
&- \int_{\Omega} (\boldsymbol{\nabla}\delta p^g)^{\mathrm{T}} \left[\frac{k^{rg} \boldsymbol{k} \rho^{ga}}{\mu^g} (-\boldsymbol{\nabla} p^g + \rho^g \boldsymbol{g}) \right] \mathrm{d}\Omega + \int_{\Gamma_{qg}} \delta p^g J^{ga} \mathrm{d}\Gamma \quad = \quad 0.
\end{aligned} \tag{A.20}$$

Mass conservaton of water species - liquid water and vapor

$$
\begin{aligned}
\int_\Omega \delta p^w \left[(\rho^w S_w + \rho^{gw}(1-S_w))\, \boldsymbol{m}\boldsymbol{\partial} \frac{\partial \boldsymbol{u}}{\partial t} \right] \mathrm{d}\Omega - \int_\Omega \delta p^w \left[\beta_{swg} \frac{\partial T}{\partial t} \right] \mathrm{d}\Omega \; + \\
+ \int_\Omega \delta p^w \left[(\rho^w + \rho^{gw}) n \left(\frac{\partial S_w}{\partial p^c} \frac{\partial p^g}{\partial t} - \frac{\partial S_w}{\partial p^c} \frac{\partial p^w}{\partial t} + \frac{\partial S_w}{\partial T} \frac{\partial T}{\partial t} + \frac{\partial S_w}{\partial \varepsilon_\mathrm{V}} \boldsymbol{m}\boldsymbol{\partial} \frac{\partial \boldsymbol{u}}{\partial t} \right) \right] \mathrm{d}\Omega \; + \\
+ \int_\Omega \delta p^w \left[n(1-S_w) \left(\frac{M_w}{TR} \frac{\partial p^{gw}}{\partial p^c} \left(\frac{\partial p^g}{\partial t} - \frac{\partial p^w}{\partial t} \right) + \frac{M_w}{TR} \left(\frac{\partial p^{gw}}{\partial T} - \frac{p^{gw}}{T} \right) \right) \frac{\partial T}{\partial t} \right] \mathrm{d}\Omega \; + \\
+ \int_\Omega (\boldsymbol{\nabla} \delta p^w)^\mathrm{T} \left[\rho^g \frac{M_a M_w}{M_g^2} \boldsymbol{D}_g \left(\frac{1}{p^g} \frac{\partial p^{gw}}{\partial p^c} (\boldsymbol{\nabla} p^g - \boldsymbol{\nabla} p^w) - \frac{p^{gw}}{(p^g)^2} \boldsymbol{\nabla} p^g \right) \right] \mathrm{d}\Omega \; + \\
- \int_\Omega (\boldsymbol{\nabla} \delta p^w)^\mathrm{T} \left[\frac{k^{rg} \boldsymbol{k} \rho^{gw}}{\mu^g} (-\boldsymbol{\nabla} p^g + \rho^g \boldsymbol{g}) \right] \mathrm{d}\Omega \; + \\
- \int_\Omega (\boldsymbol{\nabla} \delta p^w)^\mathrm{T} \left[\frac{k^{rw} \boldsymbol{k} \rho^w}{\mu^w} (-\boldsymbol{\nabla} p^w + \rho^w \boldsymbol{g}) \right] \mathrm{d}\Omega \; + \\
+ \int_{\Gamma_{qw}} \delta p^w \left[J^w + J^{gw} + \beta(\rho^{gw} - \rho^{gw}_\infty) \right] \mathrm{d}\Gamma \; = \; 0.
\end{aligned}
\tag{A.21}
$$

Enthalpy conservation equation of the multiphase medium

$$
\begin{aligned}
\int_\Omega \delta T \left[\left(\rho C_p\right)_\mathrm{eff} \frac{\partial T}{\partial t} \right] \mathrm{d}\Omega \; + \\
+ \int_\Omega \delta T \left[n \rho^w C_p^w \frac{k^{rw} \boldsymbol{k} \rho^w}{\mu^w} (-\boldsymbol{\nabla} p^w + \rho^w \boldsymbol{g}) \cdot \boldsymbol{\nabla} T \right] \mathrm{d}\Omega \; + \\
+ \int_\Omega \delta T \left[n \rho^g C_p^g \frac{k^{rg} \boldsymbol{k} \rho^{gw}}{\mu^g} (-\boldsymbol{\nabla} p^g + \rho^g \boldsymbol{g}) \cdot \boldsymbol{\nabla} T \right] \mathrm{d}\Omega \; + \\
+ \int_\Omega (\boldsymbol{\nabla} \delta T)^\mathrm{T} \left[\boldsymbol{\lambda}_\mathrm{eff} \boldsymbol{\nabla} T \right] \mathrm{d}\Omega \; + \\
- \int_\Omega \delta T \Delta H_\mathrm{vap} \left[\alpha S_w \rho^w \boldsymbol{m}\boldsymbol{\partial} \frac{\partial \boldsymbol{u}}{\partial t} \right] \mathrm{d}\Omega + \int_\Omega \delta T \Delta H_\mathrm{vap} \left[\rho^w \beta_{sw} \frac{\partial T}{\partial t} \right] \mathrm{d}\Omega \; + \\
- \int_\Omega \delta T \Delta H_\mathrm{vap} \left[\rho^w n \left(\frac{\partial S_w}{\partial p^c} \frac{\partial p^g}{\partial t} - \frac{\partial S_w}{\partial p^c} \frac{\partial p^w}{\partial t} + \frac{\partial S_w}{\partial T} \frac{\partial T}{\partial t} + \frac{\partial S_w}{\partial \varepsilon_\mathrm{V}} \boldsymbol{m}\boldsymbol{\partial} \frac{\partial \boldsymbol{u}}{\partial t} \right) \right] \mathrm{d}\Omega \; + \\
+ \int_\Omega (\boldsymbol{\nabla} \delta T)^\mathrm{T} \left[\Delta H_\mathrm{vap} \frac{k^{rw} \boldsymbol{k} \rho^w}{\mu^w} (-\boldsymbol{\nabla} p^w + \rho^w \boldsymbol{g}) \right] \mathrm{d}\Omega \; + \\
+ \int_{\Gamma_{qT}} \delta T \left[q^T + \beta_T (T - T_{ext}) \right] \mathrm{d}\Gamma \; = \; 0.
\end{aligned}
\tag{A.22}
$$

Linear momentum balance equation of the multiphase medium

$$-\int_\Omega (\boldsymbol{\partial}\delta\boldsymbol{u})^{\mathrm{T}}\left[\boldsymbol{\sigma}^{\mathrm{eff}}-\alpha(S_w p^w+S_g p^g)\boldsymbol{m}^{\mathrm{T}}\right]\mathrm{d}\Omega+\int_{\Gamma_t}\delta\boldsymbol{u}\,\bar{\boldsymbol{t}}\mathrm{d}\Gamma+\int_\Omega\delta\boldsymbol{u}\,\rho\boldsymbol{g}\mathrm{d}\Omega=0. \tag{A.23}$$

The continuous functions from the previous relations are discretized by the finite element method in the following form

$$\begin{aligned}
\boldsymbol{u}&\approx\boldsymbol{N}_u\boldsymbol{d}_u, & \boldsymbol{\partial}\boldsymbol{u}&\approx\boldsymbol{B}_u\boldsymbol{d}_u, & \delta\boldsymbol{u}&\approx\boldsymbol{N}_u\boldsymbol{w}_u, & \boldsymbol{\partial}\delta\boldsymbol{u}&\approx\boldsymbol{B}_u\boldsymbol{w}_u,\\
T&\approx\boldsymbol{N}_T\boldsymbol{d}_T, & \boldsymbol{\nabla}T&\approx\boldsymbol{B}_T\boldsymbol{d}_T, & \delta T&\approx\boldsymbol{N}_T\boldsymbol{w}_T, & \boldsymbol{\nabla}\delta T&\approx\boldsymbol{B}_T\boldsymbol{w}_T,\\
p^w&\approx\boldsymbol{N}_p\boldsymbol{d}_w, & \boldsymbol{\nabla}p^w&\approx\boldsymbol{B}_p\boldsymbol{d}_w, & \delta p^w&\approx\boldsymbol{N}_p\boldsymbol{w}_w, & \boldsymbol{\nabla}\delta p^w&\approx\boldsymbol{B}_p\boldsymbol{w}_w,\\
p^g&\approx\boldsymbol{N}_p\boldsymbol{d}_g, & \boldsymbol{\nabla}p^g&\approx\boldsymbol{B}_p\boldsymbol{d}_g, & \delta p^g&\approx\boldsymbol{N}_p\boldsymbol{w}_g, & \boldsymbol{\nabla}\delta p^g&\approx\boldsymbol{B}_p\boldsymbol{w}_g.
\end{aligned} \tag{A.24}$$

The introduction of approximations (A.24) into Equations (A.20) to (A.23) and elimination of weighting functions nodal values give the final form of the balance equations

$$\begin{aligned}
&\int_\Omega\boldsymbol{N}_p^{\mathrm{T}}\left[\rho^{ga}(1-S_w)\boldsymbol{m}\boldsymbol{B}_u\frac{\partial\boldsymbol{d}_u}{\partial t}\right]\mathrm{d}\Omega \;+\\
&-\int_\Omega\boldsymbol{N}_p^{\mathrm{T}}\left[\rho^{ga}n\left(\frac{\partial S_w}{\partial p^c}\boldsymbol{N}_p\frac{\partial\boldsymbol{d}_g}{\partial t}-\frac{\partial S_w}{\partial p^c}\boldsymbol{N}_p\frac{\partial\boldsymbol{d}_w}{\partial t}+\frac{\partial S_w}{\partial T}\boldsymbol{N}_p\frac{\partial\boldsymbol{d}_T}{\partial t}+\frac{\partial S_w}{\partial\varepsilon_{\mathrm{V}}}\boldsymbol{m}\boldsymbol{B}_u\frac{\partial\boldsymbol{d}_u}{\partial t}\right)\right]\mathrm{d}\Omega \;+\\
&-\int_\Omega\boldsymbol{N}_p^{\mathrm{T}}\left[\rho^{ga}\beta_s(1-n)(1-S_w)\boldsymbol{N}_T\frac{\partial\boldsymbol{d}_T}{\partial t}\right]\mathrm{d}\Omega \;+\\
&+\int_\Omega\boldsymbol{N}_p^{\mathrm{T}}\left[n(1-S_w)\left(\frac{M_a}{TR}\boldsymbol{N}_p\frac{\partial\boldsymbol{d}_g}{\partial t}-\frac{M_a}{T^2R}\boldsymbol{N}_T\frac{\partial\boldsymbol{d}_T}{\partial t}\right)\right]\mathrm{d}\Omega \;+\\
&+\int_\Omega\boldsymbol{N}_p^{\mathrm{T}}\left[n(1-S_w)\left(-\frac{M_a}{TR}\frac{\partial p^{gw}}{\partial p^c}\left(\boldsymbol{N}_p\frac{\partial\boldsymbol{d}_g}{\partial t}-\boldsymbol{N}_p\frac{\partial\boldsymbol{d}_w}{\partial t}\right)\right)\right]\mathrm{d}\Omega \;+\\
&-\int_\Omega\boldsymbol{N}_p^{\mathrm{T}}\left[n(1-S_w)\left(\frac{M_a}{TR}\left(\frac{\partial p^{gw}}{\partial T}-\frac{p^{gw}}{T}\right)\boldsymbol{N}_T\frac{\partial\boldsymbol{d}_T}{\partial t}\right)\right]\mathrm{d}\Omega \;+\\
&-\int_\Omega\boldsymbol{B}_p^{\mathrm{T}}\left[\rho^g\frac{M_aM_w}{M_g^2}\boldsymbol{D}_g\left(\frac{1}{p^g}\frac{\partial p^{gw}}{\partial p^c}\left(\boldsymbol{B}_p\boldsymbol{d}_g-\boldsymbol{B}_p\boldsymbol{d}_w\right)-\frac{p^{gw}}{(p^g)^2}\boldsymbol{B}_p\boldsymbol{d}_g\right)\right]\mathrm{d}\Omega \;+\\
&-\int_\Omega\boldsymbol{B}_p^{\mathrm{T}}\left[\frac{k^{rg}\boldsymbol{k}\rho^{ga}}{\mu^g}\left(-\boldsymbol{B}_p\boldsymbol{d}_g+\rho^g\boldsymbol{g}\right)\right]\mathrm{d}\Omega+\int_{\Gamma_{qg}}\boldsymbol{N}_p^{\mathrm{T}}J^{ga}\mathrm{d}\Gamma \;=\; 0.
\end{aligned} \tag{A.25}$$

$$
\begin{aligned}
\int_\Omega \boldsymbol{N}_p^{\mathrm{T}} \left[\left(\rho^w S_w + \rho^{gw}(1-S_w)\right) \boldsymbol{m}\boldsymbol{B}_u \frac{\partial \boldsymbol{d}_u}{\partial t} \right] \mathrm{d}\Omega - \int_\Omega \boldsymbol{N}_p^{\mathrm{T}} \left[\beta_{swg} \boldsymbol{N}_T \frac{\partial \boldsymbol{d}_T}{\partial t} \right] \mathrm{d}\Omega \; + \\
+ \int_\Omega \boldsymbol{N}_p^{\mathrm{T}} \left[(\rho^w + \rho^{gw}) n \left(\frac{\partial S_w}{\partial p^c} \boldsymbol{N}_p \frac{\partial \boldsymbol{d}_g}{\partial t} - \frac{\partial S_w}{\partial p^c} \boldsymbol{N}_p \frac{\partial \boldsymbol{d}_w}{\partial t} \right) \right] \mathrm{d}\Omega \; + \\
+ \int_\Omega \boldsymbol{N}_p^{\mathrm{T}} \left[(\rho^w + \rho^{gw}) n \left(\frac{\partial S_w}{\partial T} \boldsymbol{N}_p \frac{\partial \boldsymbol{d}_T}{\partial t} + \frac{\partial S_w}{\partial \varepsilon_{\mathrm{V}}} \boldsymbol{m}\boldsymbol{B}_u \frac{\partial \boldsymbol{d}_u}{\partial t} \right) \right] \mathrm{d}\Omega \; + \\
+ \int_\Omega \boldsymbol{N}_p^{\mathrm{T}} \left[n(1-S_w) \left(\frac{M_w}{TR} \frac{\partial p^{gw}}{\partial p^c} \left(\boldsymbol{N}_p \frac{\partial \boldsymbol{d}_g}{\partial t} - \boldsymbol{N}_p \frac{\partial \boldsymbol{d}_w}{\partial t} \right) \right) \right] \mathrm{d}\Omega \; + \\
+ \int_\Omega \boldsymbol{N}_p^{\mathrm{T}} \left[n(1-S_w) \left(\frac{M_w}{TR} \left(\frac{\partial p^{gw}}{\partial T} - \frac{p^{gw}}{T} \right) \boldsymbol{N}_T \frac{\partial \boldsymbol{d}_T}{\partial t} \right) \right] \mathrm{d}\Omega \; + \\
+ \int_\Omega \boldsymbol{B}_p^{\mathrm{T}} \left[\rho^g \frac{M_a M_w}{M_g^2} \boldsymbol{D}_g \left(\frac{1}{p^g} \frac{\partial p^{gw}}{\partial p^c} \left(\boldsymbol{B}_p \boldsymbol{d}_g - \boldsymbol{B}_p \boldsymbol{d}_w \right) - \frac{p^{gw}}{(p^g)^2} \boldsymbol{B}_p \boldsymbol{d}_g \right) \right] \mathrm{d}\Omega \; + \\
- \int_\Omega \boldsymbol{B}_p^{\mathrm{T}} \left[\frac{k^{rg} \boldsymbol{k} \rho^{gw}}{\mu^g} \left(-\boldsymbol{B}_p \boldsymbol{d}_g + \rho^g \boldsymbol{g} \right) \right] \mathrm{d}\Omega \; + \\
- \int_\Omega \boldsymbol{B}_p^{\mathrm{T}} \left[\frac{k^{rw} \boldsymbol{k} \rho^{w}}{\mu^w} \left(-\boldsymbol{B}_p \boldsymbol{d}_w + \rho^w \boldsymbol{g} \right) \right] \mathrm{d}\Omega \; + \qquad \text{(A.26)} \\
+ \int_{\Gamma_{qw}} \boldsymbol{N}_p^{\mathrm{T}} \left[J^w + J^{gw} + \beta(\rho^{gw} - \rho_\infty^{gw}) \right] \mathrm{d}\Gamma \;=\; 0.
\end{aligned}
$$

$$
\begin{aligned}
\int_\Omega \boldsymbol{N}_T^{\mathrm{T}} \left[\left(\rho C_p\right)_{\mathrm{eff}} \boldsymbol{N}_T \frac{\partial \boldsymbol{d}_T}{\partial t} \right] \mathrm{d}\Omega \; + \\
+ \int_\Omega \boldsymbol{N}_T^{\mathrm{T}} \left[n \rho^w C_p^w \frac{k^{rw} \boldsymbol{k} \rho^w}{\mu^w} \left(-\boldsymbol{\nabla} p_w + \rho^w \boldsymbol{g} \right) \cdot \boldsymbol{B}_T \boldsymbol{d}_T \right] \mathrm{d}\Omega \; + \\
+ \int_\Omega \boldsymbol{N}_T^{\mathrm{T}} \left[n \rho^g C_p^g \frac{k^{rg} \boldsymbol{k} \rho^{gw}}{\mu^g} \left(-\boldsymbol{\nabla} p_g + \rho^g \boldsymbol{g} \right) \cdot \boldsymbol{B}_T \boldsymbol{d}_T \right] \mathrm{d}\Omega \; + \\
+ \int_\Omega \boldsymbol{B}_T^{\mathrm{T}} \left[\boldsymbol{\lambda}_{\mathrm{eff}} \boldsymbol{B}_T \boldsymbol{d}_T \right] \mathrm{d}\Omega \; + \\
- \int_\Omega \boldsymbol{N}_T^{\mathrm{T}} \Delta H_{\mathrm{vap}} \left[\alpha S_w \rho^w \boldsymbol{m}\boldsymbol{B}_u \frac{\partial \boldsymbol{d}_u}{\partial t} \right] \mathrm{d}\Omega + \int_\Omega \boldsymbol{N}_T^{\mathrm{T}} \Delta H_{\mathrm{vap}} \left[\rho^w \beta_{sw} \boldsymbol{N}_T \frac{\partial \boldsymbol{d}_T}{\partial t} \right] \mathrm{d}\Omega \; + \\
- \int_\Omega \boldsymbol{N}_T^{\mathrm{T}} \Delta H_{\mathrm{vap}} \left[\rho^w n \left(\frac{\partial S_w}{\partial p^c} \boldsymbol{N}_p \frac{\partial \boldsymbol{d}_g}{\partial t} - \frac{\partial S_w}{\partial p^c} \boldsymbol{N}_p \frac{\partial \boldsymbol{d}_w}{\partial t} \right) \right] \mathrm{d}\Omega \; + \\
- \int_\Omega \boldsymbol{N}_T^{\mathrm{T}} \Delta H_{\mathrm{vap}} \left[\rho^w n \left(\frac{\partial S_w}{\partial T} \boldsymbol{N}_T \frac{\partial \boldsymbol{d}_T}{\partial t} + \frac{\partial S_w}{\partial \varepsilon_{\mathrm{V}}} \boldsymbol{m}\boldsymbol{B}_u \frac{\partial \boldsymbol{d}_u}{\partial t} \right) \right] \mathrm{d}\Omega \; + \\
+ \int_\Omega \boldsymbol{B}_T^{\mathrm{T}} \left[\Delta H_{\mathrm{vap}} \frac{k^{rw} \boldsymbol{k} \rho^w}{\mu^w} \left(-\boldsymbol{B}_p \boldsymbol{d}_w + \rho^w \boldsymbol{g} \right) \right] \mathrm{d}\Omega \; + \qquad \text{(A.27)} \\
+ \int_{\Gamma_{qT}} \boldsymbol{N}_T^{\mathrm{T}} \left[q^T + \beta_T (\boldsymbol{N}_T \boldsymbol{d}_T - T_{ext}) \right] \mathrm{d}\Gamma \;=\; 0.
\end{aligned}
$$

For a linear elastic solid, assuming thermal expansion effect from Equations (2.84) and (2.85)

$$\int_\Omega \boldsymbol{B}_u^{\mathrm{T}} \boldsymbol{\sigma}^{\mathrm{eff}} \mathrm{d}\Omega = \int_\Omega \boldsymbol{B}_u^{\mathrm{T}} \boldsymbol{D}_u \left(\boldsymbol{\varepsilon} - \boldsymbol{\varepsilon}_T\right) \mathrm{d}\Omega = \int_\Omega \boldsymbol{B}_u^{\mathrm{T}} \boldsymbol{D}_u \left(\boldsymbol{B}_u \boldsymbol{d}_u - \boldsymbol{m}^{\mathrm{T}} \alpha_T (\boldsymbol{N}_T \boldsymbol{d}_T - T_0)\right) \mathrm{d}\Omega, \quad \text{(A.28)}$$

the final form of the linear momentum balance equation of the multiphase medium reads

$$\begin{aligned} -\int_\Omega \boldsymbol{B}_u^{\mathrm{T}} \boldsymbol{D}_u \left(\boldsymbol{B}_u \boldsymbol{d}_u - \boldsymbol{m}^{\mathrm{T}} \alpha_T (\boldsymbol{N}_T \boldsymbol{d}_T - T_0)\right) \mathrm{d}\Omega + \int_\Omega \boldsymbol{B}_u^{\mathrm{T}} \alpha S_w \boldsymbol{m}^{\mathrm{T}} \boldsymbol{N}_p \boldsymbol{d}_w \mathrm{d}\Omega \quad + \\ \int_\Omega \boldsymbol{B}_u^{\mathrm{T}} (1 - \alpha S_w) \boldsymbol{m}^{\mathrm{T}} \boldsymbol{N}_p \boldsymbol{d}_g \mathrm{d}\Omega + \int_{\Gamma_t} \boldsymbol{N}_u \, \bar{\boldsymbol{t}} \mathrm{d}\Gamma + \int_\Omega \boldsymbol{N}_u \, \rho \boldsymbol{g} \mathrm{d}\Omega \quad = \quad 0. \quad \text{(A.29)} \end{aligned}$$

The above Equations (A.25), (A.26), (A.27), and (A.29) can be rewritten in the matrix form

$$\begin{aligned} &\begin{pmatrix} \boldsymbol{K}_{uu} & \boldsymbol{K}_{uw} & \boldsymbol{K}_{ug} & \boldsymbol{K}_{uT} \\ \boldsymbol{K}_{wu} & \boldsymbol{K}_{ww} & \boldsymbol{K}_{wg} & \boldsymbol{K}_{wT} \\ \boldsymbol{K}_{gu} & \boldsymbol{K}_{gw} & \boldsymbol{K}_{gg} & \boldsymbol{K}_{gT} \\ \boldsymbol{K}_{Tu} & \boldsymbol{K}_{Tw} & \boldsymbol{K}_{Tg} & \boldsymbol{K}_{TT} \end{pmatrix} \begin{pmatrix} \boldsymbol{d}_u \\ \boldsymbol{d}_w \\ \boldsymbol{d}_g \\ \boldsymbol{d}_T \end{pmatrix} \quad + \\ &+ \begin{pmatrix} \boldsymbol{C}_{uu} & \boldsymbol{C}_{uw} & \boldsymbol{C}_{ug} & \boldsymbol{C}_{uT} \\ \boldsymbol{C}_{wu} & \boldsymbol{C}_{ww} & \boldsymbol{C}_{wg} & \boldsymbol{C}_{wT} \\ \boldsymbol{C}_{gu} & \boldsymbol{C}_{gw} & \boldsymbol{C}_{gg} & \boldsymbol{C}_{gT} \\ \boldsymbol{C}_{Tu} & \boldsymbol{C}_{Tw} & \boldsymbol{C}_{Tg} & \boldsymbol{C}_{TT} \end{pmatrix} \begin{pmatrix} \dot{\boldsymbol{d}}_u \\ \dot{\boldsymbol{d}}_w \\ \dot{\boldsymbol{d}}_g \\ \dot{\boldsymbol{d}}_T \end{pmatrix} \quad = \quad \begin{pmatrix} \boldsymbol{f}_{ext} \\ \boldsymbol{f}_w \\ \boldsymbol{f}_g \\ \boldsymbol{f}_T \end{pmatrix}, \end{aligned} \quad \text{(A.30)}$$

where the matrices are definead as

$$\boldsymbol{K}_{uu} = \int_\Omega \boldsymbol{B}_u^{\mathrm{T}} \boldsymbol{D}_u \boldsymbol{B}_u \mathrm{d}\Omega, \tag{A.31}$$

$$\boldsymbol{K}_{uw} = -\int_\Omega \boldsymbol{B}_u^{\mathrm{T}} \alpha S_w \boldsymbol{m}^{\mathrm{T}} \boldsymbol{N}_p \mathrm{d}\Omega, \tag{A.32}$$

$$\boldsymbol{K}_{ug} = -\int_\Omega \boldsymbol{B}_u^{\mathrm{T}} (1-\alpha S_w) \boldsymbol{m}^{\mathrm{T}} \boldsymbol{N}_p \mathrm{d}\Omega, \tag{A.33}$$

$$\boldsymbol{K}_{uT} = -\int_\Omega \boldsymbol{B}_u^{\mathrm{T}} \boldsymbol{D}_u \boldsymbol{m}^{\mathrm{T}} \alpha_T \boldsymbol{N}_T \mathrm{d}\Omega, \tag{A.34}$$

$$\boldsymbol{K}_{wu} = 0, \tag{A.35}$$

$$\boldsymbol{K}_{ww} = -\int_\Omega \boldsymbol{B}_p^{\mathrm{T}} \rho^g \frac{M_a M_w}{M_g^2} \boldsymbol{D}_g \frac{1}{p^g} \frac{\partial p^{gw}}{\partial p^c} \boldsymbol{B}_p \mathrm{d}\Omega, + \int_\Omega \boldsymbol{B}_p^{\mathrm{T}} \frac{k^{rw} \boldsymbol{k} \rho^w}{\mu^w} \boldsymbol{B}_p \mathrm{d}\Omega, \tag{A.36}$$

$$\boldsymbol{K}_{wg} = \int_\Omega \boldsymbol{B}_p^{\mathrm{T}} \rho^g \frac{M_a M_w}{M_g^2} \boldsymbol{D}_g \left(\frac{1}{p^g} \frac{\partial p^{gw}}{\partial p^c} - \frac{p^{gw}}{(p^g)^2} \right) \boldsymbol{B}_p \mathrm{d}\Omega + \int_\Omega \boldsymbol{B}_p^{\mathrm{T}} \frac{k^{rg} \boldsymbol{k} \rho^{gw}}{\mu^g} \boldsymbol{B}_p \mathrm{d}\Omega, \tag{A.37}$$

$$\boldsymbol{K}_{wT} = 0, \tag{A.38}$$

$$\boldsymbol{K}_{gu} = 0, \tag{A.39}$$

$$\boldsymbol{K}_{gw} = \int_\Omega \boldsymbol{B}_p^{\mathrm{T}} \rho^g \frac{M_a M_w}{M_g^2} \boldsymbol{D}_g \left(\frac{1}{p^g} \frac{\partial p^{gw}}{\partial p^c} \right) \boldsymbol{B}_p \mathrm{d}\Omega, \tag{A.40}$$

$$\boldsymbol{K}_{gg} = \int_\Omega \boldsymbol{B}_p^{\mathrm{T}} \frac{k^{rg} \boldsymbol{k} \rho^{ga}}{\mu^g} \boldsymbol{B}_p \mathrm{d}\Omega - \int_\Omega \boldsymbol{B}_p^{\mathrm{T}} \rho^g \frac{M_a M_w}{M_g^2} \boldsymbol{D}_g \left(\frac{1}{p^g} \frac{\partial p^{gw}}{\partial p^c} - \frac{p^{gw}}{(p^g)^2} \right) \boldsymbol{B}_p \mathrm{d}\Omega, \tag{A.41}$$

$$\boldsymbol{K}_{gT} = 0, \tag{A.42}$$

$$\boldsymbol{K}_{Tu} = 0, \tag{A.43}$$

$$\boldsymbol{K}_{Tw} = \int_\Omega \boldsymbol{B}_T^{\mathrm{T}} \Delta H_{\mathrm{vap}} \frac{k^{rw} \boldsymbol{k} \rho^w}{\mu^w} \boldsymbol{B}_p \mathrm{d}\Omega \tag{A.44}$$

$$\boldsymbol{K}_{Tg} = 0, \tag{A.45}$$

$$\begin{aligned} \boldsymbol{K}_{TT} = & \int_\Omega \boldsymbol{B}_T^{\mathrm{T}} \boldsymbol{\lambda}_{\mathrm{eff}} \boldsymbol{B}_T \mathrm{d}\Omega + \int_{\Gamma_{qT}} \boldsymbol{N}_T^{\mathrm{T}} \beta_T \boldsymbol{N}_T \mathrm{d}\Gamma - \int_\Omega \boldsymbol{N}_T^{\mathrm{T}} n \rho^w C_p^w \frac{k^{rw} \boldsymbol{k} \rho^w}{\mu^w} \boldsymbol{\nabla} p_w \cdot \boldsymbol{B}_T \mathrm{d}\Omega + \\ & - \int_\Omega \boldsymbol{N}_T^{\mathrm{T}} n \rho^g C_p^g \frac{k^{rg} \boldsymbol{k} \rho^{gw}}{\mu^g} \boldsymbol{\nabla} p_g \cdot \boldsymbol{B}_T \mathrm{d}\Omega, \end{aligned} \tag{A.46}$$

$$\boldsymbol{C}_{uu} = 0, \tag{A.47}$$

$$\boldsymbol{C}_{uw} = 0, \tag{A.48}$$

$$\boldsymbol{C}_{ug} = 0, \tag{A.49}$$

$$\boldsymbol{C}_{uT} = 0, \tag{A.50}$$

$$\boldsymbol{C}_{wu} = \int_\Omega \boldsymbol{N}_p^{\mathrm{T}} \left(\rho^w S_w + \rho^{gw}(1-S_w)\right) \boldsymbol{m} \cdot \boldsymbol{B}_u \mathrm{d}\Omega + \\ + \int_\Omega \boldsymbol{N}_p^{\mathrm{T}} (\rho^w + \rho^{gw}) n \frac{\partial S_w}{\partial \varepsilon_{\mathrm{V}}} \boldsymbol{m} \cdot \boldsymbol{B}_u \mathrm{d}\Omega, \tag{A.51}$$

$$\boldsymbol{C}_{ww} = -\int_\Omega \boldsymbol{N}_p^{\mathrm{T}} (\rho^w + \rho^{gw}) n \frac{\partial S_w}{\partial p^c} \boldsymbol{N}_p \mathrm{d}\Omega - \int_\Omega \boldsymbol{N}_p^{\mathrm{T}} n (1-S_w) \frac{M_w}{TR} \frac{\partial p^{gw}}{\partial p^c} \boldsymbol{N}_p \mathrm{d}\Omega, \tag{A.52}$$

$$\boldsymbol{C}_{wg} = \int_\Omega \boldsymbol{N}_p^{\mathrm{T}} (\rho^w + \rho^{gw}) n \frac{\partial S_w}{\partial p^c} \boldsymbol{N}_p \mathrm{d}\Omega + \int_\Omega \boldsymbol{N}_p^{\mathrm{T}} n (1-S_w) \frac{M_w}{TR} \frac{\partial p^{gw}}{\partial p^c} \boldsymbol{N}_p \mathrm{d}\Omega, \tag{A.53}$$

$$\boldsymbol{C}_{wT} = -\int_\Omega \boldsymbol{N}_p^{\mathrm{T}} \beta_{swg} \boldsymbol{N}_T \mathrm{d}\Omega + \int_\Omega \boldsymbol{N}_p^{\mathrm{T}} (\rho^w + \rho^{gw}) n \frac{\partial S_w}{\partial T} \boldsymbol{N}_p \mathrm{d}\Omega + \\ + \int_\Omega \boldsymbol{N}_p^{\mathrm{T}} n (1-S_w) \frac{M_w}{TR} \left(\frac{\partial p^{gw}}{\partial T} - \frac{p^{gw}}{T} \right) \boldsymbol{N}_T \mathrm{d}\Omega, \tag{A.54}$$

$$\boldsymbol{C}_{gu} = \int_\Omega \boldsymbol{N}_p^{\mathrm{T}} \rho^{ga} (1-S_w) \boldsymbol{m} \boldsymbol{B}_u \mathrm{d}\Omega - \int_\Omega \boldsymbol{N}_p^{\mathrm{T}} \rho^{ga} n \frac{\partial S_w}{\partial \varepsilon_{\mathrm{V}}} \boldsymbol{m} \boldsymbol{B}_u \mathrm{d}\Omega, \tag{A.55}$$

$$\boldsymbol{C}_{gw} = \int_\Omega \boldsymbol{N}_p^{\mathrm{T}} \rho^{ga} n \frac{\partial S_w}{\partial p^c} \boldsymbol{N}_p \mathrm{d}\Omega + \int_\Omega \boldsymbol{N}_p^{\mathrm{T}} n (1-S_w) \frac{M_a}{TR} \frac{\partial p^{gw}}{\partial p^c} \boldsymbol{N}_p \mathrm{d}\Omega, \tag{A.56}$$

$$\boldsymbol{C}_{gg} = -\int_\Omega \boldsymbol{N}_p^{\mathrm{T}} \rho^{ga} n \frac{\partial S_w}{\partial p^c} \boldsymbol{N}_p \mathrm{d}\Omega + \int_\Omega \boldsymbol{N}_p^{\mathrm{T}} n (1-S_w) \frac{M_a}{TR} \boldsymbol{N}_p \mathrm{d}\Omega + \\ - \int_\Omega \boldsymbol{N}_p^{\mathrm{T}} n (1-S_w) \frac{M_a}{TR} \frac{\partial p^{gw}}{\partial p^c} \boldsymbol{N}_p \mathrm{d}\Omega, \tag{A.57}$$

$$\boldsymbol{C}_{gT} = -\int_\Omega \boldsymbol{N}_p^{\mathrm{T}} \rho^{ga} n \frac{\partial S_w}{\partial T} \boldsymbol{N}_p \mathrm{d}\Omega - \int_\Omega \boldsymbol{N}_p^{\mathrm{T}} \rho^{ga} \beta_s (1-n)(1-S_w) \boldsymbol{N}_T \mathrm{d}\Omega + \\ - \int_\Omega \boldsymbol{N}_p^{\mathrm{T}} n (1-S_w) \frac{M_a}{T^2 R} \boldsymbol{N}_T \mathrm{d}\Omega - \int_\Omega \boldsymbol{N}_p^{\mathrm{T}} n (1-S_w) \frac{M_a}{TR} \left(\frac{\partial p^{gw}}{\partial T} - \frac{p^{gw}}{T} \right) \boldsymbol{N}_T \mathrm{d}\Omega, \tag{A.58}$$

$$\boldsymbol{C}_{Tu} = -\int_\Omega \boldsymbol{N}_T^{\mathrm{T}} \Delta H_{\mathrm{vap}} \alpha S_w \rho^w \boldsymbol{m} \boldsymbol{B}_u \mathrm{d}\Omega - \int_\Omega \boldsymbol{N}_T^{\mathrm{T}} \Delta H_{\mathrm{vap}} \rho^w n \frac{\partial S_w}{\partial \varepsilon_{\mathrm{V}}} \boldsymbol{m} \boldsymbol{B}_u \mathrm{d}\Omega, \tag{A.59}$$

$$\boldsymbol{C}_{Tw} = \int_\Omega \boldsymbol{N}_T^{\mathrm{T}} \Delta H_{\mathrm{vap}} \rho^w n \frac{\partial S_w}{\partial p^c} \boldsymbol{N}_p \Omega, \tag{A.60}$$

$$\boldsymbol{C}_{Tg} = -\int_\Omega \boldsymbol{N}_T^{\mathrm{T}} \Delta H_{\mathrm{vap}} \rho^w n \frac{\partial S_w}{\partial p^c} \boldsymbol{N}_p \mathrm{d}\Omega, \tag{A.61}$$

$$\boldsymbol{C}_{TT} = \int_\Omega \boldsymbol{N}_T^{\mathrm{T}} \left(\rho C_p\right)_{\mathrm{eff}} \boldsymbol{N}_T \mathrm{d}\Omega + \\ + \int_\Omega \boldsymbol{N}_T^{\mathrm{T}} \Delta H_{\mathrm{vap}} \rho^w \beta_{sw} \boldsymbol{N}_T \mathrm{d}\Omega - \int_\Omega \boldsymbol{N}_T^{\mathrm{T}} \Delta H_{\mathrm{vap}} \rho^w n \frac{\partial S_w}{\partial T} \boldsymbol{N}_T \mathrm{d}\Omega, \tag{A.62}$$

and the right-hand side vectors are definead as

$$\boldsymbol{f}_{ext} = \int_{\Gamma_t} \boldsymbol{N}_u \bar{\boldsymbol{t}} \mathrm{d}\Gamma + \int_{\Omega} \boldsymbol{N}_u \rho \boldsymbol{g} \mathrm{d}\Omega - \int_{\Omega} \boldsymbol{B}_u^{\mathrm{T}} \boldsymbol{D}_u \boldsymbol{m}^{\mathrm{T}} \alpha_T T_0 \mathrm{d}\Omega, \tag{A.63}$$

$$\begin{aligned} \boldsymbol{f}_w &= -\int_{\Gamma_{qw}} \boldsymbol{N}_p^{\mathrm{T}} \left[J^w + J^{gw} + \beta(\rho^{gw} - \rho_{\infty}^{gw}) \right] \mathrm{d}\Gamma + \\ &+ \int_{\Omega} \boldsymbol{B}_p^{\mathrm{T}} \frac{k^{rg} \boldsymbol{k} \rho^{gw}}{\mu^g} \rho^g \boldsymbol{g} \mathrm{d}\Omega + \int_{\Omega} \boldsymbol{B}_p^{\mathrm{T}} \frac{k^{rw} \boldsymbol{k} \rho^w}{\mu^w} \rho^w \boldsymbol{g} \mathrm{d}\Omega, \end{aligned} \tag{A.64}$$

$$\boldsymbol{f}_g = -\int_{\Gamma_{qg}} \boldsymbol{N}_p^{\mathrm{T}} J^{ga} \mathrm{d}\Gamma + \int_{\Omega} \boldsymbol{B}_p^{\mathrm{T}} \frac{k^{rg} \boldsymbol{k} \rho^{ga}}{\mu^g} \rho^g \boldsymbol{g} \mathrm{d}\Omega, \tag{A.65}$$

$$\boldsymbol{f}_T = -\int_{\Gamma_{qT}} \boldsymbol{N}_T^{\mathrm{T}} \left[q^T - \beta_T T_{ext} \right] \mathrm{d}\Gamma - \int_{\Omega} \boldsymbol{B}_T^{\mathrm{T}} \Delta H_{\mathrm{vap}} \frac{k^{rw} \boldsymbol{k} \rho^w}{\mu^w} \rho^w \boldsymbol{g} \mathrm{d}\Omega, \tag{A.66}$$

It should be noted the values of prescribed forces in vector $\bar{\boldsymbol{t}}$, prescribed fluxes J^w, J^{gw}, J^{ga}, q^T, external values of temperature T_{ext}, and concentrations of water vapor ρ^{gw} and ρ_{∞}^{gw}, as well as the initial temperatures T_0 are approximated via FEM stated in Equations (A.24).

Bibliography

[Alonso et al., 1996] Alonso, E., Bernier, F., Volckaert, G., Directorate-General for Science, R., Development, and Commission, E. (1996). *Thermal-hydraulic-mechanical and Geochemical Behaviour of the Clay Barrier in Radioactive Waste Repositories (model Development and Validation).* OPOCE.

[Alonso et al., 1995] Alonso, E. E., Loret, A., Gens, A., and Yang, D. Q. (1995). Experimental behaviour of highly expansive double-structure clay. In Balkema, editor, *1st Int. Conference on Unsaturated Soils. Paris, France*, pages 11–16. Rotterdam.

[Alonso et al., 2011] Alonso, E. E., Romero, E., and Hofmann, E. (2011). Hydromechanical behaviour of compacted granular expansive mixtures: experimental and constitutive study. *Geotechnique*, 61(4):329–344.

[Alonso et al., 1999] Alonso, E. E., Vaunat, J., and Gens, A. (1999). Modelling the mechanical behaviour of expansive clays. *Engineering Geology*, 54:173–183.

[Anderson, 2005] Anderson, P. (2005). Thirty years of measured prestress of Swedish nuclear reactor containment. *Nuclear Engineering and Design*, 235:2323–2336.

[ASHRAE, 1993] ASHRAE, A. (1993). *ASHRAE Handbook, Fundamentals Volume*. ASHRAE.

[Bažant and Kaplan, 1996] Bažant, Z. and Kaplan, M. (1996). *Concrete at High Temperatures: Material Properties and Mathematical Models*. Longman. Harlow.

[Bažant and Xi, 1995] Bažant, Z. and Xi, Y. (1995). Continuous retardation spectrum for solidification theory of concrete creep. *Journal of Engineering Mechanics*, 121(2):281 – 288.

[Bažant, 1988] Bažant, Z. P. (1988). *Mathematical Modeling of Creep and Shrinkage of Concrete*. John Wiley&Sons, Chichester-Singapore.

[Bažant and Chern, 1985] Bažant, Z. P. and Chern (1985). Concrete creep at variable humidity: constitutive law and mechanism. *MAS*, 18:1–20. RILEM, Paris.

[Bažant et al., 2004] Bažant, Z. P., Cusatis, G., and Cedolin, L. (2004). Temperature effect on concrete creep modeled by microprestress-solidification theory. *Journal of Engineering Mechechnics - ASCE*, 130(6):691–699.

[Bažant and Jirásek, 2018] Bažant, Z. P. and Jirásek, M. (2018). *Creep and Hygrothermal Effects in Concrete Structures*. Springer.

[Bažant and Najjar, 1972] Bažant, Z. P. and Najjar, L. J. (1972). Nonlinear water diffusion in non-saturated concrete structural analysis program. *Matériaux et constructions*, 25(5):8–9. RILEM, Paris.

[Bažant and Thonguthai, 1979] Bažant, Z. P. and Thonguthai, W. (1979). Pore pressure in heated concrete walls: theoretical prediction. *Magazine of Concrete Research*, 31(107):67–76.

[Baweja and Bažant, 1995] Baweja, S. and Bažant, Z. (1995). Creep and shrinkage prediction model for analysis and design of concrete structures – model b3. *Materials and Structures*, 28(6):357–365. RILEM, Paris.

[Biot, 1941] Biot, M. A. (1941). General theory of three-dimensional consolidation. *Journal of Applied Physics*, 12:155–164.

[Biot, 1956] Biot, M. A. (1956). General solution of the equation of elasticity and consolidation for a porous material. *Journal of Applied Mechanics*, 23:91–96.

[Bishop, 1959] Bishop, A. W. (1959). The principles of effective stress. *Teknisk Ukeblad*, 106(39):859–863.

[Bittnar and Šejnoha, 1996] Bittnar, Z. and Šejnoha, J. (1996). *Numerical Methods in Structural Mechanics*. USA. ASCE Press, New York.

[Bittnar et al., 2008] Bittnar, Z., Šejnoha, J., Koudelka, T., Krejčí, T., Novák, J., Patzák, B., and Zeman, J. (2008). Technical report for JE Temelín ZS1020 - Opatření pro dlouhodobý stabilní a akceptovatelný provoz ochranných obálek JE Temelín. Technical report, Faculty of Civil Engineering, Czech Technical University in Prague. In Czech.

[Bogacki and Shampine, 1989] Bogacki, P. and Shampine, L. (1989). A 3(2) pair of Runge - Kutta formulas. *Applied Mathematics Letters*, 2(4):321 – 325.

[CEB, 2008] CEB (2008). *CEB-FIP Model Code 1990*. Thomas Telford Ltd.

[CEZ, 2021] CEZ (2021). Cez group, Čez, a. s., virtual tour web page. *http://virtualniprohlidky.cez.cz/*.

[Chen and Chen, 1975] Chen, A. and Chen, W. (1975). Constitutive relations for concrete. *Journal of Engineering Mechechnics - ASCE*, 101(EM4):465–481.

[Conti et al., 2013] Conti, R., Tamagnini, C., and Desimone, A. (2013). Critical softening in Cam-Clay plasticity: Adaptive viscous regularization, dilated time and numerical integration across stress–strain jump discontinuities. *Computer Methods in Applied Mechanics and Engineering*, 258:118–133.

[Crisfield, 1991] Crisfield, M. A. (1991). *Non-linear Finite Element Analysis of Solids and Structures*. UK. John Wiley & Sons Ltd, Chichester.

[CTU, 2010] CTU (2010). Karlův most IS. *http://iskarluvmost.fsv.cvut.cz/*.

[Darcy, 1856] Darcy, H. (1856). *Les fontaines publiques de la ville Dijon*. Dalmon. Paris.

[de Boer, 1996] de Boer, R. (1996). Highlights in the historical development of the porous media theory: toward a consistent macroscopic theory. *Applied Mechanics Review*, 49:201–262.

[de Borst, 1987] de Borst, R. (1987). Smeared cracking, plasticity, creep, and thermal loading - unified approach. *Computer Methods in Applied Mechanics and Engineering*, 62(1):89–110.

[Ding et al., 2015] Ding, Y., Huang, W., Sheng, D., and Sloan, S. W. (2015). Numerical study on finite element implementation of hypoplastic models. *Computers and Geotechnics*, 68:78 – 90.

[Dixon et al., 2002] Dixon, D., Chandler, N., Graham, J., and Gray, M. (2002). Two large-scale sealing tests conducted at Atomic Energy of Canada's underground research laboratory: The buffer-container experiment and the isothermal test. *Canadian Geotechnical Journal*, 39:503–518.

[Fernandez, 1972] Fernandez, R. (1972). *Natural convection from cylinders buried in porous media*. PhD thesis, Univ. of Calif., Berkley.

[Fick, 1855] Fick, A. (1855). Über diffusion. *Ann. der Physik und Chemie*, 94:59–86.

[Fillunger, 1913] Fillunger, P. (1913). Der auftrieb in talsperren. *Österr. Wochenschrift für den öffentl. Baudienst*, 19:532–556,567–570.

[Gallipoli et al., 2003] Gallipoli, G., Gens, A., Sharma, R., and Vaunat, J. (2003). An elasto-plastic model for unsaturated soil incorporating the effects of suction and degree of saturation on mechanical behaviour. *Géotechnique*, 53:123–135.

[Gawin et al., 1999] Gawin, D., Majorana, C. E., and Schrefler, B. A. (1999). Numerical analysis of hygro-thermic behaviour and damage of concrete at high temperature. *Mechanics of Cohesive-frictional Materials*, 4(1):37–74.

[Gens et al., 2009] Gens, A., Sánchez, M., Guimarães, L., Alonso, E., Lloret, A., Olivella, S., Villar, M., and Huertas, F. (2009). A full-scale in situ heating test for high-level nuclear waste disposal: Observations, analysis and interpretation. *Geotechnique*, 59:377–399.

[GiD, 2021] GiD (2021). Gid, the personal pre and post-processor. *https://www.gidhome.com/*.

[Grunewald, 2000] Grunewald, J. (2000). *DELPHIN 4.1–Documentation, theoretical fundamentals*. TU Dresden.

[Hassanizadeh and Gray, 1979] Hassanizadeh, M. and Gray, W. G. (1979). General conservation equations for multiphase systems: 1, averaging procedure. *Advances in Water Resources*, 2:131–144.

[Hausmannová, 2017] Hausmannová, L. (2017). *The influence of water pressure on the hydraulic conductivity and swelling pressure of Czech bentonites*. PhD thesis, Czech Technical University in Prague. In Czech.

[Hausmannová and Vašíček, 2014] Hausmannová, L. and Vašíček, R. (2014). Measuring hydraulic conductivity and swelling pressure under high hydraulic gradients. *Geological Society London Special Publications*, 400.

[Hellmich, 1999] Hellmich, C. (1999). *Shotcrete as Part of the New Austrian Tunneling Method: From Thermochemomechanical Material Modeling to Structural Analysis and Safety Assessment of Tunnels*. Institute for Strength of Materials, Vienna University of Technology, Vienna, Austria.

[Hughes, 1987] Hughes, T. J. R. (1987). *The Finite Element Method. Linear Static and Dynamic Finite Element Analysis*. Prentice-Hall, inc. Englewood Cliffs, New Jersey.

[Janda, 2013] Janda, T. (2013). Hypoplastic model for clays: Issues specific to the finite element implementation. In Topping, B. and Iványi, P., editors, *Proceedings of the Fourteenth International Conference on Civil, Structural and Environmental Engineering Computing*, Stirlingshire, United Kingdom. Civil-Comp Press. paper 193.

[Jirásek and Bažant, 2002] Jirásek, M. and Bažant, Z. P. (2002). *Inelastic Analysis of Structures*. John Wiley&Sons, Ltd, Chichester, UK.

[Koudelka and Krejčí, 2008] Koudelka, T. and Krejčí, T. (2008). An anisotropic damage model for concrete in coupled problems. In Topping, B. H. V. and Papadrakakis, M., editors, *Proceedings of the Ninth International Conference on Computational Structures Technology*, Stirlingshire, United Kingdom. Civil-Comp Press. paper 157.

[Koudelka et al., 2010] Koudelka, T., Krejčí, T., and Kruis, J. (2010). Moderate use of object oriented programming for scientific computing. In Topping, B. H. V., Adam, J. M., Pallarés, F. J., Bru, R., and Romero, M. L., editors, *Proceedings of the Seventh International Conference on Engineering Computational Technology*, Stirlingshire, United Kingdom. Civil-Comp Press. paper 68.

[Koudelka et al., 2011] Koudelka, T., Krejčí, T., and Kruis, J. (2011). *Modeling of Building constructions in SIFEL Environment*. CTU Reports. Czech Technical University in Prague, Czech Republic.

[Koudelka et al., 2017] Koudelka, T., Krejčí, T., and Kruis, J. (2017). Coupled hydro-mechanical model for expansive clays. *AIP Conference Proceedings*, 1863(1):290008.

[Koudelka et al., 2018] Koudelka, T., Krejčí, T., and Kruis, J. (2018). Coupled hydro-mechanical model for expansive clays - computer implementation. *Computers and Structures*, 1(1):20–30.

[Koudelka et al., 2009] Koudelka, T., Krejčí, T., and Šejnoha, J. (2009). Analysis of a nuclear power plant containment. In Topping, B. H. V., Costa Neves, L. F., and Barros, R. C., editors, *Proceedings of the Twelfth International Conference on Civil, Structural and Environmental Engineering Computing*, Stirlingshire, United Kingdom. Civil-Comp Press. paper 132.

[Krejčí et al., 2021] Krejčí, T., Koudelka, T., Bernardo, V., and Šejnoha, M. (2021). Effective elastic and fracture properties of regular and irregular masonry from nonlinear homogenization. *Computers & Structures*, 254.

[Krejčí et al., 2009] Krejčí, T., Koudelka, T., Šejnoha, J., and Zeman, J. (2009). Computer simulation of concrete structures subject to cyclic temperature loading. In Topping, B. H. V., Costa Neves, L. F., and Barros, R. C., editors, *Proceedings of the Twelfth International Conference on Civil, Structural and Environmental Engineering Computing*, Stirlingshire, United Kingdom. Civil-Comp Press. paper 131.

[Krejčí et al., 2019] Krejčí, T., Kruis, J., Koudelka, T., and Svoboda, J. (2019). In-situ interaction physical models at the Bukov URF, Mathematical Modeling. Technical Report 314/2018, Czech Technical University in Prague. In Czech.

[Krejčí et al., 2020] Krejčí, T., Kruis, J., and Svoboda, J. (2020). In-situ interaction physical models at the Bukov URF, Interaction experiment - progress report of phase 7-9 No. 2 - addendum. Technical Report 478/2020, Czech Technical University in Prague. In Czech.

[Krejčí et al., 2001] Krejčí, T., Nový, T., Sehnoutek, L., and Šejnoha, J. (2001). *Structure - Subsoil Interaction in view of Transport Process in Porous Media*, volume 5 of *CTU Reports*. Czech Technical University in Prague.

[Krejčí and Šejnoha, 2015] Krejčí, T. and Šejnoha, J. (2015). Evolution of temperature and moisture fields in Charles Bridge in Prague, Computational prediction and measurements. *International Journal of Architectural Heritage*.

[Kruis, 2006] Kruis, J. (2006). *Domain Decomposition Methods for Distributed Computing*. Saxe-Coburg Publications, Kippen, Stirling, Scotland.

[Kruis et al., 2021] Kruis, J., Koudelka, T., and Krejčí, T. (2001–2021). SIFEL package. *http://ksm.fsv.cvut.cz/∼sifel/*.

[Kruis et al., 2010] Kruis, J., Koudelka, T., and Krejčí, T. (2010). Efficient computer implementation of coupled hydro-thermo-mechanical analysis. *Mathematics and Computers in Simulation*, 80:1578–1588. DOI information: 10.1016/j.matcom.2008.11.010.

[Künzel and Kiessl, 1997] Künzel, H. M. and Kiessl, K. (1997). Calculation of heat and moisture transfer in exposed building components. *International Journal of Heat and Mass Transfer*, 40:159–67.

[Lemaitre and Chaboche, 1994] Lemaitre, J. and Chaboche, J. L. (1994). *Mechanics of solid materials*. Cambridge University Press, Cambridge, UK.

[Lourenco et al., 2007] Lourenco, P. B., Milani, G., Tralli, A., and Zucchini, A. (2007). Analysis of masonry structures: review of and recent trends in homogenization techniques. *Canadian Journal of Civil Engineering*, 34(11):1457–1457.

[Maděra et al., 2017] Maděra, J., Kočí, J., Kočí, V., and Kruis, J. (2017). Parallel modeling of hygrothermal performance of external wall made of highly perforated bricks. *Advances in Engineering Software*, 113:47–53. The special issue dedicated to Prof. Cyril Höschl to honour his memory.

[Maděra and Černý, 2005] Maděra, J. and Černý, R. (2005). TRANSMAT - A computer simultaion tool for modeling coupled heat and moisture transport in building materials. In *Proceedings of Workshop 2005*, pages 470–471. Faculty of Civil Engineering, Czech Technical University.

[Mašín, 2010] Mašín, D. (2010). Predicting the dependency of a degree of saturation on void ratio and suction using effective stress principle for unsaturated soils. *International Journal for Numerical and Analytical Methods in Geomechanics*, 34(1):73–90.

[Mašín, 2013] Mašín, D. (2013). Double structure hydromechanical coupling formalism and a model for unsaturated expansive clays. *Engineering Geology*, 165:73–88.

[Mašín, 2017] Mašín, D. (2017). Coupled thermohydromechanical double-structure model for expansive soils. *Journal of Engineering Mechanics*, 143(9).

[Mašín and Khalili, 2016] Mašín, D. and Khalili, N. (2016). Swelling phenomena and effective stress in compacted expansive clays. *Canadian Geotechnical Journal*, 53(1):134–147.

[Mazars and Pijaudier-Cabot, 1989] Mazars, J. and Pijaudier-Cabot, G. (1989). Continuum damage theory - application to concrete. *Journal of Engineering Mechechnics - ASCE*, 115:345–365.

[Milani, 2015] Milani, G. (2015). Four approaches to determine masonry strength domain. *Engineering and Computational Mechanics*, 168:99–121.

[Moran et al., 2018] Moran, M. J., Shapiro, H. N., Boettner, D. D., and Bailey, M. B. (2018). *Fundamentals of Engineering Thermodynamics, 9nd Edition*. J. Wiley.

[MottMacDonald, 2011] MottMacDonald (2011). Partial report on Charles Bridge, Technical Report.

[Nayak and Zienkiewicz, 1972] Nayak, G. C. and Zienkiewicz, O. C. (1972). Convient form of stress invariants for plasticity. *Proc. ASCE*, 98(4):949–954.

[Ottosen and Ristinmaa, 2005] Ottosen, N. S. and Ristinmaa, M. (2005). *The Mechanics of Constitutive Modeling*. Elsevier Science.

[Papa and Taliercio, 1996] Papa, E. and Taliercio, A. (1996). Anisotropic Damage Model for the Multiaxial Static and Fatigue Behaviour of Plain Concrete. *Engineering Fracture Mechanics*, 55(2):163–179.

[Pedersen, 1990] Pedersen, C. R. (1990). *Combined heat and moisture transfer in exposed building constructions*. PhD thesis, Technical University of Denmark, Lingby.

[Pesavento, 2000] Pesavento, F. (2000). *Non linear Modelling of Concrete as Multiphase Porous Material in High Temperature Conditions*. PhD thesis, Università degli Studi di Padova.

[Pietruszczak and Mróz, 1981] Pietruszczak, S. and Mróz, Z. (1981). Finite element analysis of deformation of strain-softening materials. *Numerical Methods in Engineering*, 17:327–334.

[Pusch et al., 1985] Pusch, R., Borgesson, L., and Ramqvist, G. (1985). Final report of the buffer mass test. volume ii: test results. Technical Report SKB-SP-TR–85-12, Stripa Project 85/12. Stockholm: SKB.

[Přikryl and Šťastná, 2010] Přikryl, R. and Šťastná, A. (2010). Contribution of clayey-calcareous silicite to the mechanical properties of structural mortared rubble masonry of medieval Charles Bridge in Prague (Czech Republic). *Engineering Geology*, 115:257–267.

[Přikryl et al., 2011] Přikryl, R., Weishauptová, Z., Novotná, M., Přikrylová, J., and Šťastná, A. (2011). Physical and mechanical properties of the repaired sandstone ashlars in the facing masonry of Charles Bridge in Prague (Czech Republic) and an analytical study for the causes of its rapid decay. *Environmental Earth Sciences*, 63(7-8):1623–1639.

[Romero et al., 2011] Romero, E., Vecchia, G. D., and Jomi, C. (2011). An insight into the water retention properties of compacted clayey soils. *Géotechnique*, 61 (4):313–328.

[Roscoe and Burland, 1968] Roscoe, K. H. and Burland, J. B. . (1968). *On the generalised stress - strain behaviour of "wet" clay*, pages 535–609. Cambridge University Press, Cambridge.

[Roscoe et al., 1963] Roscoe, K. H., Schofield, A. N., and Thurairajah, A. (1963). Yielding of clays in states wetter than critical. *Géotechnique*, 13(3):211–240.

[Rypl, 2021] Rypl, D. (2001–2021). T3D mesh generator - automatic triangulation of 3D domains. *http://mech.fsv.cvut.cz/∼dr/t3d.html*.

[Sánchez et al., 2005] Sánchez, M., Gens, A., and aes, L. D. N. G. (2005). A double structure generalized plasticity model for expansive materials. *International Journal for Numericaland Analytical Methods in Geomechanics*, 29:751–787.

[Scaringi et al., 2022] Scaringi, G., Mašín, D., Najser, J., Sun, H., and Sun, Z. (2022). Thermo-hydro-mechanical hypoplastic modelling of bentonite buffers for nuclear waste disposal: model calibration and performance. In *In preparation for Proceedings of the 20th International Conference on Soil Mechanics and Geotechnical Engineering, Sydney 2022*.

[Schofield and Wroth, 1968] Schofield, A. N. and Wroth, C. P. (1968). *Critical State Soil Mechanics*. MCGraw-Hill,New York.

[Schrefler et al., 2002] Schrefler, B. A., Brunello, P., Gawin, D., Majorana, C. E., and Pesavento, F. (2002). Concrete at high temperature with application to tunnel fire. *Computational Mechanics*, 29(1):43–51.

[Schrefler and Lewis, 1998] Schrefler, B. A. and Lewis, R. W. (1998). *The Finite Element Method in the Static and Dynamic Deformation and Consolidation of Porous Media*. 2nd Edition. John Wiley & Sons.

[Selvadurai, 1997] Selvadurai, A. (1997). Hydro-thermo-mechanics of engineered clay barriers and geological barriers. *Engineering Geology*, 47(4):311 – 312. Hydro-Thermo-Mechanics of Engineered Clay Barriers and Geological Barriers.

[Skrzypek and Ganczarski, 1999] Skrzypek, J. and Ganczarski, A. (1999). *Modeling of Material Damage and Failure of Structures*. Springer-Verlag Berlin Heidelberg, Germany.

[Sun et al., 2021] Sun, H., Scaringi, G., Mašín, D., and Najser, J. (2021). An experimental investigation on the swelling behavior of compacted b75 bentonite. *Engineering Geology*, page 106452.

[SÚRAO, 2021] SÚRAO (2021). Bukov underground research facility. *https://www.pvpbukov.cz*.

[Svoboda et al., 2019a] Svoboda, J., Vašíček, R., and Pacovská, D. (2019a). In-situ interaction physical models at the Bukov URF, Experiment Installation, Technical Report No. 5. Technical Report 371/2019, Czech Technical University in Prague. In Czech.

[Svoboda et al., 2019b] Svoboda, J., Vašíček, R., Pacovská, D., Šťástka, J., Franěk, J., Rukavičková, L., Večerník, P., and Červika, R. (2019b). In-situ interaction physical models at the Bukov URF, Interaction experiment - supporting and preparatory works. Technical Report 385/2019, Czech Technical University in Prague. In Czech.

[Sýkora et al., 2009] Sýkora, J., Vorel, J., Krejčí, T., Šejnoha, M., and Šejnoha, J. (2009). Analysis of coupled heat and moisture transfer in masonry structures. *Materials and Structures*, 42(8):1153–1167.

[Tamagnini et al., 2000] Tamagnini, C., Viggiani, G., and Chambon, R. (2000). A review of two different approaches to hypoplasticity.

[Toesca, 2014] Toesca, M. (2014). Thermo-Mechanical Analysis of Charles Bridge. Master's thesis, Faculty of Civil Engineering, Czech Technical University in Prague.

[Tschoegl, 1971] Tschoegl, N. W. (1971). A general method for determination of approximations to the spectral distributions from the transient response functions. *Rheol. Acta*, 10:595–600.

[Tschoegl, 1989] Tschoegl, N. W. (1989). *The phenomenological theory of linear viscoelastic behavior*. Germany. Springer-Verlag, Berlin.

[Ďurana et al., 2013] Ďurana, K., Maděra, J., and Černý, R. (2013). Database of climatic data as a rewarding tool for inclusion of weather observations in computational service life assessments of historical buildings. *WIT Transactions on the Built Environment*, 131:245–256.

[von Terzaghi, 1923] von Terzaghi, K. (1923). Die Berechnung der Durchässigkeitsziffer des Tones aus dem Verlauf der hydrodynamischen Spannungserscheinungen. *Sitzungsber. Akad. Wiss, Math. - Naturwiss., Section IIa*, 123(3/4):125–138.

[Šťástka et al., 2018] Šťástka, J., Pacovský, J., and Vašíček, R. (2018). Construction, Operation and Evaluation of the Mock-up-Josef Demonstration Experiment - Final Project Report. Technical Report 2014-3047, Czech Technical University in Prague, SURAO. In Czech.

[Šťastná et al., 2009] Šťastná, A., Přikryl, R., and Jehlička, J. (2009). Methodology of analytical study for provenance determination of marbles. *Journal of Cultural Heritage*, 10:82–93.

[Štěpán, 2005] Štěpán, J. (2005). Posouzení lokální napjatosti stěny ochranné obálky s uvážením oslabení stěn kabelovými kanálky. Technical Report EGP 5043-F-060137, ÚJV ŘeŽ, a.s. In Czech.

[Witzany et al., 2008] Witzany, J., Čejka, T., and Zigler, R. (2008). Failure resistance of historic stone bridge structure of charles bridge. ii: Susceptibility to floods. *Journal of Performance of Constructed Facilities*, 22(2):83–91.

[Witzany and Zigler, 2007] Witzany, J. and Zigler, R. (2007). The analysis of non-stress effects on historical stone bridge structures (monitoring, theoretical analysis, maintenance). *Journal of Civil engineering and Management*, 13(2):157–167.

[Woltman, 1974] Woltman, R. (1974). *Beiträge zur hydralischen Architektur*, volume 3. Götingen.

[Zeman et al., 2008] Zeman, J., Novák, J., Šejnoha, M., and Šejnoha, J. (2008). Pragmatic multi-scale and multi-physics analysis of Charles Bridge in Prague. *Engineering Structures*, 30(11):3365–3376.

[Zhang et al., 2001] Zhang, H., Heeres, O., Borst, R., and Schrefler, B. (2001). Implicit integration of a generalized plasticity constitutive model for partially saturated soil. *Engineering Computations*, 18:314–336.

[Zienkiewicz and Taylor, 2000] Zienkiewicz, O. C. and Taylor, R. L. (2000). *The Finite Element Method*, volume Volume 1: The Basis. Butterworth-Heinemann.